博士学位论文

华北克拉通在奴那/哥伦比亚超大陆中的位置：古地磁及地质对比综合约束

作者姓名：王 冲

指导教师：彭 澎 研究员 中国科学院地质与地球物理研究所

李正祥 教 授 澳大利亚科廷大学

Sergei Pisarevsky 博士 澳大利亚科廷大学

学位类别：理学博士

学科专业：矿物学、岩石学、矿床学

培养单位：中国科学院地质与地球物理研究所

2019 年 6 月

Paleogeographic reconstruction of the North China Craton in the supercontinent Nuna/Columbia: paleomagnetic and geological constraints

A dissertation submitted to
University of Chinese Academy of Sciences
in partial fulfillment of the requirement
for the degree of
Doctor of Science
in Mineralogy, Petrology and Economic Geology
By

Chong Wang
Supervisors: Professors Peng Peng, Zheng-Xiang Li and
Doctor Sergei Pisarevsky

Institute of Geology and Geophysics,
Chinese Academy of Sciences

June 2019

中国科学院大学
研究生学位论文原创性声明

本人郑重声明：所呈交的学位论文是本人在导师的指导下独立进行研究工作所取得的成果。尽我所知，除文中已经注明引用的内容外，本论文不包含任何其他个人或集体已经发表或撰写过的研究成果。对论文所涉及的研究工作做出贡献的其他个人和集体，均已在文中以明确方式标明或致谢。

作者签名：

日　期：

中国科学院大学
学位论文授权使用声明

本人完全了解并同意遵守中国科学院有关保存和使用学位论文的规定，即中国科学院有权保留送交学位论文的副本，允许该论文被查阅，可以按照学术研究公开原则和保护知识产权的原则公布该论文的全部或部分内容，可以采用影印、缩印或其他复制手段保存、汇编本学位论文。

涉密及延迟公开的学位论文在解密或延迟期后适用本声明。

作者签名：　　导师签名：

日　期：　　日　期：

摘 要

随着超大陆的概念被广泛的接受，重建更早时期的超大陆成为研究者的重点研究内容。目前，研究认为前寒武纪存在~1.8–1.6 Ga 形成的奴那（或称哥伦比亚）超大陆和~1.0–0.9 Ga 形成的罗迪尼亚超大陆，但对于超大陆的格局仍存争议。

本研究以华北克拉通冀东、鲁西及太行山南部的岩墙为研究对象，通过对岩墙群的年代学、地球化学和古地磁学分析探讨元古宙华北克拉通在全球古地理中的位置。通过斜锆石 U–Pb 分析，获得冀东老王家岩墙 1233 ± 27 Ma（SIMS）、密云白河涧岩墙 1206.7 ± 1.7 Ma（TIMS）、辽西清原岩墙 1214.0 ± 4.9 Ma（TIMS）和兴隆米铺岩墙 1236.3 ± 5.4 Ma（TIMS）的侵位年龄。结合前人发表的数据，认为华北~1.24–1.21 Ga 的岩浆作用从岩石化学上为亚碱性到碱性玄武质岩石系列。地球化学数据表明岩石有类似洋岛玄武岩（OIB）的微量元素特征，可能形成于板内环境。除此之外，放射状的基性岩墙群覆盖面积> 0.1 Mkm^2，暗示该期岩墙可能是由地幔柱引发的大火成岩省，命名为黎城大火成岩省，初步限定其活动时限为~1.24–1.21 Ga。

本研究在三个研究区采集了元古宙不同时代（~1.68 Ga、~1.24 Ga 和~1.21 Ga）岩墙群的古地磁样品进行分析。岩石磁学实验（热磁曲线、Lowrie 实验和磁滞回线分析）表明，这些岩墙群含载磁稳定的单畴或假单畴低钛钛磁铁矿。三条~1.68 Ga 岩墙给出的虚地磁极为 55.6°N, 258.1°E（A_{95} = 7.2°），将此结果与已报道的华北南缘<1.71–1.61 Ga（最佳估计~1.70–1.67 Ga）云梦山组的极结合，获得~1.68 Ga 古地磁极（59.8°N，265.3°E，A_{95} = 3.3°）。此外，从 9 条~1.24 Ga 岩墙中获得了古地磁极（2.6°N，165.1°E，A_{95} = 10.8°），从 1 条~1.21 Ga 岩墙中获得了虚地磁极（-23.0°N，92.5°E，A_{95} = 6.1°）。~1.24 Ga 的古地磁极通过了烘烤检验。通过对比澳大利亚陆块的古地磁极与视极移曲线，本文认为华北东北部与澳大利亚陆块西北部在~1.78–1.32 Ga 间具有亲缘性，之后发生分离。

上述解释得到了~1.73–1.32 Ga 地质记录的支持。相似的地质记录来自华北

燕辽裂谷地区和北澳麦克阿瑟盆地地区，包括：① 二者在~1.70–1.58 Ga 具有可对比的沉积记录，并在~1.65 Ga 同时出现最古老的真核生物微化石 *Valeria lophostriata*；② 铁矿层和锰矿层同时出现在二者的对应沉积层位；③ 近同期的层位中也发现了含烃层；④ 在相关地区，两个陆块同时出现了~1.73 和 1.32 Ga 基性侵入岩、~1.72 Ga 酸性侵入岩及~1.64、1.62 和 1.49 Ga 相关的火山作用记录。

综上，根据古地磁的对比及综合地质对比，本研究认为奴那/哥伦比亚超大陆时期，华北东北部与澳大利亚西北部长时间相连。

关键词：华北克拉通，基性岩墙群，大火成岩省，古地磁，奴那/哥伦比亚超大陆

Abstract

It has been proposed that the assembly of the supercontinent Nuna (also known as Columbia) occurred during ~1.8–1.6 Ga, and that of the supercontinent Rodinia occurred at ~1.0–0.9 Ga, but the exact configurations of the two early supercontinents are still in debated. The North China Craton (NCC) has abundant Precambrian geological records, but its positions in the two supercontinents are still controversal.

This study aims to explore the position of the NCC in Nuna through geochronological, geochemical and paleomagnetic analyses of mafic dykes in the Jidong, Luxi and southern Taihang regions. Through baddeleyite U–Pb analyses, dykes with ages of 1233 ± 27 Ma (SIMS), 1206.7 ± 1.7 Ma (TIMS), 1214.0 ± 4.9 Ma (TIMS) and 1236.3 ± 5.4 Ma (TIMS) have been identified. The ~1.24–1.21 Ga magmatism in the NCC are subalkaline to alkaline basaltic composition. Geochemical data indicate an intraplate tectonic setting with ocean island basalt (OIB)–like trace element signatures. In addition, the radiating dykes cover an area of > 0.1 Mkm^2, indicating a ~1.24–1.21 Ga LIP event caused by a mantle plume in the NCC, namely the Licheng LIP.

Detailed rock magnetic and pelaomagnetic analyses have been carried out on these and other previously dated mafic dykes, with ages of ~1.68, 1.24 and 1.21 Ga in the three regions of the NCC. Rock magnetic experiments, including κ–T curves, Lowrie and hysteresis loop experiments show that the main magnetic carrier is the paleomagnetically stable single (or pseudo–single) domain low–Ti titanomagnetite. Three ~1.68 Ga dykes give a mean paleopole at 55.6°N, 258.1°E (A_{95} = 7.2°). Combining this pole with previously published data from the <1.71–1.61 Ga (best estimate ~1.70–1.67 Ga) Yunmengshan Formation in southern NCC, these units give a mean ~1.68 Ga paleomagnetic pole at 59.8°N, 265.3°E (A_{95} = 3.3°, N = 18). Nine ~1.24 Ga dykes give a mean paleomagnetic pole at 2.6°N, 165.1°E (A_{95} = 10.8°), supported by a positive baked contact test. One ~1.21 Ga dyke give a VGP at -23.0°N, 92.5°E (A_{95} = 6.1°). Comparable coeval paleopoles and apparent polar wander paths for the North China and proto-Australian cratons suggest their possible connection during

~1.78–1.32 Ga, but separation after that time.

Such an interpreted long-lived connection is supported by ~1.73–1.32 Ga geological similarities between the Yanliao rift of the NCC and the McArthur Basin of the North Australian Craton. Their similarities include ① comparable sedimentary lithology, and eukaryotic microfossils *Valeria lophostriata*, ② styles of ore deposits (manganese and iron), ③ hydrocarbon-bearing potential (hydrocarbon source rocks), and ④ coeval magmatism (mafic and fesic intrusive magmatism, and volcanic events).

In summary, based on the comparable paleomagnetic data and geological histories, this work proposes a long-lived connection between the northeastern NCC and northwestern proto-Australia for the duration of the supercontinent Nuna/Columbia.

Key Words: North China Craton, Mafic dyke swarm, Large igneous province, Paleomagnetism, Supercontinent Nuna/Columbia

目 录

第1章 引言

1.1 选题背景

1912 年，魏格纳提出大陆漂移假说 (Wegener, 1912)。随后，他提出地球曾经（显生宙）存在一个超级大陆，并命名为 Pangea (Wegener, 1915)（中译为潘吉亚、泛大陆、联合古陆或盘古大陆）。上世纪六十年代，传统固定论受到挑战，新兴大陆漂移、海底扩张等学说，板块构造理论逐渐深入人心。随着对板块运动研究的深入，研究者逐渐意识到，不同陆块在更早时期也可能具有亲缘性，继而提出地质历史时期的其他超大陆，它们分别是新元古代早期的罗迪尼亚（Rodinia）超大陆 (McMenamin and McMenamin, 1990)、古元古代晚期/中元古代的奴那或哥伦比亚（Nuna/Columbia）超大陆 (Hoffman, 1997; Rogers and Santosh, 2002; Zhao et al., 2002a)。

在认识早期的超大陆之前，研究者通过对碰撞造山作用及对基性岩墙群峰期的总结（分别对应超大陆的聚合和裂解），认为存在超大陆旋回（supercontinent cycle），并预测其他超大陆的存在 (Worsley et al., 1984)。而超大陆旋回的提出是建立在对地质构造阵发性（tectonic episodicity）长期总结的基础之上，比如造山作用、大陆地壳的形成、显生宙的沉积旋回、矿床的形成等 (Nance and Murphy, 2013 及参考其中)。研究表明，地质历史中每隔 5 至 6.5 亿年甚至 10 亿年将出现一次超大陆 (Condie et al., 2015)。超大陆旋回，基本体现为全球陆块的漂移、聚合和裂解过程，但其对海平面的变化、海水的氧化还原状态、大气的氮氧含量、冰川活动及物种的演化、矿产资源 (Ernst and Youbi, 2017; Pastor-Galán et al., 2018; Pehrsson et al., 2016)，乃至地幔地球动力学等均有影响 (Li and Zhong, 2009; Zhong et al., 2007)，同时，也与地球磁场的活动相关 (Evans, 2002)，是研究地球系统科学的关键。目前，全球多个 IGCP（International Geological Correlation Programme/ International Geoscience Programme）项目，通过广泛的合作，致力于揭示超大陆的演化规律。

对超大陆的研究，最基本的任务是重建全球构型。之前，由于缺乏相关时

期的岩浆作用记录，尤其是新元古代的构造热事件，研究者认为华北克拉通（North China Craton，NCC）处于前寒武纪超大陆的边缘 (Li et al., 1996, 2008)，或没有参与超大陆的聚合和裂解过程 (Lu et al., 2008)。但随着近十多年研究的深入，研究者们在华北识别出了多期中新元古代基性岩墙群，这些岩浆作用“条形码”为探讨华北与超大陆的关系提供了依据 (Peng, 2015b 及参考其中)。目前，多数研究者认为华北参与了前寒武纪超大陆的演化，但对其在超大陆中的位置及聚合和裂解的响应时间仍存争议。其中，观点包括：

① 通过对比华北北部燕辽裂谷中新元古代地层与西伯利亚里菲纪地层，研究者认为二者可能存在亲缘性，即华北的北缘与西伯利亚西缘相连，并认为该连接广泛存在于中新元古代 (Li et al., 1996)。② 2.0–1.8 Ga 全球广泛发育造山带，研究者认为通过这些造山带及两侧基底的对比研究可恢复古大陆。基于这一思路，结合对华北前寒武纪高压麻粒岩（造山带）的研究，研究者认为 1.8 Ga 前后华北可能和西伯利亚相连 (Condie, 2002)、华北南缘和波罗地相连 (Qian, 1997; Wilde et al., 2002)、华北北缘和印度 (Zhao et al., 2002a; Zhao et al., 2011; Zhao et al., 2003)（图 1.1a）或与南美、波罗地 (Kusky et al., 2007) 相连。此外，Wan et al. (2015a) 在华北北缘发现一套变质岩石单元，通过对比研究认为，在 1.8 Ga 前后，该地区俯冲到了西伯利亚之下，认为奴那/哥伦比亚超大陆时期华北北缘与西伯利亚克拉通相连。③ 与裂解相关的基性岩墙群通常呈放射状形态产出 (Ernst et al., 1995, 2001)，如全球规模最大的岩墙群——北美麦肯齐岩墙群。如果能够厘定同期岩墙的几何学形态，并与其他陆块同期岩墙对比，即可恢复古陆形态。华北 1.78 Ga 的太行–吕梁岩墙群是中国规模最大的一期基性岩墙群 (Qian and Chen, 1987)。基于对岩墙的年代学、地球化学及产状的研究，研究者认为华北南部在该时期可能和印度、北美相连 (Hou et al., 2008; Peng et al., 2005)（图 1.1b，c）。另外，华北北部燕辽地区发育有~1.32 Ga 的基性岩床群，研究者据此认为这一时期华北可能与劳伦及西伯利亚相邻 (Zhang et al., 2009) 或华北东北部与北澳 (Zhang et al., 2017) 相邻（图 1.1f）。华北与澳大利亚陆块的亲缘性得到了部分古地磁结果的支持 (Zhang et al., 2012b)，但呈不同的连接形态（图 1.1e）。基于对 1.78 Ga 以及 0.92 Ga 岩浆作用的厘定和认识，研究者同样提出华

北南缘在该时期可能和波罗地及圣弗朗西斯科克拉通相连 (Peng, 2015b)（图 1.1d）。同样，~1.23 Ga 岩墙的发现被认为是华北北缘与圣弗朗西斯科裂解的标志 (Wang et al., 2015a)。

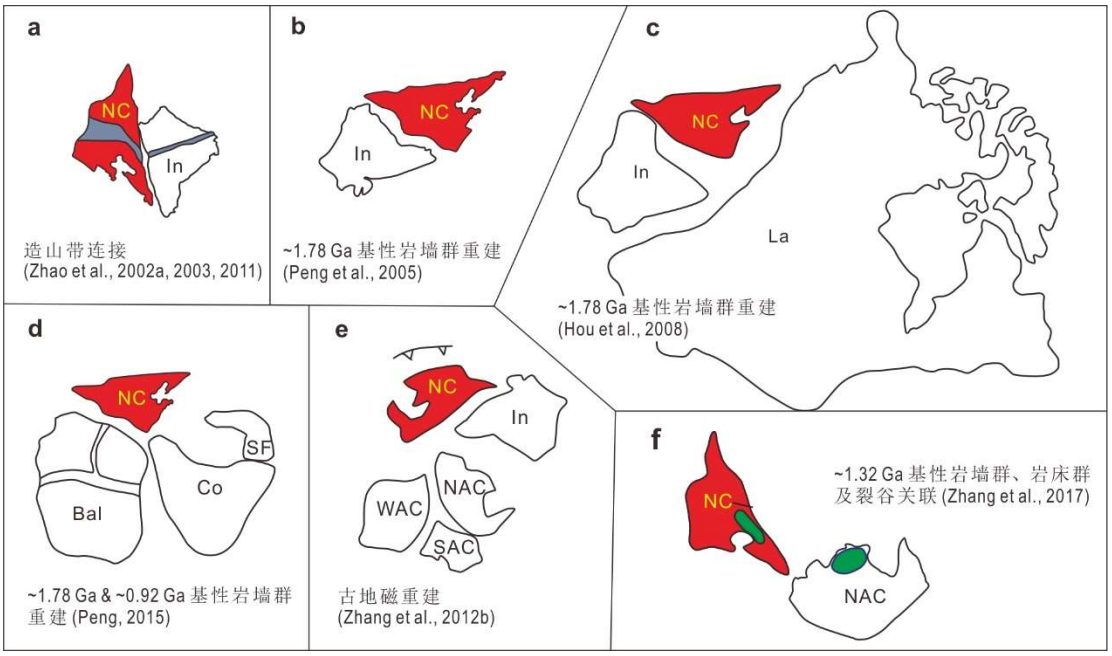

图 1.1 华北前寒武纪古大陆重建模型。详细见文中说明。NC–华北；In–印度；NAC–北澳；WAC–西澳；SAC–南澳；Bal–波罗地；Co–刚果；SF– 圣弗朗西斯科；La–劳伦

Fig. 1.1 Various models showing the surrounding paleogeography of the NCC in Proterozoic. Detailed explanations see the text. NC–North China; In–India; NAC–Northern Australia; WAC–Western Australia; SAC–Southern Australia; Bal–Baltica; Co–Congo; SF–São Francisco; La–Laurentia

1.2 选题及研究内容

1.2.1 选题依据、内容及科学问题

上述介绍中提到，在元古宙古大陆重建中，华北克拉通的相对位置存在很大的争议（图 1.1），比如华北与印度 (Chen et al., 2013; Hou et al., 2008; Peng et al., 2005; Xu et al., 2014; Zhang et al., 2012b; Zhao et al., 2002a)，与劳伦 (Hou et al., 2008)，与澳大利亚陆块 (Xu et al., 2014; Zhang et al., 2012b, 2017)，与西伯利亚 (Chen et al., 2013; Li et al., 1996)，与波罗地 (Buchan, 2013; Peng, 2015b)，及与刚果/圣弗朗西斯科 (Cederberg et al., 2016; Peng, 2015b; Xu et al., 2017) 等相邻。这些争议不仅限于华北与哪个陆块相连，而且在与某一陆块间也存在多样的连接方式，比如华北与印度（图 1.1a–c，e）。本研究以此为选题依据，以古大陆重

建中的重要载体——基性岩墙为研究对象，拟通过大火成岩省的识别、古地磁的研究及其他地质记录对比等方法，综合探索华北克拉通在前寒武纪超大陆中的位置；进而为全球超大陆的重建提供依据，为进一步探讨资源环境效应与地球动力学提供观测基础。

1.2.2 研究区选择

本研究聚焦东华北克拉通，东华北克拉通是指古元古代徐武家弧（与大同–环县断裂大致吻合）东部的华北克拉通区域 (Peng et al., 2014)。本研究以冀东－密云、鲁西及太行山南部的基性岩墙为研究对象。

天津蓟县及冀东发育有较为连续的古元古代晚期至中－新元古代盖层（~1.7–0.8？Ga），即传统认为的燕辽裂谷系。该序列可能与超大陆的裂解耦合 (Meng et al., 2011)；且该区目前报道有 1.68 Ga、1.62 Ga、1.32 Ga、1.23 Ga 和 0.775 Ga 基性岩浆作用 (Li et al., 2015; Peng et al., 2013; Wang et al., 2014a, 2015a, 2016b)，这些岩浆作用可能是对超大陆裂解过程的响应，因此，本区是探讨华北北部古地理重建的理想研究区域（见第 3 章介绍）。

从裂谷形态上讲，太行山南部为燕辽的南向分支，同样出露部分地层，并被~1.23 Ga (Peng, 2015b) 及一些时代未知的基性岩墙侵入。而鲁西地区虽然远离燕辽裂谷的沉积范围，但是报道有~1.68 Ga 和 1.62 Ga 的基性岩墙群 (Li et al., 2015; 相振群等, 2012)，这些岩浆活动可能和燕辽裂谷断陷时期的断层控制有关。因此，本研究所选择的冀东、鲁西和太行山南部地区均为中新元古代裂谷相关的区域，且已有研究表明这些地区伴随有基性岩浆侵入事件，可以以此为窗口探讨华北克拉通对超大陆的响应。

1.2.3 研究载体、方案与技术路线

（1）研究载体

本研究选择基性岩墙作为研究载体。基性岩墙是指来自地幔的基性岩浆，以扁平状侵入体的形式上侵到浅层地壳中。基性岩墙通常侵入时间较短，是一段时间之后显著的地质事件。一般大型基性岩墙成群出现，具有稳定的走向并近于直立产出。基性岩墙群在古大陆研究中具有重要的价值，放射状的基性岩

墙群可能与地幔柱作用下的大陆裂解相关，可以以此来恢复古大陆 (Ernst et al., 1995, 2001)。具体思路是，地幔柱引发的放射状基性岩墙群随大陆的裂解，分散在不同的陆块中。倘若在不同陆块中识别出同期的大型基性岩墙群，并利用地球化学特征证明这些岩体有成因联系，则能通过恢复原始几何学形态的方式重建古大陆。因此，对岩墙进行野外调查，统计产状，厘定侵位时间，是首要工作。

此外，基性岩浆侵位冷却时，磁铁矿以副矿物形式结晶；当温度持续下降，至磁铁矿的居里点~580℃时，这些矿物会记录板块位置与地球磁场信息，通过研究可获得古地磁极（paleomagnetic pole）以重建古大陆 (Halls, 2008)。后期的热构造事件可能会对原生磁信号产生影响，但通过野外检验能够判断获得的磁化信息是否为原生（见 9.3.1，烘烤检验介绍）。再者，大型基性岩墙一般（近于）直立侵入浅层地壳（倾斜在 5°范围内），具有产状自明性，这种特征便于对测得的磁化方向进行构造矫正 (Halls, 2008)。因此，基性岩墙是进行古地磁研究的优良载体。

（2）研究方案

本研究将从以下四个方面开展工作（图 1.2 ）：

① 野外调查识别岩墙，并厘定其产状和分布；

② 对岩墙进行定年，及地球化学分析；综合对比厘定岩墙期次，分析其岩石成因；

③ 对岩墙进行古地磁采样并分析，以获得古地磁极；

④ 综合古地磁数据及地质资料，探讨重建；

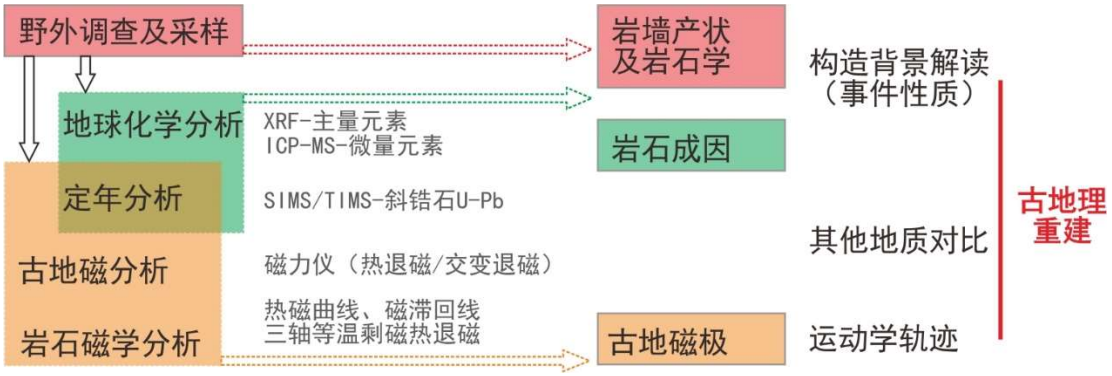

图 1.2 研究方案与技术路线

Fig. 1.2 Study method and technical roadmap

岩墙群条形码及古地磁对比（视极移曲线及同期古地磁极对比见 2.2 研究方法部分）可以为古陆重建提供线索，但最终的重建模式还需要综合地质对比。综合地质对比包括岩浆记录对比（岩墙/岩床群及大火成岩省）、沉积记录对比及沉积环境与沉积相分析、碎屑锆石指示源区对比、古生物记录对比、矿产资源种类及成因对比等。本研究拟兼顾这些进行讨论，古地磁及地质对比的综合研究将为古陆重建提供更客观更全面的依据，但每个方法亦有局限性，如何兼顾而不是顾此失彼是必须要考虑的问题。

（3）技术路线

上述工作中，对岩墙的定年及获得原生的古地磁极是难点。本研究致力于对岩墙进行斜锆石和/或锆石 U–Pb 定年。斜锆石（ZrO_2）是基性岩定年的理想矿物，因为其含有较高的铀含量、封闭温度高、成因简单 (Heaman and LeCheminant, 1993)，但基性岩若结晶不充分又往往难于获得斜锆石。锆石（$ZrSiO_4$）为硅酸盐副矿物，而基性岩浆为硅不饱和岩浆，难以结晶大量锆石。侵入岩在岩浆上升侵位过程中又会捕获围岩，继承围岩中的锆石，使得在基性岩中分选的锆石复杂多样。本研究使用岩石圈演化国家重点实验室 Cameca 离子探针对斜锆石和锆石进行原位分析；在澳大利亚科廷大学 John de Laeter 研究中心热电离质谱实验室对斜锆石进行分析。离子探针及热电离质谱分析方法成熟，但最终只有对斜锆石的分析获得了有效的年龄。因岩墙定年较为困难，研究中并不能对每条岩墙进行定年，本文结合地球化学数据（主量及微量元素）及古地磁数据对岩墙进行期次归类。

精确的年龄是古地磁应用解读的基础。除此之外，古地磁研究的难点存在于特征剩磁获得时代的确定，也就是剩磁原生性的判定。对于岩墙的研究，通常使用烘烤检验，但岩墙通过烘烤检验并非易事，详细见 9.3.1 烘烤检验介绍。此外，古地磁研究以轴向地心偶极子场假设为基础，为平均地球磁场的长期变化，需要找到同期的更多的岩墙做方向的平均（岩墙侵位冷却时间短）。但华北是地台型克拉通，盖层发育，且人口密度大，露头受人类活动影响大，在地质资料公开及便利获取有限的情况下，想要找到更多的岩墙，或者进一步通过航磁图看到分布范围，也非易事。实际重建的可靠性还往往受古地磁极数量及质

量的限制。

1.2.4 研究进展与工作量

本研究中，野外新识别岩墙＞70 条，其中对 5 条岩墙进行了斜锆石定年分析，对约 42 条进行了地球化学分析，约 40 条作为古地磁重点分析对象。结合实验结果，对华北~1.68 Ga 及~1.24–1.21 Ga 岩浆作用进行了细致研究，以此探讨华北在古元古代晚期至中元古代时期周边的古大陆。工作进度与工作量参照表 1.1 和表 1.2。

本文将介绍实验结果、重建分析、存在的问题以及未来工作计划。其中，第 1 章介绍选题概况；第 2 章介绍超大陆的研究进展与前沿；第 3 章介绍地质背景；第 4 章介绍野外调查、采样与岩相学；第 5–8 章分别介绍年代学、地球化学、古地磁学、岩石磁学和磁组构的分析方法与结果；第 9 章讨论~1.24–1.21 Ga 岩墙的岩石成因，论证其为大火成岩省的可能性，并从古地磁和地质对比的角度探讨华北与北澳克拉通在元古宙的亲缘性；第 10 章为结论及存在的问题。

表 1.1 工作进度

Table 1.1 Timeline of work

年份	2016												2017												2018												2019				
月份	8	9	10	11	12	1	2	3	4	5	6	7	8	9	10	11	12	1	2	3	4	5	6	7	8	9	10	11	12	1	2	3	4	5
文献阅读																																		
野外调查																																		
单矿物分选																																		
地球化学分析																																		
课程学习																																		
开题																																		
年代学分析																																		
古地磁分析																																		
数据解释																																		
撰写文章																																		
中期																																		
撰写毕业论文																																		
论文答辩																																		

注：2017 年 8 月至 2019 年 1 月在澳大利亚科廷大学学习

表 1.2 工作量

Table 1.2 Quantity of work

工作内容	工作量	备注
基性岩墙野外调查	＞70 条；~80 天	未变质岩墙~50 条；古地磁采样~35 天
镜下薄片观察	~80 件	与最终成果相关薄片~25 件
单矿物定年	5+10 件	有效年龄 5 件（斜锆石样品）
地球化学分析	65 组	全岩主量和微量元素；与最终成果相关数据 13 组
古地磁采样	612 件（sample）	40 条岩墙及部分围岩
磁化率各向异性分析	913 件（specimen）	40 条岩墙
古地磁分析（方向）	834 件（specimen）	含围岩样品；含交变和热退
岩石磁学－热磁曲线分析	18 件	~1.68 Ga 和~1.24–1.21 Ga 样品 13 件
岩石磁学－三轴等温剩磁热退磁分析	10 件	~1.68 Ga 和~1.24–1.21 Ga 样品
岩石磁学－磁滞回线分析	14 件	~1.68 Ga 和~1.24–1.21 Ga 样品

第2章 超大陆及重建

2.1 超大陆的概念

魏格纳最早意识到南美和南非海岸线轮廓的匹配，并提出了大陆漂移的理论，进而假想超级大陆潘吉亚的存在 (Wegener, 1915)。超大陆，顾名思义就是一个很大或超大的陆块，目前提出的包括假设的超大陆有潘吉亚（Pangea）、冈瓦纳（Gondwana）、潘诺西亚（Pannotia）(Nance and Murphy, 2018)、罗迪尼亚（Rodinia）(McMenamin and McMenamin, 1990)、奴那/哥伦比亚（Nuna/Columbia）(Hoffman, 1997; Rogers and Santosh, 2002; Zhao et al., 2002a)、（超级克拉通）凯诺兰/克洛兰（Kenorland）(Williams et al., 1991) 以及未来超大陆阿美西亚（Amasia）(Hoffman, 1999; Mitchell et al., 2012)。虽然有如此多超大陆被提出，但对超大陆的定义一直比较模糊。近些年，随着对超大陆研究的深入，尤其在探讨与地幔动力学的耦合关系方面，对超大陆概念的解读愈发重要 (如 Meert and Santosh, 2017; Pastor-Galán et al., 2018)。目前，关于超大陆有以下几种定义：

A. 几乎所有大陆的聚合体（“… so Rodinia must have been a supercontinent (i.e. a clustering of virtually all continents)” (Hoffman, 1999) ）;

B. 包含所有或者近乎所有的地球陆块的聚合体（“supercontinents are assemblies that contain all, or nearly all, of the earth’s continental block (Rogers and Santosh, 2004) ” ）;

C. 至少包含当时 75%的地壳的聚合陆块（“… a proposition that 75% of the Earth's preserved crust (of the relevant age) should be present in any reconstructed supercontinent seems reasonable (for example 75% of Archean nuclei should be part of any Archean supercontinent) ” (Meert, 2012)）;

D. 能够影响地幔对流模式及核幔边界过程的一个大陆板块（“… a ‘supercontinent’ is a single continental plate of a size capable of influencing mantle convection patterns and core–mantle boundary processes)” (Pastor-Galán et al., 2018) ）;

前两种定义比较相似，是通俗的超大陆概念。在给出 B 定义的同时，研究者也强调超大陆聚合和裂解过程在时间上的重合属性，认为超大陆应当指的是拥有最大岩石圈面积的那个时期，即“最大集成（maximum packing）”(Rogers and Santosh, 2004; Rogers and Santosh, 2009)。C 定义也主要关注超大陆的面积，

即多大的陆块能被称作超大陆。虽然 C 给出了一个参考性的阈值（75%），但很难给出一个确切的依据；在重建中，似乎没有研究者进行量化分析或强调大陆地壳的面积及超大陆的构成面积 (如 Pisarevsky et al., 2014a)。这些定义都倾向于认为冈瓦纳（Gondwana）并不是一个超大陆，有研究者称其为“半超大陆（semi-supercontinent）”，包括当今的欧亚大陆 (Evans et al., 2016a)，但对有多少半超大陆，以及为什么会产生半超大陆依然不得而知。D 定义跳出超大陆“大”的思维模式，以对地幔对流影响的角度去定义超大陆。同时，作者也认为地质历史时期可影响地幔对流的陆块大小可能是不一样的；并结合数值模拟认为，当今欧亚大陆没有影响地幔对流，其大小为地球表面积的＞10%；潘吉亚大陆足以影响地幔对流，其面积为地球表面积的 25%；而冈瓦纳大陆，其面积为地球表面积的~15%，可能是定义超大陆的一个阈值 (Pastor-Galán et al., 2018)。总之，随着对超大陆的深入研究，超大陆是什么的问题也会逐渐科学化和本质化。

2.2 研究方法

显生宙的地质记录丰富连续，借此，研究者对潘吉亚超大陆的重建进行了种种探索，积累了宝贵的经验和方法。一些方法对研究前寒武纪超大陆仍具有指导作用。经总结，有以下超大陆重建方法：

（1）匹配块体轮廓：南美洲与非洲海岸线轮廓的吻合，在大陆漂移的提出中占有一席之地。但前寒武纪块体一般经历过多期演化，原始轮廓很可能受到了改造。

（2）追踪生物群落：一些生物群落的迁移受到海或陆的限制，这为讨论两个陆块的亲缘性提供可能。比如浅水中活动的二叠纪中龙（Mesosaurus），在大洋相隔的非洲和南美洲同时出现（图 2.1a）；以及大西洋两侧的其他动物群落 (Wilson, 1966)。

（3）追踪造山记录：古生代的加里东造山作用（Caledonian Orogen），同时出现在大西洋两岸的斯堪的纳维亚－大不列颠－爱尔兰和挪威－东格陵兰地区；而劳伦东部和非洲西部又同时出现阿巴拉契亚造山作用（Appalachian Orogen），故推测在大西洋打开之前，劳伦东北部与波罗地、劳伦东部与非洲连

在一起（图 2.1b）。本世纪初，研究者主要追踪了古元古代近同期造山带并讨论其联系，提出了哥伦比亚超大陆并重建其全球构型 (Zhao et al., 2002a)。

（4）依据海底磁异常条带闭合大洋：随着新生洋盆的扩大，大洋中脊的扩张，洋中脊两侧玄武岩的磁化随地球磁场的变化呈对称分布 (Vine and Matthews, 1963)（如图 2.1c）；并表现为距离洋中脊越远，时代越老。该理论在海底扩张理论的提出及“有连史可寻”的潘吉亚再造中发挥过重要作用 (如 Seton et al., 2012)。

（5）大火成岩省重建古大陆：一般认为，地幔柱引发了超大陆的裂解，并以大火成岩省（基性岩墙群、岩床群及火山岩）作为地质体现，比如三叠纪与侏罗纪交界的中大西洋岩浆岩省（central atlantic magmatic province，CAMP）广泛出露于北美、亚马逊、波罗地、西非，被认为引发了潘吉亚的裂解 (如 May, 1971; Wilson, 1997)。地幔柱引发的裂解通常产生同期放射状的基性岩墙群 (Ernst et al., 1995, 2001)，据此可以恢复裂解前的古大陆 (Bleeker and Ernst, 2006)（图 2.1e）。

将陆块不同时期的岩浆/大火成岩省记录标记在时间轴上，形成事件条形码（barcode）；而比较不同陆块的条形码则可为追踪它们的关系提供约束，如图 2.1f 所示，陆块 A 和 B 共同经历了 T2、T3 和 T4 时期的岩浆作用事件，借此可进一步论证块体的亲缘性。

（6）古地磁重建古大陆：古地磁研究能为重建提供定量依据，单个古地磁极（paleomagnetic pole）能约束陆块相对现在的偏转角度以及古纬度。由多个古地磁极绘制成视极移曲线（apparent polar wander path，APWP），能为陆块间的运动提供更加精确的约束，即聚合后一起运动的两个块体具有相同的视极移曲线，而独立运动的块体视极移曲线则不同 (Buchan, 2013)。如图 2.1d 所示，波罗地与北美大陆在奥陶纪－志留纪至侏罗纪有近乎一致的视极移曲线，暗示二者在该段时间的亲缘性 (Butler, 1992)。

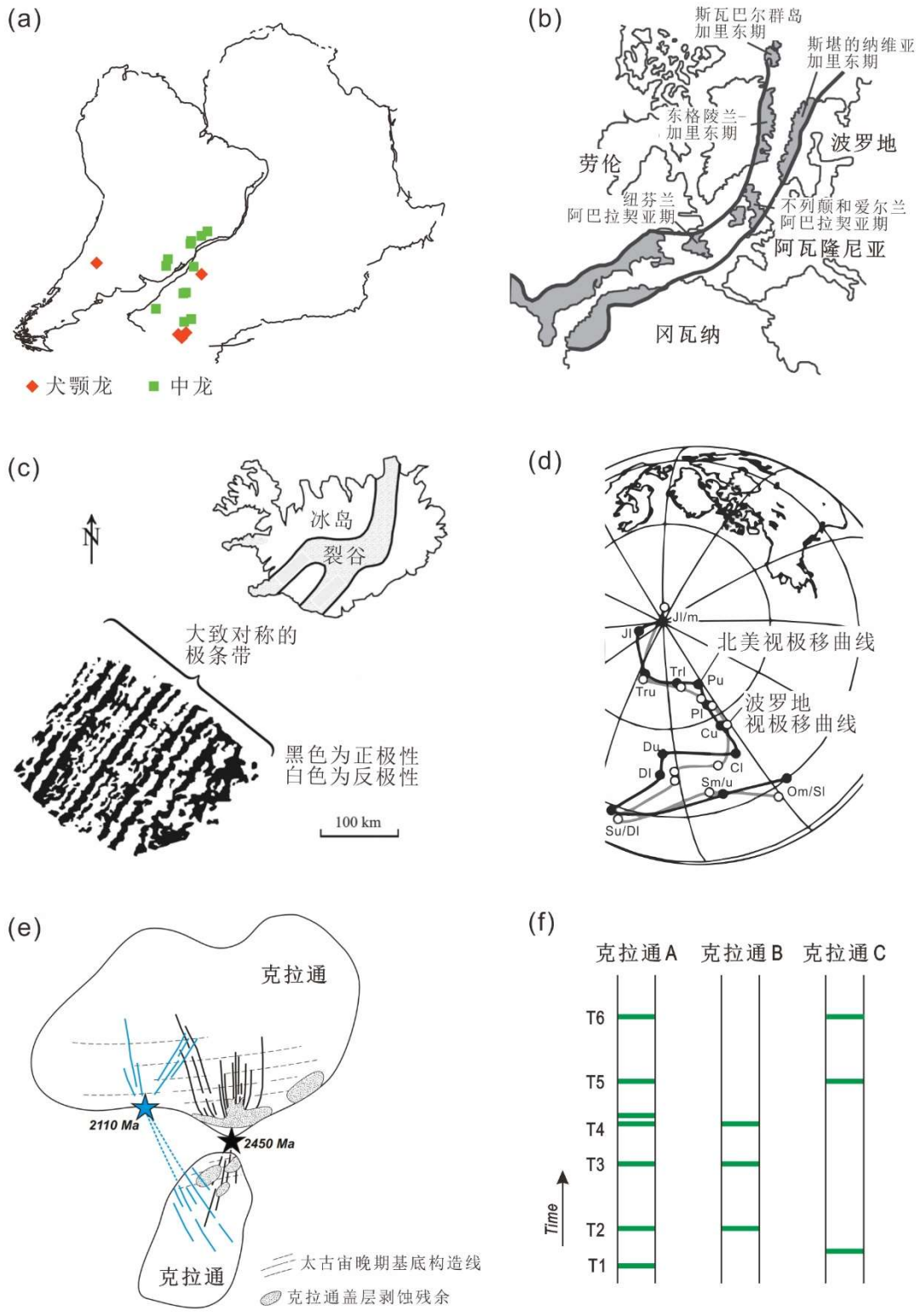

图 2.1 超大陆重建方法。（a）块体轮廓匹配与生物群落对比，图示南美洲与非洲轮廓的匹配及二叠纪至三叠纪中龙和犬颚龙的活动范围 (Trewick, 2017)；（b）追踪造山作用记录，图示大西洋打开前两侧的加里东造山与阿巴拉契亚造山带 (Slagstad et al., 2011)；（c）洋中脊两侧对称磁异常条带，图示冰岛地区的海底磁异常 (Borradaile, 2014)；（d）视极移曲线对比，图示北美与波罗地克拉通奥陶纪至侏罗纪的视极移曲线（恢复至侏罗纪时期的古地理）

(Butler, 1992)；（e）放射状岩墙群恢复古大陆 (Bleeker and Ernst, 2006)；（f）陆块岩浆/大火成岩省条形码对比。

Fig. 2.1 Supercontinental reconstruction methods. (a) Matching block outlines and fossil groups, the figure showing matched outlines of South America and Africa, and the distributions of Permaian and Triassic Mesosaurus and Cynognathus (Trewick, 2017); (b) Tracing orogenic belts, the figure showing the distributions of Caledonide and Appalachian orogenetic belts before the opening of Atlantic Ocean (Slagstad et al., 2011); (c) Symmetrical magnetic anomalies along mid-oceanic ridge, the figure showing seafloor magnetic anomalies of the SW Iceland (Borradaile, 2014); (d) APWP comparison, the figure showing the APWPs of North American and Baltica cratons from Ordovician to Jurassic (Reconstructing in Jurassic) (Butler, 1992); (e) Reconstructing paleocontinent by radial mafic dykes (Bleeker and Ernst, 2006); (f) Comparison magmatism/LIPs barcode of blocks.

本研究拟使用古地磁方法对华北克拉通在元古宙时期的位置进行约束，本文基于 Butler (1992) 对古地磁及构造应用做概要介绍。研究者普遍认为地球磁场是不断变化的，磁两极的位置亦在不断变化。但总结发现，一段时间的磁极位置的矢量平均恰好位于地理极点附近，因此研究者提出轴向地心偶极子场（geocentral axial dipole，GAD）假设，认为一段时间内的地球磁场相当于一个偶极子场，即相当于一块长方形磁铁竖着放在地球的中间。GAD 假设被认为在过去的二十亿年有效 (Evans, 2006)。而该假设获得的磁极（至少平均掉 0.1–1 Ma 跨度的磁极）则被称为古地磁极，否则被称为虚地磁极（virtual geomagnetic pole，VGP）。古地磁极是地球上的一个位置，且按照 GAD 假设应该位于地理极点，并不受观测位置和角度的影响。但随着块体的漂移，古地磁极相对现今的块体位置并不位于地理极点上，因此，对单个古地磁极的处理方法是将其拖拽到地理极点上（块体做欧拉运动），块体即可还原到当时的偏角及纬度，但无法约束经度。基于 GAD 假设，古地磁极是固定的，但块体是在漂移的；假如以块体为固定参考系，则不同时期的古地磁极是多个球面点，将这些点连在一起，即为视极移曲线。

获得可靠的古地磁极是研究的关键。目前，研究者使用最广泛的是 Van der Voo (1990) 的判断标准，总共七条，分别是：i. 有精确的定年，并假定成岩年龄和磁化年龄一致；ii. 有合适的采样方法、充足的样品（N＞24）及可靠的统计（k≥10，A_{95}≤16.0°）；iii. 有效的退磁方法获得特征剩磁；iv. 野外检测约束磁化时代；v. 样品来自构造稳定区；vi. 出现倒转极；vii. 显著区别于年轻的极。具

有精确年龄（成岩年龄和剩磁年龄）且高质量的（科学的磁清洗、平均磁场长期变化及构造校正等）古地磁极，可被称为关键极（key paleomagnetic pole）(Buchan, 2013)。

2.3 研究现状

2.3.1 聚合及裂解方式

超大陆的聚合通常以全球广泛发育的近同期或一系列的碰撞造山作用为标志，如潘吉亚聚合过程的系列造山——泛非期造山作用（形成冈瓦纳继而加入潘吉亚）(Veevers, 2003)、加里东期造山作用 (McKerrow et al., 2000)、阿巴拉契亚造山作用 (Hatcher, 2010)；罗迪尼亚聚合过程的局部陆块之间（北美、波罗地、亚马逊克拉通等）近同期的格林威尔期造山作用（Grenvillen Orogens）(Rivers, 2015)；奴那/哥伦比亚聚合过程全球多数块体经历的古元古代近同期系列造山作用 (Zhao et al., 2002a)。

按照聚合过程中俯冲大洋的类型，聚合可分为内洋的关闭（向内闭合，Introversion）、外洋的关闭（向外闭合，Extroversion）(Murphy and Nance, 2003, 2013)。依据威尔逊旋回，超大陆裂解产生洋壳（即内部大洋），随后该大洋又逐渐闭合，两边大陆焊接，此为内洋的关闭；假如裂解后超大陆外部的大洋而非内部大洋逐渐关闭，致使后期大陆焊接，则为外洋的关闭（图 2.2）；也可能存在二者混合的模式 (Murphy and Nance, 2003)。Murphy and Nance (2003) 认为，向内闭合的模式中，超大陆裂解之后形成洋壳，随后内洋闭合引起地壳增生，而增生地壳的模式年龄来自之前的内洋，该模式年龄晚于裂解时间，比如劳伦克拉通、波罗地克拉通和阿瓦隆尼亚（Avalonia）块体之间的亚皮特斯洋（Iapetus Ocean）的关闭，通过阿巴拉契亚－加里东－华力西造山（Appalachian–Caledonide–Variscan orogen）聚合形成劳俄大陆（Laurussia，或称欧美大陆）；向外闭合的模式中，外洋早于裂解存在，在外洋关闭引起地壳增生时，增生地壳的模式年龄也应该早于裂解时间，比如罗迪尼亚超大陆裂解之后，部分块体通过泛非造山关闭罗迪尼亚外大洋形成冈瓦纳大陆。古地理的分析也认为冈瓦纳的聚合源自外洋的闭合 (Hoffman, 1991)。

此外，Mitchell et al. (2012) 还提出了正交模式（Orthoversion）。该模式考虑真极移事件的发生，认为下一个超大陆形成于前一个的 90°位置（即沿着前一个超大陆俯冲大圆弧）（图 2.2）。按照这三种聚合模式预测未来的阿美西亚超大陆，Introversion 将关闭大西洋，Extroversion 将关闭太平洋，Orthoversion 将关闭北冰洋 (Mitchell et al., 2012)。

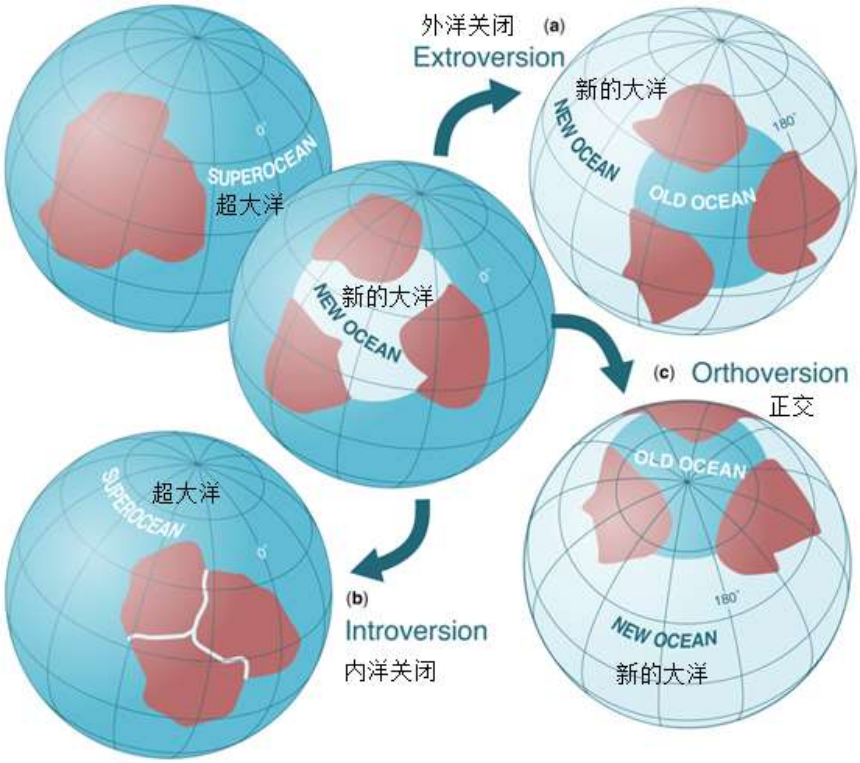

图 2.2 超大陆三种聚合的方式 (Pastor-Galán et al., 2018)

Fig. 2.2 Three ways of supercontinent assembly (Pastor-Galán et al., 2018).

传统认为，板内地幔柱/热点是引发超大陆裂解的主要原因 (Ernst et al., 1995, 2001; Li and Zhong, 2009; Li et al., 2008)，比如早侏罗世的中大西洋岩浆岩省被认为起源于地幔柱，引起大西洋的打开 (Wilson, 1997)。值得注意的是，北大西洋打开延展的位置与加里东碰撞造山带近于一致（图 2.1b）。

目前，对超大陆裂解机制有两种不同的认识，一种为“top–down”模式，即环形的俯冲带后撤引发的伸展力驱动裂解；另一种为“bottom–up”模式，即地幔柱/热点引发裂解 (Cawood et al., 2016)。数值模拟均对两种模式进行了讨论，其中，Dal Zilio et al. (2018) 认为俯冲引发的地幔流为裂解的关键，而 Zhang et al. (2018) 认为地幔柱力的作用比俯冲后撤的作用大三倍；然而，Dal Zilio (2018) 认

为两者都对超大陆的裂解有影响。

2.3.2 前寒武纪超大陆重建

（1）奴那/哥伦比亚超大陆重建概况

图 2.3 展示了奴那/哥伦比亚超大陆的五种重建模型，其中（a）图为超大陆提出伊始根据基底对比及同期造山带的重建 (Zhao et al., 2002a)，（b-e）为近几年根据古地磁资料的重建 (Evans and Mitchell, 2011; Meert and Santosh, 2017; Pisarevsky et al., 2014a; Zhang et al., 2012b)。

首先，对超大陆形成的时间有~1.8 Ga 和~1.6 Ga 两种不同的认识：前一种认为古元古代末期全球性的造山作用表明超大陆的形成 (Zhao et al., 2002a)，并有古地磁的支持 (Zhang et al., 2012b)；而后者亦从古地磁的角度认为超大陆在~1650 Ma 之后才形成 (Pisarevsky et al., 2014a)，北澳北部 Mount Isan Inlier（造山带）代表超大陆的最终形成 (Nordsvan et al., 2018; Pourteau et al., 2018)。其次，Evans and Mitchell (2011) 提出由劳伦、波罗地、西伯利亚组成超大陆的核（core of Nuna），而最近的研究认为超大陆的核还可包含华北和澳大利亚 (Kirscher et al., 2018b)。虽然古地磁数据存在~100–300 Ma 的间断，但对于劳伦－波罗地－西伯利亚的连接目前多数认为是有效的（图 2.3b–d），但也有学者认为~1500 Ma 之前西伯利亚并未加入劳伦（图 2.3e）。Evans et al. (2016c) 更新了西伯利亚中元古代的古地磁极，表明可以存在与劳伦的紧密连接（tight–fitting）或疏松连接（loose–fitting），但作者更倾向于长时间的紧密连接。而通过多期基性岩墙群的对比，Ernst et al. (2016) 认为西伯利亚的南缘与劳伦的北缘可能在元古宙长时间连接，与图 2.3c 的模型很相似。

亚马逊克拉通西北与波罗地克拉通西南的连接被称为 SAMBA（**S**outh **Am**erica–**Ba**ltica）（如图 2.3b–d），该模式主要依据古元古代末至中元古代相似的增生型造山带，尤其是 1900–1850 Ma 波罗地的 Svecofennian 造山与 1980–1810 Ma 亚马逊的 Ventuari–Tapajós 省，以及波罗地 1850–1650 Ma TIB、1640–1520 Ma Gothian 造山与 1780–1550 Ma 亚马逊的 Rio Negro–Juruena 省；根据对地质记录和地球化学的认识与对比，研究者认为该连接可能存在于~1.8–0.8 Ga (Johansson, 2009)。Pisarevsky et al. (2014a) 重新评估并比较古地磁数据，认为

SAMBA 模式在~1790 Ma 成立，但在~1420 Ma 可能不成立。

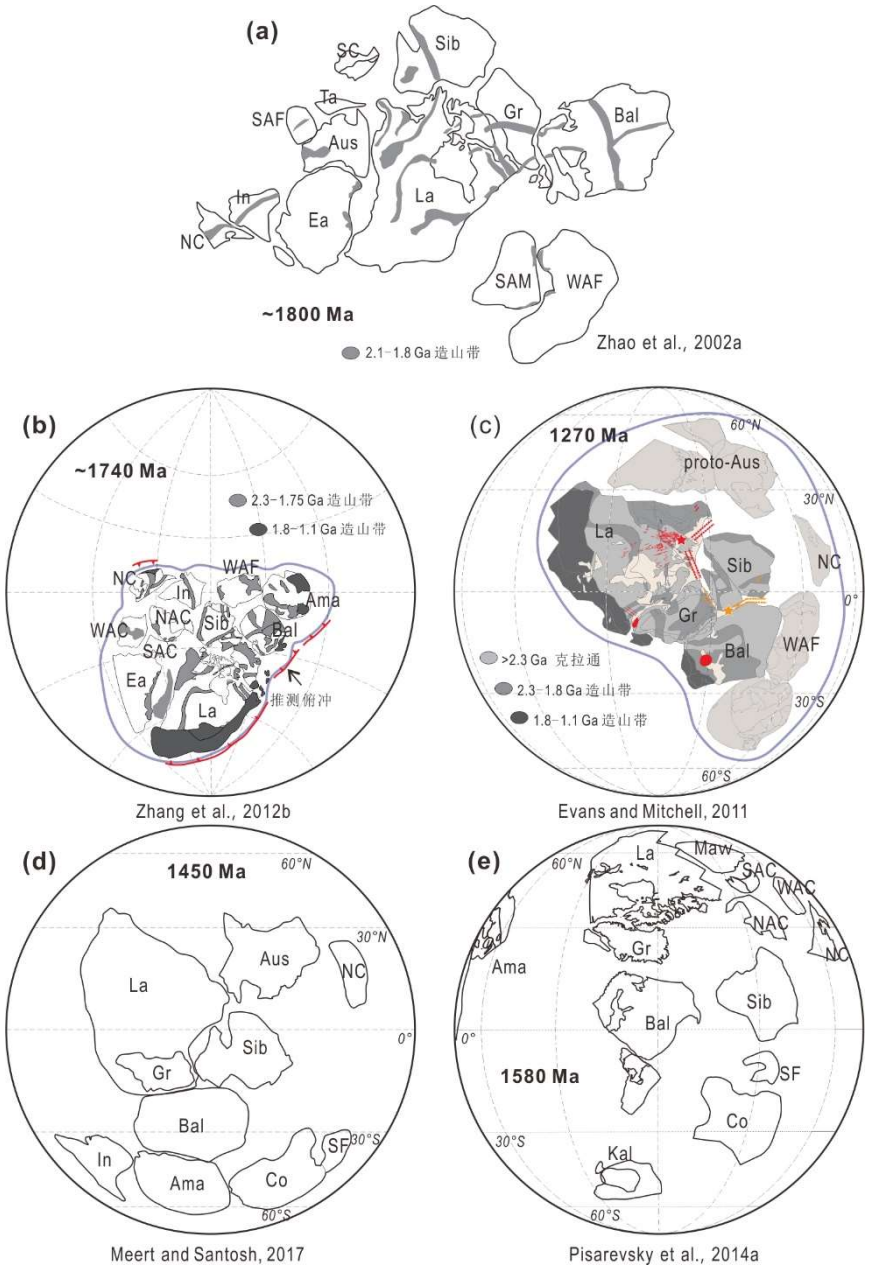

图 2.3 奴那/哥伦比亚超大陆重建模型。块体：NC–华北，SC–华南，Ta–塔里木， In–印度，Aus–澳大利亚（WAC–西澳，NAC–北澳，SAC–南澳），Ea–东南极（Maw–莫森），La–劳伦，Gr–格陵兰，Sib–西伯利亚，Bal–波罗地，SAM–南美（Ama–亚马逊，SF–圣弗朗西斯科），SAF–南非（Kal–卡拉哈里），WAF–西非，Co–刚果

Fig. 2.3 Various models of the supercontinent Nuna/Columbia. Block: NC–North China, SC–South China, Ta–Tarim, In–India, Aus–Australia (WAC–West Australian Craton, NAC–North Australian Craton, SAC–South Australian Craton), Ea–East Antarctica (Maw–Mawson), La–Laurentia, Gr–Greenland, Sib–Siberia, Bal–Baltica, SAM–South America (Ama–Amazonian, SF–São Francisco), SAF–South Africa (Kal–Kalahari), WAF–Weat Africa, Co–Congo

原澳大利亚（proto-Australia）克拉通在~1.5 Ga 之前通过多期造山作用形成，而后裂解为北澳－西澳及莫森克拉通（莫森包括南澳及延伸至南极）；莫森克拉

通在中元古代晚期，通过旋转以及侧面平移与西澳克拉通发生碰撞（Albany–Fraser 造山作用）(Boger, 2011; Cawood and Korsch, 2008)。虽然新元古代期间澳大利亚块体之间可能发生了相对旋转 (Li and Evans, 2010)，但澳大利亚与东南极的连接关系（图 2.4a）直至冈瓦纳裂解才被打破 (Boger, 2011)。

基于北澳 Elgee–Pentecost 组和华北熊耳火山岩的古地磁，Zhang et al. (2012b) 提出二者在古元古代晚期相连（图 2.3b）。但 Elgee–Pentecost 组下伏地层的基性侵入岩为~1790 Ma (Sheppard et al., 2012)，故推测该组可能不与熊耳火山岩同期。最近更新的北澳~1790 Ma 和~1320 Ma 古地磁数据 (Kirscher et al., 2018a, b)支持北澳与华北在该时间段的连接，但是连接形态略有不同（见 9.3 部分）。

Zhang et al. (2012b) 通过对比古地磁极，认为澳大利亚陆块与劳伦西缘在中元古代存在亲缘性（图 2.3b）。这一认识需要更多精确匹配的古地磁极去验证。而研究者对于二者在新元古代时期的连接则有不同的认识。SWEAT、AUSWUS 和 AUSMEX 三种连接构型本质上都是讨论新元古代时期澳大利亚－东南极克拉通与劳伦克拉通的连接关系。SWEAT 连接是指劳伦西南与东南极的连接（**S**outh**w**est US–**E**ast **A**nt**a**rctic）(Dalziel, 1991; Hoffman, 1991; Moores, 1991)，AUSWUS 是指澳大利亚与美国西部的连接（**Aus**ttalia–**w**estern **U**nited **S**tates）(Karlstrom et al., 1999)，AUSMEX 是指澳大利亚与墨西哥/劳伦克拉通西南部的连接（**Aus**tralia–**Mex**ico）(Wingate et al., 2002)（图 2.4b）。~1.59 Ga 的古地磁结果以及古元古代晚期造山带对比表明 SWEAT 连接（或与之类似的连接）可以延伸至古–中元古代（proto-SWEAT）(Betts et al., 2008; Payne et al., 2009)；该连接得到东南极和劳伦部分地质证据的支持，研究发现它们的新元古代裂谷边缘硅质碎屑岩的全岩 Nd 同位素是相似的，而南极边缘~1.4 Ga 碎屑锆石的 Hf 同位素与劳伦同期的花岗岩的 Hf 同位素一致 (Goodge et al., 2008)。最近，研究发现北澳东北部的碎屑锆石与劳伦西北部 Wernecke 超群的碎屑锆石有相似的峰期年龄 (Nordsvan et al., 2018)，暗示中元古代期间 proto-SWEAT 连接的可能性。

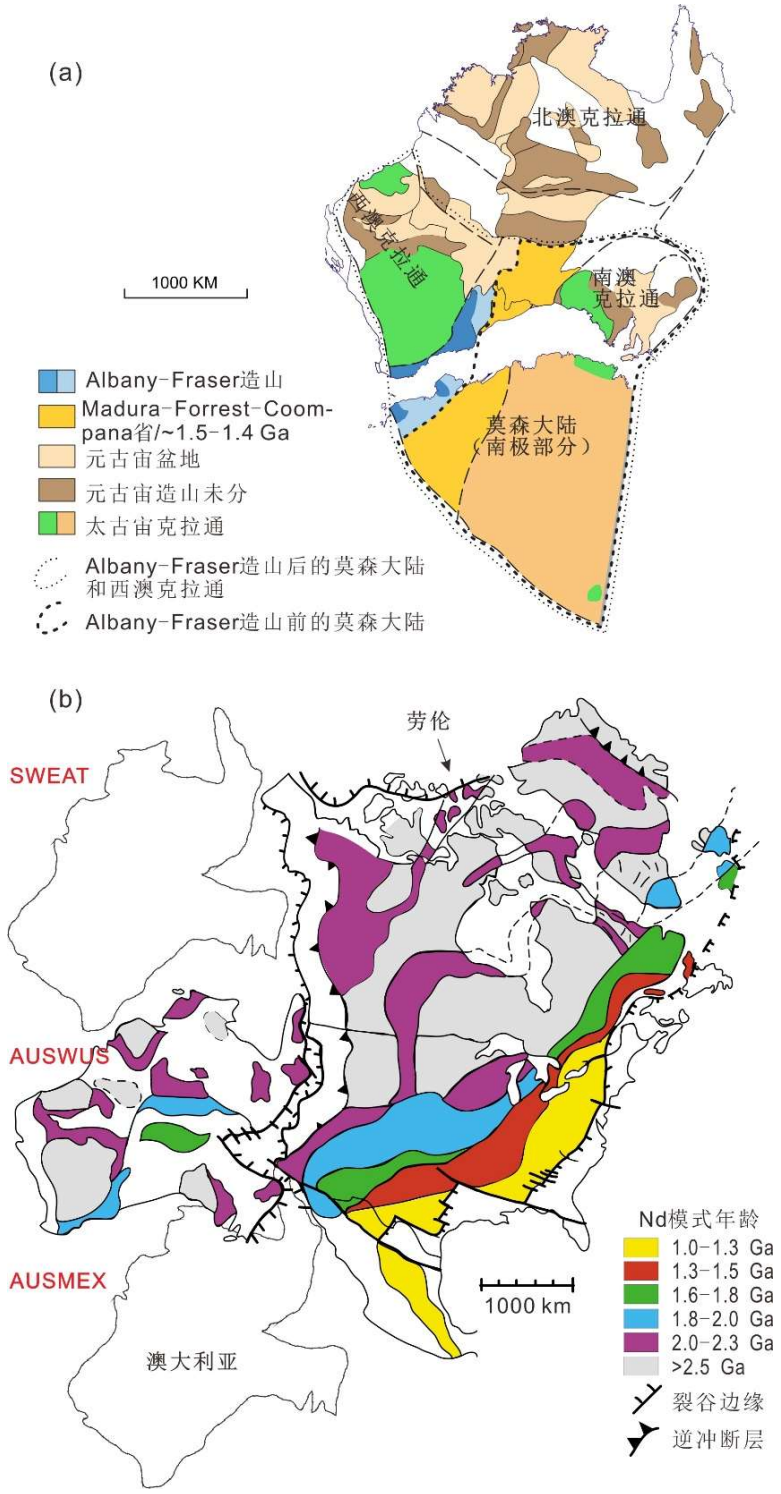

图 2.4 （a）澳大利亚与东南极新元古代时期的相对位置，修改自 Liu et al. (2018b)；（b）澳大利亚（–东南极）与劳伦元古宙连接模型，结合 Wingate et al. (2002)，修改自 Karlstrom et al. (1999)

Fig. 2.4 (a) Relative positions of the Australia and East Antarctica in Neoproterozoic, modified after Liu et al. (2018b); (b) Various models connecting Australia (–East Antarctica) and Laurentia in Proterozoic, modified after Karlstrom et al. (1999) after combining Wingate et al. (2002).

（2）罗迪尼亚超大陆重建概况

一般认为罗迪尼亚超大陆的形成时间大概为 0.9 Ga，其聚合以发育在劳伦东部、波罗地西南以及亚马逊的格林威尔期造山作用为标志 (Evans, 2009; Li et al., 2008)。通过对格林威尔期造山、新元古代裂谷及古地磁的研究，罗迪尼亚超大陆时期劳伦、波罗地、西伯利亚、亚马逊的位置已经有了较为成熟的讨论 (Li et al., 2008)（图 2.5）。其中，劳伦与西伯利亚的连接或可延续到新元古代 (Ernst et al., 2016; Evans et al., 2016c)。劳伦与波罗地的连接相对于中元古代或存在相对旋转 (Cawood and Pisarevsky, 2017)。新元古代时期，华北、刚果/圣弗朗西斯科、南非等克拉通的位置目前还在进一步探索中 (Evans et al., 2016b; Fu et al., 2015; Salminen et al., 2018)。

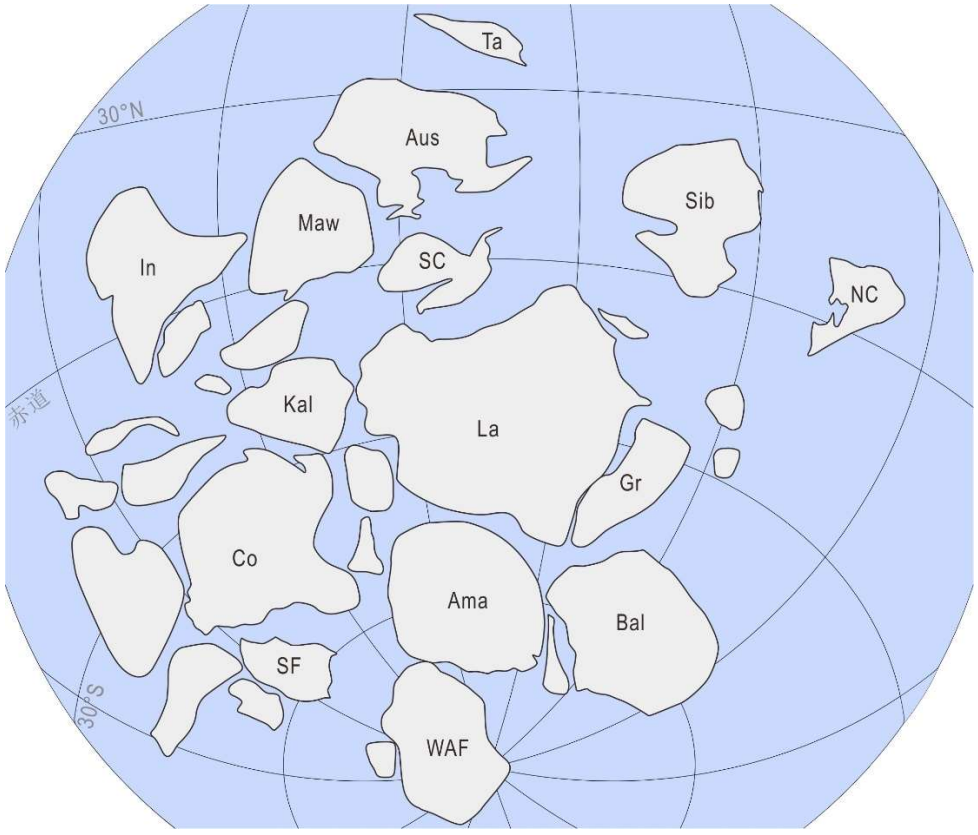

图 2.5 罗迪尼亚超大陆重建模型（简化自 Li et al. (2008)）。块体缩写同图 2.3

Fig. 2.5 Model of the supercontinent Rodinia (simplified after Li et al. (2008)). Blocks' abbreviations as Fig. 2.3

劳伦与澳大利亚－东南极的关系除了上述 SWEAT、AUSWUS 和 AUSMEX 模式（图 2.4b）之外，还有 Missing link 模式，即将华南置于劳伦西部与澳大利亚－东南极东部之间 (Li et al., 1995; Li et al., 2008)（图 2.5）。该模式的关键证据

包括：① 从~1.8 Ga 到罗迪尼亚时期，华夏是劳伦的一部分；直到 1.1–0.9 Ga 澳大利亚－东南极、扬子与劳伦－华夏才相连；② 华南作为 825 Ma 和 780 Ma 的地幔柱中心，前后分别对应澳大利亚与劳伦的同期岩浆活动；③ 相互关联的新元古代裂谷及冰川记录；④ 古地磁证据 (Li et al., 2008)。

Wen et al. (2017) 提出另外一种 Missing link 模式，即将塔里木克拉通置于劳伦与澳大利亚－东南极之间。该研究基于塔里木克拉通埃迪卡拉纪早期的古地磁数据，认为塔里木在该时期发生大尺度的旋转，且纬度变化不大；而这段时期对应罗迪尼亚的裂解，从古纬度的角度亦可将塔里木置于劳伦与澳大利亚之间，因此认为塔里木或可替代华南，成为 Missing link 的另外选择。

最近，Mulder et al. (2018) 通过对比澳大利亚东南部塔斯马尼亚 Rocky Cape 群与美国亚利桑那大峡谷 Unkar 群，发现二者具有相似的沉积成岩年龄（1.25–1.10 Ga）、相似的碎屑锆石 U–Pb 年龄分布以及 Hf 同位素值，认为中元古代晚期塔斯马尼亚与劳伦的西南相连，并通过关联劳伦 Grenville－东南极 Maud 造山与澳大利亚中部的 Musgrave 造山进一步验证。这种模式类似于 AUSMEX，但与新元古代裂谷边缘的连接（类似于 SWEAT 连接）还有差距，因此作者认为，从中元古代晚期至新元古代，澳大利亚－东南极相对劳伦发生~4000 km 的右旋运动，即由类似于 AUSMEX 模式到 SWEAT 模式转变 (Mulder et al., 2018)。

综上，目前对于前寒武纪两个超大陆的研究已经有了突破性认识，但一些块体的古地理位置仍需探索，比如西非、印度、刚果/圣弗朗西斯科、华北、华南、南非等。研究者发现，前寒武纪的两个超大陆部分构型存在相似性，比如劳伦、波罗地与西伯利亚之间，以及波罗地与亚马逊之间（图 2.4 和图 2.5），这暗示奴那/哥伦比亚超大陆到罗迪尼亚超大陆的转换可能是通过关闭内洋的方式（Introversion）(Evans et al., 2016a; Li et al., 2019)。

2.3.3 超大陆动力学

为什么会形成超大陆？超大陆为什么会裂解？是什么主宰了超大陆的聚合与裂解方式？假如存在旋回，为什么会有超大陆旋回？要回答这些动力学的问题，不仅需要对岩石圈/板块进行观测，还要考虑整个地幔的结构以及对流驱动方式。目前，研究者在非洲和太平洋下部识别出了两个巨大低速度的剪切波区

（large low shearwave velocity provinces，LLSVPs），即位于核幔边界之上的两个大的 S 波低速异常、但 P 波速度没有明显改变的热异常区，推测为超级地幔柱（superplume）(Dziewonski, 1984; Romanowicz, 2008)。统计发现，过去~300 Ma 的地幔柱绝大多数位于 LLSVP 的边界附近 (Burke et al., 2008)。

据此，Zhong et al. (2007) 和 Li and Zhong (2009) 认为环超大陆俯冲（circum-supercontinent subduction）使对蹠超级地幔柱（antipodal superplumes）形成，超级地幔柱也对应于超大陆的位置；超柱及耦合的超大陆通过真极移（true polar wander，TPW）的方式到达赤道，超柱最终引起大陆裂解。而对于超大陆的形成，则认为是 degree-1 时期的一个超级下降流（冷柱）所引起陆块的聚合 (Li and Zhong, 2009; Zhong et al., 2007)。这些推测仍需要更多的研究去验证，如对更早时期（超级）地幔柱的识别，尤其是大洋地幔柱、对更早时期真极移的识别、对超大陆聚合及裂解机制的深入探讨等 (Li and Zhong, 2009)。但是，结合金伯利岩和大火成岩省的分布统计，Torsvik et al. (2010) 认为过去的两亿年 LLSVP 是固定存在的，并有可能延伸至更早时期。另外，也有研究者认为 LLSVP 与地幔柱/大火成岩省关系甚微 (Julian et al., 2015)。

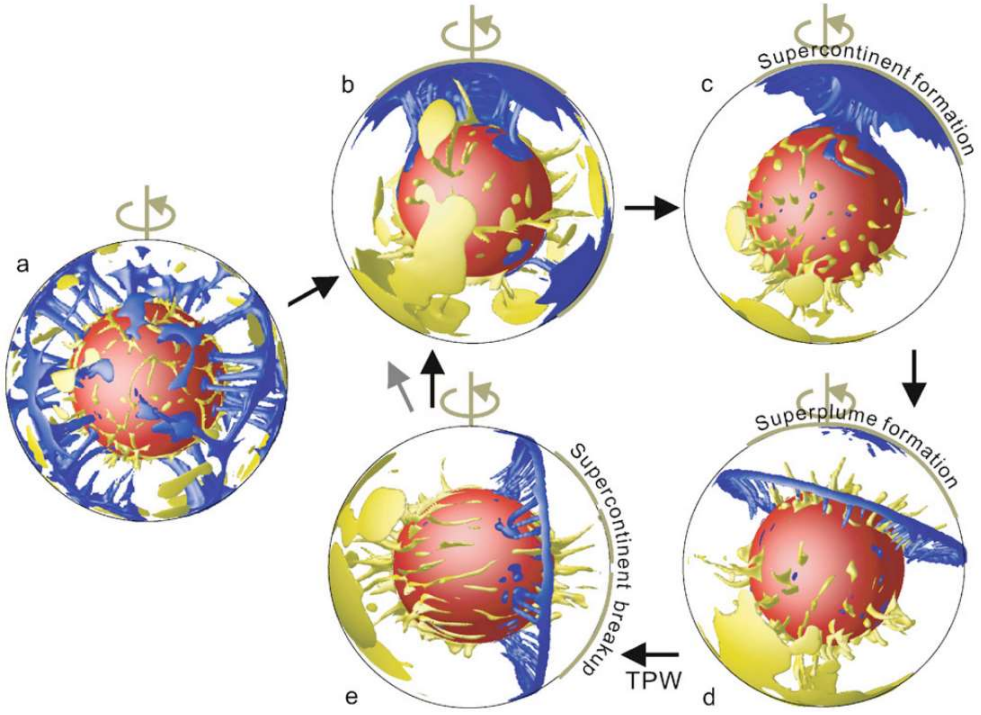

图 2.6 超大陆形成和裂解的数值模拟结果 (Li and Zhong, 2009)。TPW–真极移

Fig. 2.6 Numerical modelling results of the supercontinent's formation and break-up (Li and Zhong, 2009). TPW–True Polar Wander.

2.4 问题与研究前沿

Evans et al. (2016a) 总结了超大陆研究的十大问题，依次为：

（1） 地球上存在多少超大陆？是否存在肯罗兰，或 2.5 Ga 是否有超级克拉通的漂移？

（2） 冈瓦纳、劳亚、欧亚等半超大陆是如何影响地幔结构以及古环境？

（3） 真正的奴那/哥伦比亚和罗迪尼亚是什么样的？

（4） 超大陆聚合方式是否为向内、向外或正交？或者超大陆旋回中它们是否交替出现？

（5） 现今存在的 LLSVP 结构存在了多久，或能存在多久？地幔柱/超级地幔柱与超大陆的关系是什么？

（6） 板块构造是否有速度的限制？

（7） 埃迪卡拉纪的古地磁之谜如何解？

（8） 如何解读地磁发电机的长期行为，它是如何影响地表环境的？

（9） 全球气候对超大陆旋回有何反应？

（10）潘吉亚之前的大陆拼贴与潘吉亚之后的古地理是否对生物圈有同等重要的影响？

整体而言，准确重建前寒武纪超大陆或者重建元古宙以来所有板块的演化（full-plates reconstruction）是研究者普遍关注的问题，也是深入讨论环境生物效应与地球动力学的基础。重建过程中，对大火成岩省的研究以及补充精确的古地磁极依然任重而道远。Sergei Pisarevsky 博士曾统计全球 1.8–1.25 Ga 的古地磁极仅有 67 个，2.5–1.8 Ga 的古地磁极仅有 79 个（第七届国际岩墙会议，2016），高质量的古地磁极更少，因此亟待补充古地磁数据。根据古地磁数据并结合现有的研究，一些研究组已经做了连续重建的探索 (Merdith et al., 2017, 2019)，但如何与地质记录匹配并相互验证仍然是面临的挑战。Meert (2014) 根据现有的重建模型，发现了一个奇怪的现象：地质历史中的超大陆，劳伦、波罗地和西伯利亚，以及/或东冈瓦纳部分（印度、澳大利亚、东南极、马达加斯加）总是在一起，被称为奇怪的吸引者（strange attractors）；西冈瓦纳部分（刚果、圣弗朗西斯科、拉普拉塔河和西非）似乎总是处在一种略微分散的聚合状态，被称为

心灵上的闯入者（spiritual interlopers）；一些块体如华南、华北、卡拉哈里、塔里木，总是处在超大陆的远端，被称为孤独的漂泊者（lonely wanderers）。作者认为这种现象可能是因为研究者基于对潘吉亚的认识而对其他超大陆重建存在偏心；或者现代型式的板块构造在新元古代晚期才形成，而此前板块的水平运动依然有限 (Meert, 2014)。虽然这一现象还没有得到完全准确的观测，但问题的提出值得深思。

Li et al. (2019) 通过总结认为，由奴那/哥伦比亚到罗迪尼亚的裂解并不彻底（Introversion），由罗迪尼亚到潘吉亚的裂解比较彻底（主要为 Extroversion），而由潘吉亚到阿美西亚的裂解在目前看来并不彻底（Introversion），据此认为超大陆彻底裂解与否可能交替出现。这种演化的结果是超大洋的长期存在，比如奴那/哥伦比亚外围的超大洋历经超大陆的聚合、（不完全）裂解、下一个超大陆罗迪尼亚的聚合，伴随着罗迪尼亚超大陆较为彻底的裂解而消失，可能存在了约十亿年；而随罗迪尼亚裂解打开的大洋在潘吉亚聚合时达到最大，又随潘吉亚裂解变小直至现在仍然存在，甚至到两亿年后才消失，因此认为地球存在更长的超大洋周期，并与全球锆石 Hf 同位素和海水 Sr 同位素的变化以及铅锌矿的分布周期耦合 (Li et al., 2019)。

基于地球物理观测的板块相对运动已经取得了重大进展，但绝对板块运动（absolute plate motions），尤其是更早时期，仍需探索。古大陆重建可以以古经度变化最小的非洲、非洲固定热点、非洲活动热点以及全球活动热点为参考系 (Torsvik et al., 2008)，而对于热点是否运动（如果是，则如何运动）依然在探索中，热点的研究与 LLSVP 也密不可分 (Tarduno and Bono, 2017, 2018; Tarduno and Koppers, 2019)。另一方面，地质与数值模拟研究依然在讨论俯冲、地幔柱与聚合、裂解的关系，top–down 与 bottom–up 对超大陆作用亦在探索中 (Cawood et al., 2016; Dal Zilio, 2018; Dal Zilio et al., 2018; Murphy and Nance, 2013; Nance et al., 2014; Zhang et al., 2018)。

第3章 地质背景

3.1 华北前寒武纪地质演化

华北克拉通位于中国北部，呈倒三角形状；因其与朝鲜地区具有相似的前寒武纪地质记录，或合称为中朝克拉通（Sino-Korea Craton）。克拉通周边为显生宙造山带：南-东南为苏鲁–大别造山带，西南为祁连山造山带，北部为兴蒙造山带（中亚造山带的一部分）(Zhai, 2013)。华北克拉通是中国已知最古老的克拉通，鞍山地区出露有~3.8 Ga 的岩石 (Liu et al., 1992, 2008; Song et al., 1996; Wan et al., 2005, 2012, 2015b; Wang et al., 2015b)；而且南部的北秦岭地区还发现有≥ 4.0 Ga 的捕获锆石 (Diwu et al., 2013)。目前研究认为，克拉通早期发育有数个微陆核（old continent nucleus），之后在 2.7–2.5 Ga 经历大陆地壳巨量生长，形成集宁、迁怀、胶辽、鄂尔多斯、徐淮、许昌和阿拉善微陆块（micro-blocks），并通过绿岩带相连，初步完成克拉通化；而后发育大量壳熔花岗岩并伴随变质作用 (Zhai and Santosh, 2011; Zhai, 2011)（图 3.1a）。

元古宙早期被认为是地球环境的转折点，以大量发育苏必利尔型铁矿（2.5–2.3 Ga，成铁纪）(Huston and Logan, 2004) 为起点，之后发生休伦冰期事件（Huronian glaciation event，HGE）(Tang and Chen, 2013; Young, 2014) 及红层 $\delta^{13}C_{carb}$ 正异常（Lomagundi–Jatulian 事件）(Martin et al., 2013)，这些事件为大氧化事件（great oxidation event，GOE）的一部分，与全球水圈、大气圈的充氧密切相关。华北克拉通在古元古代早期并不发育苏必利尔型铁矿 (张连昌等, 2012)，且岩浆活动较少，为构造静寂期 (翟明国, 2013)，但已有研究表明其后的碳酸盐岩沉积响应了全球 L–J 事件 (Kong et al., 2011; Tang et al., 2011)，以及或存在休伦冰期 (滹沱群四集庄组；Chen et al., 2019)。

2.1 Ga 前后，在辽东、胶东、赞皇、五台、吕梁等地广泛存在基性侵入体，可能指示一次陆内裂谷伸展事件 (Peng et al., 2017; Wang et al., 2016c, 2017)，或为岛弧成因 (Meng et al., 2014; Yuan et al., 2015)。在 1.95–1.85 Ga，克拉通广泛遭受高级变质作用影响，下地壳高压麻粒岩和超高温麻粒岩出露于地表 (翟明国等, 1992, 1995, 1996; 郭敬辉等, 1993)。前人研究总结认为该时期的变质地体集中于

晋豫、胶辽和丰镇地区，有类似于现代陆陆碰撞造山带的特点，称其为“活动带”(Zhai and Liu, 2003; 翟明国, 2011; 翟明国和彭澎, 2007)。随着对变质事件时代及过程的细致刻画，加之一定的推测，有学者提出华北的阴山地块和鄂尔多斯地块在~1.95 Ga 沿孔兹岩带拼合成西部陆块，龙岗地块和狼林地块在~1.9 Ga 沿胶辽吉带拼合成东部陆块，最终西部陆块与东部陆块在~1.85 Ga 拼合成统一的华北克拉通 (Zhao et al., 1998, 1999a, 1999b, 2000, 2005; Zhao and Zhai, 2013)（图 3.1b）。除此之外，也有研究者认为存在沿北部展布的北方造山带 (Kusky and Li, 2003; Wan et al., 2015a; Wu et al., 2018)。Peng et al. (2014) 将古元古代末的变质作用分成两个阶段（~1.96–1.90 Ga 和~1.90–1.80 Ga），发现第一个阶段主要分布于华北西北与胶辽地区，而第二个阶段分布广泛并叠加之前的阶段；结合与第一阶段变质作用近同期的辉长–苏长岩、I 型/S 型花岗岩的研究，考虑这些岩浆与变质活动的空间展布，研究认为两个阶段的构造热活动分别对应类似于现今弧陆拼贴及陆陆拼贴的过程，认为华北克拉通内部仅存在大同－环县沿线的造山带。总之，华北古元古代的麻粒岩记录为探讨元古宙构造模式提供了窗口，而构造模式的解读需要更细致更全面的研究作为观测基础。在~1.8 Ga，华北克拉通结束广泛的热构造活动，最终完成克拉通化，开启相对稳定的盖层沉积阶段 (Zhai, 2011; 翟明国等, 2014)。

古元古代末至新元古代，克拉通发育有多个裂谷系，其中南缘有熊耳谷、东南有徐淮裂谷、北部有燕辽裂谷、渣尔泰–白云鄂博–化德裂谷 (Peng, 2015a)（图 3.1c）。

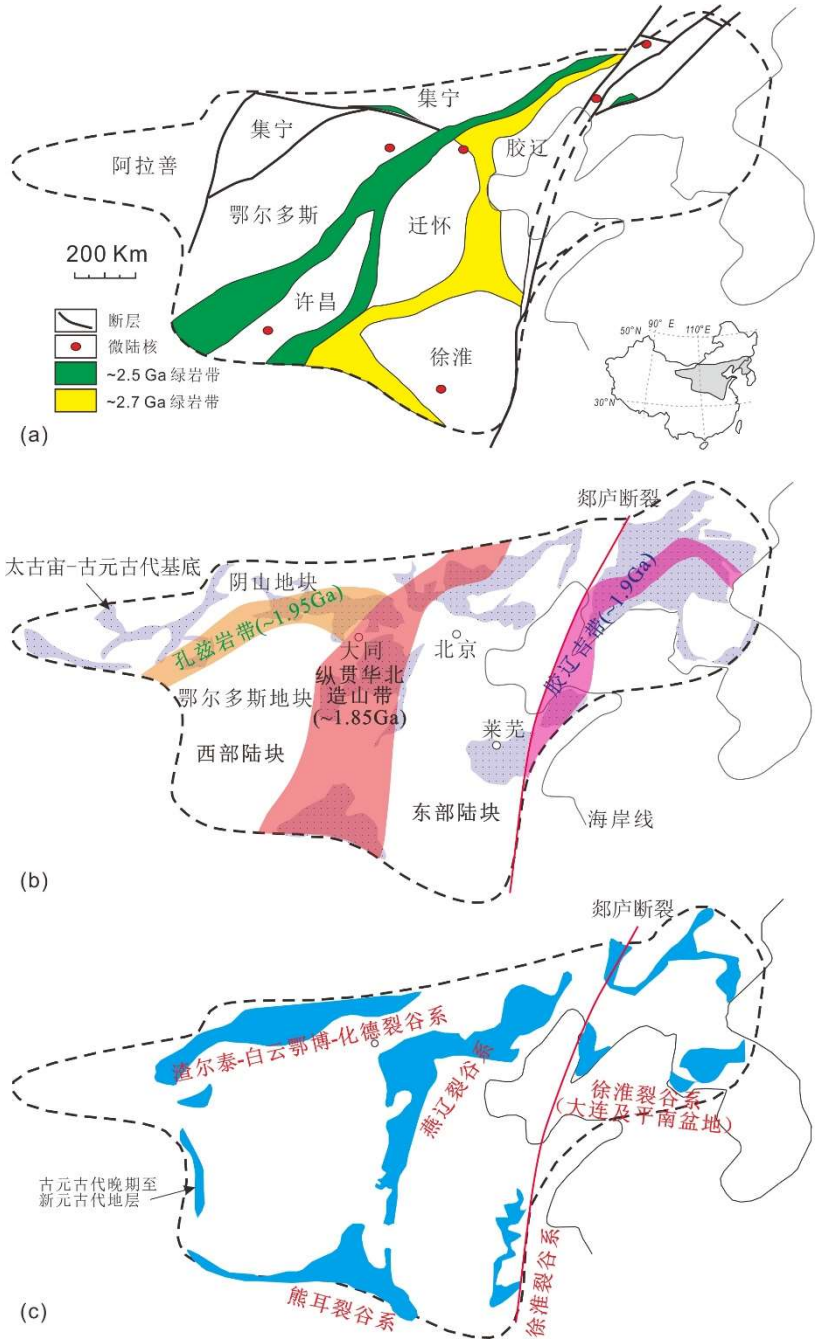

图 3.1 华北克拉通前寒武纪地质演化：太古宙微陆核、微陆块和绿岩带 (Zhai and Santosh, 2011)（a）；古元古代晚期造山带 (Zhao and Zhai, 2013)（b）；古元古代末至新元古代盖层（c），简化自 Peng et al. (2011a)

Fig. 3.1 Precambrian geological evolution of the NCC: Archean ancient nuclei, macro-blocks and greenstone belts (Zhai and Santosh, 2011) (a); Orogenic belts in the late Paleoproterozoic (Zhai and Santosh, 2011) (b); Covers from the late Paleoproterozoic to Neoproterozoic (c), simplified after Peng et al. (2011a).

（1）熊耳裂谷系

熊耳裂谷位于华北南缘，呈三岔状，其中一支伸向华北内部，另外两支沿

华北南缘分布（图 3.1c）。该裂谷从下往上依次包括熊耳群（也称西阳河群；大古石组、许山组、鸡蛋坪组、马家河组）、汝阳群（小沟背组/兵马沟组、云梦山组、白草坪组、北大尖组）和洛峪群（崔庄组、三教堂组、洛峪口组），再往上还有黄连垛组、董家组、罗圈组等（图 3.2 和图 3.3）。

熊耳群下伏太古宙、古元古代结晶基底，总厚 1000–7600 m，多数厚 3000–7000 m，出露约 7000 km^2；该群含大量的火山碎屑岩和熔岩，绝大多数火山岩为偏基性的中性–中酸性组分，即以玄武安山岩、安山质岩石为主，次为英安–流纹质岩石；该地层沉积于陆相–滨海相，喷发主体中晚期部分地区是海相 (Zhao et al., 2002b; 河南省地质矿产局, 1989; 赵太平等, 2001, 2004)。U–Pb 锆石/斜锆石年龄显示该群形成于~1.77–1.80 Ga (Zhao et al., 2004; 崔敏利等, 2010)。研究表明其火山岩很可能形成于裂谷环境 (Peng et al., 2008; Wang et al., 2016a, 2019; Zhao et al., 2002b; 孙枢等, 1985; 赵太平等, 2007)，但也有研究者提出安第斯型陆缘弧或岛弧相关背景 (He et al., 2008, 2009; Zhao et al., 2009; 贾承造, 1985)，或裂谷与岛弧的叠加 (陈衍景等, 1992)。

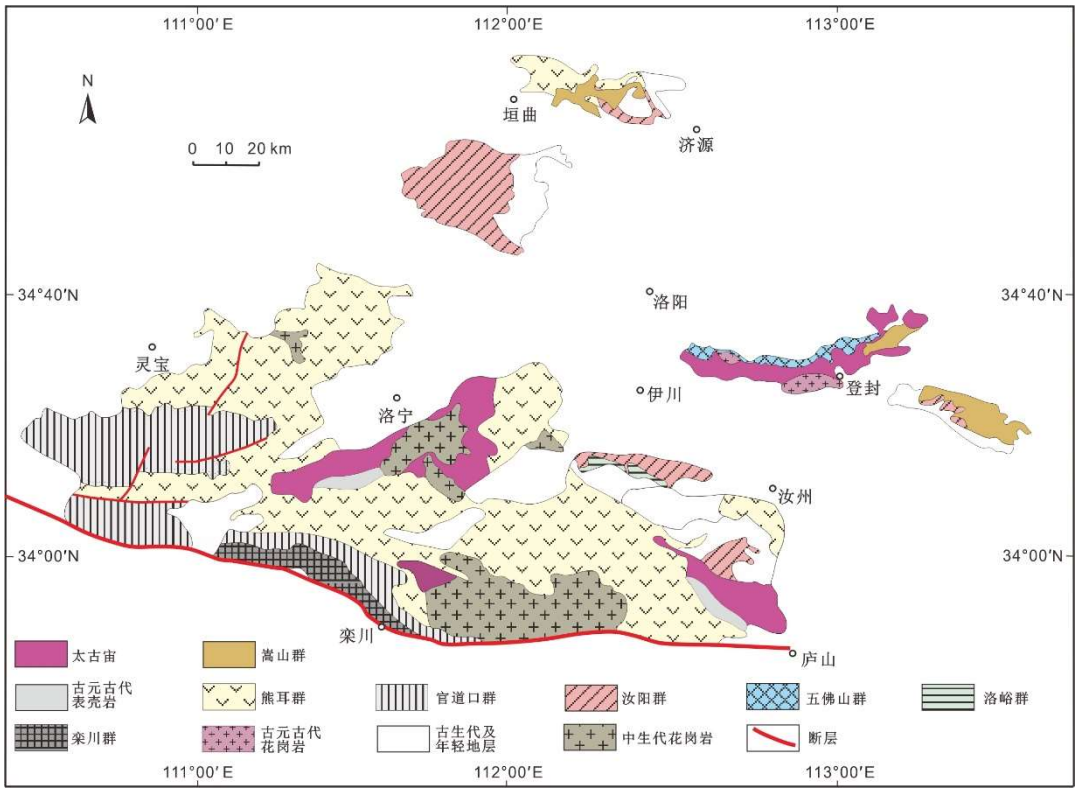

图 3.2 华北克拉通南缘熊耳裂谷系地质简图 (Hu et al., 2014a)

Fig. 3.2 Simplified geological map of the Xiong'er rift system in the southern NCC (Hu et al., 2014a)

汝阳群不整合于熊耳群之上，整合于上覆洛峪群，主要为以海相碎屑沉积为主的陆源碎屑岩–碳酸盐岩建造，总厚 700–1500 m (河南省地质矿产局, 1989)。Hu et al. (2014a) 通过限定云梦山组底部的碎屑锆石的年龄，认为汝阳群沉积时间不早于~1.74 Ga（加权平均年龄为 1744 ± 22 Ma）；与汪校锋在博士论文中展现的碎屑锆石结果类似（加权平均年龄为 1711 ± 37 Ma）(汪校锋, 2015)。苏文博等 (2012) 首次报道洛峪群洛峪口组凝灰岩的锆石 U–Pb LA–MC–ICPMS 年龄为 1611 ± 8 Ma。虽然该年龄得到了重复证实 (1640 ± 16 Ma；汪校锋, 2015)，但来自洛峪群三教堂组的磷钇矿却显示约 1400 Ma 的年龄 (Lan et al., 2014)。熊耳裂谷汝阳群、洛峪口群及上覆地层时代框架尚存疑问，但对汝阳群化石的研究却比较成熟。研究发现，汝阳群含早期真核生物化石 *Dictyosphaera*、*Shuiyousphaeridium*、*Valeria*，以及 *Plicatidium latum*、*Spiromorpha* sp. 及一种未命名的 *Valeria lophostriata* 类化石 (Pang et al., 2015)；而 *Valeria lophostriata* 化石在燕辽裂谷长城系底部也有报道 (Lamb et al., 2009)。

（2）徐淮裂谷系

考虑显生宙郯庐断裂走滑的影响 (Zhao et al., 2016)，华北克拉通徐淮地区、渤海北部大连地区以及朝鲜半岛平南盆地地区在前寒武纪可能同处于克拉通的东南缘（图 3.1c）。这些地区出露有新元古代地层（图 3.3），如在徐淮及苏鲁交界的淮河群（海相为主，总厚＞5 km；不整合于太古宙泰山群之上，从下往上依次为兰陵组、新兴组、岠山组、贾园组、赵圩组、倪园组、九顶山组、张渠组、魏集组、史家组、望山组、金山寨组和沟后组）(江苏省地质矿产局, 1984)，或被分为徐淮群、宿县群和栏杆群 (安徽省地质矿产局区域地质调查队，1985)；在辽宁地区从下往上依次为细河群（钓鱼台组、南芬组、桥头组）、五行山群（长岭子组/康家组、南关岭组、甘井子组）和金县群（营城子组、十三里台组、马家屯组、崔家屯组、兴民村组）(辽宁省地质矿产局, 1989)；在朝鲜平南盆地的直岘群（Jikhyon Group）（从下往上依次为长峰组、万峰组、长寿山组、安心岭组）及上覆司堂隅群、默川群、灭恶山群和燕滩群 (杨正赫等, 2016)。这些地层多被~0.92–0.89 Ga 的基性岩床侵入（图 3.3），暗示新元古代存在裂谷作用 (Peng et al., 2011a, 2011b; Wang et al., 2012; Zhang et al., 2016)。

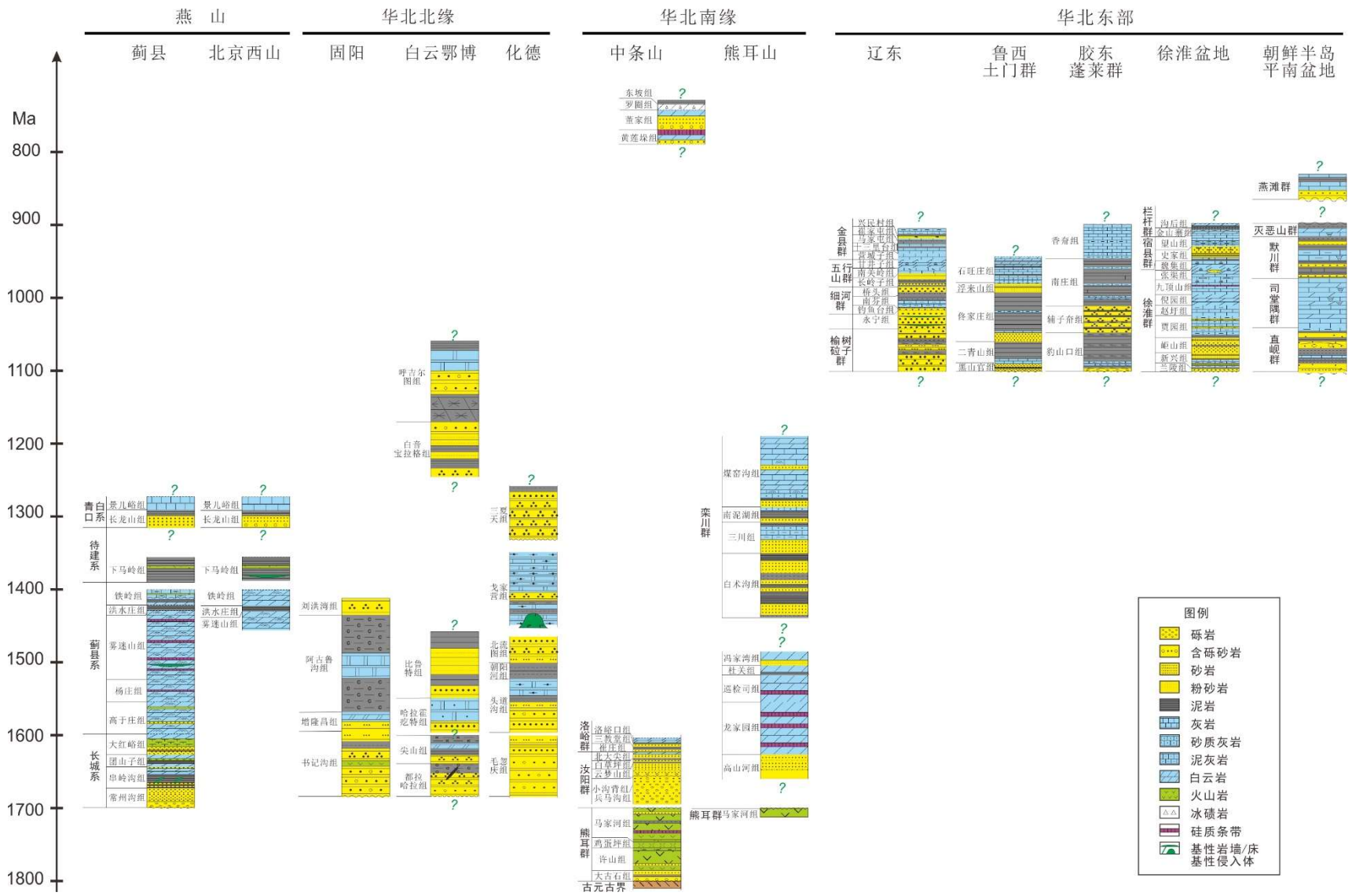

图 3.3 华北克拉通古元古代末至新元古代地层。修改自胡波 (2011)

Fig. 3.3 The strata of the NCC from the late Paleoproterozoic to Neoproterozoic. Modified after Hu (2011)

（3）燕辽裂谷系

燕辽裂谷位于华北北部，其中一支向东延伸，另一支向南伸入华北内部太行山地区（图 3.1c 和图 3.4）。裂谷自下而上依次为长城系（~1.70–1.60 Ma，碎屑岩为主；常州沟组、串岭沟组、团山子组、大红峪组）、蓟县系（~1.60–1.40 Ga，碳酸盐岩为主；高于庄组、杨庄组、雾迷山组、洪水庄组、铁岭组）、待建系（~1.40–1.35 Ma，碎屑岩为主；下马岭组）和青白口系（海绿石 K–Ar 年龄显示其为新元古代，碎屑岩为主；长龙山组/骆驼岭组、景儿峪组）（图 3.3 和图 3.4）。该裂谷经历了河口湾（~1.70–1.65？Ga）、局限海湾（1.65？–1.60 Ga）、陆表海（~1.60–1.40 Ga）、再到陆棚等河口湾局限海湾（<1.40 Ga）的沉积环境 (范文博, 2015; 阎玉忠和刘志礼, 1998)。

整套地层中发育大量化石，石敏等 (2014) 经系统研究将生物群落分为三个阶段，A 阶段为长城系下部（＞1.65？Ga），主要含泥质页岩相生物群和宏观碳质压型化石；B 阶段从团山子组至雾迷山组（~1.65？–1.48 Ga），主要包括硅化碳酸盐岩或燧石中的燧石相生物群；C 阶段包含洪水庄组及上部地层（＜1.45？Ga），主要含有宏观碳质压型化石和泥页岩相生物群。其中，在 A 阶段中识别出最古老的真核生物微化石 *Valeria lophostriata* (Javaux and Lepot, 2018; Lamb et al., 2009)；在 B 阶段的高于庄组中还识别出了分米尺度的多细胞核真核生物 (Zhu et al., 2016)。

~1.73 Ga 的基性岩墙在裂谷沉积前侵位 (Peng et al., 2012)；~1.68 Ga 的基性岩墙群与裂谷的开启近于同期 (Li et al., 2015; Wang et al., 2016b)。另外，在长城系大红峪组发育有~1.62 Ga 碱性火山岩（高钾、富铝、贫硅的碱玄岩–响质碱玄岩–响岩组合）(胡俊良等, 2007; 陆松年和李惠民, 1991)，火山活动或起于~1.64 Ga (张拴宏等, 2013)。与~1.62 Ga 同期的基性岩墙在鲁西泰山地区有报道 (相振群等, 2012)，可能为燕辽裂谷活动的产物 (Li et al., 2015)。~1.32 Ga 的基性岩床侵入该套地层中的雾迷山组、铁岭组和下马岭组 (Wang et al., 2014a; Zhang et al., 2009, 2012a, 2017)（图 3.4）。此外，还有~1.23 Ga 和 0.775 Ga 基性岩墙群发育其中或周边 (Peng, 2015b; Wang et al., 2015a, 2016b)。详细年代学信息见表 3.1。

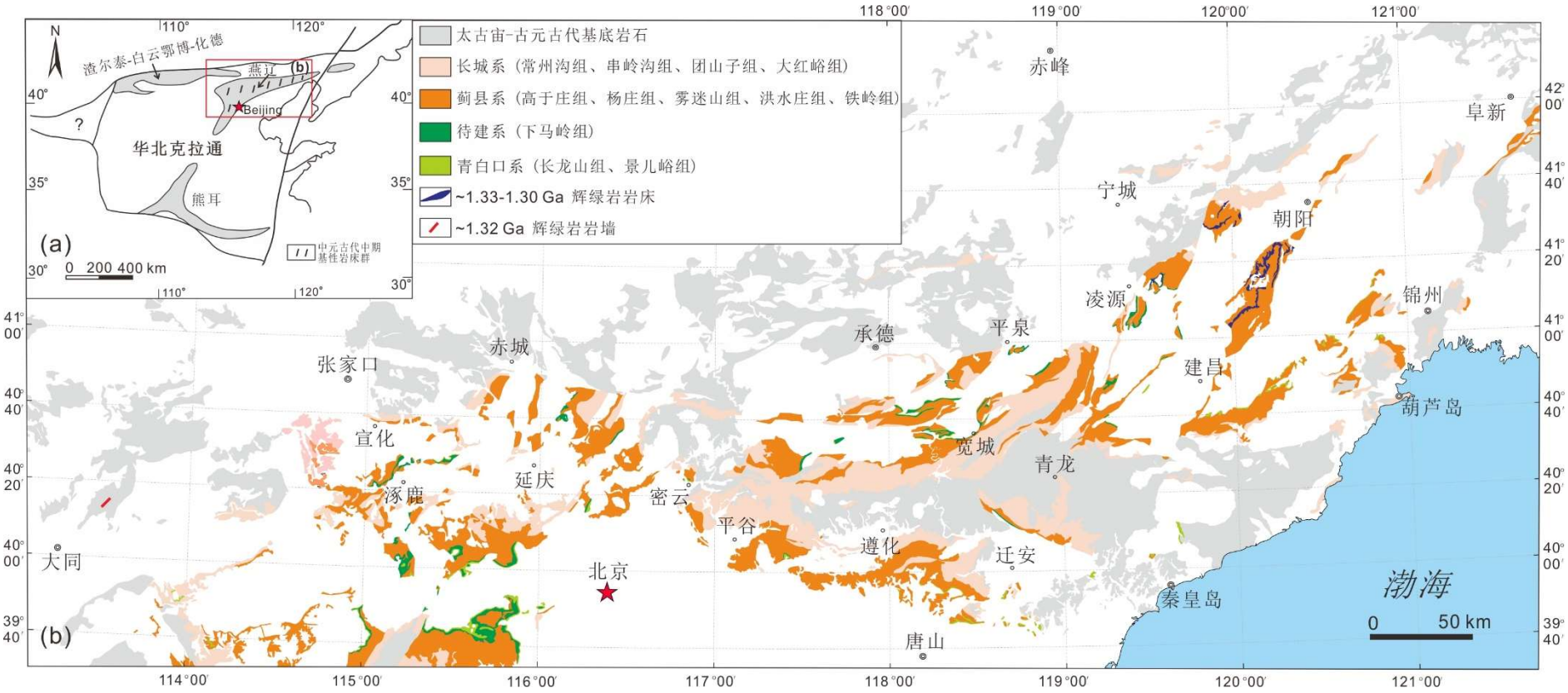

图 3.4 华北克拉通北部燕辽裂谷地质简图。修改自 Zhang et al. (2017)

Fig. 3.4 Simplified geological map of the Yanliao rift in the northern NCC. Modified after Zhang et al. (2017)

表 3.1 燕辽裂谷相关岩浆事件

Table 3.1 Magmatism related of the Yanliao rift

岩石单元	U–Pb 年龄/ Ma	参考文献
~1.73–1.67 Ga 斜长岩–纹长二长岩–碱性花岗岩–环斑花岗岩组合（图 3.8c）		
环斑花岗岩	1681 ± 10、1679 ± 10	杨进辉等, 2005
钾质花岗岩	1692 ± 19、1753 ± 23	Zhang et al., 2007
斜长岩	1693 ± 7、1715 ± 6	赵太平等, 2004
	1726 ± 9、1739 ± 43、1712 ± 15	Zhang et al., 2007
1.73 Ga 基性岩墙（图 3.8c）		
密云岩墙	1731 ± 4	Peng et al., 2012
1.68 Ga 基性岩墙		
莱芜岩墙/LX307 （图 3.8b）	1680 ± 5	Li et al., 2015
屠家沟岩墙/JD689 （图 3.8c）	1677 ± 12	Wang et al., 2016b
1.64–1.62 Ga 基性岩墙与火山岩		
泰山岩墙（图 3.8b）	1621 ± 9 / 1632 ± 4	相振群等, 2012
大红峪组火山岩（图 3.8c）	1625 ± 6	陆松年和李惠民, 1991
团山子组火山岩（图 3.8c）	1637 ± 15 / 1641 ± 4	张拴宏等, 2013
~1.23 Ga 岩墙（图 3.8c）		
黎城岩墙	1229 ± 4	Peng, 2015b
	1219 ± 4	丁继凯, 2017
卢龙岩墙	1236 ± 7	Wang et al., 2016b
青龙岩墙	1208 ± 24	Wang et al., 2015a
建平岩墙	1229 ± 4、1229 ± 10、1231 ± 16	Wang et al., 2015a
	1227 ± 3、1223 ± 6、1217 ± 13	丁继凯, 2017
~0.775 Ga 岩墙		
卢龙丁家沟岩墙	775 ± 5	Wang et al., 2016b
斑脱岩/凝灰岩		
高于庄组	1559 ± 12、1560 ± 5	李怀坤等, 2010
雾迷山组	1483 ± 13、1487 ± 16	李怀坤等, 2014
铁岭组	1437 ± 21、1439 ± 14	Su et al., 2010; 李怀坤等, 2014
下马岭组	1368 ± 12、1366 ± 9、1370 ± 11、1379 ± 12、1380 ± 36、1372 ± 18	Su et al., 2008, 2010; 高林志等, 2007; 2008a; 2008b

（4）渣尔泰－白云鄂博－化德裂谷系

在华北北部，燕辽裂谷的西侧发育有一套古元古代末到新元古代的浅变质地层序列（图 3.1c）。这些序列从西向东包括狼山群（~1.8 Ga–1.0 Ga？）(Hu et al., 2014b; Liu et al., 2017b)、渣尔泰群（＜1.7 Ga–？；从下往上依次为书记沟组、增隆昌组、阿古鲁组、刘洪湾组）、白云鄂博群（~1.8–1.2 Ga？；从下到上依次为都拉哈拉组、尖山组、哈拉霍圪特组、比鲁特组、白音宝拉格组、呼吉尔图组）(Liu et al., 2017a; Zhou et al., 2017; 周志广等, 2016) 和化德群（从下到上依次为毛忽庆组、头道沟组、朝阳河、北流图组、戈家营组和三夏天组）(Liu et al., 2014, 2018a)（图 3.3）。目前，对于这些地层的研究较为薄弱。

3.2 华北前寒武纪大火成岩省

华北克拉通前寒武纪广泛发育岩浆活动 (彭澎, 2016)，其中早前寒武纪地体普遍遭受 2.5 Ga 及 1.95–1.85 Ga 变质作用 (翟明国, 2009; 赵国春, 2009)，晚前寒武纪发育多期基性岩墙/岩床群，包括 1.78 Ga、1.73 Ga、1.68 Ga、1.62 Ga、1.32 Ga、1.23 Ga、0.92–0.89 Ga 和 0.81 Ga 岩浆作用 (Peng, 2015b 及参考其中; Wang et al., 2015a, 2016b; Zhang et al., 2016, 2017; 彭澎等, 2017) 以及 1.73–1.68 Ga 斜长岩–环斑花岗岩–纹长二长岩组合 (Zhang et al., 2007; 杨进辉等, 2005; 赵太平等, 2004)、1.80 Ga 和 1.53 Ga 的 A 型花岗岩 (Deng et al., 2016a, 2016b)。目前，被提出的前寒武纪大火成岩省有 1.78 Ga 太行–吕梁岩墙群及熊耳火山岩系 (Peng et al., 2008)、1.32 Ga 燕辽基性岩床群 (Zhang et al., 2017) 和~0.92 Ga 大石沟基性岩墙群及徐淮－旅大－沙里院基性岩床群 (Peng et al., 2011a, 2011b; Zhang et al., 2016)。

（1）1.32 Ga 燕辽基性岩床群

华北克拉通北部的燕辽裂谷系含有多层基性岩床，比如侵入串岭沟组、团山子组、雾迷山组、铁岭组和下马岭组的辉绿岩。其中，锆石/斜锆石 U–Pb 年代学结果表明雾迷山组、铁岭组和下马岭组的基性岩床侵位时代为 1305–1330 Ma (Wang et al., 2014a; Zhang et al., 2009, 2012a, 2017; 李怀坤等, 2009)。这些岩床单体有几十米到几百米厚，广泛分布于朝阳、凌源、平泉、宽城、怀来等地，覆盖面积＞0.12 Mkm^2（图 3.4）。岩石具有明显的辉绿结构，其中含辉石 35–

60%、斜长石 40–55%、磁铁矿 3–10%及角闪石 0–5%；化学成分显示为拉斑质玄武岩；Zr/Y 对 Zr 投图显示板内环境。岩床侵位前可能经历了地壳隆升（蔚县上升），因此，研究者认为其构成了中元古代的燕辽大火成岩省 (Zhang et al., 2017)。

（2）1.78 Ga 太行–吕梁岩墙群及熊耳火山岩系

华北克拉通中部的太行山、吕梁山、五台山及北部内蒙丰镇地区、南部中条山地区出露有大量大型基性岩墙群。这些岩墙群侵入到古元古代基底中，直立状产出并有冷凝边。岩墙宽多为 20–70 m，长可达数公里至几十公里；多呈 NNW–NW、少数呈 NW–EW 向（吕梁－五台地区）展布 (Qian and Chen, 1987)（图 3.5）。锆石/斜锆石 U–Pb 年代学结果显示，这些岩墙多形成于~1.78–1.76 Ga (Yang et al., 2017; 王冲等, 2016 及参考其中)，少部分形成于 1.73 Ga、1.23 Ga 及 0.92 Ga (Peng, 2015b)。其中，~1.78 Ga 岩墙群被称为太行（–吕梁）基性岩墙群 (Peng et al., 2011a)。这些岩墙多为辉绿岩－辉长岩，主要由 30–40%的单斜辉石和 50–65%的斜长石组成，常见斜长石斑晶，偶见橄榄石，蚀变相对较弱；但化学成分变化较大，主要为基性成分，也含少量中酸性组分，除正常辉长质组分外也含富 Ti–Fe–P 成分 (Peng et al., 2007; Wang et al., 2004, 2014b; 彭澎等, 2004)。

华北南部的熊耳火山岩系是与太行岩墙群近于同期的岩浆作用，前人研究表明，二者均为拉斑质岩石，且浅部岩墙与火山岩具有一致的地球化学特征，认为基性岩墙为火山岩的岩浆通道，但中北部地壳掀斜可能使得火山岩被剥蚀而未保留 (Peng et al., 2007, 2008)（图 3.5）。根据岩墙群的放射状几何学、岩墙群与火山岩的活动时间、岩浆源区、板内的构造背景、分布面积（＞0.1 Mkm^2）与体积（＞0.1 Mkm^3），研究者综合评定并认为这二者构成地幔柱引发的华北克拉通~1.78 Ga 大火成岩省 (Peng et al., 2006, 2008)（图 3.5）。

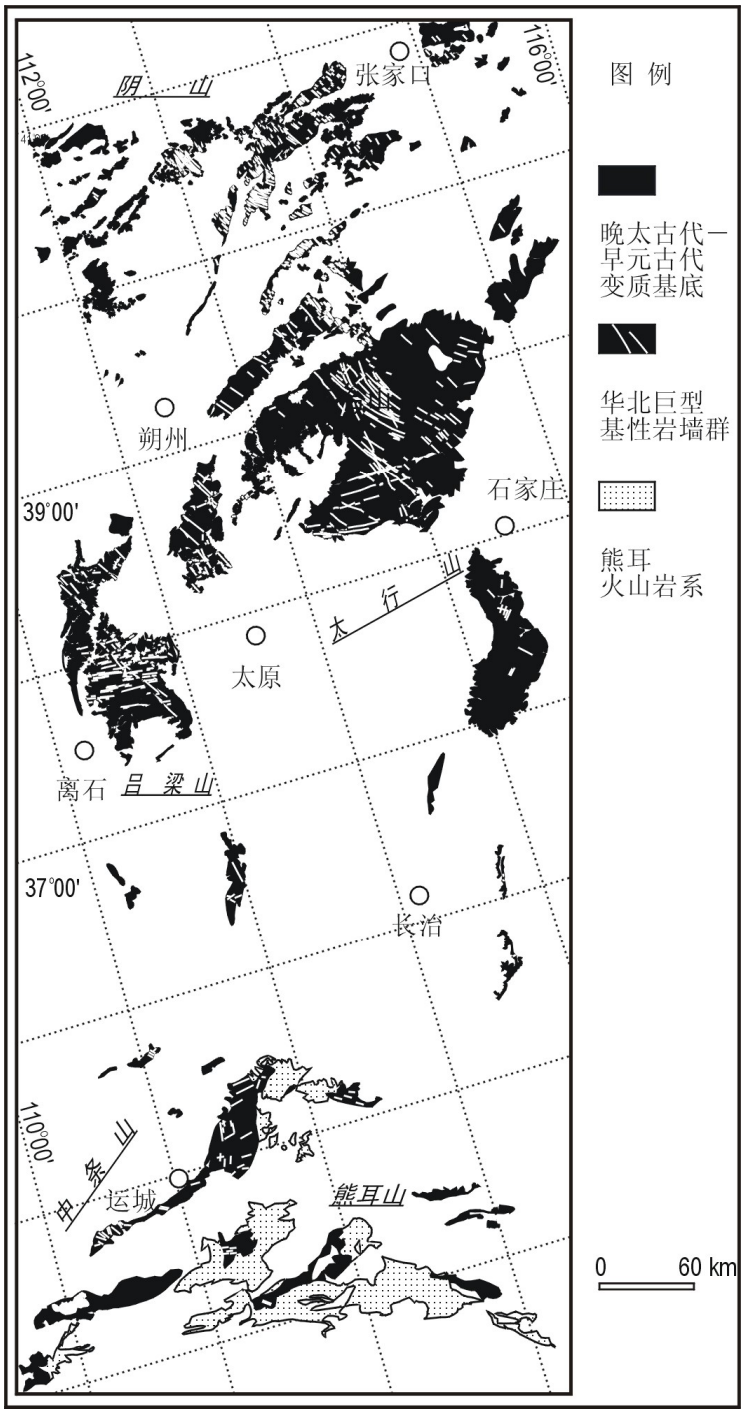

图 3.5 华北太行岩墙群和熊耳火山岩系分布简图 (彭澎, 2007)

Fig. 3.5 Simplified map of the Taihang mafic dyke swarms and the Xiong'er volcanic province of the NCC (Peng, 2007)

（3）~0.92 Ga 大石沟基性岩墙群及徐淮 – 大连 – 沙里院基性岩床群

华北克拉通中部不仅有 NW 向的 1.78 Ga 岩墙，还有 NW 向的 0.92 Ga 岩墙（图 3.6）。斜锆石定年结果显示怀安羊窖沟、恒山大石沟以及凉城桃花沟的岩墙侵位于 920–926 Ma (Peng et al., 2011a)。这些岩墙一般大于 10 m 宽，可延伸超

过 10 km；岩石由单斜辉石和斜长石组成；有 E-MORB 或 OIB 的组分，可能来自软流圈 (Peng et al., 2011a)。大石沟岩墙群的走向可延伸至华北东南缘，而东南缘出露有近于同期或稍晚期的基性岩床 (Peng et al., 2011a, b; Wang et al., 2012; Zhang et al., 2016)（图 3.6）。比如徐淮岩床主要由与地层近于平行的（石英）辉绿岩组成，岩体厚约 10–200 m，长＞10 km (Wang et al., 2012)。大连盆地中发育的同时期的岩床多出现于桥头组、长岭子组、南关岭组、甘井子组、营城子组、崔家屯组和兴民村组；岩体厚几米至几百米，长几百米至十多公里 (Zhang et al., 2016)。旅大岩床具有辉绿结构，化学成分上多为拉斑玄武质，微量元素显示具有板内的特征 (Zhang et al., 2016)。朝鲜平南盆地沙里院岩床可达 150 m 厚，超过十公里长；与同期其他地区的岩床特征类似 (Peng et al., 2011b)。考虑到该期岩浆作用的分布范围及特征，研究者认为这构成了新元古代早期的大火成岩省 (Peng et al., 2011a; Zhang et al., 2016)。

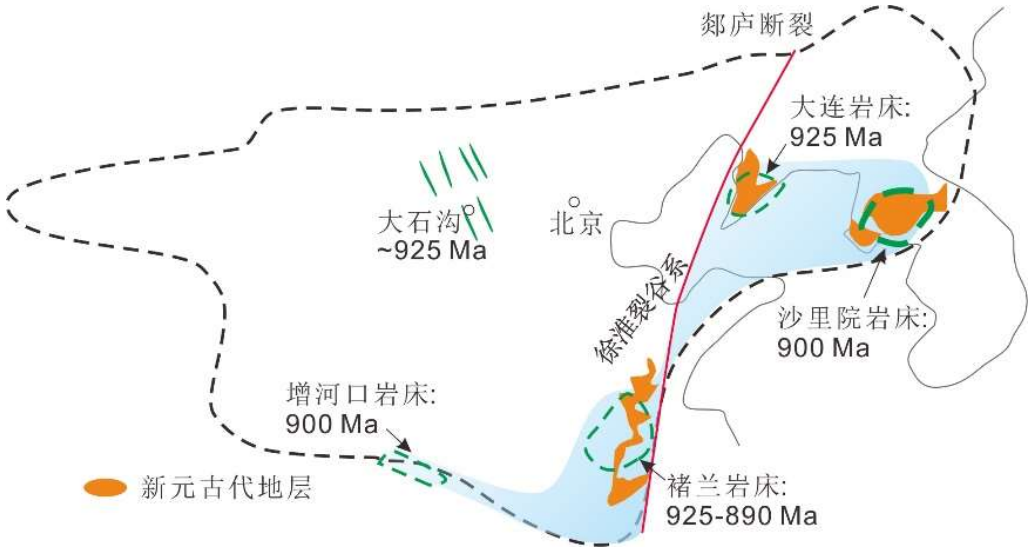

图 3.6 华北东南缘徐淮裂谷及~0.92–0.89 Ga 基性岩墙/岩床群分布简图。修改自 Peng et al. (2011a) 和 Peng (2015b)

Fig. 3.6 Schematic map of the Xuhuai rift and the ~0.92–0.89 Ga mafic dyke/sill swarms of the southeastern NCC. Modified after Peng et al. (2011a) and Peng (2015b)

3.3 华北前寒武纪古地磁研究进展

通过古地磁方法重建古大陆是重建的唯一定量方法。华北前寒武纪古地磁研究在近十五年得到了快速发展，标志性的工作始于 Henry Halls 博士对太行岩墙群的研究，其既有现代 U–Pb 定年分析，又有古地磁的科学采样分析及野外原

生性检测 (Halls et al., 2000)。目前，华北主要报道了以下古地磁极（表 3.2 和图 3.7）：

（1）1.78 Ga 太行岩墙群与熊耳火山岩系的古地磁研究

该期岩浆作用事件包含华北中部太行–吕梁岩墙群以及南部熊耳火山岩系，是华北最大规模的岩浆作用，研究程度较高，故对此事件的古地磁研究较为全面 (Halls et al., 2000; Piper et al., 2011; Xu et al., 2014, 2017; Yan et al., 2017; Zhang et al., 2012b)。Henry Halls 博士通过对华北中部岩墙的研究得到 1769.1 ± 2.5 Ma 的锆石年龄以及 36°N/247°E/A_{95} = 2.4°的古地磁极（通过烘烤检验）。而后续研究中，来自阴山地区和太行－熊耳地区的古地磁结果不一致，前者与 Halls et al. (2000) 的结果一致 (Xu et al., 2014)，Piper et al. (2011) 也同样得到类似的结果；后者熊耳火山岩的古地磁结果为 50.2°N/263.0°E/A_{95} = 4.5°（通过反转检验）(Zhang et al., 2012b)，或太行岩墙与熊耳火山岩的古地磁极平均为 41.6°N/246.3°E/A_{95} = 4.3° (Xu et al., 2014)。Zhang et al. (2012b) 将其视为两个时代的古地磁极（~1780 Ma 和~1769 Ma），但年代学的角度很难区分 1780–1760 Ma 的地质事件 (王冲等, 2016)。而 Xu et al. (2014) 认为这种情况是因为中生代或新生代太行及熊耳地区相对北部阴山地区发生了旋转。

（2）对华北南缘沉积地层的古地磁研究

Zhang et al. (2006) 对华北南缘汝阳群和洛峪群地层进行了古地磁分析，获得云梦山组下部的高温分量并通过了倒转及褶皱检验，其古地磁极为 60.6°S/87.0°E/A_{95} = 3.7°；获得白草坪组古地磁极 43.0°S/143.8°E/A_{95} = 11.1°；获得崔庄组和三教堂组古地磁极 41.0°S/44.8°E/A_{95} = 11.3°。碎屑锆石及火山灰定年研究认为这套沉积序列可能形成于古元古代晚期至中元古代早期（见 3.2 部分对熊耳裂谷的介绍），但仍缺少可靠的时代约束。

（3）对燕辽裂谷中元古代沉积地层的古地磁研究

华北蓟县地层为全球中新元古代经典地层之一，其中的红层备受古地磁研究者青睐。对杨庄组两组独立的研究获得了如下结果：17.3°N/214.5°E/ A_{95} = 5.7° (Wu et al., 2005) 和 2.4°N/190.4°E/ A_{95} = 17.1° (Pei et al., 2006)，前者通过了中–晚侏罗世褶皱的检验；后者通过了晚三叠世褶皱的检验。目前，研究者没有获得

杨庄组的直接沉积年龄，但通过下伏高于庄组 (~1.56 Ga 火山灰；李怀坤等, 2010) 及上覆雾迷山组 (~1.48 Ga 火山灰；李怀坤等, 2014) 可间接推测改组可能沉积于~1.53 Ga。吴怀春博士论文中还给出了雾迷山组和铁岭组的分析结果，分别为 20.2°N/221.4°E/ A_{95} = 3.9°（无检验）、11.6°N/187.1°E/ A_{95} = 6.3°（通过褶皱检验）(吴怀春, 2005)。

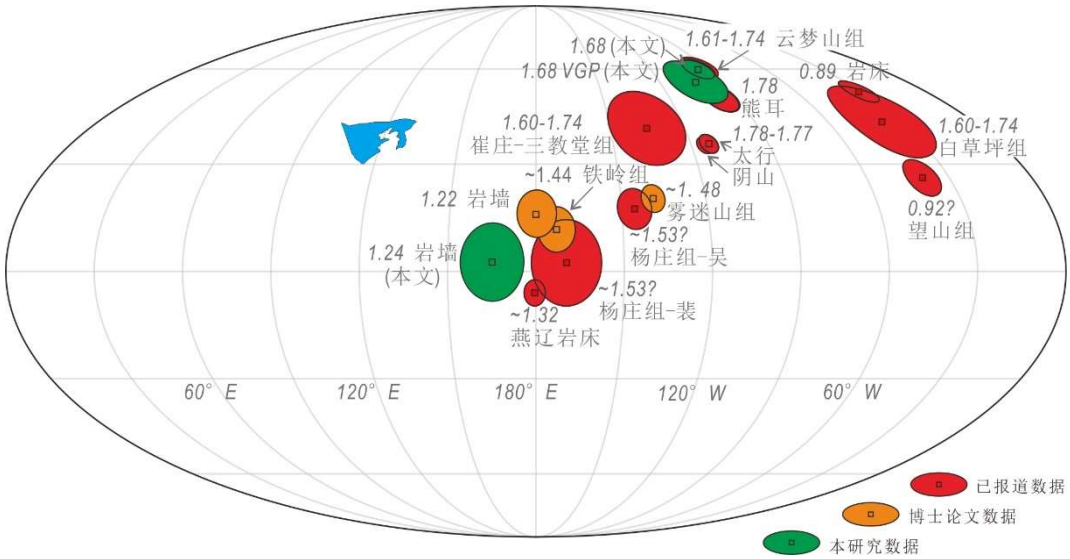

图 3.7 华北前寒武纪古地磁极

Fig. 3.7 Precambrian paleomagnetic poles of the NCC

（4）对燕辽岩床群的古地磁研究

在古地磁文章中，该期岩床被认为形成于~1.35 Ga (Chen et al., 2013)，更新的定年结果显示其侵位于~1.32 Ga (Zhang et al., 2017 及参考其中)。从中获得的古地磁极为-5.9°N/179.6°E/ A_{95} = 4.3°，通过了晚于中生代褶皱的检验 (Chen et al., 2013)。

（5）~1.22 Ga 基性岩墙的古地磁研究

丁继凯在博士论文中介绍了华北~1.22 Ga 基性岩墙群的古地磁研究，该成果包含来自冀东－辽西的三条岩墙 (Wang et al., 2015a) 以及来自华北中部的七条岩墙，部分岩墙有精确的年龄限制。该论文获得的古地磁极为 16.0°N/180.3°E/ A_{95} = 6.6°，烘烤检验来自辽西建平岩墙 (丁继凯, 2017)。

（6）对徐淮地层及岩床的古地磁研究

Fu et al. (2015) 对徐淮地区侵入望山组的岩床、望山组碳酸盐岩、侵入倪园组的岩床及贾园组碳酸盐岩进行了古地磁分析。该研究结合前人资料总结认为，

望山组岩床形成于~890 Ma，望山组沉积于 890–1120Ma 之间，倪园组岩床侵位于~925 Ma，贾园组沉积岩形成于 925–1121 Ma；并获得~890 Ma 古地磁极 52.6°N/330.0°E/ A_{95} = 5.3°（通过倒转、褶皱、烘烤检验），未烘烤的望山组古地磁极 26.1°N/320.3°E / A_{95} = 5.2°（通过褶皱检验），倪园组一条 925 Ma 岩床虚地磁极 30.9°S/136.2°E/ dm/dp = 4.0°/2.4°，贾园组虚地磁极 54.0°S/107.3°E/ A_{95} = 4.0°。望山组沉积岩与倪园组岩床极方向相近，因此望山组被认为形成于 925 Ma 前后。据此，勾勒出华北~1120–890 Ma 的视极移曲线，并将其命名为“淮北环”。

综上，目前研究者已正式报道了华北前寒武纪~1.78 Ga（太行岩墙群及熊耳火山岩）、~1.53 Ga？（杨庄组）、~1.32 Ga（燕辽岩床群）及~1.10–0.89 Ga 古地磁极（淮北群）。另有~1.44 Ga（铁岭组）及 1.22 Ga 等非正式报道的古地磁极或虚地磁极。

表 3.2 华北克拉通前寒武纪古地磁极及虚地磁极一览表

Table 3.2 Precambrian paleomagnetic data of the NCC (including paleopoles and VGPs)

岩石单元	年龄/Ga	极纬度/°	极经度/°	A_{95}/°	参考文献
熊耳群	1.78	50.2	263	4.5	Zhang et al., 2012b
太行岩墙	1.77–1.78	36	247	2.8	Halls et al., 2000
阴山岩墙	1.77–1.78	35.5	245.2	2.4	Xu et al., 2014
杨庄组–吴	~1.53?	17.3	214.5	5.7	Wu et al., 2005
杨庄组–裴	~1.53?	2.4	190.4	11.9	Pei et al., 2006
铁岭组	~1.44	11.6	187.1	6.3	吴怀春, 2005
雾迷山组	~1.48	20.2	221.4	3.9	
燕辽岩床群	~1.32	–5.9	179.6	3.6	Chen et al., 2013
望山组	0.92？	26.1	320.3	5.2	Fu et al., 2015
淮北岩墙	0.89	52.3	329.3	3.5	
建平–平山岩墙	1.22	16	180.3	6.6	丁继凯, 2017
云梦山组下部	＜1.74	60.6	267	3.7	
白草坪组	1.60–1.74	43	323.8	11.1	Zhang et al., 2006
三教堂和崔庄组	1.60–1.74	41	224.8	11.3	

3.4 研究区地质概况

本研究涉及三个地区：冀东、鲁西及太行山南部地区（图 3.8）。

冀东地区位于华北北部，区域上位于燕辽裂谷东部范围内，出露部分裂谷中新元古代地层（图 3.8c）。盖层序列下伏太古宙结晶基底，基底主要由遵化－青龙单元、迁西－迁安单元和滦县－卢龙单元以断层或剪切的方式连接组成。

遵化－青龙地体主要由新太古代片麻岩和表壳岩组成，并含少量的基性–超基性侵入岩体。迁西－迁安地体以 2.5–2.6 Ga 的岩浆作用和高级变质作用为主要特征，广泛发育花岗质侵入体、片麻岩及少量表壳岩系。滦县－卢龙地体由 2.6–2.5 Ga 角闪岩、黑云母角闪岩、条带状铁建造（BIF）组成，并经历 2.5 Ga 角闪岩相变质 (贺高品等, 1991; 魏春景, 2018)。除此之外，曹庄杂岩含有冥古宙至古太古代的物质 (Nutman et al., 2011; 万渝生等, 2009)。

鲁西地块位于华北克拉通的东部，主要包括郯庐断裂以西、兰考－聊城断裂及盐山断裂以东、渤海湾盆地以南，以及合肥盆地以北的地区。该区主要出露太古宙泰山岩群，遭受绿片岩相至角闪岩相变质作用，包括雁翎关组、山草峪组和柳杭组（此处群组不同于地层群组概念，仅代表岩石单元）。雁翎关组和柳杭组主要由 2.75–2.70 Ga 角闪岩、细粒云母（角闪）片麻岩、科马提质变火山岩和片岩组成；山草峪组主要由细粒云母片麻岩夹有层状角闪岩及云母片岩组成，时代稍年轻 (Wan et al., 2010; 曹国权, 1996)。鲁西只有局部地区被新元古代土门群（黑山官组、二青山组、佟家庄组、浮来山组、石旺庄组）覆盖 (Hu et al., 2012)。

太行山南部前寒武纪岩石单元主要包括太古宙赞皇杂岩、古元古代甘陶河群以及上覆燕辽裂谷相关的沉积盖层。赞皇群由角闪岩、TTG 片麻岩、麻粒岩、石英岩、片岩、大理岩、变泥质岩及混合岩组成 (河北省地质矿产局, 1989)。甘陶河群不整合于赞皇群之上，从下往上由南四掌组、南寺组和蒿葶组组成，遭受绿片岩相变质（据高邑 1：20 万地质图，1996）。本区古元古代晚期至新元古代地层出露不全。

岩墙在这些地区出露广泛。在冀东地区，前人初步厘定了岩墙的期次，认为该区存在 3–5 期变质及未变质岩墙 (宋述光, 1990; 赵文浩, 1988; 陈曼云, 1990)。另外，本区报道有 2504–2516 Ma 的超基性到基性正长岩岩墙，并认为其代表了克拉通化 (Li et al., 2010)。Wang et al. (2015a) 在本区北部青龙地区及东部邻区识别出了 1208–1244 Ma 岩墙（图 3.8c），认为是~1230 Ma 华北下部的地幔柱所引起。笔者之前的工作显示，冀东存在~1680 Ma（斜锆石）、~1230 Ma（斜锆石）及~775 Ma（锆石）基性岩墙事件 (Wang et al., 2016b)（图 3.8c）。在鲁西地区，

晚前寒武纪基性岩墙被命名为牛岚单元（依据 K–Ar 和 Rb–Sr 年龄），常成群分布，长可达 5 km，宽 1–20 m 局部可达 220 m，出露面积约 13 km^2 (山东省第四地质矿产勘查院, 2003)。最新的斜锆石 U–Pb 定年研究表明，鲁西地区存在~1.68 Ga 和~1.62 Ga 的 N–NW 向基性岩墙 (Li et al., 2015; 相振群等, 2012)。此外，研究者还报道郯庐断裂带内存在~1.21 Ga 的基性侵入体 (锆石 U–Pb，1209 ± 6 Ma; Peng et al., 2013)。在太行山南部，相比较于北侧的太行山区，本区岩墙出露并不广泛，目前仅报道有黎城~1.23 Ga 的岩墙 (Peng, 2015b)，该岩体侵入长城系常州沟组、串岭沟组，周围其他走向一致的岩墙亦侵入赞皇群（左权 1：20 万地质图，1972）。

综上，从目前的资料可推测这三个研究区是受燕辽裂谷活动影响的地区，至少记录有~1.68 Ga、~1.62 Ga 和~1.23–1.21 Ga 的基性岩墙侵入事件，这些记录能够为探讨奴那/哥伦比亚时期的地质演化提供载体。

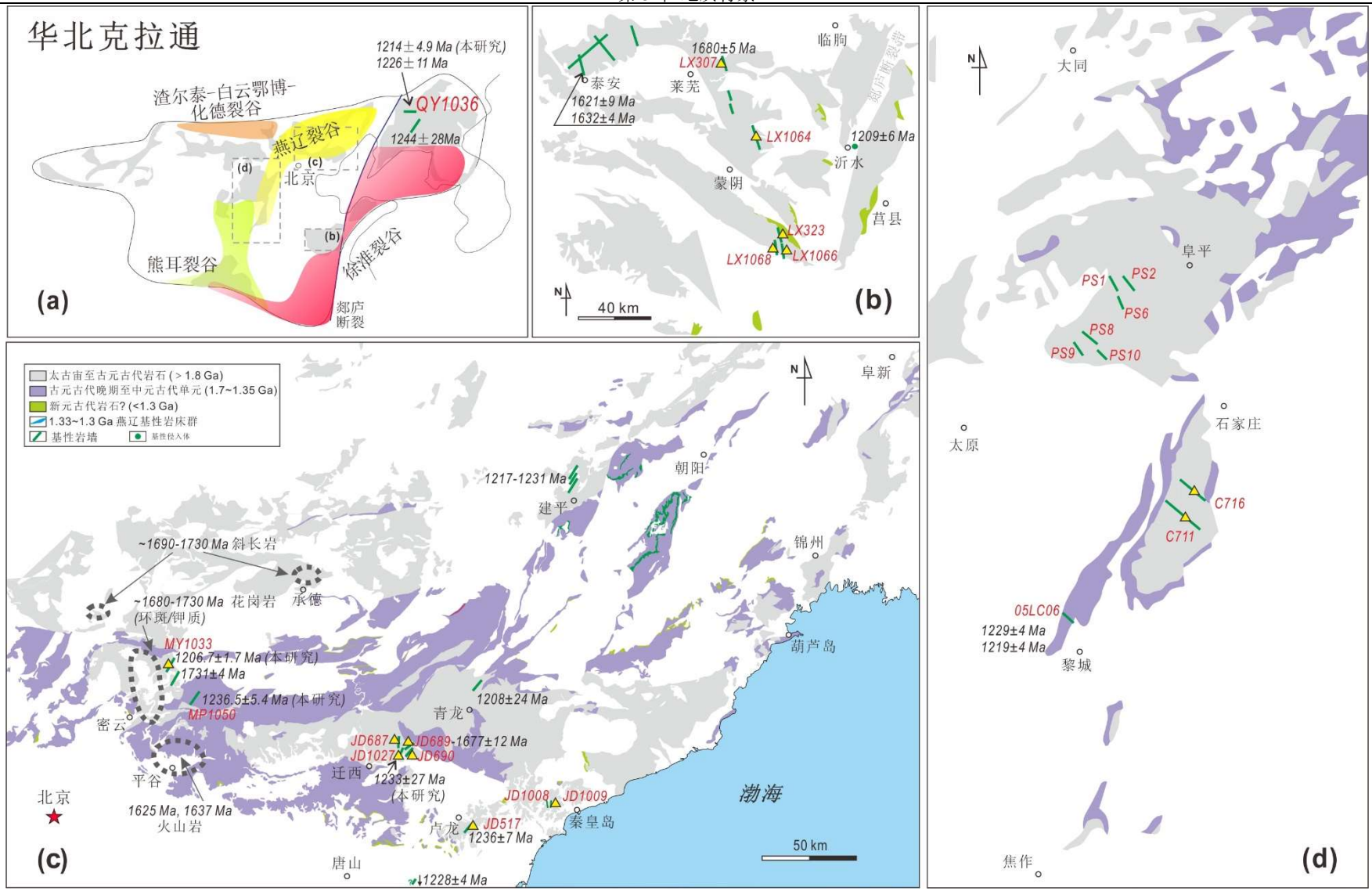

图 3.8 研究区地质简图：（a）华北克拉通，标有古元古代末至新元古代裂谷；（b–d）分别为鲁西、北京至冀东及太行山南部地区。三角形代表古地磁采样位置

Fig. 3.8 Sketched geological map of the study areas. (a) NCC, with distributions of late Paleoproterozoic to Neoproterozoic rifts; (b–d) Luxi, Beijing to Jidong, and southern Taihang Mt. respectively. Triangles represent paleomagnetic sample locations.

第4章 野外调查、采样与岩相学

4.1 野外调查

本研究在三个研究区调查岩墙＞70 条，其中未变质变形的岩墙约 50 条。除了 MP1050 岩墙外，其他岩墙均侵入太古宙结晶基底，多数岩墙可见冷凝边（图 4.1）。这些岩墙直立或近于直立产出（图 4.1b，d–f）。地质图显示 MP1050 切穿长城系串岭沟组、团山子组、大红峪组和蓟县系高于庄组（六道河 1:5 万地质图，1995），但因露头状况较差，并未得到更多调查。在冀东地区，岩墙多以 NE 至 NEE 向展布，少部分岩墙呈 NNE 向或近于 N–S 向（图 3.8c）；这些岩墙多数＞10 m 宽，常见~20 m 宽，密云白河涧岩墙可达~80 m 宽。在鲁西地区，岩墙多以 NNW 至 N–S 向展布，少部分岩墙为 NE 向展布（如泰山地区的 NE 向岩墙）（图 3.8b），且目前已证实 NNW–NW 走向的岩墙至少存在~1.68 Ga 和~1.62 Ga 两期 (Li et al., 2015; 相振群等, 2012)；岩墙宽数米到几十米不等，但多数＞10 m。在太行山南部调查的两条的岩墙均为 NW 向（图 3.8d），宽 20–30 m。

本研究依据年代学、地球化学及古地磁学结果，厘定出 16 条岩墙作为主要研究对象，它们分别是：冀东老王家岩墙（JD1027）、老李家岩墙（JD687）、屠家沟两条岩墙（JD689 和 690）、茆家沟岩墙（JD517）、西桐叶岩墙（JD1008）、东桐叶岩墙（JD1009）、密云白河涧岩墙（MY1033）、承德米铺岩墙（MP1050）（图 3.8c）；鲁西邹家篮子岩墙（LX307）、五彩庄岩墙（LX323）、焦坡岩墙（LX1064）、下盐店岩墙（LX1066）、高家围子岩墙（LX1068）（图 3.8b）；太行山南部南沟岩墙（C711）和任家洞岩墙（C716）（图 3.8d）。其中，笔者之前的工作已厘定出 JD517 和 JD689 的侵位时代，分别为 1236 ± 7 Ma 和 1677 ± 12 Ma (Wang et al., 2016b)；而 LX307 的侵位时代为 1680 ± 5 Ma (Li et al., 2015)。

4.2 岩相学

在冀东地区，JD1027 岩墙位于迁西县太平寨镇老王家村村西，该岩墙与之前报道的 JD687 岩墙 (Wang et al., 2016b) 空间相距几公里（图 3.8c）。老王家岩墙走向约 24°，宽度＞30 m；其岩体侵入太古宙片麻岩中，但冷凝边风化破碎严

重。该岩墙中间部位岩石呈粗粒结构（图 4.1a）。西桐叶岩墙（JD1008）和东桐叶岩墙（JD1009）走向近于 N–S（~350–002°）（图 3.8c）。JD1008 岩墙不足 10 m 宽，可追索的露头约有 200 m；JD1009 岩墙露头在小山丘上，出露~10 m 宽，与周围的农耕区相区分，但未见冷凝边。 这些岩墙主要由斜长石（50–55%）和辉石（35–40%）组成，含少量黑云母、Fe–Ti 氧化物及锆石副矿物（图 4.1g, h）。

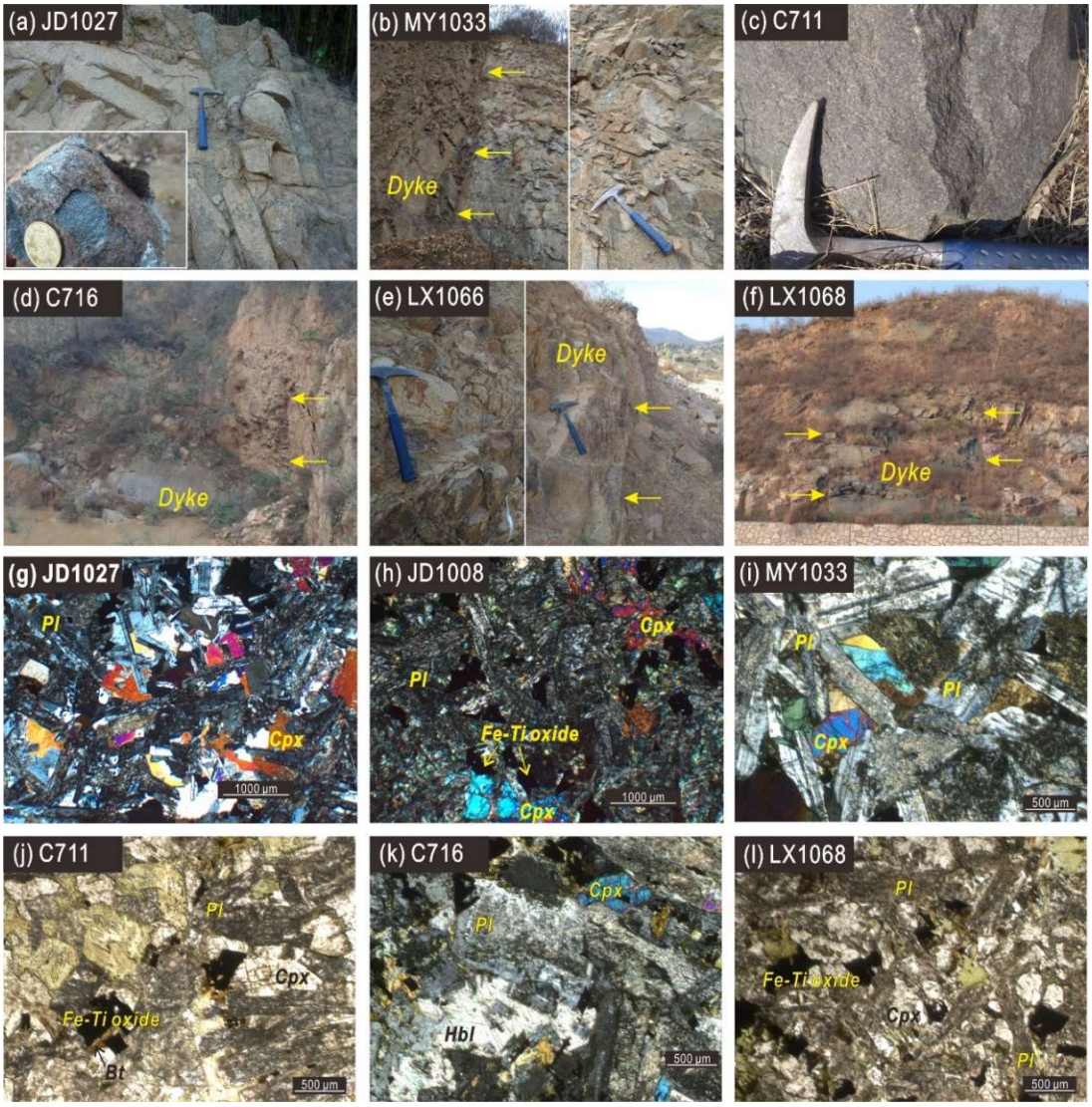

图 4.1 岩墙代表性野外照片（a–f）及镜下照片（g–l）。（b，d–f）箭头指向（近于）垂直的岩墙与围岩的界线。（j）和（l）为单偏光；（g–i）和（k）为正交偏光。Pl–斜长石、Cpx–单斜辉石、Hbl–角闪石、Bt–黑云母

Fig. 4.1 Representative photos of outcrops (a–f) and thin sections micro-photographs (g–l) of the studied dykes. Arrows in (b, d–f) indicate (near) vertical and regular boundaries between mafic dykes and country rocks. Micro-photographs (j) and (l) are under single polarized and (g–i, k) are under cross polarized lights. Pl–plagioclase, Cpx–clinopyroxene, Hbl–hornblende, Bt–biotite

白河涧岩墙（MY1033）位于密云县东北方向（图 3.8c）。该岩墙走向约为 35°，~80 m 宽，可追索两侧的冷凝边（图 4.1b）。岩石为辉绿岩，具有典型的辉绿结构（图 4.1i）。米铺岩墙（MP1050）位于承德市兴隆县米铺村附近，在白河涧岩墙的东南方（图 3.8c）。该岩墙沿 NE 向展布，岩石呈粗粒结构，但风化严重。

在鲁西地区，岩墙 LX323、LX1064、LX1066 和 LX1068 呈 NNW 向展布（~350°）（图 3.8b），10–20 m 宽。其围岩均为花岗质岩石，故很容易识得岩墙与围岩的界线（图 4.1e–f）。LX323 岩墙来自沂南五彩庄，该区岩墙密集，可在不同露头追索岩墙。LX1064 岩墙来自蒙阴县焦坡村，该岩墙在之前的报道中被描述过 (Wang et al., 2007)，其由 ~40%的单斜辉石和~50%的斜长石及少量角闪石、黑云母、石英以及蚀变矿物绿泥石组成（样品 05SD-21）(Wang et al., 2007)。LX1066 和 LX1068 岩墙均来自费县相家庄、下盐店和高家围子地区。该区岩墙密度较大，除上述两条岩墙之外还有走向相近的窄岩墙。LX1068 岩墙含有较多的斜长石，辉绿结构明显，但矿物蚀变严重（图 4.1l）。

在华北克拉通中部，岩墙 C711 和 C716 分别来自河北省临城县南沟村和赞皇县任家洞村。C711 和 C716 均侵入太古宙赞皇群；岩墙＞15 m 宽，NW 向展布（~310°）（图 3.8d）。露头剖面上可见岩墙的球形风化。岩石主要由斜长石（~50%）和辉石组成（~40%），含角闪石（2–5%；可见清晰的解理）、黑云母（2–5%）和 Fe–Ti 氧化物（~5%）（图 4.1j–k）。

整体上，岩墙中的斜长石颗粒长超过 1 mm，但有不同程度的钠黝帘化；单斜辉石相对斜长石较小较为新鲜，Fe–Ti 氧化物通常 0.1–0.5 mm，通常以自形矿物出现在斜长石和辉石之间（图 4.1g–l）。

4.3 采样

按照研究设计，本研究在野外除进行基本地质调查外，还进行了定年、地球化学以及古地磁学的采样。一般同一条岩墙共用一个点号，除非同一岩墙的两个露头相距较远。岩墙点号的记录格式为“区域/地名首字母+GPS 号”，如图 3.8b 中的“LX323”，代表鲁西地区 323 号岩墙。进行年代学分析的样品一般采

自较宽岩墙（＞15 m）的中心部位，样品重约 10–20 kg。进行地球化学分析的样品分散采自岩墙的边部与中间位置，根据肉眼观察岩相的变化及露头情况选取 2–4 块手标本大小的新鲜样品。年代学样品与地球化学样品的编号方法一致，即“GPS 号+小地名首字母+样品编号”，如定年样品 1027LWJ1（见 5.2 部分）代表冀东 1027 号老王家岩墙样品 1。

在野外，使用便携式汽油钻机钻取古地磁样品，并使用定向器及磁罗盘对样品定向。如果天气允许，同时记录太阳罗盘信息，以校正定向数据。采样中，尽量选择边部细粒部分，但边部往往破碎或风化严重，难以取样。多数样品来自多个新鲜的岩体或露头，竭力避免“马蜂窝”式采法（局部露头大量密集采样），确保样品具有代表性。其中，GPS 编号为 1009、1027、517、687 和 689 的五条岩墙，每条岩墙至少含两个局部露头，但每个采点的取样稍密集；本研究最终选取其中~12 个较具有代表性的样品进行分析。对于其他岩墙，每条岩墙只有一个采点，含 6–16 个较为分散的样品（视露头情况而定，平均每条 12 个样品）。同时，本研究尽量寻找坚硬的围岩采样，以尝试进行烘烤检验。

本研究以“GPS-露头-1A/B/C”或“GPS-1A/B/C”的形式标记古地磁样品，即样品号的第一个数字代表野外 GPS 点号；最后一个数字代表样品号码。个别岩墙样品存在中间数字，则代表露头编号，通常为1–3，若不存在中间数字则说明岩墙只有一个大采点。若一个样品切成了 2–3 块小样品（specimens），则用 A/B/C 区分，通常 A 为远离露头表面的内部新鲜样品，按照字母顺序则样品更加接近露头表面；若样品只切成 1 块（specimen），则没有字母后缀。如“1027-2-3B”代表1027号岩墙2号露头的第3块样品，第3块样品切成了多个小样品，此样品为B样品；如“1056-3”即代表 1056 号岩墙的第 3 块样品（sample），该岩墙只有一个采点且该样品只切成了一块小样品。在磁化率各项异性（AMS）测量之后，部分标准样品被等分切成了两块小样品，其中底部的标记为 L，上部的标记为U。对于围岩样品的编号，与此类似。

对于年代学分析，本研究成功从白河涧岩墙（MY1033）、米铺岩墙（MP1050）和老王家岩墙（JD1027）中分选出了斜锆石。除此之外，辽宁北部清原的一条岩墙（12LN54-1）显示 LA–ICPMS 锆石 U–Pb 年龄为 1226 ± 11 Ma

(Wang et al., 2015a)，本研究从该岩墙中获得了斜锆石，使用 TIMS 方法对此重新定年（QY1036，样品 1036QY1）。本文新补充的地球化学数据来自老王家（JD1027）、西桐叶（JD1008）、东桐叶（JD1009）、任家洞（C716）、南沟（C711）、五彩庄（LX323）、焦坡（LX1064）、相家庄（LX1066）和高家围子（LX1068）九条岩墙，共 13 组数据。岩石成因的分析，同时总结了前人报道的数据，以统筹分析。对于古地磁研究，本文介绍的结果来自 13 条岩墙，而西桐叶岩墙（JD1008）露头较差、米铺岩墙（MP1050）岩石较软、清原岩墙（QY1036）位于郯庐断裂东侧，未对这三条岩墙进行古地磁取样。

第5章 年代学

5.1 分析方法

本研究在两个实验室进行斜锆石的分选，其一是在中国科学院地质与地球物理研究所岩矿制样与分析实验室使用 Wilfley800 型摇床分选斜锆石 (Söderlund and Johansson, 2002)；其二在廊坊宇恒矿岩技术服务公司先使用摇床进行粗选，然后使用重矿物淘洗盘加磁选机进一步分选。最终，从编号为 JD1027、MY1033、QY1036 和 MP1050 的岩墙中分别获得了~40 颗、44 颗、24 颗、16 颗斜锆石，但整体上颗粒较小（＜100 × 40 μm）。岩墙 JD1027 的定年分析在岩石圈演化国家重点实验室完成，使用 Cameca 1280 型离子探针；岩墙 MY1033、QY1036 和 MP1050 的定年分析在澳大利亚科廷大学 John de Laeter 研究中心完成，具体在西澳大学完成化学熔样处理，在科廷大学的热电离质谱实验室使用 Thermo Triton Plus 完成分析。

离子探针的分析遵循 Li et al. (2009) 的程序。在分析之前，矿物颗粒被固定在环氧树脂靶上，剖光使其露出矿物表面。然后通过背散色图像、透射光和反射光图像观察矿物形态、有无裂缝或包裹体，尽可能避开瑕疵分析。测试过程中的吹氧技术尽可能降低斜锆石晶体光轴效应的影响，以提高 $^{207}Pb/^{206}Pb$ 的分析精度 (Li et al., 2010)。同时分析了斜锆石标样 *Phalaborw* 以监测 Pb 同位素分馏。由于斜锆石一般有较低的普通 Pb 含量，因此使用现代地壳中平均的 Pb 组分 (Stacey and Kramers, 1975) 作为斜锆石的普通 Pb 组成，以校正原始数据 (Li et al., 2010)。

对于热电离质谱（TIMS）分析， 除了用浓缩蒸馏 HNO_3 和 HCl 清洗颗粒之外，没有进行其他前处理。在测量之前，样品中加入了 $^{205}Pb-^{235}U$ 内部示踪剂溶液，并在西澳大学的超净实验室中熔解。熔解是通过 HF 蒸气实现的，使用 Teflon 微胶囊在 Parr 压力容器中放置，在 230℃的烘箱中持续放置六天。在 HCl 和 H_3PO_4 中重新熔解所得残余物，并置于一个去气的精制的铼单丝上，带有 5 μL 硅酸凝胶。以 UO_2 的形式测量铀含量。使用 SRM981 和 SRM 982 监测分馏。质量分馏为 0.04 ± 0.09%/ amu，使用的 U 衰变常数来自 Jaffey et al. (1971)。使

用 Tripoli（来自 CIRDLES.org）和 Isoplot 软件包处理数据并绘图。斜锆石晶体的重量是通过显微照片的测量和第三维的估计获得，不确定度为 50%。

5.2 分析结果

分析结果如表 5.1 所示。

（1）冀东老王家岩墙（样品 1027LWJ1）

老王家岩墙中的斜锆石呈棕色板状，大小约 50–80 μm × 10–20 μm（图 5.1a）。由于晶体颗粒较小，仅分析了 6 颗斜锆石（共 6 个分析点）。$^{206}Pb/^{204}Pb$ 比值为 1069–47966。其中，四组分析结果的 $^{207}Pb/^{206}Pb$ 的表面年龄为 1202–1246 Ma（图 5.1a）。所有分析结果的 $^{207}Pb/^{206}Pb$ 加权平均年龄为 1233 ± 27 Ma（MSWD = 0.55）。据观察，斜锆石颗粒周围没有锆石生长边，因此两个分析点较高的误差可能来自分析过程中普通 Pb 的混染，也可能是因为分析束斑覆盖到了矿物的边部（点 3）或者矿物内部缝隙（点 6）（图 5.1a），这会使得通过现代地壳平均 Pb 进行的校正不准，以致出现较大的误差 (王冲等, 2016)。但考虑到较一致的 $^{207}Pb/^{206}Pb$ 年龄，我们认为~1233 Ma 代表了该岩墙的结晶年龄。

（2）密云白河涧岩墙（样品 1033BHJ1）

对该岩墙的 5 颗斜锆石进行热电离质谱分析。其 U 含量为 85–218 ppm；Th/U 低于 0.10。可能由于微晶锆石的生长，部分数据不谐和（图 5.1b），指示存在铅丢失。一致的 $^{207}Pb/^{206}Pb$ 年龄说明铅丢失为最近，因此其加权平均年龄可代表结晶年龄。5 颗矿物的 $^{207}Pb/^{206}Pb$ 平均年龄为 1206.7 ± 1.7 Ma（2σ，MSWD = 1.09）。

（3）清原岩墙（样品 1036QY1）

清原岩墙位于辽宁北部，郯庐大断裂东侧。本研究分析了 6 颗斜锆石。这些斜锆石都很小，U 含量为 178–276 ppm；Th/U 同样小于 0.10。虽然 2 颗斜锆石的分析结果谐和，但其中 4 颗的结果不谐和（图 5.1c）。所有的 $^{207}Pb/^{206}Pb$ 年龄一致，指示铅丢失为最近，其加权平均年龄为 1214.0 ± 4.9 Ma（2σ，MSWD = 0.49）。本研究认为其代表岩墙侵位年龄。该年龄与之前报道的定年结果（1226

± 11 Ma，锆石 LA–ICPMS (Wang et al., 2015a) ）在误差范围内一致。

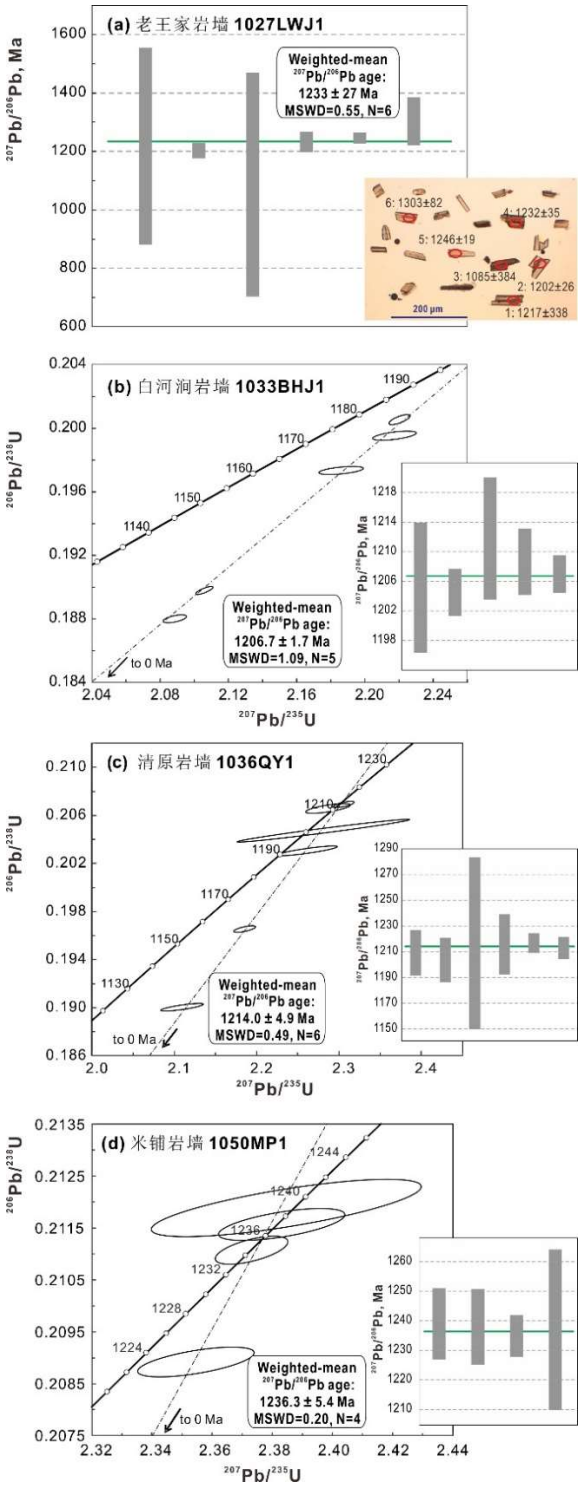

图 5.1 斜锆石 U–Pb 定年结果。（a）老王家岩墙样品 1027LWJ1，插图为透射光下的斜锆石照片；（b–d）依次为白河涧岩墙样品 1033BHJ1、清原岩墙样品 1036QY1 和米铺岩墙样品 1050MP1

Fig. 5.1 Baddeleyite U–Pb dating results. (a) sample 1027LWJ1 from Laowangjia dyke (JD1027) with mineral picture under transmitted light; (b–d) are samples 1033BHJ1 from Baihejian dyke, 1036QY1 from Qingyuan dyke, and 1050MP1 from Mipu dyke, respectively.

（4）兴隆米铺岩墙（样品 1050MP1）

对该岩墙的 4 颗斜锆石进行分析，其 U 含量为 139–198 ppm，Th/U 低于 0.06。三颗矿物的分析结果近于谐和，所有分析的 $^{207}Pb/^{206}Pb$ 加权平均年龄为 1236.3 ± 5.4 Ma（MSWD = 0.49）（图 5.1d），为岩墙的结晶年龄。该岩墙的分析结果与老王家岩墙的结果（图 5.1a）及冀东地区茆家沟岩墙的斜锆石离子探针分析结果 (1236 ± 7 Ma；Wang et al., 2016b) 相近。

根据前人年代学报道及本研究定年结果，本文总结从古元古代晚期到中元古代，东华北克拉通发育有多期基性岩墙/岩床侵入事件，主要有~1.73–1.68 Ga 的非造山岩浆作用（环斑花岗岩、斜长岩等）、~1.68 Ga 基性岩墙群、~1.64 Ga 火山作用、~1.62 Ga 基性岩墙与火山岩、~1.32 Ga 燕辽岩床群与大同岩墙，以及 ~1.23 Ga 的基性岩浆作用 (Peng, 2015b; Wang et al., 2015a, 2016b; Zhang et al., 2017; 本文)。

表 5.1 斜锆石 U–Pb 定年数据表

Table 5.1 U–Pb isotopic data for baddeleyites dating

束斑	^{204}Pb (cps.)	$^{206}Pb/^{204}Pb$	$^{207}Pb/^{206}Pbc$	± 1σ %	$^{207}Pb/^{206}Pb$ (Ma)	± 1σ %
Sample 1027LWJ1						
1	48.8	1069	0.081	8.59	1217.0	338
2	12.6	6699	0.080	0.66	1202.3	26
3	17.1	7766	0.076	9.58	1084.6	384
4	56.6	1358	0.081	0.89	1232.2	35
5	2.2	47966	0.082	0.48	1246.2	19
6	5.8	17229	0.084	2.12	1303.2	82

颗粒	重量 (μg)	U (ppm)	Pb_c (pg)	mol% Pb*	Th/U	$^{206}Pb/^{204}Pb$	$^{207}Pb/^{206}Pb$	± 2σ (%)	$^{207}Pb/^{235}U$	± 2σ (%)	$^{206}Pb/^{238}U$	± 2σ (%)	ρ	$^{206}Pb/^{238}U$ Age (Ma)	± 2σ (Ma)	$^{207}Pb/^{206}Pb$ Age (Ma)	± 2σ (Ma)
样品 1033BHJ1																	
1	0.1	131	0.9	94	0	197	0.0803	0.5	2.186	0.5	0.197369	0.1	0.5	1161.17	1.22	1205	8.8
2	0.1	174	0.3	97	0.1	572	0.0803	0.2	2.221	0.2	0.200563	0.1	0.7	1178.34	1.5	1205	3.2
3	0.1	85	0.3	95	0.1	330	0.0806	0.4	2.218	0.5	0.199551	0.1	0.6	1172.91	1.38	1212	8.2
4	0.1	164	0.5	94	0.1	346	0.0805	0.2	2.087	0.3	0.188052	0.1	0.6	1110.81	1.19	1209	4.5
5	0.2	218	0.5	99	0.1	977	0.0804	0.1	2.105	0.2	0.18983	0.1	0.8	1120.45	1.22	1207	2.5
样品 1036QL1																	
1	0.2	231	0.4	92	0.1	1377	0.0805	0.9	2.11	1	0.190042	0.1	0.8	1121.6	1.58	1209	17.6
2	0.1	193	0.6	94	0.1	428	0.0803	0.9	2.287	1	0.206590	0.2	0.7	1210.62	1.91	1204	17.2
3	0.2	276	3.1	81	0.1	245	0.0808	3.4	2.281	3.8	0.204732	0.4	1.0	1200.69	4.57	1217	66.6
4	0.2	178	0.4	97	0	938	0.0808	1.2	2.262	1.3	0.203065	0.2	0.9	1191.77	1.91	1216	23.3
5	0.2	224	0.3	91	0.1	1596	0.0808	0.4	2.306	0.5	0.206913	0.1	0.7	1212.35	1.27	1217	7.6
6	0.2	180	0.3	95	0	1345	0.0807	0.4	2.186	0.5	0.196529	0.1	0.7	1156.65	1.26	1213	8.6
样品 1050MP1																	
1	0.2	187	1.8	84	0.03	146	0.08174	0.61	2.3547	0.67	0.208917	0.11	0.6	1223.04	1.38	1239	11.9
2	0.1	187	1.1	82	0.01	121	0.08170	0.65	2.3832	0.72	0.211568	0.12	0.6	1237.17	1.47	1238	12.8
3	0.2	198	0.6	95	0.06	401	0.08154	0.36	2.3731	0.42	0.211071	0.10	0.6	1234.52	1.28	1235	7.1
4	0.1	139	0.7	79	0.06	89	0.08163	1.39	2.3847	1.54	0.211886	0.21	0.8	1238.86	2.65	1237	27.2

1027LWJ1: cps. = 每秒的计数（counts per second）；$^{207}Pb/^{206}Pbc$ = 已校正的 $^{207}Pb/^{206}Pb$；

1033BHJ1、1036QL1 和 1050MP1: Pb_c = 总普通 Pb，包括空白本底 （每个分析为 0.8 ± 0.3 pg）

空白组分 $^{206}Pb/^{204}Pb = 18.55 \pm 0.63$，$^{207}Pb/^{204}Pb = 15.50 \pm 0.55$，$^{208}Pb/^{204}Pb = 38.07 \pm 1.56$ (均为 2σ)； $^{206}Pb/^{204}Pb$–$^{207}Pb/^{204}Pb$ 相关性为 0.9.

Th/U 计算自放射成因的 $^{208}Pb/^{206}Pb$ 和年龄；测量的同位素根据示踪剂及质量分馏（0.04 ± 0.09 %/amu）校正；

ρ = 放射成因的 $^{207}Pb/^{235}U$ 与 $^{206}Pb/^{238}U$ 误差相关系数；与 ^{206}Pb 相关的比值已根据 $^{230}Th/^{238}U$ 初始不平衡（使用结晶环境中 Th/U = 4）校正；

第6章 地球化学

6.1 分析方法

地球化学分析包括全岩主量及微量元素分析，其中，老王家（JD1027）、西桐叶（JD1008）、东桐叶（JD1009）和任家洞（C716）共四条岩墙的六组数据完成于中国科学院地质与地球物理研究所；南沟（C711）、五彩庄（LX323）、焦坡（LX1064）、相家庄（LX1066）和高家围子（LX1068）共五条岩墙的七组数据完成于澳实矿物实验室 – 澳实分析检测（广州）有限公司。

首先，将代表性的样品磨成 200 目粉末。对于在研究所进行的主量元素分析，烘干后先在马弗炉 1000°C 灼烧一小时，冷却至室温后再称重，以灼烧前、后的重量差计算烧失量，之后将样品与四硼酸锂（$Li_2B_4O_7$）助溶剂混合熔制成玻璃片，最后在 X 射线荧光光谱（XRF）AXIOS Minerals 仪器中测量。对于在研究所进行的微量元素分析，先将粉末样品在混合酸（HNO_3 + HF）及 200°C 的条件下放置七天熔解，然后在电感耦合等离子质谱（Inductively Coupled Plasma Mass Spectrometry，ICPMS）ELEMENT 仪器中测量。在澳实实验室进行的主量元素分析流程与上述主量分析流程大致相同，区别在于测量烧失量的是另外一份称取的样品，分析仪器是 PANalytical PW2424。在澳实实验室进行的微量元素分析，其中 Cr 和 Ni 元素是使用高氯酸、硝酸和氢氟酸消解，蒸至近干后用稀盐酸溶解定容，使用 ICPMS Agilent 7900 仪器分析；取另一份样品，并加入偏硼酸锂/四硼酸锂熔剂混合均匀，在 1025°C 以上的熔炉中熔化，冷却后用硝酸、盐酸和氢氟酸定容，再用 ICPMS Agilent 7700x 仪器分析其他元素。

上述分析中，主量元素的分析精度均优于 5%，微量元素的精度均优于 10%。

6.2 分析结果

根据年代学结果（图 5.1）及对应样品的地球化学特征（图 6.1 和图 6.2），本文新的地球化学数据均属于 1.24–1.21 Ga 岩墙群，分析结果如表 6.1 所示。元素图解及微量相关配分型式图（图 6.1 和图 6.2）同样呈现了已报道的、并有 U–Pb 定年约束的同期地球化学数据（见附录）。

被分析的岩墙 SiO_2 含量变化范围为 48.4–53.2 wt.%，MgO 含量变化范围为 4.40–6.22 wt.%（表 6.1）；结合已报道的本期岩浆作用数据，可发现该期岩墙的

SiO_2 与 MgO 存在负相关关系，而其中硅含量稍高的 LX323 和 LX1066 岩墙（SiO_2＞52 wt.%）含有较低的镁含量（图 6.1）；所有数据中镁含量最低的样品来自黎城岩墙，其硅含量为 49.1 wt.%（样品 05LC06，附录）。 岩石有较高的 TiO_2 含量（>1.61 wt.%）及正常的全铁组分（tFe_2O_3 = 11.1–14.7 wt.%）（表 6.1）；但二者与 MgO 的相关趋势并不明显（图 6.1）。 Mg# 值为 42.0–52.7（Mg# = 100 × MgO/ (FeO_{total} + MgO)，分子比）（表 6.1）。Al_2O_3 和 CaO 的变化范围分别为 13.6–17.0 wt.%、5.90–10.4 wt.%；全碱（Na_2O + K_2O）含量为 3.34–6.22 wt.%（表 6.1）。整体上，随着 MgO 含量的降低，CaO 含量有微弱的降低趋势（图 6.1）。

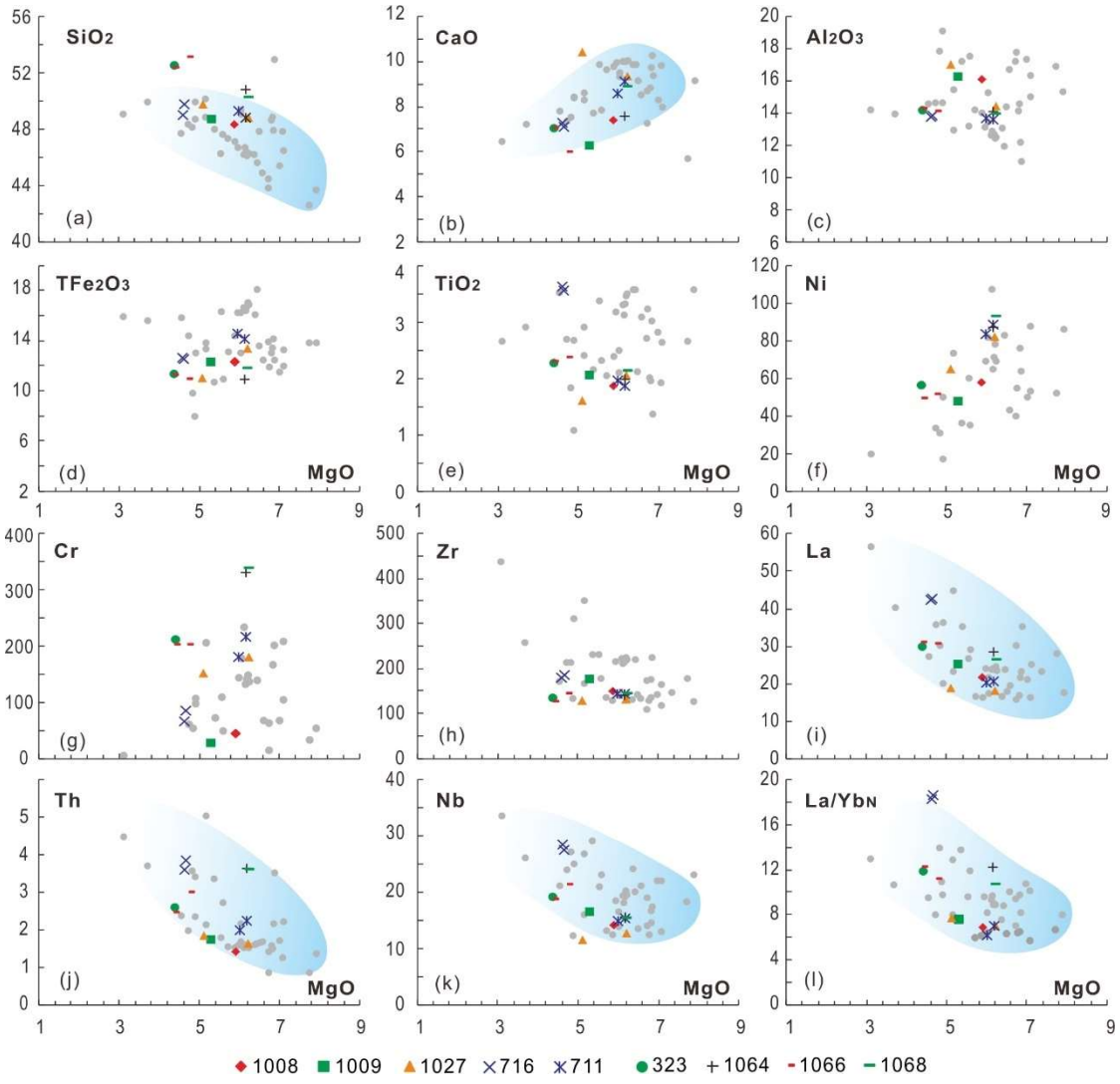

图 6.1 全岩主量和微量元素对 MgO 协变图解。灰色圆圈为已报道的数据（N = 37，见附录）

Fig. 6.1 Whole-rock major and trace elements vs. MgO diagrams. Grey dots represent reported data (N = 37, see Supplementary file)

被分析的岩墙相容元素 Cr 和 Ni 的含量分别为 28–336 ppm 和 48–93 ppm（表

6.1），整体上 Cr 与 MgO 含量变化无关联，但 Ni 与 MgO 似乎呈正相关（图 6.1）。

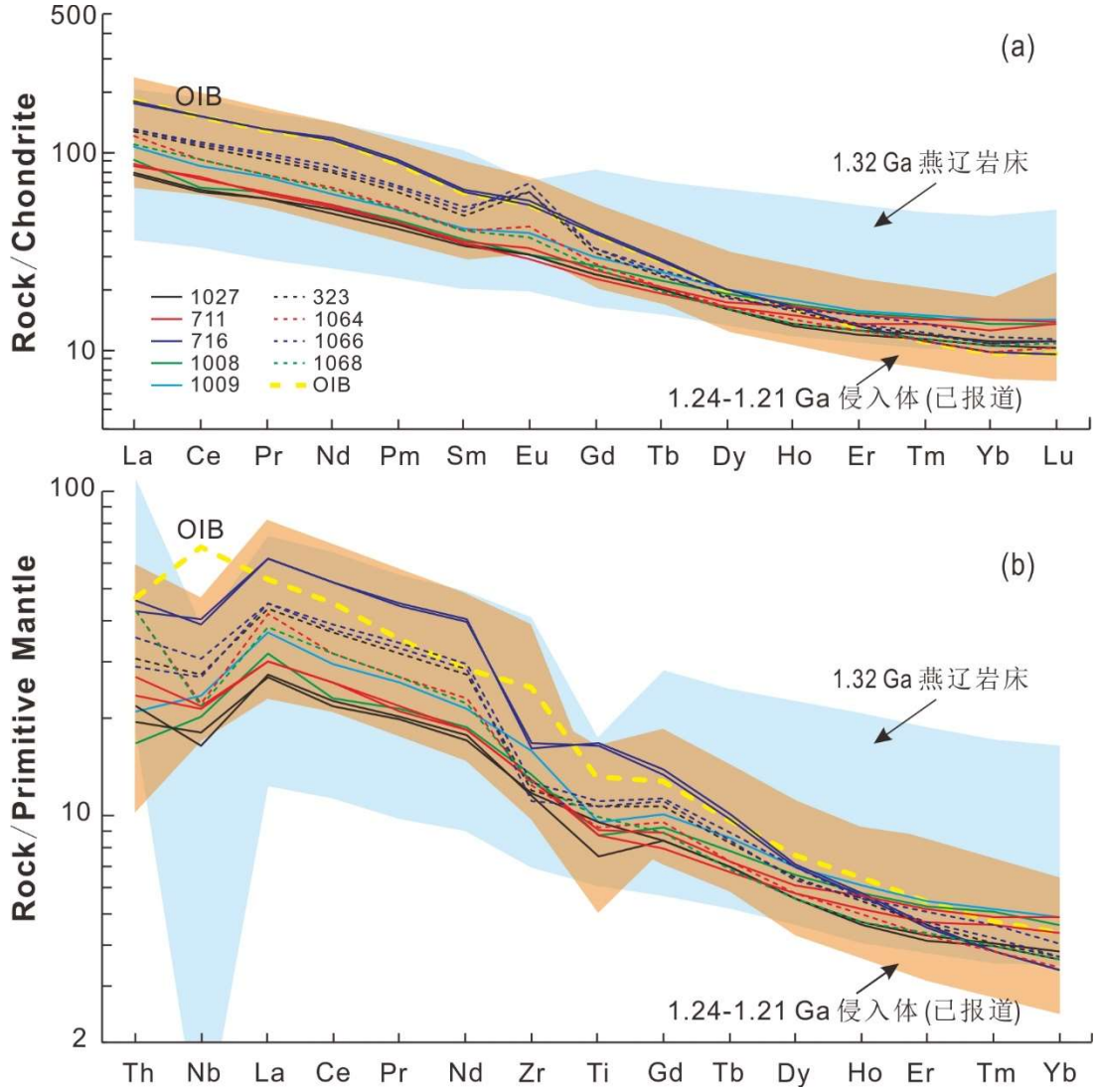

图 6.2 球粒陨石标准化稀土配分图（a）和原始地幔标准化蛛网图（b）。球粒陨石及原始地幔标准值来自 Sun and McDonough (1989)。1.24–1.21 Ga 侵入体数据见附录。华北 1.32 Ga 燕辽岩床的数据（N = 45）来自 Zhang et al. (2017)

Fig. 6.2 Chondrite-normalized REE patterns (a) and primitive mantle-normalized multi-element spider-grams (b). Chondrite normalized values and primitive mantle values are from Sun and McDonough (1989). Complied data of the 1.24–1.21 Ga mafic intrusions see Supplementary file. Data of the 1.32 Ga Yan–Liao sills (N = 45) in the NCC are from Zhang et al. (2017).

本研究的样品有中到高的总稀土含量（ΣREE = 107–235 ppm），并富集轻稀土（La/Yb_N = 6.15–18.6，球粒陨石标准化），新的样品里轻稀土富集程度最高和最低的岩墙均位于华北中部（表 6.1），轻稀土较为富集的样品还包含冀东及其北部建平的岩墙（附录），但冀东也包含轻稀土富集相对较小的样品，如老王家岩墙（表 6.1）。Eu 异常值为 0.97–1.73（$Eu/Eu^* = Eu_N/[(Sm_N) \times (Gd_N)]^{1/2}$），鲁

表 6.1 岩墙全岩主量元素（wt.%）和微量元素（ppm）数据

Table 6.1 Whole-rock major (wt.%) and trace (ppm) elements data of the dykes

Sample	1008XT1	1009DT1	1027LW1	1027LW2	716RJD1	716RJD2	711NG22	711NG4	323WCZ2	1064JP1	1066XZ1	1066XZ2	1068-2
SiO_2	48.4	48.7	49.8	48.8	49.1	49.7	49.3	48.8	52.5	50.8	52.4	53.2	50.3
TiO_2	1.87	2.07	1.61	2.07	3.63	3.56	1.97	1.87	2.29	2.00	2.30	2.39	2.15
Al_2O_3	16.1	16.3	17.0	14.4	13.8	13.9	13.7	13.6	14.2	14.1	14.3	14.1	13.9
tFe_2O_3	12.4	12.4	11.1	13.4	12.7	12.6	14.7	14.2	11.4	11.0	11.3	11.0	11.8
MnO	0.16	0.18	0.15	0.20	0.19	0.19	0.23	0.21	0.20	0.19	0.20	0.21	0.18
MgO	5.88	5.28	5.09	6.21	4.6	4.64	5.98	6.16	4.38	6.15	4.39	4.74	6.22
CaO	7.40	6.25	10.43	9.31	7.27	7.10	8.57	9.12	7.04	7.55	7.02	5.93	8.89
Na_2O	3.37	3.67	2.47	2.13	3.78	3.77	2.20	2.15	3.61	3.70	3.79	3.94	2.76
K_2O	1.97	2.28	0.87	1.34	2.12	2.31	1.52	1.36	2.22	1.88	2.01	2.28	1.66
P_2O_5	0.31	0.42	0.22	0.21	0.60	0.57	0.21	0.19	0.29	0.23	0.28	0.29	0.23
LOI	2.96	2.70	2.00	2.30	2.08	2.14	1.91	2.42	1.92	2.45	2.15	2.02	2.05
Total	100.8	100.2	100.7	100.4	99.8	100.5	100.2	100.1	100.1	100.1	100.1	100.1	100.1
Mg#	48.7	46.0	47.8	48.1	42.0	42.4	44.9	46.5	43.4	52.7	43.7	46.2	51.3
Cr	44.2	27.9	151	181	65.7	85.3	181	215	212	329	202	202	336
Ni	57.7	47.7	65.4	82.4			84.0	88.7	56.9	87.6	49.6	51.6	93.0
Rb	62.0	83.7	21.1	45.0	50.6	53.9	72.3	53.4	49.1	96.6	52.1	60.1	96.0
Ba	1091	950	335	618	1157	1266	389	313	853	881	710	830	478
Th	1.42	1.76	1.84	1.64	3.59	3.86	2.00	2.26	2.59	3.63	2.46	2.99	3.61
U	0.41	0.51	0.44	0.42	0.86	0.89	0.44	0.59	0.66	1.02	0.61	0.70	0.93
Nb	14.3	16.8	11.7	12.9	28.7	27.5	15.1	15.4	19.2	15.8	18.9	21.5	15.5
Ta	0.88	1.02	0.78	0.85	1.72	1.68	1.3	1.3	1.3	1.4	1.2	1.5	1.1
La	21.7	25.1	18.7	18.1	42.2	42.7	20.4	20.6	29.9	28.5	30.8	30.7	26.2
Ce	40.5	51.7	39.7	38.8	92.7	91.9	45.5	45.3	65.4	56.2	66.2	68.6	56.4
Pr	5.91	7.07	5.57	5.48	12.5	12.3	5.81	6.03	8.71	7.39	9.09	9.42	7.37

Sample	1008XT1	1009DT1	1027LW1	1027LW2	716RJD1	716RJD2	711NG22	711NG4	323WCZ2	1064JP1	1066XZ1	1066XZ2	1068-2
Sr	835	716	447	347	901	894	293	324	534	479	531	520	492
Nd	25.1	29.0	23.8	22.9	54.8	53.4	24.7	25.0	36.9	31.1	37.9	39.4	30.0
Zr	149	176	128	130	179	185	143	143	133	139	124	142	141
Hf	3.81	4.41	3.57	3.67	4.93	4.98	4.0	3.9	3.5	3.6	3.3	3.9	3.7
Sm	5.54	6.2	5.21	5.13	9.85	9.58	5.43	5.18	7.34	6.05	7.58	8.04	6.05
Eu	1.75	2.26	1.77	1.74	3.29	3.16	1.88	1.65	3.68	2.45	4.02	3.66	2.16
Gd	5.46	6.04	4.99	4.97	8.18	7.91	5.23	4.68	6.29	5.64	6.64	6.72	5.29
Tb	0.84	0.92	0.75	0.75	1.09	1.05	0.78	0.72	0.88	0.78	0.90	0.95	0.74
Dy	4.84	5.15	4.08	4.04	5.17	5.13	4.44	4.20	4.70	4.24	4.69	5.10	4.07
Y	26.1	25.9	18.9	19.7	22.1	21.6	22.0	20.8	21.3	19.1	21.2	22.2	19.1
Ho	0.95	1.0	0.75	0.76	0.94	0.92	0.93	0.84	0.89	0.81	0.91	0.91	0.77
Er	2.50	2.61	1.98	2.06	2.20	2.16	2.46	2.25	2.19	2.06	2.24	2.44	2.08
Tm	0.37	0.38	0.29	0.30	0.28	0.28	0.36	0.34	0.30	0.28	0.31	0.34	0.29
Yb	2.28	2.38	1.76	1.86	1.65	1.65	2.38	2.14	1.81	1.67	1.81	1.99	1.77
Lu	0.34	0.36	0.26	0.28	0.24	0.24	0.35	0.34	0.28	0.26	0.28	0.29	0.27
Eu*	0.97	1.13	1.06	1.05	1.12	1.11	1.08	1.02	1.66	1.28	1.73	1.52	1.17
REE	118	140	110	107	235	232	121	119	169	147	173	179	143
Nb/Y	0.546	0.647	0.618	0.657	1.30	1.27	0.686	0.740	0.901	0.827	0.892	0.968	0.812
La/Sm	3.91	4.05	3.59	3.54	4.28	4.46	3.76	3.98	4.07	4.71	4.06	3.82	4.33
Th/Nb	0.10	0.10	0.16	0.13	0.13	0.14	0.13	0.15	0.13	0.23	0.13	0.14	0.23
Nb/La	0.66	0.67	0.63	0.71	0.68	0.64	0.74	0.75	0.64	0.55	0.61	0.70	0.59
La/Yb_N	6.82	7.56	7.62	7.00	18.3	18.6	6.15	6.90	11.85	12.24	12.21	11.07	10.62
Th/Yb	0.62	0.74	1.05	0.88	2.17	2.35	0.84	1.06	1.43	2.17	1.36	1.50	2.04
Nb/Yb	6.25	7.05	6.65	6.96	17.3	16.7	6.34	7.20	10.6	9.46	10.4	10.8	8.76
Zr/Y	5.69	6.79	6.76	6.60	8.07	8.57	6.50	6.88	6.24	7.28	5.85	6.40	7.38

tFe_2O_3 = 以 Fe_2O_3 表达的全铁；Mg# = 100 × MgO/ (FeO_{total} + MgO)，分子比；Eu* = $Eu_N/[(Sm_N) \times (Gd_N)]^{1/2}$；$La/Yb_N$，球粒陨石标准化之后的比值，标准化值来自 Sun and McDonough (1989)

西地区的岩墙表现不同程度的正 Eu 异常（1.17–1.73）（图 6.2a 和表 6.1），冀东地区的样品亦如此（附录）。在原始地幔蛛网图上，La 元素相对于 Nb 和 Ce 富集；除 JD1008 和 1009 岩墙外，其余样品 Nb 相对 Th 和 La 显示不同程度的有亏损；部分岩墙样品（如鲁西和华北中部）显示相对 Nd 和 Ti 而亏损 Zr；Ti 相对于 Zr 和 Gd 或富集或亏损或变化不大（图 6.2b）。

整体而言，鲁西的样品具有高 Si、低 Ca 和 Fe、高 Cr 的特征，同时显示正 Eu 异常；而冀东和华北中部的岩墙地球化学特征变化范围较大，尤其表现在主量元素含量、Eu 异常及轻重稀土的分馏（图 6.1、图 6.2、表 6.1 和附录）。

第7章 古地磁学

7.1 退磁方法

在野外钻取的样品，切样并重新标号之后，首先使用卡帕桥仪器（AGICO MFK1–FA Kappabridge）测量磁化率各向异性（anisotropy of magnetic susceptibility，AMS）（限于 25.4 mm × 22 mm 的标准样品）。随后进行退磁实验。

通常有两种退磁方法：交变退磁（Alternating-field demagnetization）以及热退磁（Thermal demagnetization）。交变退磁，即将样品置于交变磁场中退磁，交变场呈正弦变化且振幅随时间呈线性降低。由于样品的旋转，每次操作可清除样品天然剩磁中小于所设置最高磁场的部分。由低到高设置交变磁场（通常由 5 mT 逐步增加到 100 mT），逐步退磁并逐步测量剩磁。交变退磁能有效清除次生的天然剩磁（如多畴颗粒记载）而保留特征剩磁信息（如单畴或假单畴颗粒信息）；但能加载的最高交变场有限，一般为 100–110 mT。一般来说，交变退磁难以清除含赤铁矿岩石的次生天然剩磁组分，因为其往往有较高的矫顽力（高于交变场）。热退磁，即将样品逐步加热（温度由低到高）并在零磁空间中冷却，并逐步测量剩磁。每一步的加热，都能清除阻尼温度低于灼烧温度的磁性矿物颗粒的天然剩磁。这些被清除掉的天然剩磁组分为粘滞剩磁（VRM）（包括短的驰豫时间的单畴颗粒剩磁）。如果加热温度超过了阻尼温度或者居里温度，则特征剩磁的信息也会被清除。

本研究中，多数样品使用热退磁，少数样品使用交变退磁。一般交变退磁选择相对靠近岩体外部的 B 样品（specimen），而对应相对靠近岩体内部的 A 样品（specimen）则进行热退磁。拟进行交变退磁且天然剩磁较高（NRM＞10 A/m）的样品，使用交变退磁仪进行退磁，并使用旋转磁力仪（AGICO Spinner JR-6A）测量剩磁；天然剩磁不高（NRM＜10 A/m）的样品，可以直接在 2G 755 RAPID 型超导磁力仪中自动交变退磁并测量。对于热退磁分析，一般使用 MMTD 或 TD-48-SC 热退磁烤箱对样品进行加热，加热温度从 100°C 到 580°C（520°C 以上以 10°C 为加热间隔，总共加热约 17 步），并通风冷却；然后测量剩磁，多数使用 2G 755 RAPID 超导磁力仪，少数使用 Spinner JR-6A 旋转磁力仪测量。本研究对研究区内的~1.68 Ga 及~1.24–1.21 Ga 基性岩墙进行古地磁学

分析，所有实验完成于澳大利亚科廷大学古地磁实验室。

获得的退磁数据，使用主成分分析法计算剩磁矢量 (Kirschvink, 1980)，近乎所有的样品的最大角偏差（maximum angle of deviation，MAD）均小于 10°。在 Puffinplot 软件中计算并获得采点水平（岩墙）的稳定磁化方向 (Lurcock and Wilson, 2012)。每条岩墙的虚地磁极在 Puffinplot 中获得，并通过 Fisher 统计进一步获得同期的古地磁极。

7.2 分析结果

7.2.1 ~1.68 Ga 岩墙

本研究对~1.68 Ga 的两条定年岩墙 (JD689 和 LX307；Li et al., 2015; Wang et al., 2016b) 及另外一条岩墙（JD690）进行古地磁退磁分析。JD690 与定年岩墙具有相似的磁化方向。分析中同时使用交变和热退两种退磁方法，但热退更有效。

岩墙 LX307（1680 ± 5 Ma；图 3.8b）约 35 m 宽。该岩墙的样品含有两组高温分量（high temperature component，HTC）。四个样品（A 组）显示低倾角及北北东向下的特征剩磁（ChRM）方向（D = 26.0°, I = 17.0°, α_{95} = 8.2°）（图 7.1a，图 7.2a 和表 7.1）。另外五个样品（B 组）显示分散的中到高的倾角（四个向下，一个向上；图 7.2a）。图 7.2d 中，方形为该采点的轴向地心偶极子极（D/I = 0°/53.7°），三角形为现代地球磁场方向（Present Geomagnetic Field，PGF）（D/I = 354°/55°；来自国际地磁参考场 IGRF，下同）。从该岩墙中得到的低温分量（low temperature component，LTC）（D = 13.3°, I = 54.8°，α_{95} = 11.5°）与这两个方向接近（图 7.2d 和表 7.2）。

岩墙 JD689（1677 ± 12 Ma；图 3.8c）约 12 m 宽。该岩墙的绝大多数样品具有较高的天然剩磁（NRM），其含量从 1.9 到 1080 A/m（图 7.2b）。退磁显示样品一般具有一个分量，且这些分量的方向较为分散（图 7.1b 和图 7.2b）。其花岗岩围岩也显示不稳定的剩磁方向。因此，本研究认为该岩墙的多数样品遭受了雷击，这一推断从 Qn 指数 (Radhakrishnamurthy, 1993) 中得到了验证。Qn = M_{NRM}/(Km×H)（M_{NRM}、Km 和 H 分别代表天然剩磁强度、初始磁化率和磁化时的地球磁场强度），该指数用于衡量天然磁场引发的磁化，因此高的值可能受雷击的影响。样品的 Qn 指数多数大于 10（图 7.2b 和表 7.3）。只有一个样品（689-

3-9）显示较低的天然剩磁与 Qn 值（表 7.3），并且与同期 LX307 岩墙中的 A 组高温剩磁方向相近（图 7.1b 和图 7.2a–b）。

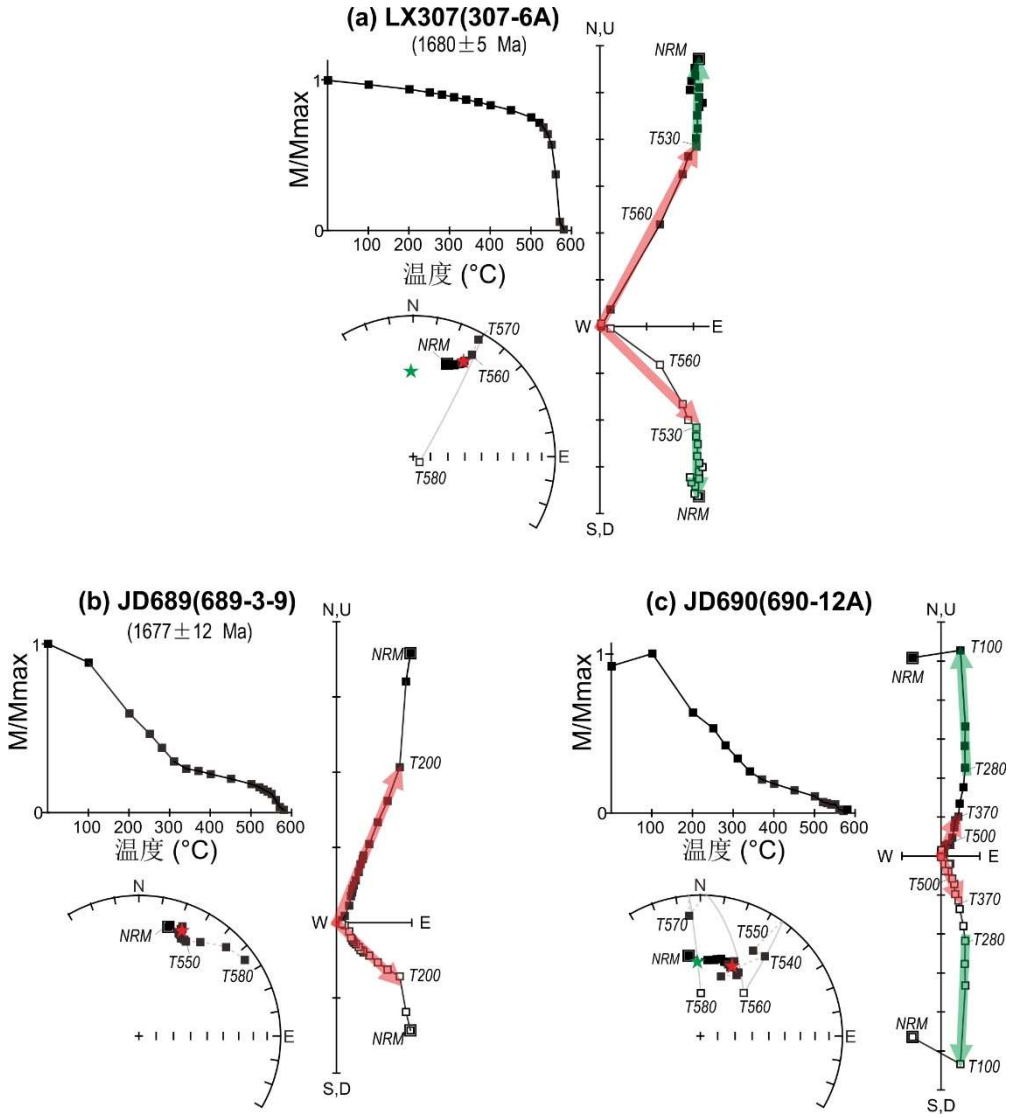

图 7.1 ~1.68 Ga 岩墙代表性退磁样品，含剩磁强度、退磁方向等面积投影（实心及空心方形分别代表下半球及上半球投影）以及正交投影（实心及空心方形分别代表水平面及垂向面的投影）。红色和绿色箭头分别代表高温和低温组分。

Fig. 7.1 Representative demagnetization data of the ~1.68 Ga dykes, plotted as remanence intensity vs. temperature, equal-area stereo-plots (solid/open are directions in the lower/upper hemisphere), and orthogonal projection diagrams (solid/open square points indicate vector end points projected onto the horizontal/vertical plane). Directions of HTC and LTC are shown by red and green arrows respectively.

岩墙 JD690 约 1.5 m 宽，位于 JD689 岩墙东南约 150 m 处（图 3.8c）。其中，有六个样品的天然剩磁为 51–77 A/m，Qn 指数 >10（图 7.2c 和表 7.3），这些样品也很可能遭受了雷击。剩余的 6 个样品具有较低的天然剩磁（≤6.7 A/m），其高温组分方向为 D = 17.3°，I = 23.9°，α_{95} = 20.8°（图 7.1c、图 7.2c 和表 7.1）。低温组分（通常在 100–280°C 解阻）的平均方向为 D = 0.3°，I = 45.1°，α_{95} =

12.9°（图 7.2e 和表 7.2）。该低温组分方向与现代场的方向（D/I = 352°/59°）及偶极子场的方向（D/I = 0°/49.8°）接近（图 7.2e）。从这三条岩墙中得到的极方向为 55.6°N，258.1°E，A_{95} = 7.2°（表 7.1）。

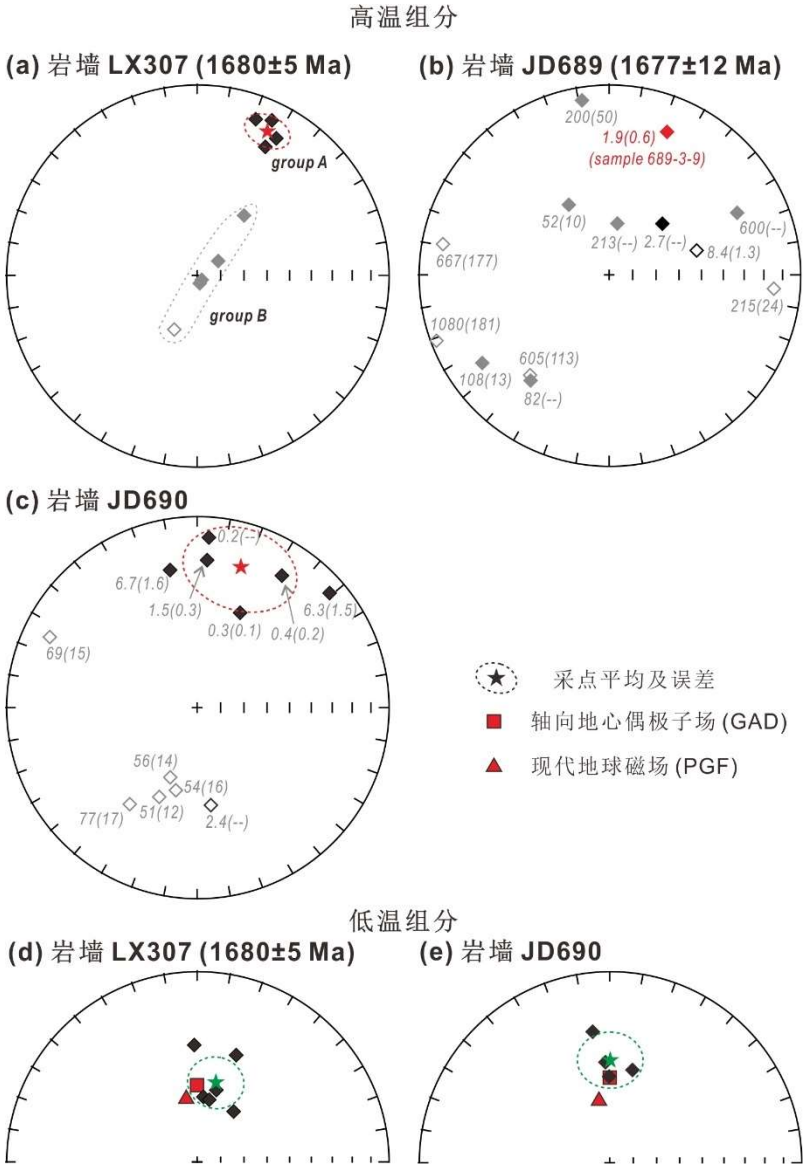

图 7.2 ~1.68 Ga 岩墙高温（a–c）和低温（d–e）分量等面积投影图。每个菱形代表一个样品，实心/空心菱形代表下半球/上半球的投影。采点平均方向以星形及 95%置信椭圆虚线表示。（b–c）样品旁标注有天然剩磁含量（单位 A/m），括号内为 Qn 指数，灰色的样品可能遭受了雷击。

Fig. 7.2 Equal-area projections of the high temperature (a–c) and low temperature (d–e) remanence directions of the ~1.68 Ga dykes. Each diamond point represents one sample. Solid/open symbols are projections on the lower/upper hemisphere. Site mean directions are represented by stars with dashed circles showing the 95% confidence cone. Some samples in (b) and (c) are marked with NRM values (A/m) and Qn ratios in brackets, and grey samples are likely struck by lightning.

表 7.1 岩墙退磁高温组分

Table 7.1 Paleomagnetic high temperature components of the dykes

岩墙编号	年龄 (Ma)	年龄参考文献	宽度 (m)	走向 (°)	纬度 (°N)	经度 (°E)	n/N	磁偏角 (°)	磁倾角 (°)	α_{95} (°)	极纬度 (°N)	极经度 (°E)	A_{95} (°)
~1.68 Ga 岩墙高温分量													
LX307	1680 ± 4	Li et al., 2015	~35	~340	36.278	117.890	4/9	26.0	17.0	8.2	53.6	250.9	6.1
JD690			~1.5	~30	40.250	118.533	6/12	17.3	23.9	20.8	58.4	264.9	16.3
JD689	1677 ± 12	Wang et al., 2016b	>10	~65	40.250	118.532	1/13	22.0	20.2		54.3	259.3	
									3 条岩墙采点平均		**55.6**	**258.1**	**7.2**
~1.24 Ga 岩墙高温分量													
JD517	1236 ± 7	Wang et al., 2016b	>15	~34	39.857	118.920	10/13	107.0	48.3	5.6	6.8	176.0	5.9
JD687			~25	~4	40.261	118.482	12/12	118.9	44.5	10.8	–2.7	170.4	10.8
JD1027	1233 ± 27	本研究	30–40	~24	40.245	118.486	8/12	130.3	36.6	5.4	–13.8	165.9	4.8
C711			>15	~310	37.400	114.187	11/11	98.0	21.0	2.7	0.4	190.7	2.0
C716			>15	~310	37.574	114.304	15/15	114.0	49.4	2.9	1.7	166.4	3.1
LX323			~15	~345	35.396	118.181	13/15	132.1	60.3	2.8	–1.6	152.1	3.7
LX1064			10	~350	35.872	118.120	7/15	101.9	69.3	1.9	21.5	157.5	3.0
LX1066			~20	~352	35.350	118.193	10/11	124.8	54.4	3.4	–2.9	160.6	3.9
LX1068			~15	~352	35.341	118.181	11/11	123.7	71.8	3.7	13.6	146.2	6.1
									9 条岩墙采点平均		**2.6**	**165.1**	**10.8**
									除 LX1064，8 条平均		**0.2**	**166.1**	**11.0**
~1.24 Ga 围岩高温分量 – 烘烤检验													
JD1027					烘烤的岩石~3 m		8/8	127.3	27.7	7.6			
					未烘烤的岩石>100 m		5/8	215.5	–54.1	10.8			
JD687					烘烤的岩石~0.35 m		5/6	118.7	52.6	15.0			
~1.21 Ga 岩墙高温分量													
MY1033	1206.7 ± 1.7	本研究	~80	~35	40.617	117.083	13/13	204.5	39.5	6.5	–23.0	92.5	6.1

n/N = 计算的样品/测量的样品；α_{95} = 采点平均方向的 95%置信椭圆；A_{95} = 极的 95% 置信椭圆

表 7.2 岩墙退磁低温组分

Table 7.2 Paleomagnetic low temperature components of the dykes

岩墙编号	年龄 (Ma)	年龄参考文献	宽度 (m)	走向 (°)	纬度 (°N)	经度 (°E)	n/N	磁偏角 (°)	磁倾角 (°)	α_{95} (°)
~1.68 Ga 岩墙低温分量										
LX307	1680 ± 4	Li et al., 2015	~35	~340	36.278	117.890	6/9	13.3	54.8	11.5
JD690			~1.5	~30	40.250	118.533	4/12	0.3	45.1	12.9
~1.24 Ga 岩墙低温分量										
JD517	1236 ± 7	Wang et al., 2016b	>15	~34	39.857	118.920	8/13	329.2	41.5	13.2
JD687			~25	~4	40.261	118.482	11/12	344.7	52.3	7.1
JD1027	1233 ± 27	本研究	30–40	~24	40.245	118.486	8/12	316.6	51.4	17.6
C716			>15	~310	37.574	114.304	15/15	342.2	34.9	8.7
LX1064			10	~350	35.872	118.120	8/15	20.9	48.4	8.7
LX1066			~20	~352	35.350	118.193	8/11	352.5	35.2	15.3
LX1068			~15	~352	35.341	118.181	6/11	350.4	74.4	11.9
~1.21 Ga 岩墙低温分量										
MY1033	1206.7 ± 1.7	本研究	~80	~35	40.617	117.083	11/13	1.3	73.3	8.9

n/N = 计算的样品/测量的样品；

α_{95} = 采点平均方向的 95%置信椭圆；

表 7.3 岩墙 JD689 和 JD690 部分样品的 Qn 指数

Table 7.3 Part paleomagnetic Qn ratios of the dykes JD689 and JD690

样品	Km (SI)	M_{NRM} (A/m)	Qn	样品	Km (SI)	M_{NRM} (A/m)	Qn
岩墙 JD689				岩墙 JD690			
689-1-4	0.075	200	50	690-1	0.087	69	15
689-1-6		2.7		690-2	0.043	~0.4	~0.2
689-1-8	0.167	215	24	690-3A	0.082	77	17
689-1-13A	0.148	108	13	690-4L		~2.4	
689-1-14		600		690-5	0.098	1.5	0.3
689-1-15	0.120	8.4	1.3	690-6	0.077	51	12
689-1-17	0.099	605	113	690-7A	0.063	54	16
689-1-19	0.111	1080	181	690-8A	0.077	56	14
689-3-1	0.070	667	177	690-9L		~0.2	
689-3-2		213		690-10	0.076	~6.3	~1.5
689-3-5A	0.096	~52	10	690-11A	0.075	6.7	1.6
689-3-7		82		690-12A	0.051	0.3	0.1
689-3-9	0.061	1.9	0.6				

$Qn = M_{NRM}/(Km \times H)$；$M_{NRM}$ = 天然剩磁强度；Km = 初始磁化率；H = 周围的磁场强度，以当前该位置地球磁场强度 54 μT 代替（来自国际地磁参考场 IGRF 模型）

7.2.2 ~1.24 Ga 和 1.21 Ga 岩墙

来自 JD517、JD1027 以及 MP1050 岩墙的定年结果显示它们侵位于~1235 Ma（图 3.8）。岩墙 JD687 与定年岩墙 JD517 具有相似的地球化学特征，因此被认为是同期岩墙 (Wang et al., 2016b)，相似的磁化方向也支持此结论。同样，相似的磁化方向也出现在岩墙 C711、C716、LX323、LX1064、LX1066 及 LX1068（图 7.3、图 7.4 和表 7.1）。从热退及交变退磁中均获得了东–南东向，中到低倾角向下的稳定特征剩磁。其解阻温度接近~580°C，表明主要载磁矿物为磁铁矿（图 7.3a–f）。此外，样品中并没有出现对蹠的极（图 7.3 和图 7.4）。虽然锆石定年结果显示 LX1064 结晶于~1.84 Ga (Wang et al., 2007)，但该期年龄并未得到有效证实 (Peng, 2015b)。基于相近的磁化方向（图 7.3、图 7.4 和表 7.1），以及可比较的地球化学特征（图 6.1、图 6.2 及 9.1 部分），本研究认为这些岩墙均属于~1.24 Ga。华北中部的 C711 和 C716 两条岩墙位置接近，产状接近，并有相似的矿物学特征（图 3.8d 和图 4.1j，k），这也支持这些岩墙同期的推断。岩墙 JD1009 呈较大范围的天然剩磁（4–61 A/m），并有散乱的特征剩磁方向；考虑到该采点位于山丘之上，本研究怀疑其可能遭受了雷击，在后面的讨论中将其排除在外。

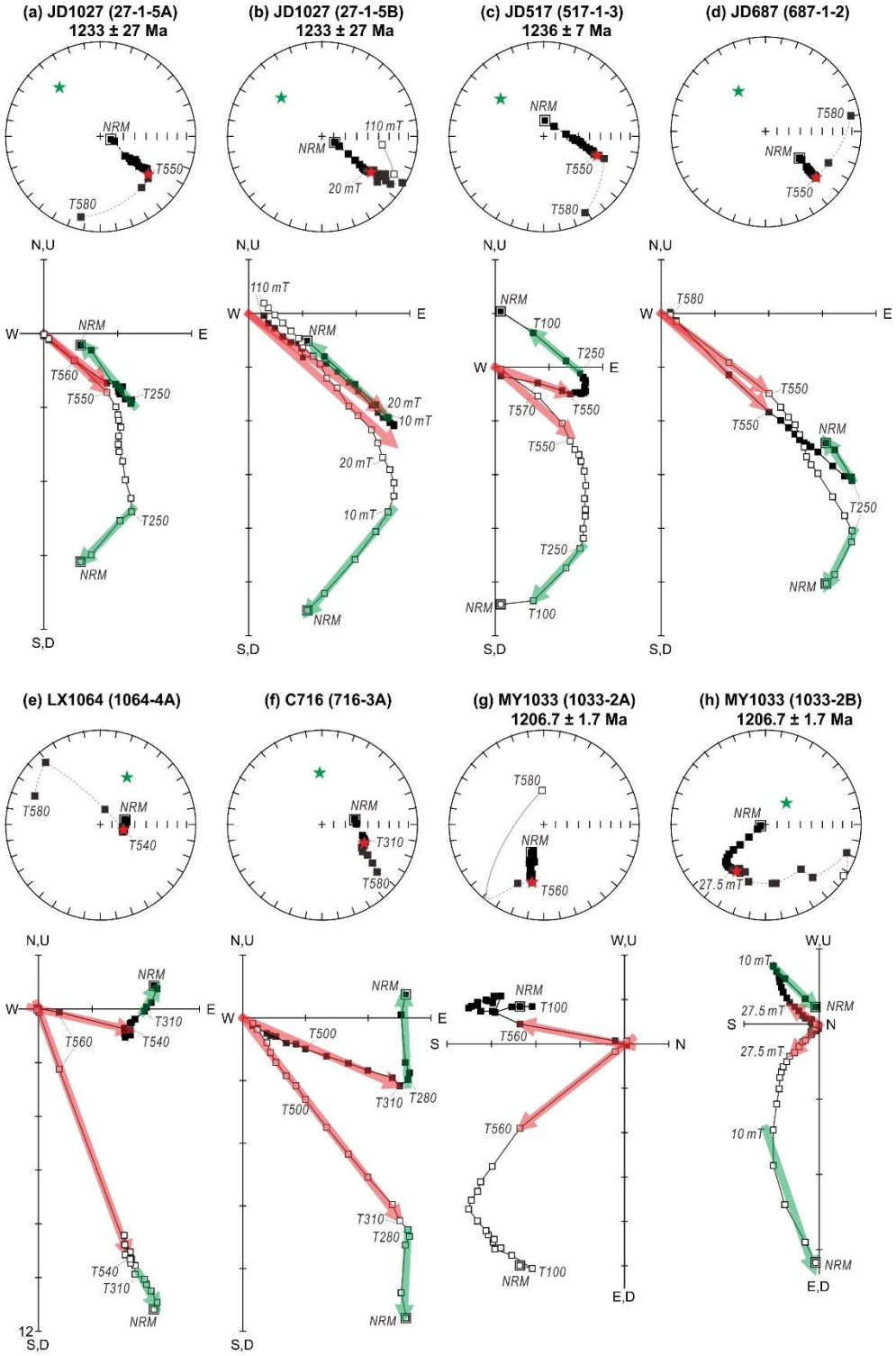

图 7.3 1.24 Ga 岩墙（a–f）及 1.21 Ga 岩墙（g–h）代表性样品的的热退磁及交变退磁结果：等面积投影（实心及空心点分别对应于下半球及上半球投影；红色及绿色箭头分别对应于高温及低温组分）及正交平面投影（实心及空心点分别代表在水平面及垂直面的投影；红色及绿色星形分别代表高温及低温平均方向）

Fig. 7.3 Representative thermal and AF demagnetizations of the 1.24 Ga (a–f) and the 1.21 Ga (g–h) dykes: equal area stereoplots (solid/open square points correspond for downward/ upward-pointing magne-tizations; Red and green stars are mean directions of the HTC and LTC, respectively), and orthogonal projection diagrams (solid/open square points show vector end points projections onto the horizontal/vertical plane; Red and green arrows are HTC and LTC, respectively).

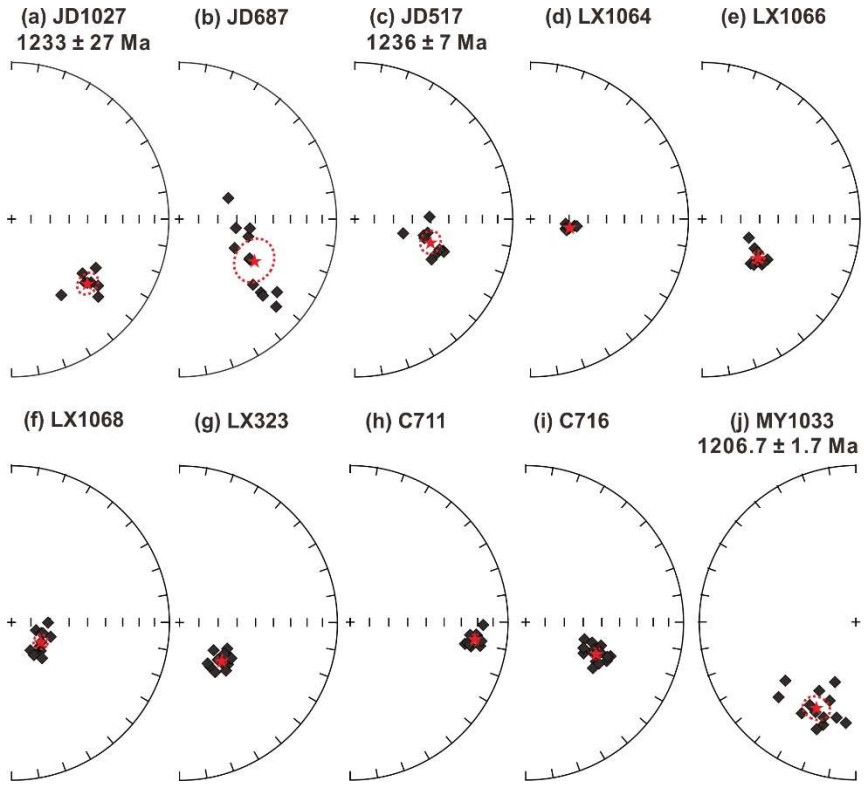

图 7.4 1.24–1.21 Ga 岩墙高温分量等面积投影。每个菱形代表一个样品；红色星形及虚线代表采点平均方向及 95%置信误差。实心菱形代表下半球的矢量。

Fig. 7.4 Equal-area projections showing the HTCs of the 1.24–1.21 Ga dyke. Each diamond represents one sample. Red stars and surround dashed line represent the site-mean directions and α_{95} ovals. Solid symbols represent lower hemisphere vectors.

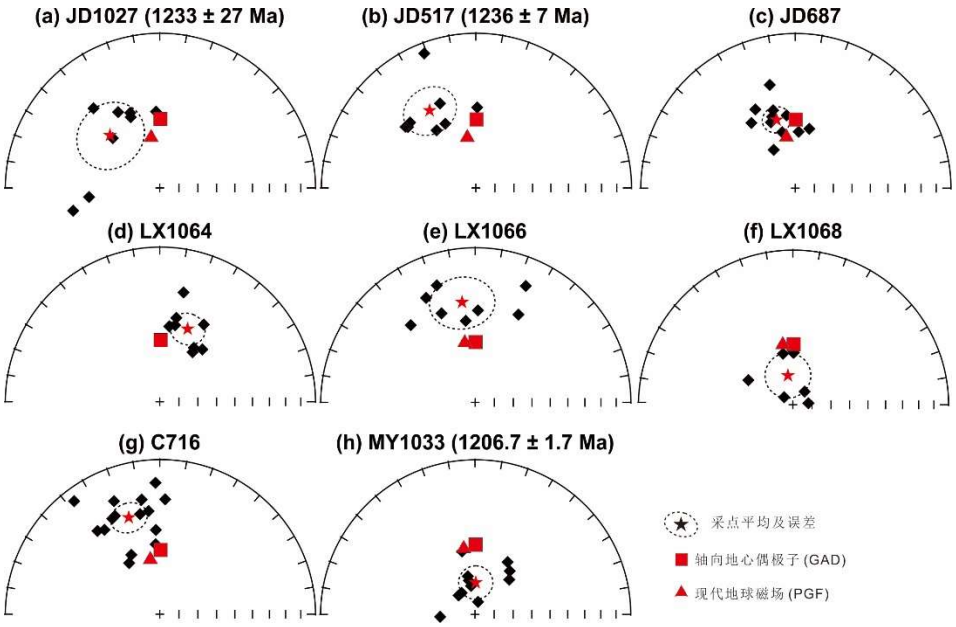

图 7.5 1.24–1.21 Ga 岩墙低温分量等面积投影图。每个菱形代表一个样品，红色星形及虚线代表采点平均方向及 95%置信误差。实心菱形代表下半球的矢量。

Fig. 7.5 Equal-area projections showing the LTCs of the 1.24–1.21 Ga dyke. Each diamond represents one sample. Red stars and surround dashed line represent the site-mean directions and α_{95} ovals. Solid symbols represent lower hemisphere vectors.

九条岩墙的平均古地磁极为 2.6°N，165.1°E，A_{95} = 10.8°（表 7.1）。其中七条岩墙（除了 LX323 和 C716）分离出了低温组分，绝大多数低温组分和现代地球磁场及轴向地心偶极子场接近（图 7.5 和表 7.2）。

岩墙 MY1033（1206.7 ± 1.7 Ma）位于密云县（图 3.8c）。该岩墙比其他岩墙年轻~30 Ma，且有不同的剩磁方向，即西南向向下（图 7.4j）。热退磁在 540–580°C 分离出了特征剩磁；交变退磁在> 40 mT 时解阻（图 7.3g–h）。平均磁化方向为 D = 204.5°，I = 39.5°，α_{95} = 6.5°；对应的极为-23.0°N，92.5°E，A_{95} = 6.1°（表 7.1）。仅有的一条岩墙磁化方向不能平均地球磁场的长期变化，故该结果应该被视为虚地磁极。低温组分的方向为 D = 1.3°，I = 73.3°，α_{95} = 8.9°，与现代地球磁场及偶极子场的方向接近（图 7.5h 和表 7.2）。

第8章 岩石磁学和磁组构

对样品中载磁矿物种类及特征的识别，有助于判断岩石剩磁的类型，辅助分析特征剩磁是否为原生剩磁。本研究通过测量磁化率随温度变化曲线、三轴等温剩磁热退磁和磁滞回线分析载磁矿物的性质。实验完成于澳大利亚科廷大学古地磁实验室。

8.1 磁化率随温度变化曲线

将物质放在磁场（magnetic field），会诱发磁化（induced magnetization），其被磁化的能力即为磁化率（magnetic susceptibility）。通常，顺磁性物质（paramagnetic material）如黑云母、黏土矿物的磁化率为正，反磁性物质（diamagnetic material）如碳酸盐岩、石英的磁化率为负，铁磁性物质的磁化率不是简单的常量。一些物质具有磁化率各向异性，即沿不同的方向磁化的能力不同。对于铁磁性材料，其在一定温度下的最大磁化称为饱和磁化（saturation magnetization，Js），随着温度的升高，饱和磁化会在居里点时降至零。另外，研究发现温度升高到居里点之前，单畴载磁矿物的磁化率或者短期的诱发磁化会加强，呈现一个峰值，称为 Hopkinson 效应（或 Hopkinson 峰值）；但多畴颗粒峰值不明显 (Dunlop and Özdemir, 1997)。而不同的的载磁矿物因有不同的解阻温度，这一信息会反映在磁化率的变化上，因此，磁化率随温度变化曲线（κ–T，又称热磁曲线 thermal-magnetic curve）可以反映载磁矿物类型和磁畴信息。磁化率随温度的变化曲线也可以显示加热中是否有矿物相的变化，无矿物相变化的样品则显示可逆的曲线特征。

本研究使用多功能卡帕桥磁化率仪 MFK-1FA 连接 CS4 温度装置测量磁化率。将粉末状样品置于空气中，从室温以 14°C 每分钟的速度加热到 700°C，然后以相同的速度冷却到室温。最终的数据扣除实验装置本底值，结果如图 8.1 所示。

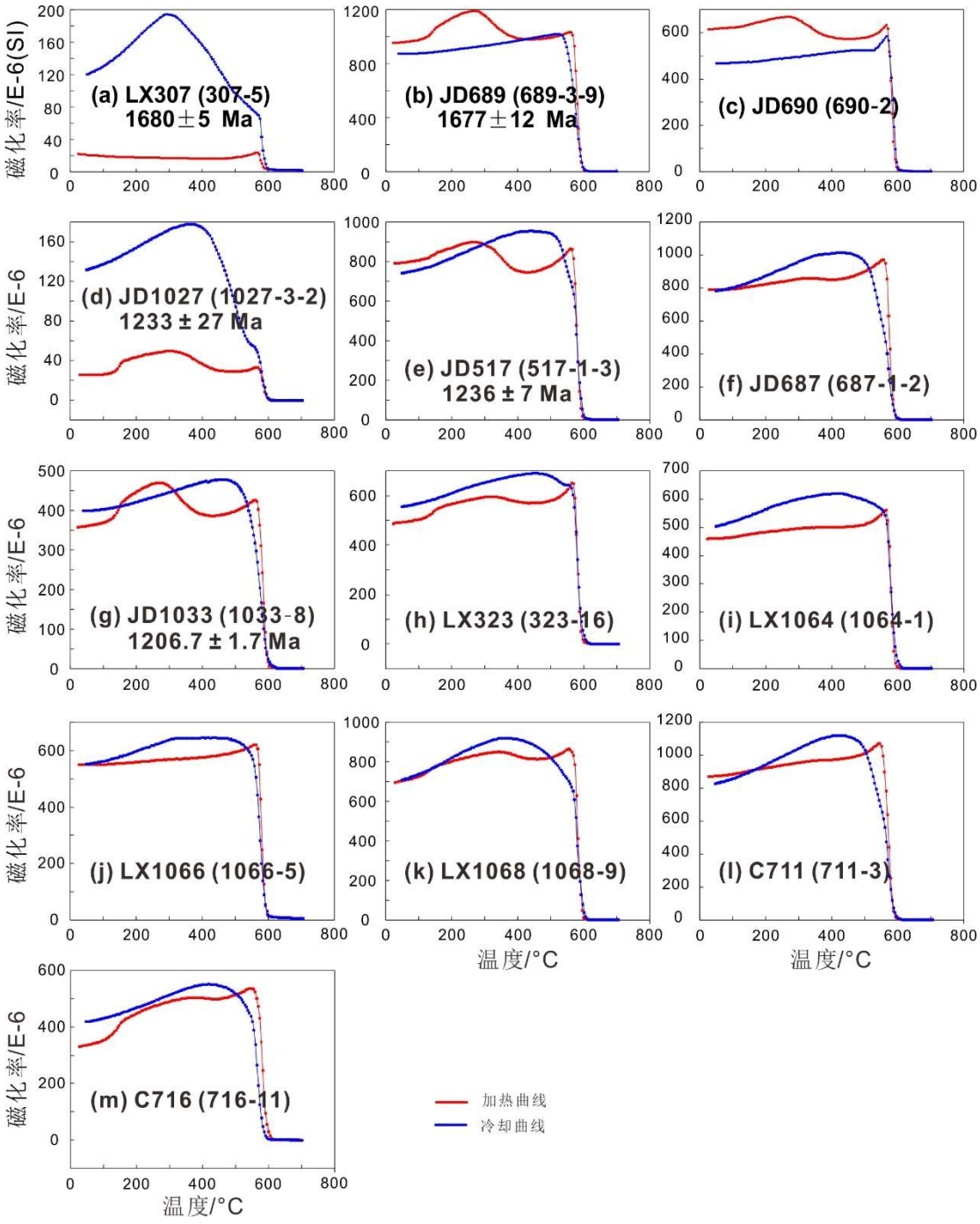

图 8.1 代表性样品热磁曲线图。（a–c）为~1.68 Ga 岩墙；（d–m）为~1.24–1.21 Ga 岩墙

Fig. 8.1 Representative samples of thermomagnetic curves. (a–c) of the ~1.68 Ga dykes; (d–m) of the ~1.24–1.21 Ga dykes

所有的样品均在~580°C 时解阻（图 8.1），表明主要的载磁矿物为磁铁矿。多数样品的热磁曲线显示有 Hopkinson 峰 (Dunlop and Özdemir, 1997)（图 8.1），表明出现载磁稳定的单畴或假单畴低钛钛磁铁矿。一些样品有近乎可逆的加热与冷却热磁曲线，且曲线起伏变化平缓，比如样品 JD687、LX1064、LX1066 和 C711（图 8.1f，i，j 和 l），说明即使在高温时，也很少有矿物发生转变。但是，

也有一些样品的热磁曲线在 200–300°C 区间升高（图 8.1b–e，g，h 和 m），是因为弱磁性矿物在加热过程转化成磁化率较高的成分（如铁的氢氧化物转换成磁赤铁矿），或在特定粒径下亚铁磁性矿物在加热过程中解阻；加热曲线在 300–400°C 区间降低（如图 8.1b–e 和 g），可能因为亚稳定状态下磁赤铁矿或者铁硫化物的分解。图 8.1a 和 d 的冷却曲线磁化率明显高于加热曲线的磁化率，可能是在加热过程中新生成了亚铁磁性矿物。

8.2 三轴等温剩磁热退磁实验

通常，铁磁性矿物有不同的矫顽力和热磁特征，比如磁铁矿和磁赤铁矿有相似的最大矫顽力，但有不同的解阻温度；磁赤铁矿、钛磁铁矿和磁黄铁矿虽然有相近的解阻温度，但存在不同的矫顽力（表 8.1）。据此，可以通过等温热退磁分析判断载磁矿物的种类和特征。改进之后的实验流程为：在样品的三个垂直的轴上使用脉冲磁化仪分别加载不同强度的磁化，比如加载 5 T（或 4 T、3 T）、0.4 T（或 0.35 T）和 0.12 T；之后对样品进行逐步热退磁，分析不同轴上的剩磁变化及解阻情况 (Lowrie, 1990)。本研究使用 Magnetic Measurements MMPM5 型脉冲磁化仪（pulse magnetiser），分别对样品的 z、x 和 y 轴加载 3 T、0.4 T 和 0.12 T 的磁场。热退磁之后的分析结果如图 8.2 所示。

表 8.1 常见铁磁性矿物的最大剩磁矫顽力和解阻温度 (Lowrie, 1990)
Table 8.1 Maximum remanent coercivities and unblocking temperatures of some ferromagnetic material (Lowrie, 1990).

铁磁性矿物	磁铁矿 Magnetite	磁赤铁矿 maghemite	钛磁铁矿 titanomagnetite		磁黄铁矿 pyrrhotite	赤铁矿 hematite	针铁矿 goethite
			x = 0.3	x = 0.6			
最大矫顽力（T）	0.3	0.3	0.2	0.1	0.5–1	1.5–5	＞5
最大解阻温度（℃）	575	~350	350	150	325	675	80–120

结果显示，所有样品含有较高的软磁组分（soft component，＜0.12 T），且在 520–600°C 解阻（图 8.2），说明样品中含有较多的低钛钛磁铁矿。此外，多数分析的样品显著含有不同比例的中间组分（medium component，0.12–0.4 T）且在 520–600°C 解阻（如图 8.2a–h），说明出现稳定的单畴或假单畴磁铁矿颗粒。样品中或含有极低的硬磁组分（hard component，0.4–3 T），可能与极低量的赤铁矿有关。该实验说明样品的磁颗粒以低矫顽力磁铁矿为主，可能为单畴或假

单畴。

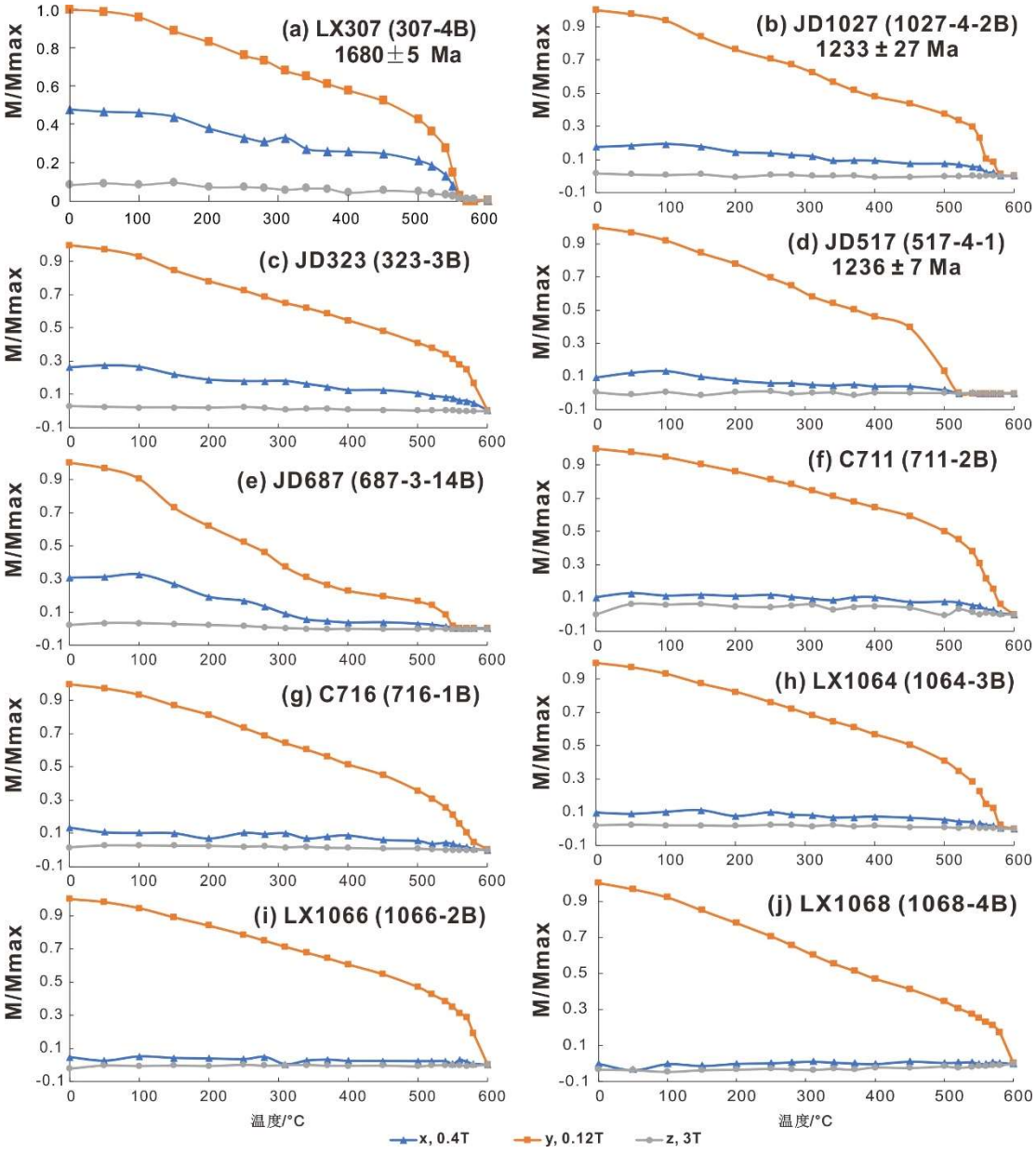

图 8.2 代表性样品三轴等温热退磁图。（a）为~1.68 Ga 岩墙，（b–j）为~1.24 Ga 岩墙

Fig. 8.2 Representative samples of thermal demagnetization of triaxially IRM. (a) of the ~1.68 Ga dyke; (b–j) of the ~1.24 Ga dykes

8.3 磁滞回线分析

暴露在外界磁场中的铁磁性矿物，在外界场移除后磁化信息并不会直接降为零，而是能够保持记录外界场的方向信息，这种现象称为磁滞（hysteresis）；而磁化的路径相对于外界场的曲线被称为磁滞回线（hysteresis loop）。磁滞回线定量显示饱和磁化强度（Js 或 Ms）、剩余磁化强度（Jr 或 Mr）、矫顽力（Hc 或 Bc）、剩磁矫顽力（Hr 或 Br）等参数。研究发现不同相的磁性矿物及不同状态

的磁畴具有不同形态的磁滞回线 (Tauxe, 2010)，单畴磁铁矿、赤铁矿及假单畴的剩余强度与饱和强度之比（Mr/Ms）分别为 0.5、~1.0、＜0.5（图 8.3d–f）；而赤铁矿和单畴磁铁矿的混合呈鹅颈形（goose-necked）（图 8.3g），单畴磁铁矿和超顺磁的混合呈蜂腰形（wasp-waisted）或大肚形（pot-bellied）（图 8.3h–i）。

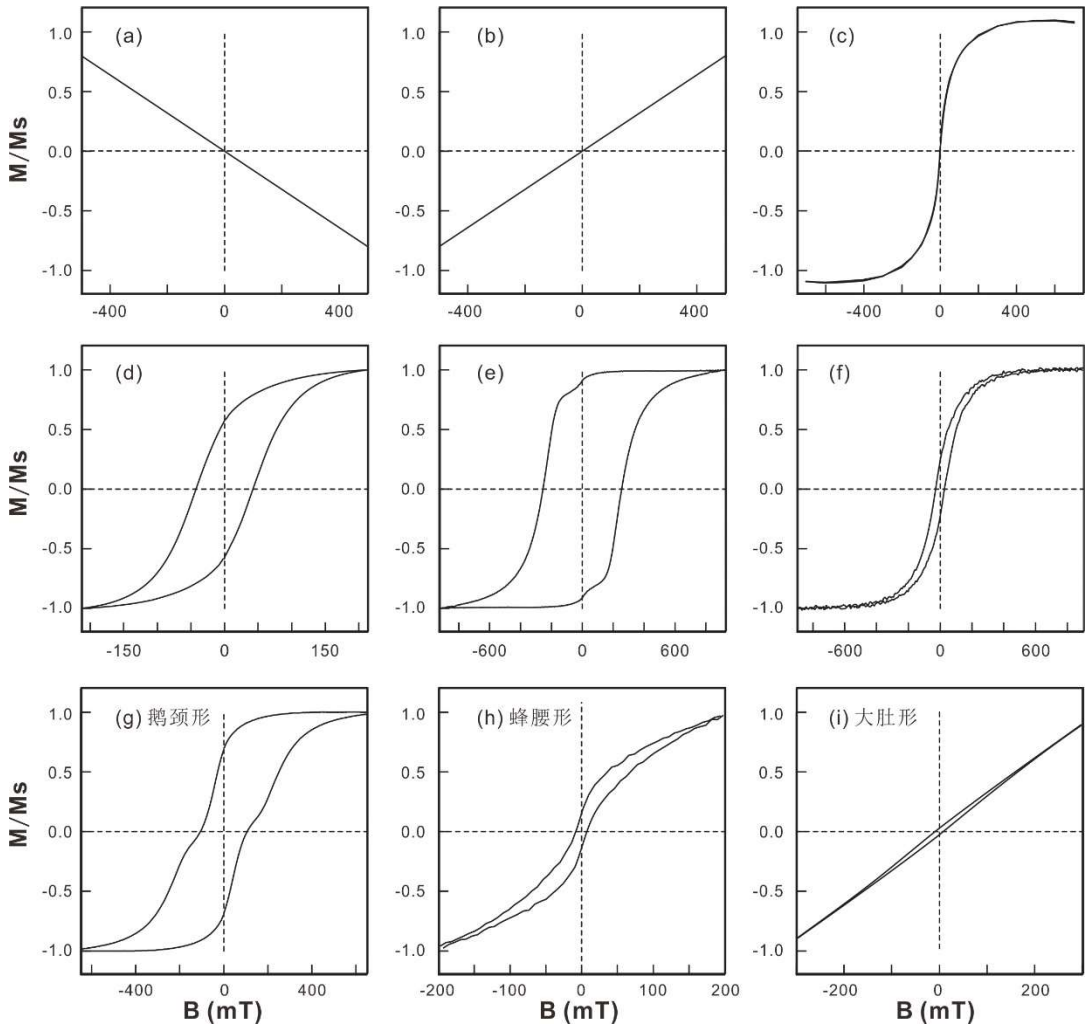

图 8.3 单一端元（a–f）及多端元混合（d-i）的磁滞回线 (Tauxe, 2010)。（a）反磁性；（b）顺磁性；（c）超顺磁单轴；（d）单轴各向异性的单畴磁铁矿；（e）起源于磁晶各向异性的单畴镜面磁铁矿；（f）假单畴；（g）赤铁矿和单畴磁铁矿（鹅颈形）；（h）单畴和超顺磁磁铁矿（蜂腰形）；（i）单畴和细粒超顺磁磁铁矿（大肚形）。

Fig. 8.3 Hysteresis of end-member (a–f) and mixture (g–i) (Tauxe, 2010). (a) diamagnetic, (b) paramagnetic, (c) superparamagnetic, (d) single domain magnetite with uniaxial anisotropy, (e) single domain specular hematite with magnetocrystal anisotropy, (f) pseudo-single domain, (g) hematite and single domain magnetite (goose-necked), (h) single domain and superparamagnetic domain magnetite (wasp-waisted), (i) single domain and fine-grained superparamagnetic magnetite (pot-bellied).

本研究使用可变场居里磁秤（Petersen Instruments Variable Field Translation Balance，VFTB）测量磁滞回线，获得的数据使用 Hysteresis Loop analysis box（HystLab）自动处理并成图 (Paterson et al., 2018)。

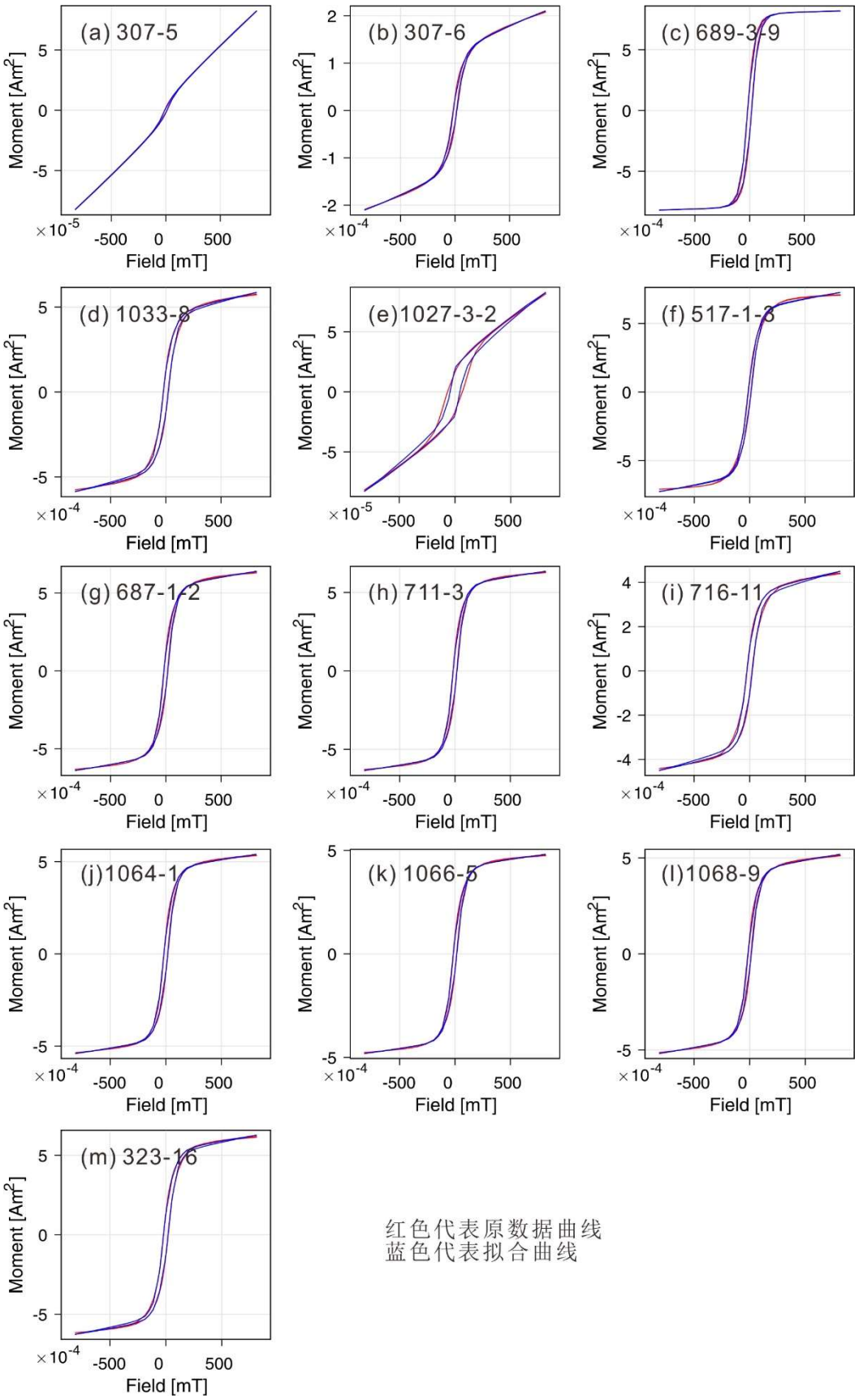

图 8.4 代表性样品的磁滞回线。（a–c）为~1.68 Ga 岩墙，（d–m）为~1.24–1.21 Ga 岩墙

Fig. 8.4 Representative samples of hysteresis loops. (a–c) of the ~1.68 Ga dyke; (d–m) of the ~1.24–1.21 Ga dykes

分析结果显示，多数样品的磁滞回线呈假单畴状形态（图 8.3f 和图 8.4）；但样品 307-5、307-6 和 1027-3-2 呈类似于蜂腰形形态（图 8.4a–b，e），可能为单畴和超顺磁的混合组分。多数样品的磁滞回线在 500 mT 之前均已闭合，但样品 307-5、307-6 和 1027-3-2 仍未饱和，可能含有高矫顽力矿物。除了 1027-3-2 外，其余样品的矫顽力一般低于 25 mT，剩磁矫顽力通常低于 60 mT（表 8.2）。其剩余磁化强度与饱和磁化强度之比（Mr/Ms）均低于 0.3（表 8.2），暗示绝大多数样品含假单畴磁铁矿。来自老王家岩墙的 1027-3-2 样品，加热过程中可能有强磁性矿物生成，故而难以饱和（图 8.4e）；热磁冷却曲线明显高于加热曲线（图 8.1d）也反映此信息。

Day 投图中，代表性的样品落入假单畴区域（图 8.5），这也与磁滞回线的形态信息吻合（图 8.4）。理论实验认为，假单畴可能来自单畴和多畴颗粒的混合 (Dunlop, 2002)。如果情况如此，绝大多数样品可能包含了 20–50% 的单畴颗粒，但个别样品单畴组分稍低，如样品 307-5（图 8.5）。

表 8.2 代表性样品的磁滞回线参数

Table 8.2 Representative samples of hysteresis loop parameters

样品	Ms/ Am^2 /E–04	Bc/ mT	Br/ mT	Mr/Ms	Br/Bc	Ms/ Am^2 /E–04	Bc/ mT	Br/ mT	Mr/Ms	Br/Bc
	原数据					拟合数据				
307-5	0.83	10.1	46.1	0.02	4.6	0.83	10.3	58.9	0.02	5.7
307-6	2.09	14.5	47.7	0.13	3.3	2.10	17	53.3	0.12	3.1
689-3-9	8.18	17.4	54	0.24	3.1	8.20	18.7	53	0.23	2.8
1027-3-2	0.82	66.4	121.9	0.20	1.8	0.83	44.1	65.1	0.23	1.5
517-1-3	7.08	11.9	55.2	0.13	4.6	7.26	13.4	54.3	0.12	4.1
687-1-2	6.32	16.5	44	0.19	2.7	6.40	17.6	48	0.17	2.7
711-3	6.29	16.6	43.7	0.21	2.6	6.35	17.9	47.8	0.18	2.7
716-11	4.41	22.7	73.7	0.22	3.2	4.50	24.5	57.1	0.23	2.3
1064-1	5.35	16.5	49.5	0.19	3.0	5.40	17.7	52.6	0.18	3.0
1066-5	4.76	15.1	46.1	0.18	3.1	4.81	16.3	48.3	0.16	3.0
1068-9	5.13	13.1	48.6	0.16	3.7	5.19	15.3	52.1	0.15	3.4
323-16	6.17	19.9	59.4	0.21	3.0	6.27	21	55	0.20	2.6
1033-8	5.75	20.9	63.4	0.21	3.0	5.86	22.6	55.5	0.21	2.5

总之，通过热磁曲线、磁滞回线及三轴等温剩磁热退磁实验分析可以得出，虽然样品中含有一些载磁不稳定的多畴颗粒，和/或超顺磁颗粒，但岩墙中均含有一些稳定的单畴或假单畴磁铁矿，这些是高温组分的主要磁载体。

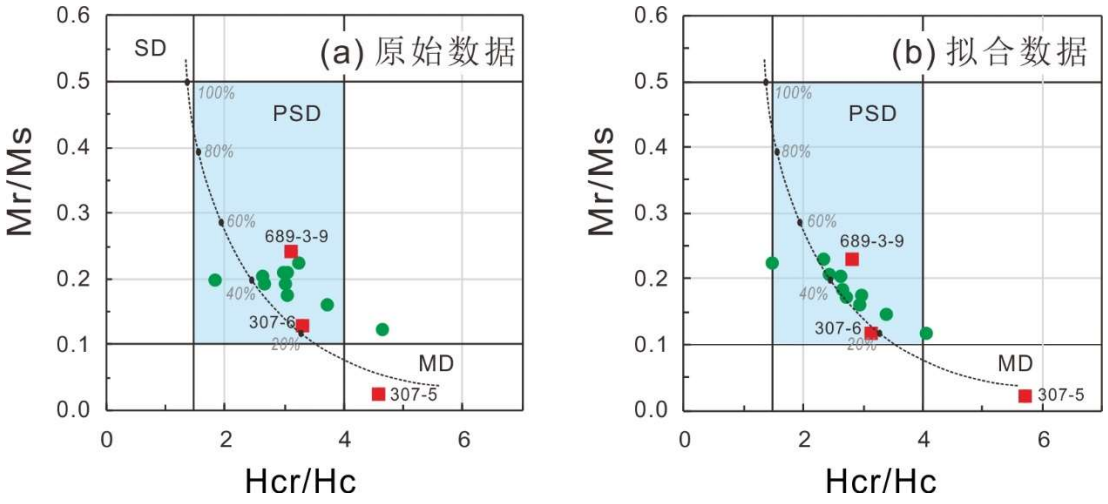

图 8.5 代表性样品的 Day 投图 (Day et al., 1977)。虚线代表单畴与多畴以不同比例混合的理论曲线 (Dunlop, 2002)。方形和圆形分别代表~1.68 Ga、~1.24–1.21 Ga 岩墙样品

Fig. 8.5 Representative samples of Day plot (Day et al., 1977). Dashed line represents the theoretical mixing curve between MD and SD magnetite grains at different percentages (Dunlop, 2002). Square and dots represent samples from ~1.68 Ga and ~1.24–1.21 Ga dykes, respectively.

8.4 磁组构

磁组构是指通过磁各向异性研究岩石组构，主要包括磁化率各向异性（anisotropy of magnetic susceptibility，AMS）、非磁滞剩磁各向异性（anisotropy of anhysteretic remanent magnetization，AARM）和等温剩磁各向异性（anisotropy of isothermal remanent magnetization，AIRM）等。本研究在退磁之前使用卡帕桥 MFK1–FA 测量磁化率各向异性，数据则使用 Anisoft5 软件呈现。平均磁化率是指三个磁化率轴（$K_1 \geq K_2 \geq K_3$）的平均。各向异性度 $P = K_1/K_3$，或 $Pj = \exp(2((\eta_1 - \eta_m)^2 + (\eta_2 - \eta_m)^2 + (\eta_3 - \eta_m)^2))^{1/2}$，$\eta_i = \ln K_i$；$\eta_m = (\eta_1 \times \eta_2 \times \eta_3)^{-3}$，代表岩石中磁性矿物优先方向的强度。磁组构的形状（AMS 椭球体）通过参数 T 定义，$T = 2 \times \ln(K_1/K_2) / \ln(K_2/K_3) - 1$，其值 0~1 和 -1~0 分别代表扁圆（平面组构）和扁长形状（线性组构）(Tarling and Hrouda, 1993)。

本文展示了两条具有正常磁组构岩墙的结果（图 8.6）。正常磁组构是指 K_1 和 K_2 轴的平面平行于岩墙的走向，K_3 轴垂直于岩墙走向。这两条岩墙的磁各向异性参数 P 和 Pj 都＜1.10。岩墙 C711 有过半的正 T 值（T 值为 AMS 椭球参数），暗示以扁圆组构（oblate fabric）为主；而岩墙 JD1027 有过半的负 T 值，说明以扁长组构（prolate fabric）为主。

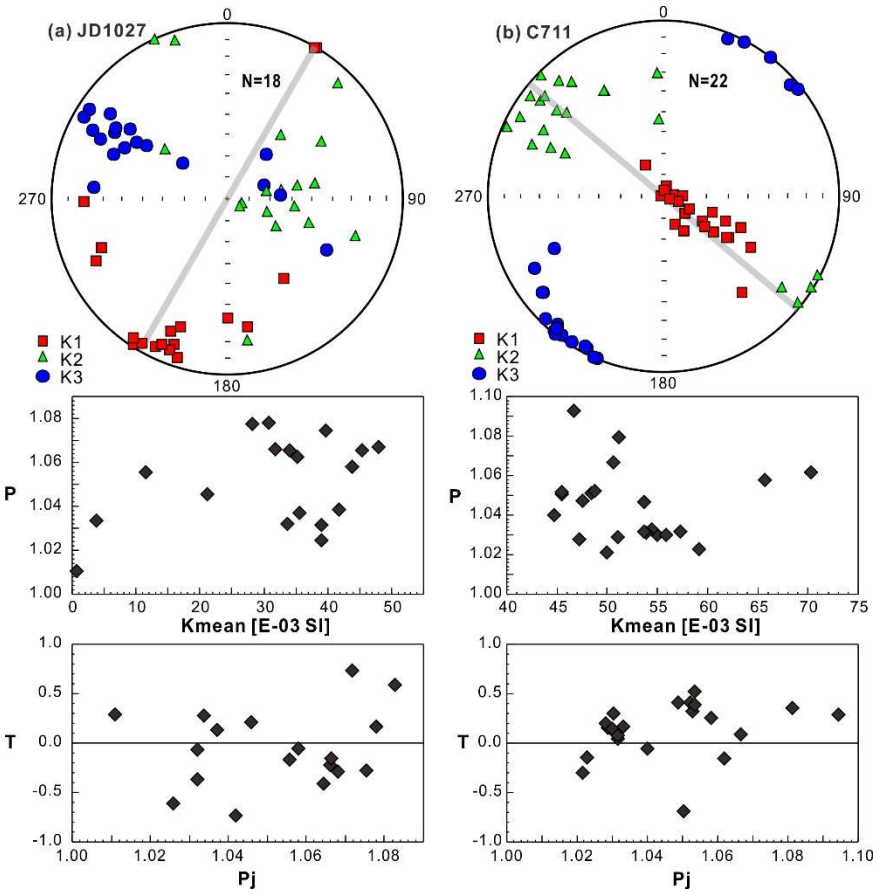

图 8.6 岩墙的地理坐标系下等面积投影磁化率各向异性图。灰线为岩墙的走向

Fig. 8.6 Equal-area projections of anisotropy of magnetic susceptibility (AMS) of the dykes in geographic coordinates. Grey line marks trend of dyke

第9章 讨论

9.1 华北~1.24–1.21 Ga 岩墙群的岩石成因

研究者之前报道了华北不同地区的~1.23 Ga 基性岩浆作用（表 9.1）。本研究通过定年结果、地球化学特征及磁化方向识别出更多的~1.24–1.21 Ga 岩浆作用，结合新的地球化学数据及已报道的数据（表 6.1 和附录），对该期事件的岩石成因进行分析。

为估计蚀变对全岩元素的影响，本文分别以烧失量（LOI）及 Zr 元素对其他主量及微量元素作协变图解（图 9.1 和图 9.2），发现：① 包括全碱，绝大多数元素与烧失量的相关性不明显，但一些元素如 Al、Ca 和 Rb 似乎与烧失量存在相关性，可能跟斜长石的蚀变有关，与镜下观察对应（图 4.1g–l）；② 不活动元素 Zr 与高场强元素 Nb、Ta、Hf 及 Th、REE（La 和 Sm）以及 U 或存在强的正相关关系（相关系数 R^2＞0.3），但与大离子亲石元素 Rb、Sr 和 Ba 的相关性较弱。综上表明，蚀变对高场强元素的影响较小，可能对大离子亲石元素有一定的影响。

鉴于上述情况，本文使用微量元素及硅碱图对岩石进行化学分类。Zr/TiO_2 对 Nb/Y 分类图显示样品较为集中，多数呈碱性玄武岩系列特点，少部分样品投在碱性与亚碱性系列的边界或亚碱性系列区域；硅碱图中也得到了相似的结果（图 9.3）。值得注意的是，Zr/TiO_2 对 Nb/Y 的分类图解来自数据统计 (Pearce and Cann, 1973)，虽然碱性和亚碱性玄武岩的判别界线在 Nb/Y = 0.65 附近，但根据数据统计，Nb/Y = 0.47–1.3 既包含亚碱性岩石，又包含碱性岩石 (Floyd and Winchester, 1975)，且 Nb/Y 与碱性之间也没有必然相关性 (Pearce and Cann, 1971, 1973; Floyd and Winchester, 1975)。总之，本期岩墙中，这种连续变化的亚碱性到碱性特征可能反映了岩浆房的演化过程，或受结晶分异过程影响。

观察数据发现，该期岩墙的高 Nb/Y 主要来自样品中高的 Nb 含量（≥11.7 ppm）（图 6.1k），黎城岩墙 Nb 甚至高达 33.5 ppm（附表），属于富 Nb 至高 Nb 玄武质岩石（Hastie et al., 2011）。而且，本期岩墙普遍含有较高的 TiO_2 含量（多数＞1.5 wt.%），同为高 Ti 玄武质岩石。

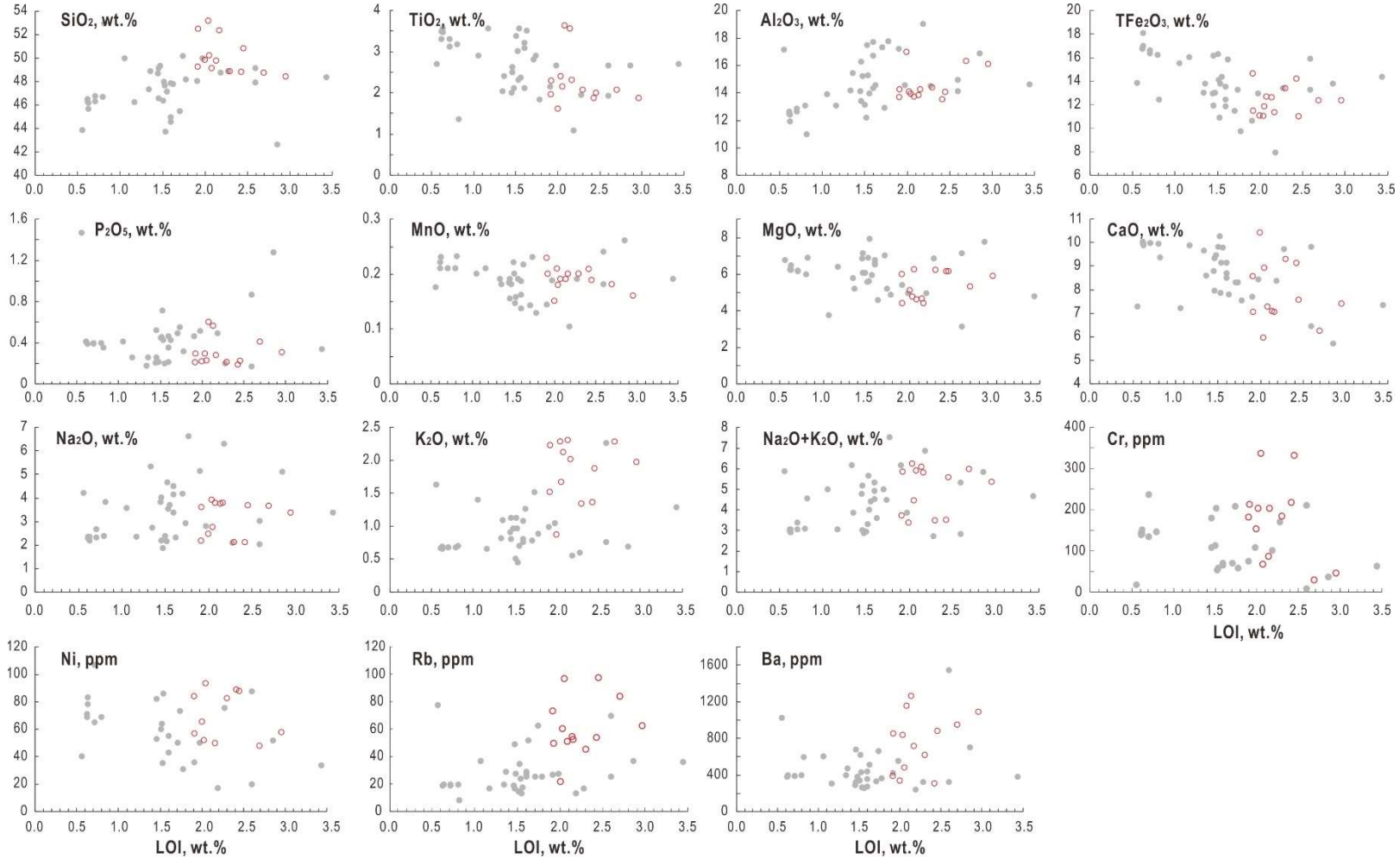

图 9.1 1.24–1.21 Ga 岩墙元素对烧失量（LOI）图解。红色圆圈为本文样品，灰色圆圈为编录的样品（附件）。

Fig. 9.1 Loss on ignition (LOI) vs. whole-rock elements of the 1.24–1.21 Ga dykes. Red dots are new data in this study; grey dots are compiled data (supplementary file).

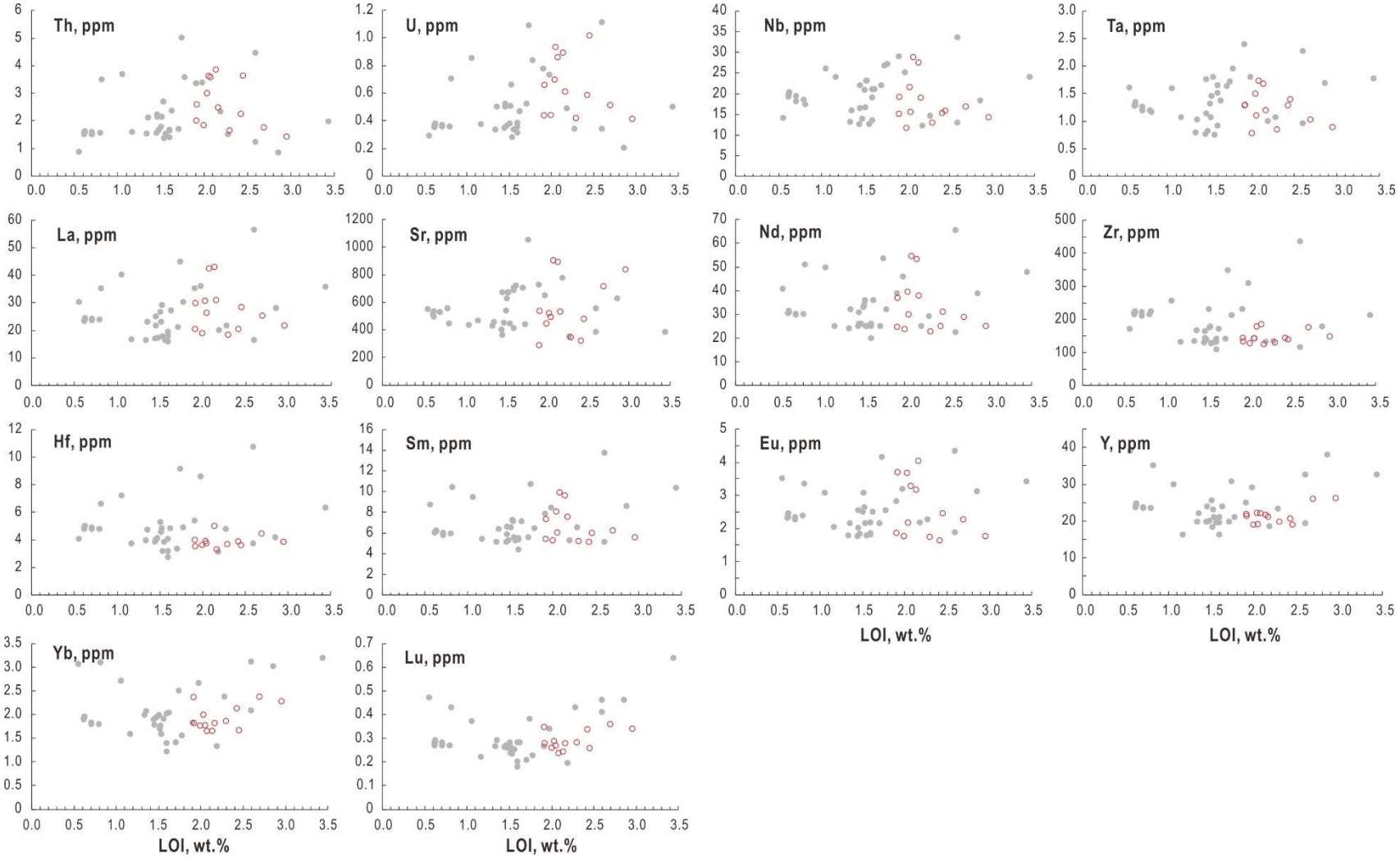

图 9.1 续

Fig. 9.1 continued

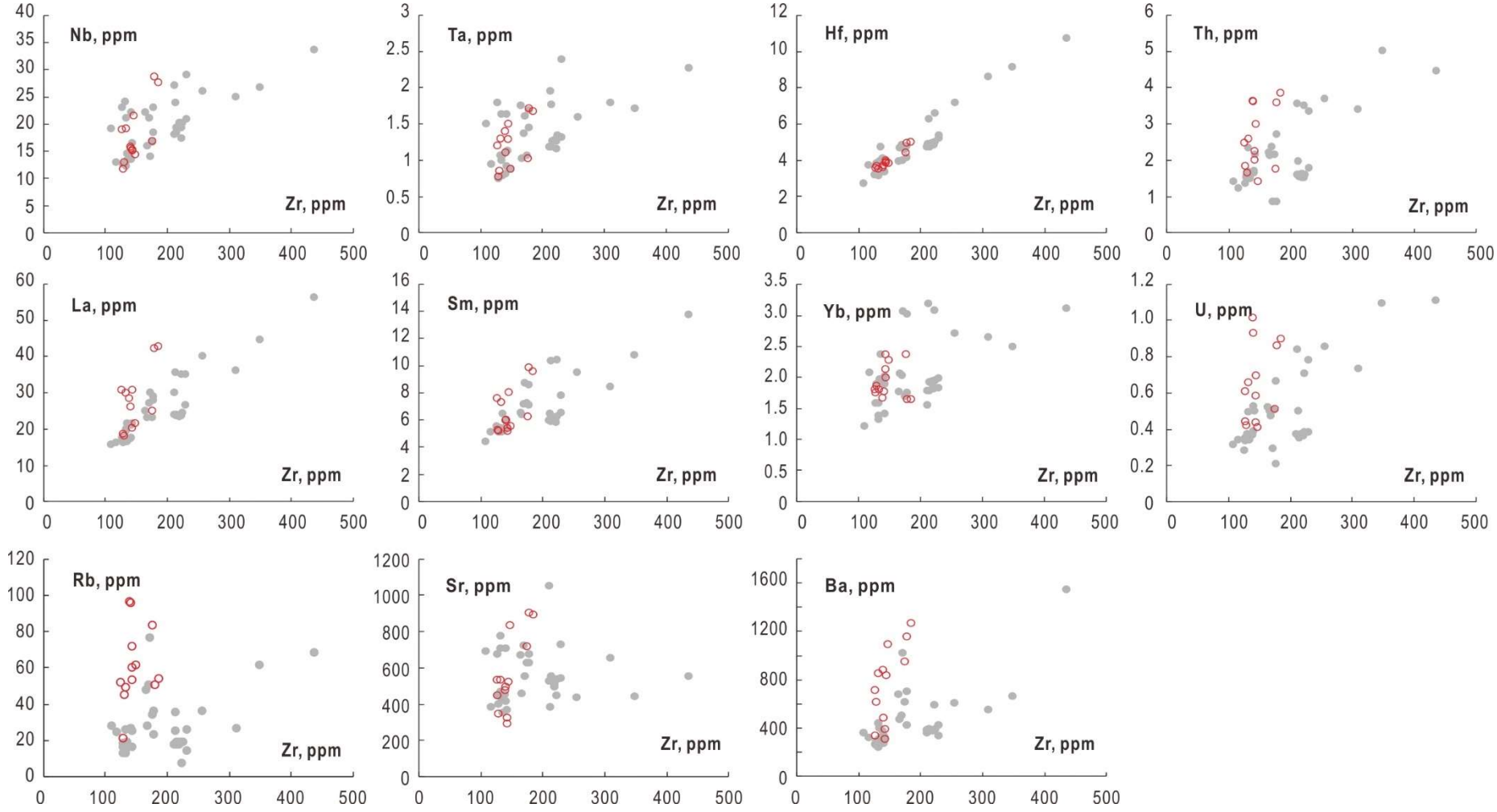

图 9.2 1.24–1.21 Ga 岩墙锆元素对其他元素图解。红色圆圈为本文新数据，灰色圆圈为编录的样品（附件）。

Fig. 9.2 Zr vs. whole-rock elements of the 1.24–1.21 Ga dykes. Red dots are new data in this study; grey dots are compiled data (supplementary file).

为衡量是否存在地壳混染，本研究选取灵敏元素进行分析。Nb/La的降低以及 Th/Nb 的增高（图 9.4a）似乎揭示了侵位过程中的混染。但是，Th/Nb、Th、Nb、La 与 MgO 之间的线性相关性（图 6.1i–k 和图 9.4b），暗示上述变化也可能由岩浆分异引起。在老王家岩墙中发现一些捕获锆石，说明存在一定的混染，但可能对地球化学成分的影响不显著；而在建平、青龙以及清原岩墙中又只发现极少的继承锆石 (Wang et al., 2015a)。同时，Th/Yb 对 Nb/Yb 图解（图 9.4e）也暗示一些样品存在微弱的混染 (Pearce, 2008)。综上，本文认为该期岩墙在侵位中存在不均一以及不显著的地壳混染。

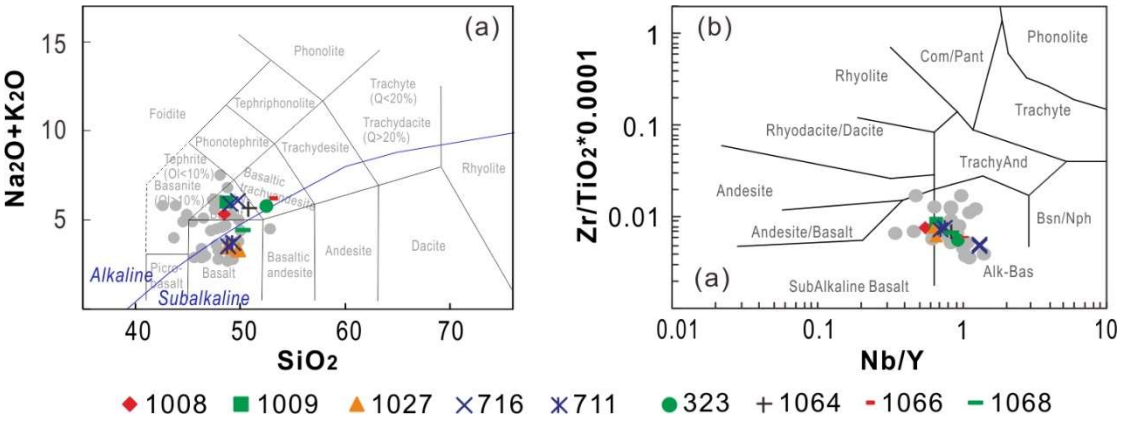

图 9.3 岩石化学分类。（a）硅碱图 (Cox, 2013)；（b）Zr/TiO_2 对 Nb/Y 图 (Winchester and Floyd, 1977)。灰色圆圈为编录的样品（附件）

Fig. 9.3 Chemical classification of rocks. (a) Total alkalis vs. silica (TAS) diagram (Cox, 2013); (b) Zr/TiO_2 vs. Nb/Y diagram (Winchester and Floyd, 1977). Grey dots are compiled data (supplementary file).

值得注意的是，具有相对老的年龄（>1230 Ma，以 JD1027 和 JD517 岩墙为代表）的样品与那些相对年轻（<1210 Ma，以 MY1033 和沂水侵入体为代表）的样品具有相似的地球化学特征，但似乎时代稍老的样品有更低的全铁，并有较高的镁值（表 6.1 和附录），可能反映了早期阶段岩浆的性质。早期样品的这一特征在鲁西岩墙中也存在（图 6.1d）。此外，早期样品的元素含量变化范围相对较大（表 6.1 和附录），但稀土配分型式大致相同（图 6.2a）。通过连续变化的元素、近平行的稀土配分特征以及蛛网图（图 6.1、图 6.2、图 9.3 和图 9.4），以及较为集中的同位素值 (Peng et al., 2013; Wang et al., 2015a, 2016b)，本研究认为虽然岩浆作用持续了约 30 Ma，但其岩浆源区相对单一，且整体上性质稳定。

该期岩墙群样品的 MgO 含量不超过 8 wt.%，Mg#通常小于 56（表 6.1 和附表），说明它们并非来自原始岩浆。MgO 与 Al_2O_3、tFe_2O_3（全铁）、TiO_2、Cr、Ni 之间并不存在明显的线性趋势 (图 6.1c–g)，因此岩浆分异过程可能比较微弱，

这也在 La/Sm 对 La 图解中有所体现（图 9.4c）。在岩浆演化的早期阶段，岩浆主要经历了部分熔融过程，因为在 La/Sm 与 La 中存在倾斜的线性趋势；在晚期阶段，当 La 含量达到~30 ppm 时，岩浆演化转换为弱的结晶分异作用。该期部分岩石显示正 Eu 异常（图 6.2a），反映斜长石在岩浆中的堆积。

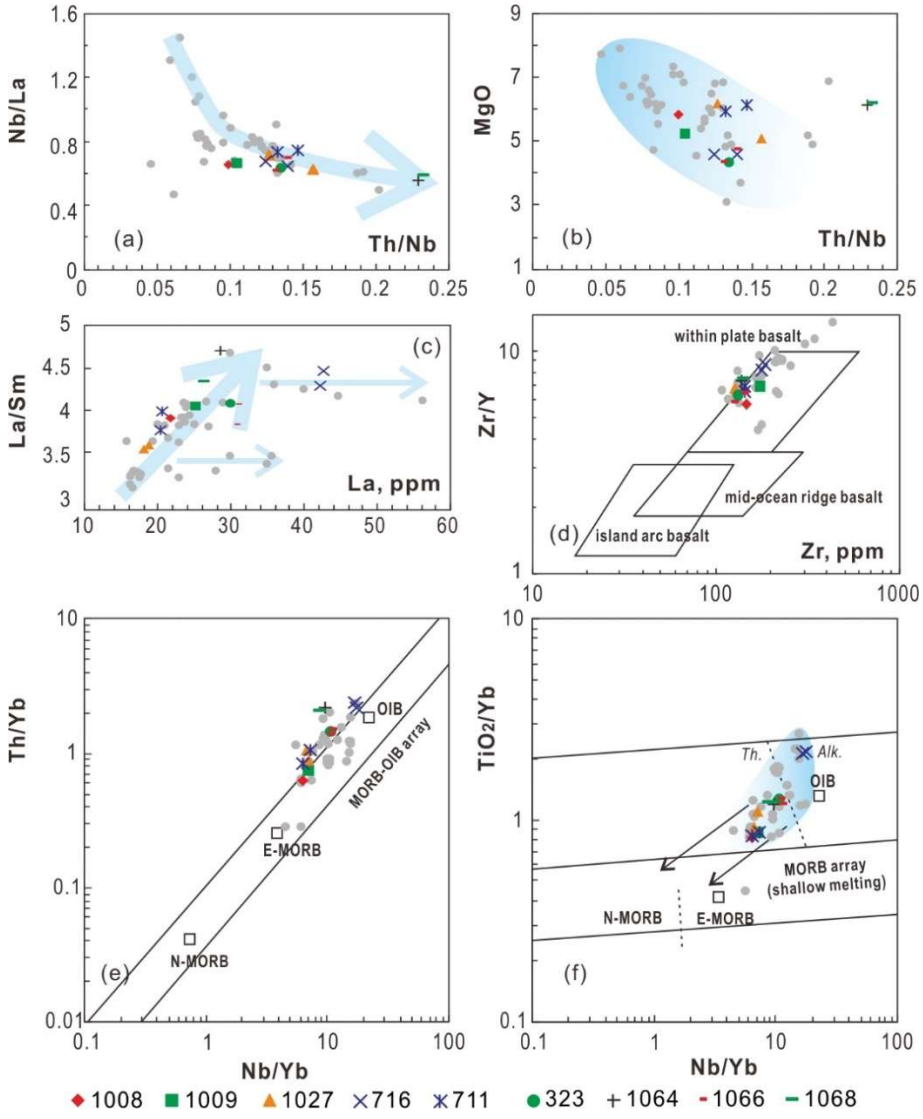

图 9.4 1.24–1.21 Ga 岩墙元素（比值）图解。灰色圆圈为编录的样品（附件）
Fig. 9.4 Trace elements ratio diagrams of the 1.24–1.21 Ga dykes. Grey dots are compiled data (supplementary file).

La/Yb_N 主要从 6.8 连续地变化至 13.9，个别样品高达 18.6（图 6.11 和图 6.2a），这一特征很可能与不同程度的部分熔融有关。La/Yb_N 最高的样品出现在太行山南的 716 号岩墙，该岩墙样品呈碱性玄武岩特征（图 9.3），但蛛网图特征与其他样品近于一致，如 Nb 相对 Th 和 La 的亏损（图 6.2）。所有样品有较高的稀土总量 （96–308 ppm）、较高的 La/Yb_N（6.15–18.6）（表 6.1 和附表）， 显示不同于 MORB 的地球化学特征。Th–Nb 特征显示样品有 OIB 的属性，并与 E-MORB

有微弱的交互趋势（图 9.4e）。高的 TiO_2/Yb 比值（图 9.4f）暗示石榴子石残余以及岩石起源于厚的陆下岩石圈之下的熔体 (Pearce, 2008)。图 9.4e 和 f 中，从 OIB 到 MORB 的趋势反映了热的地幔流上升与岩石圈地幔的相互作用 (Pearce, 2008)。另外，高 Ti 特征也被认为和地幔柱作用有关 (Peng et al., 2007; Xu et al., 2001)。一些样品的 εHf (t = 1230 Ma) 为 1.8–10 (Wang et al., 2015a)，εNd (t = 1230 Ma) 为 0–1.6 (Peng et al., 2013; Wang et al., 2016b)，指示岩浆起源于同位素亏损的地幔源区。综上，本文认为该事件可能起源于地幔柱。

9.2 华北~1.24–1.21 Ga 大火成岩省论证

大火成岩省（LIP）通常指短时间内的巨量岩浆活动，一般与裂解有关，也可与矿产资源的形成以及环境效应相关 (Ernst, 2014)。其可通过岩浆体积、面积、持续时间、岩浆脉次，以及构造背景等识别 (Ernst, 2014 及参考其中)。~1.24–1.21 Ga 岩墙在华北克拉通出露广泛（表 9.1），一些大火成岩省的指示特征可以在该期岩墙中得到发现。

首先，在野外中这些岩墙并不是可以连续追索，一般可识别数百米到几公里，这为估计总的覆盖面积和岩浆体积造成了障碍。但这些岩墙一般至少 10 m 宽，符合大火成岩省的判断尺度 (Ernst, 2014)。结合古地磁数据识别出的同期岩墙，尤其是在太行山南部识别的岩墙（平山岩墙；图 3.8d）(丁继凯, 2017)，并恢复郯庐断裂的影响，保守估计这期事件在华北的覆盖面积将超过 0.1×10^6 km^2。如果纳入白云鄂博地区的小岩墙 (1227 ± 60 Ma，Sm–Nd 等时线年龄；Yang et al., 2011)，覆盖面积和体积将更大。此外，朝鲜半岛中西部京畿道西部的基性岩墙和二长岩侵入体结晶于 1222–1259 Ma (Kim et al., 2018)，可能与本文的基性侵入体有关联。受限于露头情况，在野外一般难以追踪岩墙的长度；但本期岩墙单体较宽，推测其可能会延伸很远，比如 JD1027 和 MY1033 岩墙。

其次，通过大量的 U–Pb 定年总结，该事件由 1244 Ma 持续到 1207 Ma，跨度约 30 Ma。考虑到年龄误差的不确定性，以及地球化学特征的相似性（图 6.1、图 6.2 和图 9.4），本文认为这些侵入体属于同一事件。Ernst (2014) 总结道，超过 20 Ma 的大火成岩省一般都不是连续侵位，而是由数个短的脉次组成。然而，目前的定年结果很难判断脉次，但大概能分为>1230 Ma、~1220 Ma 以及~1207–1210 Ma 三组。

表 9.1 华北克拉通 1.24–1.21 Ga 岩浆作用一览表

Table 9.1 Summary information of 1.24–1.21 Ga magmatism in the North China Craton

位置	产出形式	走向	年龄/Ma	定年方法	参考文献
鲁西沂水*	侵入体		1209 ± 6	Zr–S	Peng et al., 2013
吉林通化*	岩墙	NE	1244 ± 28	Zr–L	裴福萍等, 2013
辽西建平	岩墙–南	38°	1229 ± 10	Zr–L	Wang et al., 2015a
			1217 ± 13	Zr–S	丁继凯, 2017
	岩墙–中	38°	1229 ± 4, 1231 ± 16	Zr–L	Wang et al., 2015a
			1226.9 ± 3.4	Zr–S	丁继凯, 2017
	岩墙–北	38°	1222.9 ± 6.1	Zr–S	丁继凯, 2017
辽北清原*	岩墙	EW	1226 ± 11	Zr–L	Wang et al., 2015a
			1214.0 ± 4.9	Bd–T	本文
冀东青龙	岩墙	40°	1208 ± 24	Zr–L	Wang et al., 2015a
冀东滦南	岩株、岩墙?		1228 ± 4	Bd–S	相振群, 2014
黎城	岩墙	NW	1229 ± 4	Bd–S	Peng, 2015b
			1219.1 ± 4.3	Bd–S	丁继凯, 2017
卢龙茆家沟	岩墙	32°	1236 ± 7	Bd–S	Wang et al., 2016b
唐山迁西	岩墙	32°	1233 ± 27	Bd–S	本文
密云白河涧	岩墙	30°	1206.7 ± 1.7	Bd–T	本文
兴隆米铺	岩墙	NE	1236.3 ± 5.4	Bd–T	本文

位置标注“*”代表郯庐断裂东侧样品；Zr–锆石，Bd–斜锆石；S、L 和 T 分别代表 SIMS、LA–ICPMS 和 TIMS 方法

第三，这些岩体出露于华北克拉通内部，有板内的地球化学特征（图 9.4d）。基于野外观察以及分析，本研究认为这些基性岩体构成了华北 1.24–1.21 Ga 由地幔柱引发的大火成岩省，并命名为黎城大火成岩省（源自 Peng (2015b) 对黎城岩墙的命名）。岩墙的放射状形态指示该地幔柱位于华北克拉通东南。

磁化率各向异性被广泛应用于评估岩浆流的方向 (如 Ernst and Baragar, 1992; 潘小青等, 2012)。研究表明，只有正常磁组构能有效反映岩浆流的信息 (Rochette et al., 1992; Rochette et al., 1991)。本研究 JD1027 岩墙的正常磁组构呈现低倾角的 K_1 轴（图 8.6a），表明岩浆在该地区以侧方向流动为主而远离岩浆中心。与此相反，C711 岩墙的正常磁组构呈现中到高倾角的 K_1 轴（图 8.6b），反映岩浆源区可能距此区域相对较近。据此，磁组构结果亦倾向认为该事件的岩浆中心可能位于华北的东南。

9.3 古地磁极及重建

9.3.1 华北~1.68 和 1.24 Ga 古地磁极原生性

通过岩墙获得的古地磁极或虚地磁极，要证明其剩磁的原生性，最直接的办法是进行野外的烘烤接触检验（baked contact test）。其基本原理为，岩墙侵位时烘烤其围岩，使近距离接触的围岩磁化，获得与岩墙一致的磁化方向；而远处的围岩未被磁化，其磁化方向应与岩墙的不同（图 9.5）。如果得到上述结果，则称通过了烘烤检验，否则为未通过烘烤检验。

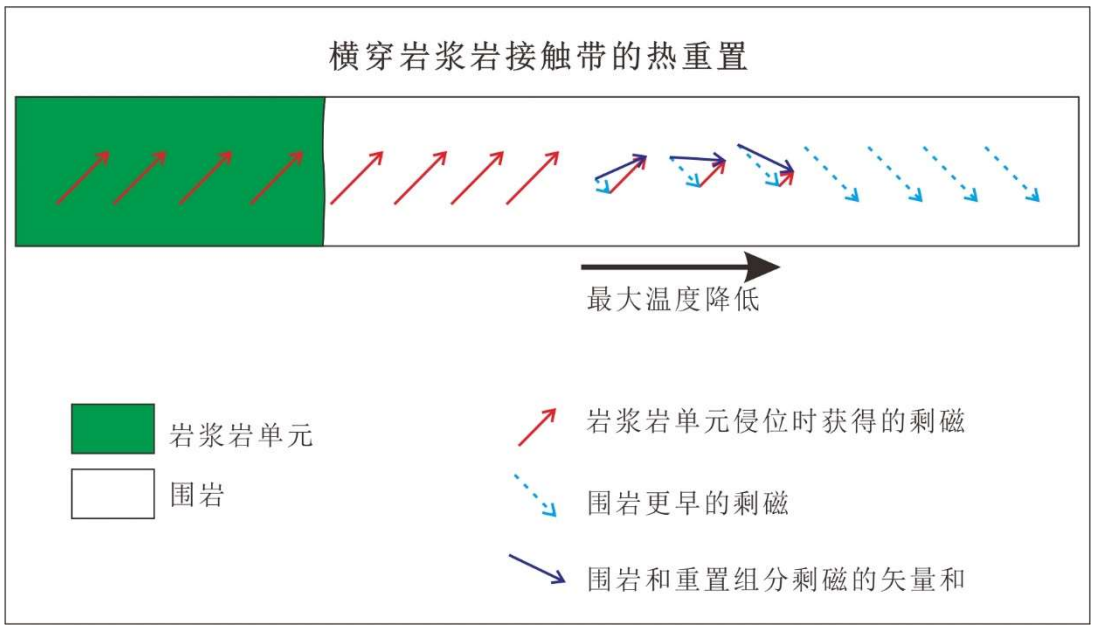

图 9.5 从侵入岩到围岩远处的剩磁方向图 (Buchan, 2007)。假定沿着剖面，围岩有相似的磁性矿物，并假定烘烤带和混杂带都是获得的热剩磁

Fig. 9.5 Direction of remanent magnetization of intrusive and its country rocks (Buchan, 2007). It is assumed that the country rocks contain similar magnetic minerals and both the baked zone and the hybrid zone experience thermoremanent magnetization.

实际中，前寒武纪基性岩墙的围岩一般为花岗岩或片麻岩，但从花岗岩中一般难以获得稳定的特征剩磁，而片麻岩又容易风化变软造成取样困难，或围岩被第四系覆盖，这些都为烘烤检验的实现制造了障碍。另外，考虑到后期区域地质事件的可能影响，以及其他情况的产生（氧化、风化等），完整的烘烤检验还应包含以下的信息：① 未烘烤围岩的磁化方向应该早于岩墙侵位时获得；② 在烘烤的围岩与未烘烤的围岩之间存在渐变磁化的混杂带 (Buchan, 2007)。因此，较为理想的烘烤检验方法是从岩墙的边部向远处围岩连续采样得到从烘烤带、混杂带到未烘烤带的连续变化的磁化方向（图 9.5），这样的采样检验被称作烘烤接触剖面检验（baked contact profile test），假如能得到连续稳定的特征剩

磁方向，则检验结果的可信程度比较高 (Buchan, 2007; Buchan et al., 1993; Buchan and Schwarz, 1981)。但这种情况亦很难实现，因为本身岩墙完整的烘烤实验都很难实现，更何况再证实未烘烤围岩的原生性，或证明未烘烤围岩剩磁获得的时间早于岩墙结晶时间。此外，围岩不一定有能够连续采样的露头，即使露头连续也可能难以获得稳定的特征剩磁。

由于基性岩墙是最容易获得稳定特征剩磁的材料，且能通过定年确定其形成时代。因此，较好的烘烤检验情况是寻找两条相交的岩墙，在相交区域采样测试 (Halls, 2008)，比如对华北太行岩墙群的烘烤检验 (Xu et al., 2014)。

本研究对岩墙 JD1027 和 JD687（图 3.8c）进行了烘烤检验分析，两条岩墙的围岩均为片麻岩。JD1027 是一条宽约 30 m 的岩墙，本研究在距离岩墙边部约 3 m 及~100 m 部位采集了围岩样品。这些围岩均给出了较为稳定的磁化方向，其中近处围岩为中等倾角东南向向下的特征剩磁方向，与岩墙的平均方向一致；远处围岩为中等倾角西南向向上的特征剩磁方向（图 9.6a）。该结果说明岩墙侵位时烘烤了近处的围岩，但是很可能没有烘烤远处的围岩。本研究认为该结果通过了烘烤检验，认为岩墙的剩磁为原生剩磁。

对于约 25 m 宽的 JD687 岩墙，本研究在距离岩墙边界约 35 cm 处和超过 35 m 处采集了围岩样品。近处围岩与岩墙的磁化方向相近，说明很可能受到了烘烤；但远处围岩的磁化方向较为分散，难以给出可靠的平均方向（图 9.6b）。此结果为不完全的烘烤检验。

虽然本研究的~1.68 Ga 岩墙没有烘烤检验判断其剩磁的原生性，但多种证据表明这些剩磁可能是原生的。首先，本研究的岩墙未变质变形，具有明显的辉绿结构 (Li et al., 2015; Wang et al., 2016b)。一些蚀变与低温过程（<300°C）有关，高的解阻温度（550–580°C）被蚀变过程影响的可能微乎其微。其次，岩石磁学研究显示样品中含古地磁稳定的单畴或假单畴磁铁矿（图 8.1a–c、图 8.2a、图 8.4a–c 和图 8.5）。再者，在 JD689 岩墙的区域内（图 3.8c），~1.32 Ga 和 1.24–1.22 Ga 的岩墙通过了古地磁的野外检验 (Chen et al., 2013; 丁继凯, 2017 及本研究)，说明~1.32 Ga 之后没有广泛的重磁化事件发生。除此之外，研究区内并没有出现 1.60–1.35 Ga 的岩浆作用 (Peng, 2015b)，这也排除了本研究~1.68 Ga 岩墙在此期间被重磁化的可能。3 条岩墙中获得的 55.6°N, 258.1°E, A_{95} = 7.2°（表 7.1）很可能代表~1.68 Ga 的虚地磁极。

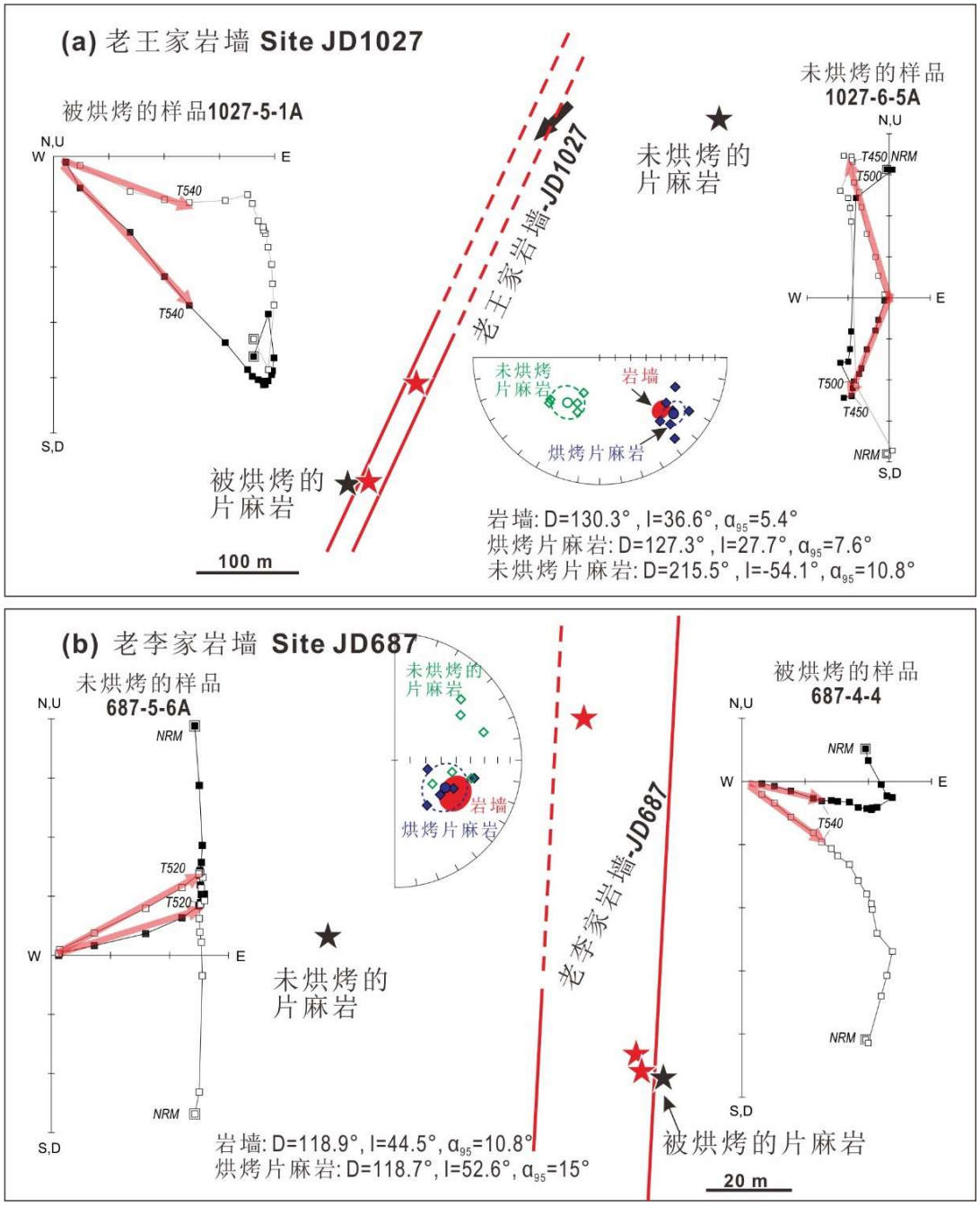

图 9.6 岩墙 JD1027（a）与 JD687（b）的烘烤检验。图含采样位置（星形）、代表性围岩的退磁（实心和空心方块分别指向水平和垂直面的投影）及样品的等面积投影（实心和空心菱形分别对应向下和向上的磁化方向）

Fig. 9.6 Baked contact tests for dykes JD1027 (a) and JD687 (b). Each includes sample locations (stars), representative demagnetization of host gneisses (solid/open square points show vector end points projections onto the horizontal/vertical plane) and equal area stereoplots (solid/open square points correspond for downward / upward–pointing magnetizations).

本研究发现，~1.68 Ga 的虚地磁极与云梦山组下部的古地磁极 (60.6°N, 267.0°E, A_{95} = 3.7°；Zhang et al., 2006) 非常接近（图 9.7）。云梦山组沉积于华北克拉通南部，之前的 Rb–Sr 定年指示其形成于中元古代晚期，但新的火山灰 U–Pb 定年及碎屑锆石约束其形成于古元古代晚期，大概在<1.71 Ga 和>1.61 Ga 之间 (Hu et al., 2014a; 汪校锋, 2015; 苏文博等, 2012)（图 9.7）。假定云梦山组开始沉积于~1.70 Ga，并假设古元古代晚期沉积速率近于一致，则根据地层厚度与绝对年龄所限定的云梦山组沉积上限为~1.67 Ga（表 9.2）。

云梦山组下部的古地磁极通过了褶皱检验及倒转检验，被认为是原生极。而该组下部的单个采点磁化方向与本研究~1.68 Ga 采点磁化方向重叠，云梦山组的估计沉积时间也恰好推断为~1.68 Ga 前后（图 9.7 和表 9.2）。因此，本文将此 18 个采点（3 条岩墙和 15 个地层采点）的结果结合在一起，得到一个华北~1.68 Ga 平均古地磁极，为 59.8°N，265.3°E，A_{95} = 3.3°（图 9.7）。

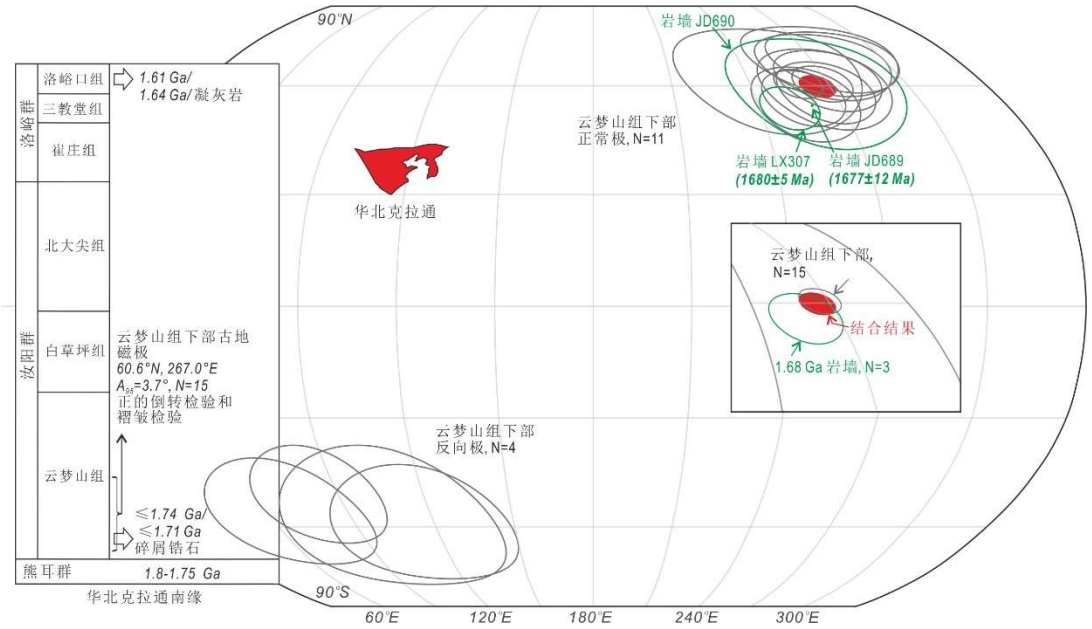

图 9.7 ~1.68 Ga 岩墙的虚地磁极与云梦山组下部古地磁极 (Zhang et al., 2006) 比较。云梦山组下部碎屑锆石的最小年龄来自 Hu et al. (2014a) 和汪校锋 (2015)；洛峪口组火山灰的年龄来自苏文博等 (2012)。推测的地层时代见表 9.2

Fig. 9.7 A comparison of VGPs from the studied ~1.68 Ga dykes and paleopole from the lower Yunmengshan Formation (Zhang et al., 2006). Minimal ages of detrital zircons at the base of the Yunmengshan Formation are from Hu et al. (2014a) and Wang (2015). Ages of tuffs from the Luoyukou Formation are from Su et al. (2012). Details of age estimation are in Table 9.2.

表 9.2 推测的汝阳群和洛峪群沉积时代

Table 9.2 Presumed depositional ages of Ruyang and Luoyu groups

群	组		厚度 (m)	年龄 (Ma)	建议的年龄 (Ma)
洛峪群	洛峪口组	IV段	70	1611 (顶部火山灰) (苏文博等, 2012)	
		III段	30		
		II段	100		~1615 ± 4
		I段	20		~1620 ± 1
	三教堂组		51.7		~1623 ± 2
	崔庄组		157		~1631 ± 7
汝阳群	北大尖组		186.4		~1646 ± 8
	白草坪组		167		~1660 ± 7
	云梦山组		394	<1711 (底部碎屑锆石) (Hu et al., 2014a; 汪校锋, 2015)	~1683 ± 17

厚度来自对汝阳地区地层的测量 (河南省地质矿产局, 1989)

9.3.2 古地磁重建

本文获取了华北~1.68 Ga 和~1.24 Ga 的古地磁极，获取了华北~1.21 Ga 的虚地磁极。经查文献，发现澳大利亚陆块在此期间有较为丰富的古地磁极，尤其是一些与华北近于同期的极；且华北与澳大利亚的关系一直不明晰 (如 Zhang et al., 2012b, 2017)，因此后面的内容将着重检测华北与澳大利亚在元古宙时期的古地理关系。

按照 Van der Voo (1990) 的质量判断标准尽量选择可靠的古地磁极，结果见表 9.3。其中，多数极具有精确的年龄，但一些来自地层中的极缺乏直接限定的年龄，比如华北蓟县系杨庄组的沉积时代是根据其下伏高于庄组（凝灰岩~1560 Ma）及上覆雾迷山组（凝灰岩 1480–1490 Ma）间接限定；比如北澳的 Emmerugga 白云岩、Tooganinie 组和 Mallapunyah 组的沉积时代亦是通过上下地层所间接约束 (Ahmad et al., 2013)。此外， Elgee 和 Pentecost 组下伏地层里的辉绿岩岩床结晶于~1.79 Ga (Sheppard et al., 2012)，虽然目前没有直接证明 Elgee 和 Pentecost 组里的岩床与此同期，但根据经验，这两个组可能早于~1.79 Ga 沉积。另一个值得注意的情况是，在近于同期的岩体或者同一套地层中得到不一致的古地磁极，虽然结果不一致但仍有野外检验作为支撑（表 9.3）。这种情况在华北以及北澳古地磁数据里都有体现，如华北蓟县系杨庄组的两个独立的研究及不同结果，近同期的太行-阴山岩墙群与熊耳火山岩的独立研究及不同结果；如北澳~1.73 Ga 以及~1.65 Ga 前后的古地磁极研究结果（表 9.3）。

古地磁重建在 GPlates 软件（www.gplates.org）平台中完成。从图 9.8a 中可以发现，华北的 1.78 Ga、1.68 Ga、1.64–1.62 Ga 和 1.53 Ga 古地磁极分别与北澳的 1.79 Ga、1.71 Ga、1.67–1.65 Ga 和 1.59 Ga 古地磁极接近。虽然北澳~1.32 Ga 的古地磁极还未正式报道 (Kirscher et al., 2018b)，但图 9.8a 的重建对应华北与北澳~1.32 Ga 的磁极重叠（Uwe Kirscher，个人交流）。因此，二者在~1.78 Ga 和 1.32 Ga 期间可能有相似的视极移曲线。考虑部分古地磁极质量以及年龄的不确定性，图 9.8a 简单勾勒了这段时间的视极移曲线（粗黄线）。假如上述分析成立，则这两个陆块很可能在~1.78 Ga 到 1.32 Ga 时期具有亲缘性，并且保持固定的形态长期不变。

~1.32 Ga 至~1.21 Ga，华北的视极移曲线与澳大利亚的不同，暗示二者在~1.32 Ga 之后可能经历了不同的漂移轨迹（图 9.8a）。基于~1.24–1.21 Ga 古地磁极的重建表明，~1.32 Ga 之后华北与澳大利亚陆块均向北漂移且已分离（图 9.8b）。

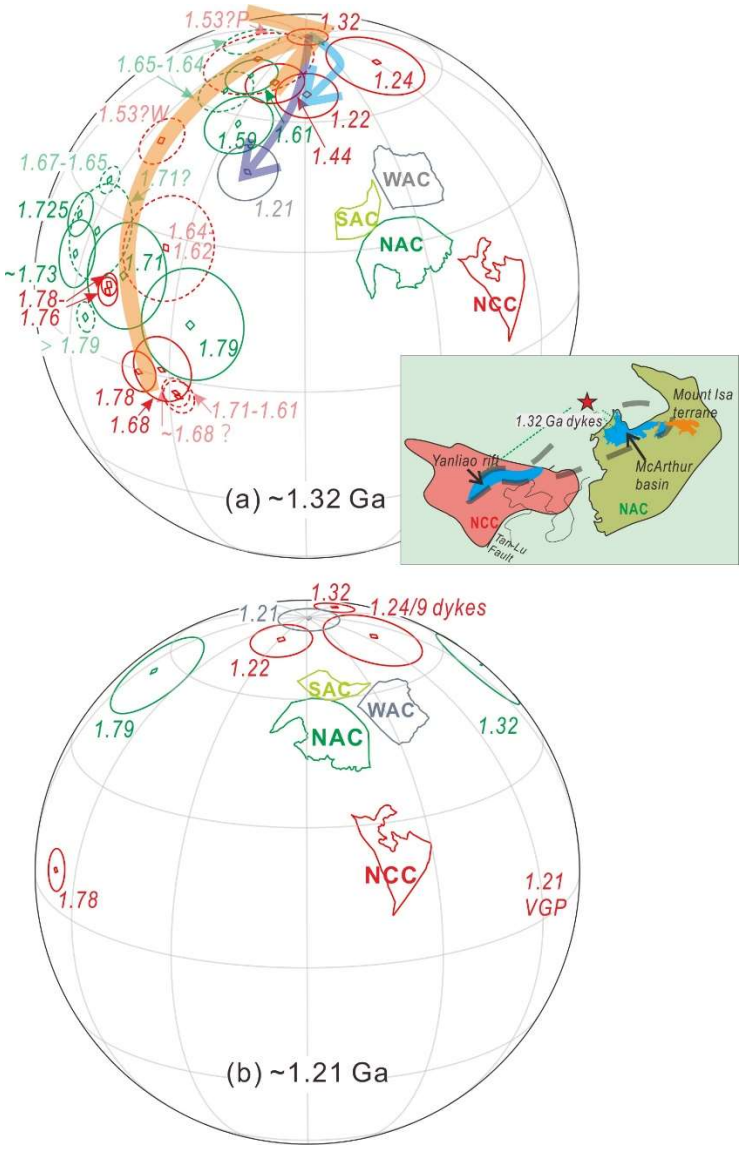

图 9.8 古地磁重建~1.32 Ga（a）及~1.21 Ga（b）华北与澳大利亚的相对位置。（a）选取的~1.8–1.3 Ga 华北的古地磁极（红色）及北澳的古地磁极（绿色）表明二者可以有相似的~1.78–1.32 Ga 视极移曲线（粗黄线）；而 1.32 Ga 之后二者有不同的视极移曲线，说明可能发生了分离。插图为与之对应的重建，可对比的~1.32 Ga 放射状基性岩墙群和推测的地幔柱由 Zhang et al. (2017) 提出。（b）图展示~1.21 Ga 华北与澳大利亚相对的位置。古地磁极旁标注有年龄，单位为 Ga；虚线代表为推测的年龄。原澳大利亚陆块模型来自 Li and Evans (2010)。欧拉旋转参数见表 9.4。NCC–华北克拉通，NAC–北澳克拉通，WAC–西澳克拉通，SAC–南澳克拉通。

Fig. 9.8 Paleomagnetic reconstruction between the NCC and proto-Australia at ~1.32 Ga (a) and ~1.21 Ga (b). (a) Selected ~1.8–1.3 Ga paleomagnetic poles showing the comparable APWP (bold yellow line) between the NCC (red) and the NAC (green); while the different APWPs after ~1.32 Ga indicating their separation. Insert figure showing schematic paleogeography corresponding to the similar paleomagnetic reconstruction. The comparable model of the ~1.32 Ga radial dykes and plume centre was proposed by Zhang et al. (2017). (b) showing the relative configuration between the NCC and proto–Australia at ~1.21 Ga. The paleopoles are marked with ages in Ga. Dashed poles have putative ages only. The proto–Australia configuration is after Li and Evans (2010). Euler rotation parameters are in Table 9.4. NCC–North China Craton, NAC–North Australian Craton, WAC–West Australian Craton, SAC–South Australian Craton.

表 9.3 华北和澳大利亚陆块~1.8–1.3 Ga 古地磁极

Table 9.3 Selected ~1.8–1.3 Ga paleomagnetic poles for the North China and Australia blocks

序号	岩石单元	年龄(Ga)	极纬度(°N)	极经度(°E)	A_{95}(°)	质量因子	参考文献
华北陆块							
1	熊耳火山岩	1.78	50.2	263.0	4.5	+++–+++	Zhang et al., 2012b
2	太行基性岩墙群	1.78–1.76	36.0	247.0	3.0	++++++–+	Halls et al., 2000
3	阴山基性岩墙群	1.78–1.76	35.5	245.2	2.4	++++++–+	Xu et al., 2014
4	莱芜和屠家沟岩墙群–3 个采点	1.68	55.6	258.1	7.2	+–+–+–+	本研究
5	庐山和汝阳地区云梦山组下部–15 个采点	*1.71– 1.61*	60.6	267.0	3.7	–+++++++	Zhang et al., 2006
4+5	~1.68 Ga 岩墙与云梦山组下部结合–18 个采点	~1.68?	59.8	265.3	3.3	–+++++++	本研究
6	庐山和汝阳地区崔庄组和三教堂组砂岩	*1.64–1.62?*	41.0	224.8	11.3	–++–+++	Zhang et al., 2006
7	蓟县杨庄组白云岩	*1.53?*	17.3	214.5	5.7	–+++++++	Wu et al., 2005
8	蓟县杨庄组白云岩	*1.53?*	2.4	190.4	11.9	–+++++++	Pei et al., 2006
9	蓟县铁岭组石灰岩	1.44	11.6	187.1	6.3	++++++–+	吴怀春, 2005
10	燕辽基性岩床群	1.32	5.9	359.6	4.3	++++++–+	Chen et al., 2013
11	冀东、鲁西、华北中部岩墙群（黎城 LIP）	1.24	2.6	165.1	10.8	++++++–+	本研究
12	建平、平山岩墙群	1.22	16.0	180.3	6.6	++++++–+	丁继凯, 2017
13	密云白河涧岩墙（VGP）	1.21	–23.0	92.5	6.1	+–+–+–+	本研究
澳大利亚陆块							
14	Elgee 和 Pentecost 组	*＞1.79*	5.4	31.8	3.2	–++++––	Li, 2000; Schmidt and Williams, 2008
15	Hart 岩床/辉绿岩	1.79	6.9	2.6	12.0	+++–+++	Kirscher et al., 2018a
16	Peters Creek 火山岩–上部	1.725	26.0	41.0	4.8	+++++++	Idnurm, 2000
17	Wollogorang 组	~1.73	17.9	38.2	7.2	+–++++–	Idnurm et al., 1995
18	Fiery Creek 组	*1.71?*	23.9	31.8	10.4	–++–+––	Idnurm, 2000
19	West Branch 火山岩	1.71	15.9	20.5	11.3	+++++––	Idnurm, 2000

序号	岩石单元	年龄(Ga)	极纬度(°N)	极经度(°E)	A_{95}(°)	质量因子	参考文献
20	Mallapunyah 组	*1.67–1.65*	35.0	34.3	3.1	+ + + + + + +	Idnurm et al., 1995
21	Tooganinie 组	*1.65–1.64*	61.0	6.7	6.1	+ + + + + + +	Idnurm et al., 1995
22	Emmerugga 白云岩	*1.65–1.64*	79.1	22.6	6.1	+ + + + + – –	Idnurm et al., 1995
23	Balbirini 白云岩–下部	1.61	66.1	357.5	5.7	+ + + – + + +	Idnurm, 2000
24	Balbirini 白云岩–上部	1.59	52.0	356.1	7.5	+ + + – + + +	Idnurm, 2000
25	WAC– Gnowangerup–Fraser 岩墙群	1.21	–55.8	143.9	6.5	+ + + + + + –	Pisarevsky et al., 2014b

斜体表示推断的年龄。A_{95}为 95%置信椭圆。质量因子 (Van der Voo, 1990) 从左往右依次为：岩石有较为精确的年龄并假定磁化时代与此相同，充足的样品（N>24）以及可靠的统计（k ≥10, A_{95} ≤ 16.0°）；合适的退磁；正的野外检验；有构造上的控制以及克拉通的构造环境；出现反向极；不与年轻的极相似 。当满足这些时标为“+”，不满足时标为“–”。

表 9.4 欧拉旋转参数（相对于绝对框架）
Table 9.4 Euler rotation parameters (to the absolute framework)

克拉通	欧拉极纬度 (°N)	欧拉极经度 (°E)	旋转量 (°)	克拉通	欧拉极纬度 (°N)	欧拉极经度(°E)	旋转量 (°)
1.32 Ga（表 9.3a）				~1.21 Ga（表 9.3a）			
华北	–32.72	–44.19	–124.58	华北	–28.56	–59.28	–101.23
北澳	–4.44	–55.92	–178.78	北澳	–8.42	–80.02	–132.82
西澳	–7.96	–47.31	–214.38	西澳	–14.45	–67.02	–162.38
南澳	–7.96	–47.31	–214.38	南澳	–14.45	–67.02	–162.38

9.4 古大陆重建的地质约束

Zhang et al. (2017) 主要通过~1.32 Ga 放射状的基性岩墙群连接了华北东北部与北澳北部。本文注意到，通过古地磁重建的~1.78–1.32 Ga 华北与澳大利亚陆块的相对位置（图 9.8a）与上述模型相似。北澳麦克阿瑟盆地（McArthur Basin）被认为与华北燕辽裂谷具有相关性 (Zhang et al., 2017)，但如何相关仍不得而知。麦克阿瑟盆地由岩相、时代以及地层关系分为五个不整合的单元（package）：Redbank（~1.82? –1.71 Ga）、Goyder（1.71–1.67 Ga）、Glyde（1.67–1.60 Ga）、Favenc（1.60–1.58 Ga）和 Wilton（1.5–1.35? Ga），每个单元在不同的地方划分有不同的群且连续沉积 (Ahmad et al., 2013; Rawlings, 1999)。本文选取麦克阿瑟盆地北部的 Katherine River 群（~1.82? –1.71 Ga）和 Parsons Range 群（~1.71–1.67 Ga）及盆地南部的 McArthur 群（~1.67–1.60 Ga）、Nathan 群（~1.60–1.58 Ga）和 Roper 群（~1.5–1.35? Ga），将其与燕辽裂谷做地质对比，细致探讨二者之间的相关性。

（1）地层及化石记录

华北燕辽裂谷和北澳麦克阿瑟盆地在~1.70–1.60 Ga 均接受碎屑沉积，夹有部分碳酸盐岩沉积（燕辽长城系及麦克阿瑟群~1.64 Ga 白云岩）（图 9.9）。两者在~1.40 Ga 之后也都记录碎屑岩为主的沉积。~1.70–1.60 Ga 二者均为非深海相沉积环境（Rawlings, 1999; 阎玉忠和刘志礼, 1998），但据此仍难以建立盆地之间的联系。燕辽裂谷长城系团山子组与上覆大红峪组之间的不整合、大红峪组与上覆高于庄组之间的不整合在时代上可能与麦克阿瑟盆地麦克阿瑟群内部的不整合、麦克阿瑟群与上覆 Parsons Range 群的不整合一致，但目前对麦克阿瑟盆地不整合的性质了解甚少 (Ahmad et al., 2013; Rawlings, 1999)。华北长城系被认为沉积于断陷时期，与裂谷的活动有关 (如温献德, 1997)，而同期的北澳麦克阿瑟群的沉积也可能与裂谷活动有关 (构造背景尚有争议; Ahmad et al., 2013)。

最古老的真核生物微化石 *Valeria lophostriata* 同时出现在近于同期的燕辽长城系底部以及麦克阿瑟群的 Mallapunyah 组（图 9.9）(Javaux and Lepot, 2018; Lamb et al., 2009)。这些化石都显示有复杂的壁结构，具有同心条纹。

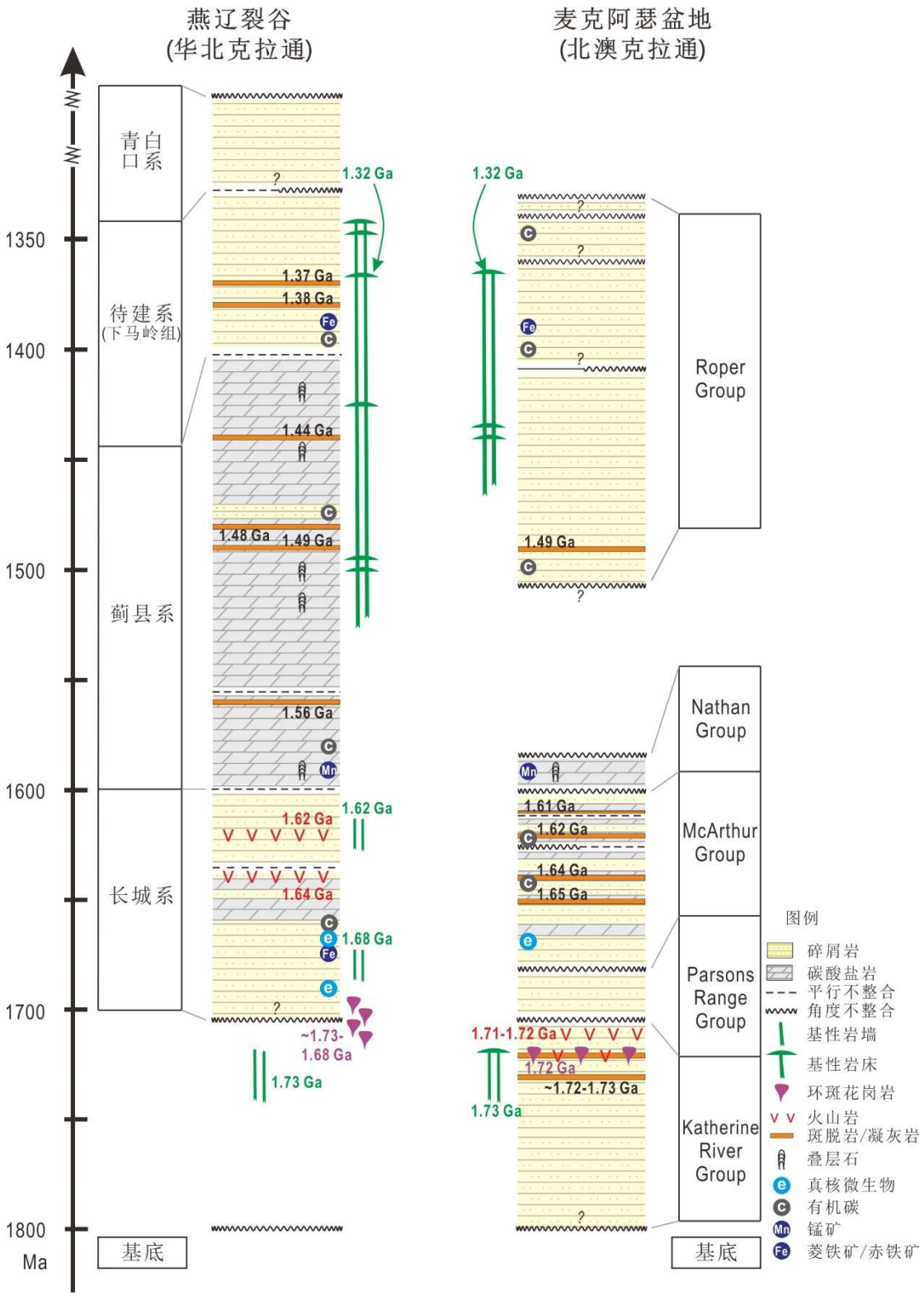

图 9.9 华北燕辽裂谷与北澳麦克阿瑟盆地构造地层的时空关系。燕辽裂谷与麦克阿瑟地层柱分别改编自 Su et al. (2010) 和 Ahmad et al. (2013)

Fig. 9.9 Time–space diagram outlining tectonostratigraphic correlations between the Yanliao Rift of the NCC and the McArthur Basin of the NAC. Columns of the Yanliao Rift and McArthur Basin are compiled after Su et al. (2010) and Ahmad et al. (2013), respectively.

两个盆地的沉积记录也存在不一致。其中，燕辽缺失~1.70 Ga 之前的地层，但麦克阿瑟盆地却较好的记录了~1.70 Ga 之前砂岩为主的沉积。另外，北澳缺失 1.58–1.50 Ga 期间的记录（图 9.9），这种缺失可能是由于 Mount Isa 造山作用的影响 (Rawlings, 1999)。Isan 造山带出露于麦克阿瑟盆地的东南部，其在~1.60–1.50 Ga 的造山作用引发了 E–W 及 NWW–SEE 向不同程度的地壳缩短、断层活动、盆地倒转以及区域性的扳转 (Giles et al., 2006; O'dea et al., 1997; Spampinato et al., 2015)。这些作用引起了邻区的麦克阿瑟盆地 NEE–SWW 向的缩短 (Rawlings, 1999)。除此之外，部分地层的不一致也可能由大的沉积系统的侧向变化 (Ahmad et al., 2013) 引起。

（2）岩浆作用事件

在燕辽地区，~1.73 Ga 的密云基性岩墙侵入于太古宙岩石单元中（图 1c 和图 8）(Peng et al., 2012)。与此类似，~1.73 Ga 的 Oenpelli 基性岩床（辉绿岩）侵入 Katherine River 群的砂岩（图 9.9）及邻区的 Pine Creek 造山带 (Whelan et al., 2016)。之后，在麦克阿瑟盆地的西北部，~1.72 Ga 的 Jimbu 花岗岩侵位于 Katherine River 群中（图 9.9），该花岗岩含钾长石斑晶，并含钠长石等细粒微晶基质 (Rawlings and Page, 1999)。在~1.73–1.68 Ga，环斑花岗岩或富钾花岗岩、斜长岩、纹长二长岩以及碱性花岗岩等侵入燕辽裂谷基底中（图 3.8c 和图 9.9）。另外，燕辽裂谷记录了~1.64 和 1.62 Ga 的火山喷发；而同期的火山灰在麦克阿瑟盆地中被发现 (Page et al., 2000; 张拴宏等, 2013; 陆松年和李惠民, 1991)（图 9.9），考虑到这两个时期的火山岩在全球分布并不广泛 (Ernst and Youbi, 2017)，说明两个地区可能位于相邻的区域。同时，1.49–1.48 Ga 的火山灰在这两个盆地中都有报道 (Ahmad et al., 2013; 李怀坤等, 2014)（图 9.9）。

~1.32 Ga 的基性侵入岩在两个盆地中都有记录（图 9.9）：华北的大同岩墙群（1326 ± 4 Ma）和燕辽岩床群（~1323 Ma）（图 3.4）(Peng, 2015b; Zhang et al., 2017)，以及北澳的 Galiwinku 岩墙群（1324–1329 Ma）和 Derim–Derim 岩床群（1324 ± 4 Ma）(Whelan et al., 2016)。华北 1.32 Ga 岩浆作用覆盖面积>1.2×10^5 km^2，并有岩浆作用前的地壳上升，以及板内岩浆的属性，因此被解释成大火成岩省 (Zhang et al., 2017)。北澳 Galiwinku 岩墙群及 Derim–Derim 岩床同样也产出于广阔的地区 (Whelan et al., 2016)，很可能是地幔柱的产物。Zhang et al. (2017) 认为燕辽裂谷下马岭组与其上青白口系的不整合（蔚县上升）以及麦克

阿瑟盆地 Roper 群与其上寒武系之间的不整合代表 1.32 Ga 大火成岩省之前的抬升，很可能与奴那/哥伦比亚超大陆的裂解有关。

综上，两个盆地的相关区域均有同期并相似的基性和酸性岩浆侵入，以及火山作用相关的单元，这暗示两个区域的壳幔活动具有行为和属性的一致性。

（3）矿产资源

在燕辽裂谷蓟县系以及麦克阿瑟盆地 Nathan 群的白云岩中，发现有锰矿 (Fan et al., 1999; Ferenczi, 2001)（图 9.9）。锰矿均以不规则的透镜状或细脉状产出，并都出现在浅海沉积物中，也暗示盆地相同的沉积环境。

在这两个盆地中，也都发现有铁矿层（图 9.9）。麦克阿瑟盆地 Roper 群上部的 Sherwin 组由页岩、砂质泥岩以及砂岩组成，并夹有透镜状鲕粒到豆状的夹层，夹有中粒到粗粒鲕绿泥石菱铁矿 (Ferenczi, 2001)。铁矿由赤铁矿和/或针铁矿以及硅铁矿组成。鲕绿泥石及赤铁矿部分在成岩作用后由菱铁矿替代，产生硅质（燧石）胶结。在燕辽裂谷下马岭组的中部（1.40–1.35? Ga）发现有层状的菱铁矿并有少量赤铁矿 (Tang et al., 2018)。菱铁矿中含有小的赤铁矿包裹体，说明在早期成岩过程中发生了铁的置换 (Tang et al., 2018)。

（4）含烃潜力评估

在麦克阿瑟盆地麦克阿瑟群和 Roper 群中发现有几套烃源岩（图 9.9）(Ahmad et al., 2013)。其中，在~1.64 Ga 的地层中有较高的总有机碳含量（TOC；可达 8%) 以及较高的氢指数（HI），说明具有较高的成熟度 (Lee and Brocks, 2011)。Roper 群中部含 TOC 约 1–3%（可高达 8–12%），HI 变化较大 (Volk et al., 2003)。与此类似，燕辽裂谷地层也被用于评价含油潜力（图 9.9）。其中，长城系中部以及下马岭组 TOC 含量分别为 0.6–15%（平均 2%）及 3–21%（平均 5.2%）(Zhao et al., 2018).

综上，华北克拉通与北澳克拉通在~1.73–1.32 Ga 具有多维的地质相似性，包括燕辽裂谷和麦克阿瑟盆地的可对比性、岩浆作用、矿产资源等的相似性，暗示二者在该时期的亲缘性。同时，古地磁的重建形态与放射状岩墙群的重建比较吻合。上述古地磁分析与地质对比共同支持华北东北缘与澳大利亚西北缘长时间的相连。视极移曲线显示，在~1.32–1.21 Ga 两个陆块发生分离，可能对应于~1.32 Ga 大火成岩省的裂解事件，并与地层不整合吻合。

Wang et al. (2015a) 将华北 1.24–1.21 Ga 岩浆作用与劳伦、波罗地和圣弗朗

西斯科克拉通~1.27–1.21 Ga 的岩浆作用建立联系，认为它们来自同一地幔柱。该解释需要这些块体在~60 Myr 漂移通过同一热点 (Wang et al., 2015a)，与全球古地磁重建的古地理似乎不协调，尤其是在板块运动速度方面 (Pisarevsky et al., 2014a)。本文提出一个可能的解释：黎城大火成岩省可能是~1.32 Ga 燕辽地幔柱再次活动的产物。古地磁结果显示，~1.32 Ga 之后华北与北澳独立向北漂移，古地磁约束的运动暗示之前的地幔柱在~1.24–1.21 Ga 很可能位于华北的东南。而华北~1.32 Ga 和~1.24–1.21 Ga 岩浆作用有相似的 εNdt 值 (0–2; Peng et al., 2013; Wang et al., 2016b; Zhang et al., 2012a)，暗示可能有相似的岩浆源区。其稀土配分型式及蛛网图的差异（图 6.2）可能由不同的熔体深度、熔融程度或结晶分异程度引起。但是，由于缺乏其他地质的对比约束，目前难以判断~1.24–1.21 Ga 黎城大火成岩省是否作用于克拉通边缘。

第10章 结论及存在的问题

（1） 本研究通过斜锆石离子探针与热电离质谱高精度定年获得了华北克拉通部分岩墙的形成年龄（1233 ± 27 Ma、1206.7 ± 1.7 Ma、1214.0 ± 4.9 Ma 和 1236.3 ± 5.4 Ma）。

（2） 通过分析 1.24–1.21 Ga 基性侵入岩的岩石成因。认为该事件是由地幔柱引发的大火成岩省，并命名为黎城大火成岩省。

（3） 通过古地磁及岩石磁学分析，结合前人研究成果，本研究获得了华北克拉通~1.68 Ga 古地磁极（59.8°N，265.3°E，A_{95} = 3.3°），~1.24 Ga 古地磁极（2.6°N，165.1°E，A_{95} = 10.8°，9 条岩墙，通过烘烤检验）以及~1.21 Ga 虚地磁极（-23.0°N，92.5°E，A_{95} = 6.1°，1 条岩墙）。

（4） 通过对比澳大利亚陆块的古地磁极，本文认为华北与澳大利亚陆块在~1.78–1.32 Ga 具有亲缘性，在~1.21 Ga 处于分离状态。

（5） 华北燕辽裂谷地区与北澳麦克阿瑟盆地地区地层及古生物、岩浆作用、矿产资源、含油潜力等多方面的地质相似性，支持奴那/哥伦比亚超大陆时期华北东北部与澳大利亚西北部的亲缘性。

本研究综合古地磁研究及地质对比论证了华北与澳大利亚陆块在~1.78–1.32 Ga 期间的亲缘性，但未回答二者之间的亲缘方式，即二者是否通过造山作用相连接；如果是，则是何种方式的造山，与哪些造山带相关；如果不是，那二者之间如何关联。回答以上问题需要继续深入细致的研究，这也是认识前寒武纪构造体制的关键问题。另外，本研究提到在~1.32 Ga 期间发生裂解，有地层不整合作为呼应，但对不整合性质的研究依然薄弱，如何科学可靠的分析不整合的性质是值得思考的问题。此外，对~1.24 Ga 岩墙的烘烤检验仍然存在瑕疵，本文并不能说明未烘烤的围岩的剩磁是原生剩磁，或说明未烘烤围岩的剩磁比岩墙剩磁获得的早。对于其他时期的古地磁，仍需进一步的工作。

参考文献

安徽省地质矿产局区域地质调查队, 1985. 安徽省地层志前寒武系分册. 安徽科学技术出版社, 合肥.

曹国权, 1996. 鲁西早前寒武纪地质. 地质出版社, 北京.

陈曼云, 1990. 高级变质区变基性岩脉群的研究——以太平寨—金厂峪地区为例. 地质学报 66, 157–169.

陈衍景, 富士谷, 强立志, 1992. 评熊耳群和西洋河群形成的构造背景. 地质论评 38, 325–333.

崔敏利, 张宝林, 彭澎, 张连昌, 沈晓丽, 郭志华, 黄雪飞, 2010. 豫西崤山早元古代中酸性侵入岩锆石/斜锆石 U–Pb 测年及其对熊耳火山岩系时限的约束. 岩石学报 26, 1541–1549.

丁继凯, 2017. 华北克拉通~1.22 Ga 基性岩墙古地磁学和年代学研究及其对超大陆演化的意义. 中国地质大学（北京）, p. 112.

范文博, 2015. 华北克拉通中元古代下马岭组地质特征及研究进展——下马岭组研究百年回眸. 地质论评 61, 1383–1406.

高林志, 张传恒, 史晓颖, 宋彪, 王自强, 刘耀明, 2008a. 华北古陆下马岭组归属中元古界的锆石 SHRIMP 年龄新证据. 科学通报, 2617–2623.

高林志, 张传恒, 史晓颖, 周洪瑞, 王自强, 2007. 华北青白口系下马岭组凝灰岩锆石 SHRIMP U–Pb 定年. 地质通报 26, 249–255.

高林志, 张传恒, 尹崇玉, 史晓颖, 王自强, 刘耀明, 刘鹏举, 唐烽, 宋彪, 2008b. 华北古陆中、新元古代年代地层框架 SHRIMP 锆石年龄新依据. 地球学报 29, 366–376.

郭敬辉, 翟明国, 张毅刚, 李永刚, 阎月华, 张雯华, 1993. 怀安蔓菁沟早前寒武纪高压麻粒岩混杂岩带地质特征、岩石学和同位素年代学. 岩石学报 9, 329–341.

河北省地质矿产局, 1989. 河北省北京市天津市区域地质志. 地质出版社, 北京.

贺高品, 卢良兆, 叶慧文, 靳是琴, 叶挺松, 1991. 冀东和内蒙古东南部早前寒武纪变质作用演化. 吉林大学出版社, 长春.

河南省地质矿产局, 1989. 河南省区域地质志. 地质出版社, 北京.

胡波, 2011. 华北克拉通古元古代末—新元古代沉积盆地的时空格架及地质事件——来自碎屑锆石 U–Pb 年代学的制约. 中国科学院地质与地球物理研究所博士后出站报告, 北京.

胡俊良, 赵太平, 徐勇航, 陈伟, 2007. 华北克拉通大红峪组高钾火山岩的地球化学特征及其岩石成因. 矿物岩石 27, 70–77.

贾承造, 1985. 熊耳群火山岩系岩石地球化学特征及其大地构造意义. 河南国土资源 2, 39–43.

江苏省地质矿产局, 1984. 江苏省及上海市区域地质志. 地质出版社, 北京.

辽宁省地质矿产局, 1989. 辽宁省区域地质志. 地质出版社, 北京.

李怀坤, 陆松年, 李惠民, 孙立新, 相振群, 耿建珍, 周红英, 2009. 侵入下马岭组的基性岩床的锆石和斜锆石 U–Pb 精确定年——对华北中元古界地层划分方案的制约. 地质通报 28, 1396–1404.

李怀坤, 苏文博, 周红英, 相振群, 田辉, 杨立公, Huff, W.D., Ettensohn, F., 2014. 中–新元古界标准剖面蓟县系首获高精度年龄制约——蓟县剖面雾迷山组和铁岭组斑脱岩锆石 SHRIMPU–Pb 同位素定年研究. 岩石学报 30, 2999–3012.

李怀坤, 朱士兴, 相振群, 苏文博, 陆松年, 周红英, 耿建珍, 李生, 杨锋杰, 2010. 北京延庆高于庄组凝灰岩的锆石 U–Pb 定年研究及其对华北北部中元古界划分新方案的进一步约束. 岩石学报 26, 2131–2140.

陆松年, 李惠民, 1991. 蓟县长城系大红峪组火山岩的单颗粒锆石 U–Pb 法准确定年. 地球学报 12, 137–146.

潘小青, 沈忠悦, 董传万, 陈汉林, 程晓敢, 杨树锋, 张志亮, 2012. 海南万宁辉长岩体及辉绿岩脉侵位机制的磁组构证据. 科学通报 57, 2086–2093.

裴福萍, 叶轶凡, 王枫, 曹花花, 路思明, 杨德彬, 2013. 吉林通化地区中元古代辉绿岩墙的发现及其地质意义. 吉林大学学报 43, 110–118.

彭澎，2007. 华北巨型基性岩墙群和熊耳火山岩系：一个 1780 Ma 地幔柱成因大岩浆岩省？中国科学院地质与地球物理研究所博士后出站报告, 北京.

彭澎, 2016. 华北陆块前寒武纪岩墙群及相关岩浆岩地质图说明书. 科学出版社, 北京.

彭澎, 王欣平, 周小童, 王冲, 孙风波, 苏向东, 陈亮, 郭敬辉, 翟明国, 2017. 8.1 亿年千里山基性岩墙群的厘定及其对华北克拉通西部地质演化的启示. 岩石学报 34, 1191–1203.

彭澎, 翟明国, 张华锋, 赵太平, 倪志耀, 2004. 华北克拉通 1.8Ga 镁铁质岩墙群的地球化学特征及其地质意义: 以晋冀蒙交界地区为例. 岩石学报 20, 439–456.

山东省第四地质矿产勘查院, 2003. 山东省区域地质. 山东省地图出版社, 济南.

宋述光, 1990. 冀东太平寨地区变质岩脉群研究. 长春地质学院学报, 63–70.

石敏, 冯庆来, 朱士兴, 2014. 华北中元古代燕山盆地生物群演化及其与地质事件的耦合关系. 中国科学:地球科学, 1124–1141.

孙枢, 张国伟, 陈志明, 1985. 华北断块区南部前寒武纪地质演化. 冶金工业出版社, 北京.

苏文博, 李怀坤, 徐莉, 贾松海, 耿建珍, 周红英, 王志宏, 蒲含勇, 2012. 华北克拉通南缘洛峪群–汝阳群属于中元古界长城系——河南汝州洛峪口组层凝灰岩锆石 LA–MC–ICPMS U–Pb 年龄的直接约束. 地质调查与研究 35, 96–108.

王冲, 彭澎, 王欣平, 李秋立, 徐希阳, 杨书艳, 2016. 华北太行岩墙群斜锆石生长世代和 U–Pb 年龄及其对岩浆演化的启示. 岩石学报 32, 646–658.

汪校锋, 2015. 华北南缘中—新元古代地层年代学研究及其地质意义. 中国地质大学, p. 120.

万渝生, 刘敦一, 董春艳, A, N., SA, W., 王伟, 颉颃强, 殷小艳, 周红英, 2009. 中国最老岩石和

锆石. 岩石学报 25, 1793–1807.

魏春景, 2018. 冀东地区新太古代麻粒岩相变质作用及其大地构造意义. 岩石学报 34, 895–912.

温献德, 1997. 华北北部中、上元估计的大陆裂谷模式和地层划分. 前寒武纪研究进展 20, 21–28.

吴怀春, 2005. 华北蓟县地区中元古界古地磁研究及其古大陆再造意义. 中国地质大学(北京) , p. 133.

相振群, 2014. 华北克拉通中元古代岩浆事件群与成矿作用. 中国地质大学（北京）, p. 227.

相振群, 李怀坤, 陆松年, 周红英, 李惠民, 王惠初, 陈志宏, 牛健, 2012. 泰山地区古元古代末期基性岩墙形成时代厘定——斜锆石 U–Pb 精确定年. 岩石学报 28, 2831–2842.

杨进辉, 吴福元, 柳小明, 谢烈文, 2005. 北京密云环斑花岗岩锆石 U–Pb 年龄和 Hf 同位素及其地质意义. 岩石学报 21, 1633–1644.

杨正赫, 彭澎, 郑哲寿, 朴雄, 文正根, 金哲贤, 苟贤哲, 2016. 朝鲜平南盆地古元古界–下古生界沉积岩碎屑锆石年龄谱对比及意义. 岩石学报 32, 3155–3179.

阎玉忠, 刘志礼, 1998. 中国北方燕山盆地长城纪生物群落和古环境关系探讨. 微体古生物学报, 249–266.

翟明国, 2009. 华北克拉通两类早前寒武纪麻粒岩(HT–HP 和 HT–UHT)及其相关问题. 岩石学报 25, 1753–1771.

翟明国, 2011. 克拉通化与华北陆块的形成. 中国科学:地球科学 41, 1037–1046.

翟明国, 2013. 华北前寒武纪成矿系统与重大地质事件的联系. 岩石学报 29, 1759–1773.

翟明国, 胡波, 彭澎, 赵太平, 2014. 华北中—新元古代的岩浆作用与多期裂谷事件. 地学前缘 21, 100–119.

翟明国, 郭敬辉, 李永刚, 闫月华, 张雯华, 李江海, 1995. 华北太古宙退变质榴辉岩的发现及其含义. 科学通报 40, 1590–1590.

翟明国, 郭敬辉, 阎月华, 韩秀伶, 李永刚, 1992. 中国华北太古宙高压基性麻粒岩的发现及初步研究. 中国科学, 1325–1330.

翟明国, 郭敬辉, 阎月华, 李永刚, 李江海, 张雯华, 1996. 太古宙克拉通型下地壳剖面：华北怀安–丰镇–尚义的麻粒岩–角闪岩系. 岩石学报 12, 222–238.

翟明国, 彭澎, 2007. 华北克拉通古元古代构造事件. 岩石学报 23, 2665–2682.

张连昌, 翟明国, 万渝生, 郭敬辉, 代堰锫, 王长乐, 刘利, 2012. 华北克拉通前寒武纪 BIF 铁矿研究:进展与问题. 岩石学报 28, 3431–3445.

张拴宏, 赵越, 叶浩, 胡健民, 吴飞, 2013. 燕辽地区长城系串岭沟组及团山子组沉积时代的新制约. 岩石学报 29, 2481–2490.

赵国春, 2009. 华北克拉通基底主要构造单元变质作用演化及其若干问题讨论. 岩石学报 25, 1772–1792.

赵太平, 陈福坤, 翟明国, 夏斌, 2004. 河北大庙斜长岩杂岩体锆石 U–Pb 年龄及其地质意义. 岩石学报 20, 685–690.

赵太平, 徐勇航, 翟明国, 2007. 华北陆块南部元古宙熊耳群火山岩的成因与构造环境：事实与争议. 高校地质学报 13, 191–206.

赵太平, 周美夫, 金成伟, 关鸿, 李惠民, 2001. 华北陆块南缘熊耳群形成时代讨论. 地质科学 36, 326–334.

赵文浩, 1988. 冀东地区变质基性岩墙群的基本特征. 长春地质学院学报, 401–408.

周志广, 王果胜, 张达, 谷永昌, 朱卫平, 柳长峰, 赵孝旗, 胡萌萌, 2016. 内蒙古四子王旗地区侵入白云鄂博群辉长岩的年龄及其对白云鄂博群时代的约束. 岩石学报 32, 1809–1822.

Ahmad, M., Dunster, J., Munson, T., 2013. Chapter 15: McArthur Basin: in Ahmad M and Munson TJ (compilers). Geology and mineral resources of the Northern Territory. Northern Territory Geological Survey, Special Publication 5.

Betts, P.G., Giles, D., Schaefer, B.F., 2008. Comparing 1800–1600Ma accretionary and basin processes in Australia and Laurentia: Possible geographic connections in Columbia. Precambrian Research 166, 81–92.

Bleeker, W., Ernst, R., 2006. Short–lived mantle generated magmatic events and their dyke swarms: the key unlocking Earth's paleogeographic record back to 2.6 Ga. Dyke swarms–time markers of crustal evolution, 3–26.

Boger, S.D., 2011. Antarctica — Before and after Gondwana. Gondwana Research 19, 335–371.

Borradaile, G., 2014. Understanding geology through maps. Elsevier.

Buchan, K.L., 2007. Baked contact test, in: Gubbins, D.H.–B.E. (Ed.), Encyclopedia of Geomagnetism Paleomagnetism. Springer, Dordrecht, the Netherlands, p. 35–39.

Buchan, K.L., 2013. Key paleomagnetic poles and their use in Proterozoic continent and supercontinent reconstructions: A review. Precambrian Research 238, 93–110.

Buchan, K.L., Mortensen, J.K., Card, K.D., 1993. Northeast–trending Early Proterozoic dykes of southern Superior Province: multiple episodes of emplacement recognized from integrated paleomagnetism and U–Pb geochronology. Canadian Journal of Earth Sciences 30, 1286–1296.

Buchan, K.L., Schwarz, E.J., 1981. Uplift estimated from remanent magnetization: Munro area of Superior Province since 2150 Ma ago. Canadian Journal of Earth Sciences 18, 1164–1173.

Burke, K., Steinberger, B., Torsvik, T.H., Smethurst, M.A., 2008. Plume Generation Zones at the margins of Large Low Shear Velocity Provinces on the core–mantle boundary. Earth and Planetary Science Letters 265, 49–60.

Butler, R.F., 1992. Paleomagnetism: magnetic domains to geologic terranes. Blackwell Scientific Publications Boston.

Cawood, P.A., Korsch, R.J., 2008. Assembling Australia: Proterozoic building of a continent. Precambrian Research 166, 1–35.

Cawood, P.A., Pisarevsky, S.A., 2017. Laurentia–Baltica–Amazonia relations during Rodinia

assembly. Precambrian Research 292, 386–397.

Cawood, P.A., Strachan, R.A., Pisarevsky, S.A., Gladkochub, D.P., Murphy, J.B., 2016. Linking collisional and accretionary orogens during Rodinia assembly and breakup: Implications for models of supercontinent cycles. Earth and Planetary Science Letters 449, 118–126.

Cederberg, J., Söderlund, U., Oliveira, E.P., Ernst, R.E., Pisarevsky, S.A., 2016. U–Pb baddeleyite dating of the Proterozoic Pará de Minas dyke swarm in the São Francisco craton (Brazil)–implications for tectonic correlation with the Siberian, Congo and North China cratons. Gff 138, 219–240.

Chen, L., Huang, B., Yi, Z., Zhao, J., Yan, Y., 2013. Paleomagnetism of ca. 1.35Ga sills in northern North China Craton and implications for paleogeographic reconstruction of the Mesoproterozoic supercontinent. Precambrian Research 228, 36–47.

Chen, Y., Chen, W., Li, Q., Santosh, M., Li, J., 2019. Discovery of the Huronian Glaciation Event in China: Evidence from glacigenic diamictites in the Hutuo Group in Wutai Shan. Precambrian Research 320, 1–12.

Condie, K., Pisarevsky, S.A., Korenaga, J., Gardoll, S., 2015. Is the rate of supercontinent assembly changing with time? Precambrian Research 259, 278–289.

Condie, K.C., 2002. Breakup of a Paleoproterozoic Supercontinent. Gondwana Research 5, 41–43.

Cox, K.G., 2013. The interpretation of igneous rocks. Springer Science & Business Media.

Dal Zilio, L., 2018. Subduction–driven Earth machine. Nature Geoscience 11, 229–229.

Dal Zilio, L., Faccenda, M., Capitanio, F., 2018. The role of deep subduction in supercontinent breakup. Tectonophysics 746, 312–324.

Dalziel, I.W.D., 1991. Pacific margins of Laurentia and East Antarctica–Australia as a conjugate rift pair: Evidence and implications for an Eocambrian supercontinent. Geology 19, 598–601.

Day, R., Fuller, M., Schmidt, V.A., 1977. Hysteresis properties of titanomagnetites: Grain–size and compositional dependence. Physics of the Earth and Planetary Interiors 13, 260–267.

Deng, X., Peng, T., Zhao, T., 2016a. Geochronology and geochemistry of the late Paleoproterozoic aluminous A–type granite in the Xiaoqinling area along the southern margin of the North China Craton: Petrogenesis and tectonic implications. Precambrian Research 285, 127–146.

Deng, X., Zhao, T., Peng, T., 2016b. Age and geochemistry of the early Mesoproterozoic A-type granites in the southern margin of the North China Craton: Constraints on their petrogenesis and tectonic implications. Precambrian Research 283, 68–88.

Diwu, C., Sun, Y., Wilde, S.A., Wang, H., Dong, Z., Zhang, H., Wang, Q., 2013. New evidence for ~4.45 Ga terrestrial crust from zircon xenocrysts in Ordovician ignimbrite in the North Qinling Orogenic Belt, China. Gondwana Research 23, 1484–1490.

Dunlop, D.J., 2002. Theory and application of the Day plot (Mrs/Ms versus Hcr/Hc) 1. Theoretical curves and tests using titanomagnetite data. Journal of Geophysical Research: Solid Earth 107, EPM 4–1–EPM 4–22.

Dunlop, J.D., Özdemir, Ö., 1997. Rock Magnetism: Fundamentals and frontiers. Cambridge

University Press, p. 1–573.

Dziewonski, A.M., 1984. Mapping the lower mantle: determination of lateral heterogeneity in P velocity up to degree and order 6. Journal of Geophysical Research: Solid Earth 89, 5929–5952.

Ernst, R., Grosfils, E., Mege, D., 2001. Giant dike swarms: Earth, venus, and mars. Annual Review of Earth Planetary Sciences 29, 489–534.

Ernst, R., Head, J., Parfitt, E., Grosfils, E., Wilson, L., 1995. Giant radiating dyke swarms on Earth and Venus. Earth–Science Reviews 39, 1–58.

Ernst, R.E., 2014. Large igneous provinces. Cambridge University Press.

Ernst, R.E., Baragar, W.R.A., 1992. Evidence from magnetic fabric for the flow pattern of magma in the Mackenzie giant radiating dyke swarm. Nature 356, 511–513.

Ernst, R.E., Hamilton, M.A., Söderlund, U., Hanes, J.A., Gladkochub, D.P., Okrugin, A.V., Kolotilina, T., Mekhonoshin, A.S., Bleeker, W., LeCheminant, A.N., Buchan, K.L., Chamberlain, K.R., Didenko, A.N., 2016. Long–lived connection between southern Siberia and northern Laurentia in the Proterozoic. Nature Geoscience 9, 464–469.

Ernst, R.E., Youbi, N., 2017. How Large Igneous Provinces affect global climate, sometimes cause mass extinctions, and represent natural markers in the geological record. Palaeogeography, Palaeoclimatology, Palaeoecology 478, 30–52.

Evans, D., 2002. True polar wander and supercontinents. Tectonophysics 362, 303–320.

Evans, D., Li, Z.X., Murphy, J., 2016a. Four-dimensional context of Earth's supercontinents. Geological Society, London, Special Publications 424, SP424. 412.

Evans, D.A., 2006. Proterozoic low orbital obliquity and axial-dipolar geomagnetic field from evaporite palaeolatitudes. Nature 444, 51–55.

Evans, D.A.D., 2009. The palaeomagnetically viable, long-lived and all-inclusive Rodinia supercontinent reconstruction. Geological Society, London, Special Publications 327, 371–404.

Evans, D.A.D., Mitchell, R.N., 2011. Assembly and breakup of the core of Paleoproterozoic–Mesoproterozoic supercontinent Nuna. Geology 39, 443–446.

Evans, D.A.D., Trindade, R.I.F., Catelani, E.L., D'Agrella-Filho, M.S., Heaman, L.M., Oliveira, E.P., Söderlund, U., Ernst, R.E., Smirnov, A.V., Salminen, J.M., 2016b. Return to Rodinia? Moderate to high palaeolatitude of the São Francisco/Congo craton at 920 Ma. Geological Society, London, Special Publications 424, 167–190.

Evans, D.A.D., Veselovsky, R.V., Petrov, P.Y., Shatsillo, A.V., Pavlov, V.E., 2016c. Paleomagnetism of Mesoproterozoic margins of the Anabar Shield: A hypothesized billion-year partnership of Siberia and northern Laurentia. Precambrian Research 281, 639–655.

Fan, D., Yang, P., Wang, R., 1999. Characteristics and origin of the middle Proterozoic Dongshuichang chambersite deposit, Jixian, Tianjin, China. Ore Geology Reviews 15, 15–29.

Ferenczi, P., 2001. Iron ore, manganese and bauxite deposits of the Northern Territory. Northern

Territory Geological Survey.

Floyd, P.A., Winchester, J.A., 1975. Magma type and tectonic setting discrimination using immobile elements. Earth and Planetary Science Letters 27, 211-218.

Fu, X., Zhang, S., Li, H., Ding, J., Li, H., Yang, T., Wu, H., Yuan, H., Lv, J., 2015. New paleomagnetic results from the Huaibei Group and Neoproterozoic mafic sills in the North China Craton and their paleogeographic implications. Precambrian Research 269, 90–106.

Giles, D., Betts, P.G., Aillères, L., Hulscher, B., Hough, M., Lister, G.S., 2006. Evolution of the Isan Orogeny at the southeastern margin of the Mt Isa Inlier. Australian Journal of Earth Sciences 53, 91–108.

Goodge, J.W., Vervoort, J.D., Fanning, C.M., Brecke, D.M., Farmer, G.L., Williams, I.S., Myrow, P.M., DePaolo, D.J., 2008. A Positive Test of East Antarctica–Laurentia Juxtaposition Within the Rodinia Supercontinent. 321, 235–240.

Halls, H., 2008. The importance of integrating paleomagnetic studies of Proterozoic dykes with U–Pb geochronology and geochemistry. Indian Dyke: Geochemistry, Geophysics and Geochronology, 19–40.

Halls, H.C., Li, J., Davis, D., Hou, G., Zhang, B., Qian, X., 2000. A precisely dated Proterozoic palaeomagnetic pole from the North China craton, and its relevance to palaeocontinental reconstruction. Geophysical Journal International 143, 185–203.

Hastie, A.R., Mitchell, S.F., Kerr, A.C., Minifie, M.J., Millar, I.L., 2011. Geochemistry of rare high-Nb basalt lavas: Are they derived from a mantle wedge metasomatised by slab melts? Geochimica et Cosmochimica Acta 75, 5049-5072.

Hatcher, R.D., Jr., 2010. The Appalachian orogen: A brief summary, in: Tollo, R.P., Bartholomew, M.J., Hibbard, J.P., Karabinos, P.M. (Eds.), From Rodinia to Pangea: The Lithotectonic Record of the Appalachian Region. Geological Society of America.

He, Y., Zhao, G., Sun, M., Wilde, S.A., 2008. Geochemistry, isotope systematics and petrogenesis of the volcanic rocks in the Zhongtiao Mountain: An alternative interpretation for the evolution of the southern margin of the North China Craton. Lithos 102, 158–178.

He, Y., Zhao, G., Sun, M., Xia, X., 2009. SHRIMP and LA–ICP–MS zircon geochronology of the Xiong'er volcanic rocks: Implications for the Paleo–Mesoproterozoic evolution of the southern margin of the North China Craton. Precambrian Research 168, 213–222.

Heaman, L.M., LeCheminant, A.N., 1993. Paragenesis and U–Pb systematics of baddeleyite (ZrO2). Chemical Geology 110, 95–126.

Hoffman, P., 1997. Tectonic genealogy of North America, in: van der Pluijm, B.A., Marshak, S. (Ed.), Earth structure: An introduction to structural geology. McGraw-Hill, New York, pp. 459–464.

Hoffman, P.F., 1991. Did the breakout of Laurentia turn Gondwanaland inside-out? Science 252, 1409–1412.

Hoffman, P.F., 1999. The break-up of Rodinia, birth of Gondwana, true polar wander and the

snowball Earth. Journal of African Earth Sciences 28, 17–33.

Hou, G., Santosh, M., Qian, X., Lister, G.S., Li, J., 2008. Configuration of the Late Paleoproterozoic supercontinent Columbia: Insights from radiating mafic dyke swarms. Gondwana Research 14, 395–409.

Hu, B., Zhai, M., Li, T., Li, Z., Peng, P., Guo, J., Kusky, T.M., 2012. Mesoproterozoic magmatic events in the eastern North China Craton and their tectonic implications: Geochronological evidence from detrital zircons in the Shandong Peninsula and North Korea. Gondwana Research 22, 828–842.

Hu, G., Zhao, T., Zhou, Y., 2014a. Depositional age, provenance and tectonic setting of the Proterozoic Ruyang Group, southern margin of the North China Craton. Precambrian Research 246, 296–318.

Hu, J., Gong, W., Wu, S., Liu, Y., Liu, S., 2014b. LA–ICP–MS zircon U–Pb dating of the Langshan Group in the northeast margin of the Alxa block, with tectonic implications. Precambrian Research 255, 756–770.

Huston, D.L., Logan, G.A., 2004. Barite, BIFs and bugs: evidence for the evolution of the Earth's early hydrosphere. Earth and Planetary Science Letters 220, 41–55.

Idnurm, M., 2000. Towards a high resolution Late Palaeoproterozoic–earliest Mesoproterozoic apparent polar wander path for northern Australia. Australian Journal of Earth Sciences 47, 405–429.

Idnurm, M., Giddings, J., Plumb, K., 1995. Apparent polar wander and reversal stratigraphy of the Palaeo–Mesoproterozoic southeastern McArthur Basin, Australia. Precambrian Research 72, 1–41.

Jaffey, A., Flynn, K., Glendenin, L., Bentley, W.t., Essling, A., 1971. Precision measurement of half–lives and specific activities of U 235 and U 238. Physical Review C 4, 1889.

Javaux, E.J., Lepot, K., 2018. The Paleoproterozoic fossil record: Implications for the evolution of the biosphere during Earth's middle-age. Earth-Science Reviews 176, 68–86.

Johansson, Å., 2009. Baltica, Amazonia and the SAMBA connection—1000 million years of neighbourhood during the Proterozoic? Precambrian Research 175, 221–234.

Julian, B., Foulger, G., Hatfield, O., Jackson, S., Simpson, E., Einbeck, J., Moore, A., 2015. Hotspots in hindsight. The Geological Society of America Special Paper 514, 105–121.

Karlstrom, K.E., Harlan, S.S., Williams, M.L., McLelland, J., Geissman, J.W., Ahall, K.–I., 1999. Refining Rodinia: Geologic evidence for the Australia–western US connection in the Proterozoic. GSA Today 9, 1–7.

Kim, S.W., Cho, D.-L., Lee, S.-B., Kwon, S., Park, S.-I., Santosh, M., Kee, W.-S., 2018. Mesoproterozoic magmatic suites from the central-western Korean Peninsula: Imprints of Columbia disruption in East Asia. Precambrian Research 306, 155–173.

Kirscher, U., Liu, Y., Li, Z.X., Mitchell, R.N., Pisarevsky, S.A., Denyszyn, S., Nordsvan, A., 2018a. Paleomagnetism of the Hart Dolerite (Kimberley, Western Australia) – a two-stage assembly

of the supercontinent Nuna? Precambrian Research. https://doi.org/10.1016/j.precamres.-2018.12.026

Kirscher, U., Mitchell, R., Liu, Y., Li, Z., Cox, G., Nordsvan, A., Wang, C., Pisarevsky, S., 2018b. Long lived supercontinent Nuna-updated paleomagnetic constraints from Australia, AGU Fall Meeting Abstracts.

Kirschvink, J., 1980. The least-squares line and plane and the analysis of palaeo-magnetic data. Geophysical Journal of the Royal Astronomical Society 62, 699–718.

Kong, F., Yuan, X., Zhou, C., 2011. Paleoproterozoic glaciation: Evidence from carbon isotope record of the Hutuo Group, Wutai Mountain area of Shanxi Province, China. Chinese Science Bulletin 56, 2922–2930.

Kusky, T., Li, J., Santosh, M., 2007. The Paleoproterozoic North Hebei Orogen: North China craton's collisional suture with the Columbia supercontinent. Gondwana Research 12, 4–28.

Kusky, T.M., Li, J., 2003. Paleoproterozoic tectonic evolution of the North China Craton. Journal of Asian Earth Sciences 22, 383–397.

Lamb, D., Awramik, S., Chapman, D., Zhu, S., 2009. Evidence for eukaryotic diversification in the ~1800 million-year-old Changzhougou Formation, North China. Precambrian Research 173, 93–104.

Lan, Z., Li, X., Chen, Z.Q., Li, Q., Hofmann, A., Zhang, Y., Zhong, Y., Liu, Y., Tang, G., Ling, X., Li, J., 2014. Diagenetic xenotime age constraints on the Sanjiaotang Formation, Luoyu Group, southern margin of the North China Craton: Implications for regional stratigraphic correlation and early evolution of eukaryotes. Precambrian Research 251, 21–32.

Lee, C., Brocks, J.J., 2011. Identification of carotane breakdown products in the 1.64 billion year old Barney Creek Formation, McArthur Basin, northern Australia. Organic geochemistry 42, 425–430.

Li, Q.-L., Li, X.-H., Liu, Y., Tang, G.-Q., Yang, J.-H., Zhu, W.-G., 2010. Precise U–Pb and Pb–Pb dating of Phanerozoic baddeleyite by SIMS with oxygen flooding technique. Journal of Analytical Atomic Spectrometry 25, 1107–1113.

Li, T., Zhai, M., Peng, P., Chen, L., Guo, J., 2010. Ca. 2.5 billion year old coeval ultramafic-mafic and syenitic dykes in Eastern Hebei: Implications for cratonization of the North China Craton. Precambrian Research 180, 143–155.

Li, X.H., Liu, Y., Li, Q.L., Guo, C.H., Chamberlain, K.R., 2009. Precise determination of Phanerozoic zircon Pb/Pb age by multicollector SIMS without external standardization. Geochemistry, Geophysics, Geosystems 10.

Li, Y., Peng, P., Wang, X., Wang, H., 2015. Nature of 1800–1600Ma mafic dyke swarms in the North China Craton: Implications for the rejuvenation of the sub–continental lithospheric mantle. Precambrian Research 257, 114–123.

Li, Z.X., 2000. Palaeomagnetic evidence for unification of the North and West Australian cratons by ca. 1.7 Ga: new results from the Kimberley Basin of northwestern Australia. Geophysical

Journal International 142, 173–180.

Li, Z.X., Zhang, L., Powell, C.M., 1995. South China in Rodinia: Part of the missing link between Australia–East Antarctica and Laurentia? Geology 23, 407–410.

Li, Z.X., Zhong, S., 2009. Supercontinent–superplume coupling, true polar wander and plume mobility: Plate dominance in whole–mantle tectonics. Physics of the Earth and Planetary Interiors 176, 143–156.

Li, Z.X., Bogdanova, S.V., Collins, A.S., Davidson, A., De Waele, B., Ernst, R.E., Fitzsimons, I.C.W., Fuck, R.A., Gladkochub, D.P., Jacobs, J., Karlstrom, K.E., Lu, S., Natapov, L.M., Pease, V., Pisarevsky, S.A., Thrane, K., Vernikovsky, V., 2008. Assembly, configuration, and break-up history of Rodinia: A synthesis. Precambrian Research 160, 179–210.

Li, Z.X., Evans, D.A.D., 2010. Late Neoproterozoic 40 intraplate rotation within Australia allows for a tighter-fitting and longer-lasting Rodinia. Geology 39, 39–42.

Li, Z.X., Mitchell, R.N., Spencer, C.J., Ernst, R., Pisarevsky, S., Kirscher, U., Murphy, J.B., 2019. Decoding Earth's rhythms: Modulation of supercontinent cycles by longer superocean episodes. Precambrian Research 323, 1–5.

Li, Z.X., Zhang, L., Powell, C.M., 1996. Positions of the East Asian cratons in the Neoproterozoic supercontinent Rodinia. Australian Journal of Earth Sciences 43, 593–604.

Liu, C., Zhao, G., Liu, F., 2014. Detrital zircon U–Pb, Hf isotopes, detrital rutile and whole–rock geochemistry of the Huade Group on the northern margin of the North China Craton: Implications on the breakup of the Columbia supercontinent. Precambrian Research 254, 290–305.

Liu, C., Zhao, G., Liu, F., Shi, J., 2017a. Detrital zircon U–Pb and Hf isotopic and whole-rock geochemical study of the Bayan Obo Group, northern margin of the North China Craton: Implications for Rodinia reconstruction. Precambrian Research 303, 372–391.

Liu, C., Zhao, G., Liu, F., Shi, J., 2017b. Late Precambrian tectonic affinity of the Alxa block and the North China Craton: Evidence from zircon U–Pb dating and Lu–Hf isotopes of the Langshan Group. Precambrian Research 326, 312–332.

Liu, D., Wilde, S.A., Wan, Y., Wu, J., Zhou, H., Dong, C., Yin, X., 2008. New U–Pb and Hf isotopic data confirm Anshan as the oldest preserved segment of the North China Craton. American Journal of Science 308, 200–231.

Liu, D.Y., Wu, J.S., Shen, Q.H., Nutman, A.P., Compston, W., 1992. Remnants of ≥3800 Ma crust in the Chinese part of the Sino-Korean craton. Geology 20, 339–342.

Liu, X., Li, S., Li, X., Zhao, S., Wang, T., Yu, S., Dai, L., Zhou, Z., Guo, R., 2018a. Detrital zircon U–Pb geochronology and provenance of the Sanxiatian Formation (Huade Group) in the North China Craton: Implications for the breakup of the Columbia supercontinent. Precambrian Research 310, 305–319.

Liu, Y., Li, Z.X., Pisarevsky, S.A., Kirscher, U., Mitchell, R.N., Stark, J.C., Clark, C., Hand, M., 2018b. First Precambrian palaeomagnetic data from the Mawson Craton (East Antarctica) and

tectonic implications. Scientific reports 8, 16403–16403.

Lowrie, W., 1990. Identification of ferromagnetic minerals in a rock by coercivity and unblocking temperature properties. Geophysical research letters 17, 159–162.

Lu, S., Zhao, G., Wang, H., Hao, G., 2008. Precambrian metamorphic basement and sedimentary cover of the North China Craton: a review. Precambrian Research 160, 77–93.

Lurcock, P.C., Wilson, G.S., 2012. PuffinPlot: A versatile, user-friendly program for paleomagnetic analysis. Geochemistry, Geophysics, Geosystems 13, http://doi.org.10.1029/2012gc004098

Martin, A.P., Condon, D.J., Prave, A.R., Lepland, A., 2013. A review of temporal constraints for the Palaeoproterozoic large, positive carbonate carbon isotope excursion (the Lomagundi–Jatuli Event). Earth-Science Reviews 127, 242–261.

May, P.R., 1971. Pattern of Triassic-Jurassic Diabase Dikes around the North Atlantic in the Context of Predrift Position of the Continents. GSA Bulletin 82, 1285–1292.

McKerrow, W.S., Mac Niocaill, C., Dewey, J.F., 2000. The Caledonian Orogeny redefined. 157, 1149–1154.

McMenamin, M.A., McMenamin, D.L.S., 1990. The emergence of animals: the Cambrian breakthrough. Columbia University Press.

Meert, J.G., 2012. What's in a name? The Columbia (Paleopangaea/Nuna) supercontinent. Gondwana Research 21, 987–993.

Meert, J.G., 2014. Strange attractors, spiritual interlopers and lonely wanderers: The search for pre-Pangean supercontinents. Geoscience Frontiers 5, 155–166.

Meert, J.G., Santosh, M., 2017. The Columbia supercontinent revisited. Gondwana Research 50, 67–83.

Meng, E., Liu, F. L., Liu, P.H., Liu, C.H., Yang, H., Wang, F., Shi, J.R., Cai, J., 2014. Petrogenesis and tectonic significance of Paleoproterozoic meta-mafic rocks from central Liaodong Peninsula, northeast China: Evidence from zircon U–Pb dating and in situ Lu–Hf isotopes, and whole–rock geochemistry. Precambrian Research 247, 92–109.

Meng, Q.R., Wei, H.H., Qu, Y.Q., Ma, S.X., 2011. Stratigraphic and sedimentary records of the rift to drift evolution of the northern North China craton at the Paleo- to Mesoproterozoic transition. Gondwana Research 20, 205–218.

Merdith, A.S., Collins, A.S., Williams, S.E., Pisarevsky, S., Foden, J.D., Archibald, D.B., Blades, M.L., Alessio, B.L., Armistead, S., Plavsa, D., Clark, C., Müller, R.D., 2017. A full-plate global reconstruction of the Neoproterozoic. Gondwana Research 50, 84–134.

Merdith, A.S., Williams, S.E., Brune, S., Collins, A.S., Müller, R.D., 2019. Rift and plate boundary evolution across two supercontinent cycles. Global and Planetary Change 173, 1–14.

Mitchell, R.N., Kilian, T.M., Evans, D.A., 2012. Supercontinent cycles and the calculation of absolute palaeolongitude in deep time. Nature 482, 208–211.

Moores, 1991. Southwest U.S.–East Antarctic (SWEAT) connection A hypothesis. Geology 19, 425–428.

Mulder, J.A., Karlstrom, K.E., Halpin, J.A., Merdith, A.S., Spencer, C.J., Berry, R.F., McDonald, B., 2018. Rodinian devil in disguise: Correlation of 1.25–1.10 Ga strata between Tasmania and Grand Canyon. Geology 46, 991–994.

Murphy, J.B., Nance, R.D., 2003. Do supercontinents introvert or extrovert?: Sm–Nd isotope evidence. Geology 31, 873–876.

Murphy, J.B., Nance, R.D., 2013. Speculations on the mechanisms for the formation and breakup of supercontinents. Geoscience Frontiers 4, 185–194.

Nance, R.D., Murphy, J.B., 2013. Origins of the supercontinent cycle. Geoscience Frontiers 4, 439–448.

Nance, R.D., Murphy, J.B., 2018. Supercontinents and the case for Pannotia. Geological Society, London, Special Publications 470, SP470. 475.

Nance, R.D., Murphy, J.B., Santosh, M., 2014. The supercontinent cycle: A retrospective essay. Gondwana Research 25, 4–29.

Nordsvan, A.R., Collins, W.J., Li, Z.X., Spencer, C.J., Pourteau, A., Withnall, I.W., Betts, P.G., Volante, S., 2018. Laurentian crust in northeast Australia: Implications for the assembly of the supercontinent Nuna. Geology 46, 251–254.

Nutman, A.P., Wan, Y., Du, L., Friend, C.R.L., Dong, C., Xie, H., Wang, W., Sun, H., Liu, D., 2011. Multistage late Neoarchaean crustal evolution of the North China Craton, eastern Hebei. Precambrian Research 189, 43–65.

O'dea, M., Lister, G., MacCready, T., Betts, P., Oliver, N., Pound, K., Huang, W., Valenta, R., 1997. Geodynamic evolution of the Proterozoic Mount Isa terrain. Geological Society, London, Special Publications 121, 99–122.

Page, R., Jackson, M., Krassay, A., 2000. Constraining sequence stratigraphy in north Australian basins: SHRIMP U–Pb zircon geochronology between Mt Isa and McArthur River. Australian Journal of Earth Sciences 47, 431–459.

Pang, K., Tang, Q., Yuan, X.L., Wan, B., Xiao, S., 2015. A biomechanical analysis of the early eukaryotic fossil Valeria and new occurrence of organic-walled microfossils from the Paleo-Mesoproterozoic Ruyang Group. Palaeoworld 24, 251–262.

Pastor-Galán, D., Nance, R.D., Murphy, J.B., Spencer, C.J., 2018. Supercontinents: myths, mysteries, and milestones. Geological Society, London, Special Publications 470, SP470. 416.

Paterson, G.A., Zhao, X., Jackson, M., Heslop, D., 2018. Measuring, Processing, and Analyzing Hysteresis Data. Geochemistry, Geophysics, Geosystems 19, 1925–1945.

Payne, J.L., Hand, M., Barovich, K.M., Reid, A., Evans, D.A.D., 2009. Correlations and reconstruction models for the 2500–1500 Ma evolution of the Mawson Continent. 323, 319–355.

Pearce, J.A., 2008. Geochemical fingerprinting of oceanic basalts with applications to ophiolite classification and the search for Archean oceanic crust. Lithos 100, 14–48.

Pearce, J.A., Cann, J.R., 1971. Ophiolite origin investigated by discriminant analysis using Ti, Zr

and Y. Earth and Planetary Science Letters 12, 339–349.

Pearce, J.A., Cann, J.R., 1973. Tectonic setting of basic volcanic rocks determined using trace element analyses. Earth and Planetary Science Letters 19, 290–300.

Pehrsson, S.J., Eglington, B.M., Evans, D.A.D., Huston, D., Reddy, S.M., 2016. Metallogeny and its link to orogenic style during the Nuna supercontinent cycle. Geological Society, London, Special Publications 424, 83–94.

Pei, J., Yang, Z., Zhao, Y., 2006. A Mesoproterozoic paleomagnetic pole from the Yangzhuang Formation, North China and its tectonics implications. Precambrian Research 151, 1–13.

Peng, P., 2015a. Late Paleoproterozoic–Neoproterozoic (1800–541 Ma) Mafic Dyke Swarms and Rifts in North China. 171–204.

Peng, P., 2015b. Precambrian mafic dyke swarms in the North China Craton and their geological implications. Science China Earth Sciences 58, 649–675.

Peng, P., Bleeker, W., Ernst, R.E., Söderlund, U., McNicoll, V., 2011a. U–Pb baddeleyite ages, distribution and geochemistry of 925Ma mafic dykes and 900Ma sills in the North China craton: Evidence for a Neoproterozoic mantle plume. Lithos 127, 210–221.

Peng, P., Liu, F., Zhai, M., Guo, J., 2012. Age of the Miyun dyke swarm: Constraints on the maximum depositional age of the Changcheng System. Chinese Science Bulletin 57, 105–110.

Peng, P., Wang, X., Windley, B.F., Guo, J., Zhai, M., Li, Y., 2014. Spatial distribution of ~1950–1800Ma metamorphic events in the North China Craton: Implications for tectonic subdivision of the craton. Lithos 202–203, 250–266.

Peng, P., Yang, S., Su, X., Wang, X., Zhang, J., Wang, C., 2017. Petrogenesis of the 2090 Ma Zanhuang ring and sill complexes in North China: A bimodal magmatism related to intra–continental process. Precambrian Research 303, 153–170.

Peng, P., Zhai, M.G., Guo, J.H., 2006. 1.80–1.75 Ga mafic dyke swarms in the central North China craton: implications for a plume-related break-up event, in: Hanski, E., Mertanen, S., Rämö, T., Vuollo, J. (Eds.), Dyke Swarms – Time Markers of Crustal Evolution. Taylor & Francis, London, p. 75–87.

Peng, P., Zhai, M.G., Guo, J.H., Kusky, T., Zhao, T.P., 2007. Nature of mantle source contributions and crystal differentiation in the petrogenesis of the 1.78 Ga mafic dykes in the central North China craton. Gondwana Research 12, 29–46.

Peng, P., Zhai, M.G., Li, Q., Wu, F., Hou, Q., Li, Z., Li, T., Zhang, Y., 2011b. Neoproterozoic (~900Ma) Sariwon sills in North Korea: Geochronology, geochemistry and implications for the evolution of the south-eastern margin of the North China Craton. Gondwana Research 20, 243–254.

Peng, P., Zhai, M., Ernst, R.E., Guo, J., Liu, F., Hu, B., 2008. A 1.78 Ga large igneous province in the North China craton: The Xiong'er Volcanic Province and the North China dyke swarm. Lithos 101, 260–280.

Peng, P., Zhai, M., Zhang, H., Guo, J., 2005. Geochronological Constraints on the Paleoproterozoic

Evolution of the North China Craton: SHRIMP Zircon Ages of Different Types of Mafic Dikes. International Geology Review 47, 492–508.

Peng, T., Wilde, S.A., Fan, W., Peng, B., Mao, Y., 2013. Mesoproterozoic high Fe–Ti mafic magmatism in western Shandong, North China Craton: Petrogenesis and implications for the final breakup of the Columbia supercontinent. Precambrian Research 235, 190–207.

Piper, J.D.A., Jiasheng, Z., Huang, B., Roberts, A.P., 2011. Palaeomagnetism of Precambrian dyke swarms in the North China Shield: The ~1.8 Ga LIP event and crustal consolidation in late Palaeoproterozoic times. Journal of Asian Earth Sciences 41, 504–524.

Pisarevsky, S.A., Elming, S.-Å., Pesonen, L.J., Li, Z.X., 2014a. Mesoproterozoic paleogeography: Supercontinent and beyond. Precambrian Research 244, 207–225.

Pisarevsky, S.A., Wingate, M.T.D., Li, Z.X., Wang, X.C., Tohver, E., Kirkland, C.L., 2014b. Age and paleomagnetism of the 1210Ma Gnowangerup–Fraser dyke swarm, Western Australia, and implications for late Mesoproterozoic paleogeography. Precambrian Research 246, 1–15.

Pourteau, A., Smit, M.A., Li, Z.X., Collins, W.J., Nordsvan, A.R., Volante, S., Li, J., 2018. 1.6 Ga crustal thickening along the final Nuna suture. Geology 46, 959–962.

Qian, X., 1997. Tectonic correlation of the Precambrian evolution of the North China craton with the Baltic shield, Precambrian geology and metamorphic petrology: proceedings of the 30th International Geological Congress, Beijing, China, 4–14 August 1996. Vsp, p. 43.

Qian, X., Chen, Y., 1987. Late Precambrian mafic dyke swarms of the North China craton, Mafic Dykes Swarms. Geology Association of Canada Special Paper, pp. 385–391.

Radhakrishnamurthy, C., 1993. M–26. Magnetism and Basalts. GSI Publications 1.

Rawlings, D., 1999. Stratigraphic resolution of a multiphase intracratonic basin system: the McArthur Basin, northern Australia. Australian Journal of Earth Sciences 46, 703–723.

Rawlings, D., Page, R., 1999. Geology, geochronology and emplacement structures associated with the Jimbu Microgranite, McArthur Basin, Northern Territory. Precambrian Research 94, 225–250.

Rivers, T., 2015. Tectonic Setting and Evolution of the Grenville Orogen: An Assessment of Progress Over the Last 40 Years. Geoscience Canada 42, 77–124.

Rochette, P., Jackson, M., Aubourg, C., 1992. Rock magnetism and the interpretation of anisotropy of magnetic susceptibility. 30, 209–226.

Rochette, P., Jenatton, L., Dupuy, C., Boudier, F., Reuber, I., 1991. Diabase Dikes Emplacement in the Oman Ophiolite: A Magnetic Fabric Study with Reference to Geochemistry. Springer Netherlands, Dordrecht, pp. 55–82.

Rogers, J.J., Santosh, M., 2004. Continents and supercontinents. Oxford University Press.

Rogers, J.J.W., Santosh, M., 2002. Configuration of Columbia, a Mesoproterozoic Supercontinent. Gondwana Research 5, 5–22.

Rogers, J.J.W., Santosh, M., 2009. Tectonics and surface effects of the supercontinent Columbia. Gondwana Research 15, 373–380.

Romanowicz, B., 2008. Using seismic waves to image Earth's internal structure. Nature 451, 266–268.

Salminen, J., Hanson, R., Evans, D.A.D., Gong, Z., Larson, T., Walker, O., Gumsley, A., Söderlund, U., Ernst, R., 2018. Direct Mesoproterozoic connection of the Congo and Kalahari cratons in proto-Africa: Strange attractors across supercontinental cycles. Geology 46, 1011–1014.

Schmidt, P.W., Williams, G.E., 2008. Palaeomagnetism of red beds from the Kimberley Group, Western Australia: implications for the palaeogeography of the 1.8 Ga King Leopold glaciation. Precambrian Research 167, 267–280.

Seton, M., Müller, R.D., Zahirovic, S., Gaina, C., Torsvik, T., Shephard, G., Talsma, A., Gurnis, M., Turner, M., Maus, S., Chandler, M., 2012. Global continental and ocean basin reconstructions since 200Ma. Earth-Science Reviews 113, 212–270.

Sheppard, S., Page, R., Griffin, T., Rasmussen, B., Fletcher, I., Tyler, I., Kirkland, C., Wingate, M., Hollis, J., Thorne, A., 2012. Geochronological and isotopic constraints on the tectonic setting of the c. 1800 Ma Hart Dolerite and the Kimberley and Speewah Basins, northern Western Australia. Geological Survey of Western Australia Record 7, 1–28.

Slagstad, T., Davidsen, B., Daly, J.S., 2011. Age and composition of crystalline basement rocks on the Norwegian continental margin: offshore extension and continuity of the Caledonian–Appalachian orogenic belt. Journal of the Geological Society 168, 1167–1185.

Söderlund, U., Johansson, L., 2002. A simple way to extract baddeleyite (ZrO_2). Geochemistry, Geophysics, Geosystems 3, 1 of 7–7 of 7.

Song, B., Nutman, A.P., Liu, D., Wu, J., 1996. 3800 to 2500 Ma crustal evolution in the Anshan area of Liaoning Province, northeastern China. Precambrian Research 78, 79–94.

Spampinato, G.P.T., Betts, P.G., Ailleres, L., Armit, R.J., 2015. Structural architecture of the southern Mount Isa terrane in Queensland inferred from magnetic and gravity data. Precambrian Research 269, 261–280.

Stacey, J.S., Kramers, J.D., 1975. Approximation of terrestrial lead isotope evolution by a two–stage model. Earth and Planetary Science Letters 26, 207–221.

Su, W., Li, H., Huff, W., Ettensohn, F., Zhang, S., Zhou, H., Wan, Y., 2010. SHRIMP U–Pb dating for a K-bentonite bed in the Tieling Formation, North China. Chinese Science Bulletin 55, 3312–3323.

Su, W., Zhang, S., Huff, W.D., Li, H., Ettensohn, F.R., Chen, X., Yang, H., Han, Y., Song, B., Santosh, M., 2008. SHRIMP U–Pb ages of K-bentonite beds in the Xiamaling Formation: Implications for revised subdivision of the Meso– to Neoproterozoic history of the North China Craton. Gondwana Research 14, 543–553.

Sun, S.S., McDonough, W.S., 1989. Chemical and isotopic systematics of oceanic basalts: implications for mantle composition and processes. Geological Society, London, Special Publications 42, 313–345.

Tang, D., Shi, X., Jiang, G., Wu, T., Ma, J., Zhou, X., 2018. Stratiform siderites from the

Mesoproterozoic Xiamaling Formation in North China: Genesis and environmental implications. Gondwana Research 58, 1–15.

Tang, H., Chen, Y., 2013. Global glaciations and atmospheric change at ca. 2.3 Ga. Geoscience Frontiers 4, 583–596.

Tang, H., Chen, Y., Wu, G., Lai, Y., 2011. Paleoproterozoic positive $\delta^{13}C_{carb}$ excursion in the northeastern Sino-Korean craton: Evidence of the Lomagundi Event. Gondwana Research 19, 471–481.

Tarduno, J.A., Bono, R., 2018. Hotspot and LLSVP Motion, AGU Fall Meeting Abstracts.

Tarduno, J.A., Bono, R.K., 2017. Hotspot motion caused the Hawaiian–Emperor Bend and LLSVPs are not fixed, AGU Fall Meeting Abstracts.

Tarduno, J.A., Koppers, A.A.P., 2019. WHEN HOTSPOTS MOVE: The New View of Mantle Dynamics Made Possible by Scientific Ocean Drilling. Oceanography 32, 150–152.

Tarling, D., Hrouda, F., 1993. Magnetic anisotropy of rocks. Springer Science & Business Media.

Tauxe, L., 2010. Essentials of Paleomagnetism. University of California Press.

Torsvik, T.H., Burke, K., Steinberger, B., Webb, S.J., Ashwal, L.D., 2010. Diamonds sampled by plumes from the core–mantle boundary. Nature 466, 352–355.

Torsvik, T.H., Müller, R.D., Van der Voo, R., Steinberger, B., Gaina, C., 2008. Global plate motion frames: Toward a unified model. Reviews of Geophysics 46.

Trewick, A.S., 2017. Plate Tectonics in Biogeography, in: Richardson, D., Castree, N., Goodchild, F.M., Kobayashi, A., Liu, W., Marston, A.R. (Eds.), The International Encyclopedia of Geography.

Van der Voo, R., 1990. The reliability of paleomagnetic data. Tectonophysics 184, 1–9.

Veevers, J.J., 2003. Pan-African is Pan-Gondwanaland: Oblique convergence drives rotation during 650–500 Ma assembly. Geology 31, 501–504.

Vine, F.J., Matthews, D.H.J.N., 1963. Magnetic anomalies over oceanic ridges. 199, 947–949.

Volk, H., Dutkiewicz, A., George, S., Ridley, J., 2003. Oil migration in the Middle Proterozoic Roper Superbasin, Australia: evidence from oil inclusions and their geochemistries. Journal of Geochemical Exploration 78, 437–441.

Wan, B., Windley, B.F., Xiao, W., Feng, J., Zhang, J.e., 2015a. Paleoproterozoic high–pressure metamorphism in the northern North China Craton and implications for the Nuna supercontinent. Nature communications 6, 8344.

Wan, Y.S., Liu, D.Y., Dong, C.Y., Xie, H.Q., Kröner, A., Ma, M.Z., Liu, S.J., Xie, S.W., Ren, P., 2015b. Formation and Evolution of Archean Continental Crust of the North China Craton, in: Zhai, M. (Ed.), Precambrian Geology of China. Springer Berlin Heidelberg, Berlin, Heidelberg, pp. 59–136.

Wan, Y., Liu, D., Nutman, A., Zhou, H., Dong, C., Yin, X., Ma, M., 2012. Multiple 3.8–3.1 Ga tectono-magmatic events in a newly discovered area of ancient rocks (the Shengousi Complex), Anshan, North China Craton. Journal of Asian Earth Sciences 54–55, 18–30.

Wan, Y., Liu, D., Song, B., Wu, J., Yang, C., Zhang, Z., Geng, Y., 2005. Geochemical and Nd isotopic compositions of 3.8 Ga meta-quartz dioritic and trondhjemitic rocks from the Anshan area and their geological significance. Journal of Asian Earth Sciences 24, 563–575.

Wan, Y., Liu, D., Wang, S., Dong, C., Yang, E., Wang, W., Zhou, H., Ning, Z., Du, L., Yin, X., Xie, H., Ma, M., 2010. Juvenile magmatism and crustal recycling at the end of the Neoarchean in Western Shandong Province, North China Craton: Evidence from SHRIMP zircon dating. American Journal of Science 310, 1503–1552.

Wang, C., He, X., Carranza, E.J.M., Cui, C., 2019. Paleoproterozoic volcanic rocks in the southern margin of the North China Craton, central China: Implications for the Columbia supercontinent. Geoscience Frontiers. https://doi.org/10.1016/j.gsf.2018.10.007

Wang, C., Lu, Y., He, X., Wang, Q., Zhang, J., 2016a. The Paleoproterozoic diorite dykes in the southern margin of the North China Craton: Insight into rift-related magmatism. Precambrian Research 277, 26–46.

Wang, C., Peng, P., Wang, X., Yang, S., 2016b. Nature of three Proterozoic (1680 Ma, 1230 Ma and 775 Ma) mafic dyke swarms in North China: Implications for tectonic evolution and paleogeographic reconstruction. Precambrian Research 285, 109–126.

Wang, Q.H., Yang, H., Yang, D.B., Xu, W.L., 2014a. Mid-Mesoproterozoic (~1.32Ga) diabase swarms from the western Liaoning region in the northern margin of the North China Craton: Baddeleyite Pb–Pb geochronology, geochemistry and implications for the final breakup of the Columbia supercontinent. Precambrian Research 254, 114–128.

Wang, Q., Yang, D., Xu, W., 2012. Neoproterozoic basic magmatism in the southeast margin of North China Craton: Evidence from whole-rock geochemistry, U–Pb and Hf isotopic study of zircons from diabase swarms in the Xuzhou–Huaibei area of China. Science China Earth Sciences 55, 1461–1479.

Wang, W., Liu, S., Santosh, M., Zhang, L., Bai, X., Zhao, Y., Zhang, S., Guo, R., 2015a. 1.23 Ga mafic dykes in the North China Craton and their implications for the reconstruction of the Columbia supercontinent. Gondwana Research 27, 1407–1418.

Wang, X., Peng, P., Wang, C., Yang, S., 2016c. Petrogenesis of the 2115 Ma Haicheng mafic sills from the Eastern North China Craton: Implications for an intra–continental rifting. Gondwana Research 39, 347–364.

Wang, X., Peng, P., Wang, C., Yang, S., Söderlund, U., Su, X., 2017. Nature of three episodes of Paleoproterozoic magmatism (2180 Ma, 2115 Ma and 1890 Ma) in the Liaoji belt, North China with implications for tectonic evolution. Precambrian Research 298, 252–267.

Wang, X., Zhu, W., Luo, M., Ren, X., Cui, X., 2014b. Approximately 1.78 Ga mafic dykes in the Lüliang Complex, North China Craton: Zircon ages and Lu-Hf isotopes, geochemistry, and implications. Geochemistry, Geophysics, Geosystems 15, 3123–3144.

Wang, Y. F., Li, X.H., Jin, W., Zhang, J.H., 2015b. Eoarchean ultra-depleted mantle domains inferred from ca. 3.81 Ga Anshan trondhjemitic gneisses, North China Craton. Precambrian Research

263, 88–107.

Wang, Y., Fan, W., Zhang, Y., Guo, F., Zhang, H., Peng, T., 2004. Geochemical, $^{40}Ar/^{39}Ar$ geochronological and Sr–Nd isotopic constraints on the origin of Paleoproterozoic mafic dikes from the southern Taihang Mountains and implications for the ca. 1800Ma event of the North China Craton. Precambrian Research 135, 55–77.

Wang, Y., Zhao, G., Fan, W., Peng, T., Sun, L., Xia, X., 2007. LA–ICP–MS U–Pb zircon geochronology and geochemistry of Paleoproterozoic mafic dykes from western Shandong Province: Implications for back-arc basin magmatism in the Eastern Block, North China Craton. Precambrian Research 154, 107–124.

Wegener, A., 1912. Die entstehung der kontinente. Geologische Rundschau 3, 276–292.

Wegener, A., 1915. Die Entstehung der Kontinente und Ozeane: Braunschweig. Sammlung Vieweg, 94.

Wen, B., Evans, D.A., Li, Y.X., 2017. Neoproterozoic paleogeography of the Tarim Block: An extended or alternative “missing-link” model for Rodinia? Earth and Planetary Science Letters 458, 92–106.

Whelan, J.A., Beyer, E.E., Donnellan, N., Bleeker, W., Chamberlin, K.R., Söderlund, U., Ernst, R.E., 2016. 1.4 billion years of Northern Territory geology: Insights from collaborative U–Pb zircon and baddeleyite dating, Annual Geoscience Exploration Seminar (AGES) Proceedings, Alice Springs, Northern Territory 15–16 March 2016.

Wilde, S.A., Zhao, G., Sun, M., 2002. Development of the North China Craton During the Late Archaean and its Final Amalgamation at 1.8 Ga: Some Speculations on its Position Within a Global Palaeoproterozoic Supercontinent. Gondwana Research 5, 85–94.

Williams, H., Hoffman, P.F., Lewry, J.F., Monger, J.W.H., Rivers, T., 1991. Anatomy of North America: thematic geologic portrayals of the continent. Tectonophysics 187, 117–134.

Wilson, J.T., 1966. Did the Atlantic Close and then Re-Open? Nature 211, 676–681.

Wilson, M., 1997. Thermal evolution of the Central Atlantic passive margins: continental break-up above a Mesozoic super-plume. Journal of the Geological Society 154, 491–495.

Winchester, J.A., Floyd, P.A., 1977. Geochemical discrimination of different magma series and their differentiation products using immobile elements. Chemical Geology 20, 325–343.

Wingate, M.T.D., Pisarevsky, S.A., Evans, D.A.D., 2002. Rodinia connections between Australia and Laurentia: no SWEAT, no AUSWUS? 14, 121–128.

Worsley, T.R., Nance, D., Moody, J.B., 1984. Global tectonics and eustasy for the past 2 billion years. Marine Geology 58, 373–400.

Wu, C., Zhou, Z., Zuza, A.V., Wang, G., Liu, C., Jiang, T., 2018. A 1.9-Ga Mélange Along the Northern Margin of the North China Craton: Implications for the Assembly of Columbia Supercontinent. Tectonics 37, 3610–3646.

Wu, H., Zhang, S., Li, Z.X., Li, H., Dong, J., 2005. New paleomagnetic results from the Yangzhuang Formation of the Jixian System, North China, and tectonic implications. Chinese Science

Bulletin 50, 1483–1489.

Xu, H., Yang, Z., Peng, P., Ge, K., Jin, Z., Zhu, R., 2017. Magnetic fabrics and rock magnetism of the Xiong'er volcanic rocks and their implications for tectonic correlation of the North China Craton with other crustal blocks in the Nuna/Columbia supercontinent. Tectonophysics 712–713, 415–425.

Xu, H., Yang, Z., Peng, P., Meert, J.G., Zhu, R., 2014. Paleo-position of the North China craton within the supercontinent Columbia: Constraints from new paleomagnetic results. Precambrian Research 255, 276–293.

Yan, Y., Chen, L., Huang, B., Yi, Z., Zhao, J., 2017. Magnetic fabric constraint on tectonic setting of Paleoproterozoic dyke swarms in the North China Craton, China. Precambrian Research. http://doi.org/10.1016/j.precamres.2017.12.006

Yang, K.F., Fan, H.R., Santosh, M., Hu, F.F., Wang, K.Y., 2011. Mesoproterozoic mafic and carbonatitic dykes from the northern margin of the North China Craton: Implications for the final breakup of Columbia supercontinent. Tectonophysics 498, 1–10.

Yang, S., Peng, P., Qin, Z., Wang, X., Wang, C., Zhang, J., Zhao, T., 2017. Genetic relationship between 1780Ma dykes and coeval volcanics in the Lvliang area, North China. Precambrian Research. https://doi.org/10.1016/j.precamres.2017.10.004

Young, G.M., 2014. Contradictory correlations of Paleoproterozoic glacial deposits: Local, regional or global controls? Precambrian Research 247, 33–44.

Yuan, L., Zhang, X., Xue, F., Han, C., Chen, H., Zhai, M., 2015. Two episodes of Paleoproterozoic mafic intrusions from Liaoning province, North China Craton: Petrogenesis and tectonic implications. Precambrian Research 264, 119–139.

Zhai, M.G., Santosh, M., 2011. The early Precambrian odyssey of the North China Craton: A synoptic overview. Gondwana Research 20, 6–25.

Zhai, M., 2011. Cratonization and the Ancient North China Continent: A summary and review. Science China Earth Sciences 54, 1110–1120.

Zhai, M., 2013. The main old lands in China and assembly of Chinese unified continent. Science China Earth Sciences 56, 1829–1852.

Zhai, M., Liu, W., 2003. Palaeoproterozoic tectonic history of the North China craton: a review. Precambrian Research 122, 183–199.

Zhang, N., Dang, Z., Huang, C., Li, Z.X., 2018. The dominant driving force for supercontinent breakup: Plume push or subduction retreat? Geoscience Frontiers 9, 997–1007.

Zhang, S.H., Liu, S.W., Zhao, Y., Yang, J.H., Song, B., Liu, X.M., 2007. The 1.75–1.68 Ga anorthosite-mangerite-alkali granitoid-rapakivi granite suite from the northern North China Craton: Magmatism related to a Paleoproterozoic orogen. Precambrian Research 155, 287–312.

Zhang, S.H., Zhao, Y., Li, X.H., Ernst, R.E., Yang, Z.Y., 2017. The 1.33–1.30 Ga Yanliao large igneous province in the North China Craton: Implications for reconstruction of the Nuna

(Columbia) supercontinent, and specifically with the North Australian Craton. Earth and Planetary Science Letters 465, 112–125.

Zhang, S.H., Zhao, Y., Santosh, M., 2012a. Mid-Mesoproterozoic bimodal magmatic rocks in the northern North China Craton: Implications for magmatism related to breakup of the Columbia supercontinent. Precambrian Research 222–223, 339–367.

Zhang, S.H., Zhao, Y., Yang, Z.Y., He, Z.F., Wu, H., 2009. The 1.35Ga diabase sills from the northern North China Craton: Implications for breakup of the Columbia (Nuna) supercontinent. Earth and Planetary Science Letters 288, 588–600.

Zhang, S.H., Zhao, Y., Ye, H., Hu, G.H., 2016. Early Neoproterozoic emplacement of the diabase sill swarms in the Liaodong Peninsula and pre-magmatic uplift of the southeastern North China Craton. Precambrian Research 272, 203–225.

Zhang, S., Li, Z.X., Evans, D.A.D., Wu, H., Li, H., Dong, J., 2012b. Pre-Rodinia supercontinent Nuna shaping up: A global synthesis with new paleomagnetic results from North China. Earth and Planetary Science Letters 353–354, 145–155.

Zhang, S., Li, Z., Wu, H., 2006. New Precambrian palaeomagnetic constraints on the position of the North China Block in Rodinia. Precambrian Research 144, 213–238.

Zhao, G., Cawood, P.A., Wilde, S.A., Sun, M., 2002a. Review of global 2.1–1.8 Ga orogens: implications for a pre-Rodinia supercontinent. Earth-Science Reviews 59, 125–162.

Zhao, G., He, Y., Sun, M., 2009. The Xiong'er volcanic belt at the southern margin of the North China Craton: Petrographic and geochemical evidence for its outboard position in the Paleo–Mesoproterozoic Columbia Supercontinent. Gondwana Research 16, 170–181.

Zhao, G., Li, S., Sun, M., Wilde, S.A., 2011. Assembly, accretion, and break–up of the Palaeo–Mesoproterozoic Columbia supercontinent: record in the North China Craton revisited. International Geology Review 53, 1331–1356.

Zhao, G., Sun, M., Wilde, S.A., Li, S., 2003. Assembly, Accretion and Breakup of the Paleo-Mesoproterozoic Columbia Supercontinent: Records in the North China Craton. Gondwana Research 6, 417–434.

Zhao, G., Sun, M., Wilde, S.A., Sanzhong, L., 2005. Late Archean to Paleoproterozoic evolution of the North China Craton: key issues revisited. Precambrian Research 136, 177–202.

Zhao, G., Wilde, S.A., A. Cawood, P., Lu, L., 1999a. Tectonothermal history of the basement rocks in the western zone of the North China Craton and its tectonic implications. Tectonophysics 310, 37–53.

Zhao, G., Wilde, S.A., Cawood, P.A., Lu, L., 1998. Thermal Evolution of Archean Basement Rocks from the Eastern Part of the North China Craton and Its Bearing on Tectonic Setting. International Geology Review 40, 706–721.

Zhao, G., Wilde, S.A., Cawood, P.A., Lu, L., 1999b. Thermal evolution of two textural types of mafic granulites in the North China craton: evidence for both mantle plume and collisional tectonics. Geological Magazine 136, 223–240.

Zhao, G., Zhai, M., 2013. Lithotectonic elements of Precambrian basement in the North China Craton: Review and tectonic implications. Gondwana Research 23, 1207–1240.

Zhao, G.C., Wilde, S.A., Cawood, P.A., Lu, L.Z., 2000. Petrology and P–T path of the Fuping mafic granulites: implications for tectonic evolution of the central zone of the North China craton. Journal of Metamorphic Geology 18, 375–391.

Zhao, T.P., Zhou, M.F., Zhai, M., Xia, B., 2002b. Paleoproterozoic Rift–Related Volcanism of the Xiong'er Group, North China Craton: Implications for the Breakup of Columbia. International Geology Review 44, 336–351.

Zhao, T., Zhai, M., Xia, B., Li, H., Zhang, Y., Wan, Y., 2004. Zircon U–Pb SHRIMP dating for the volcanic rocks of the Xiong'er Group: Constraints on the initial formation age of the cover of the North China Craton. Chinese Science Bulletin 49, 2495–2502.

Zhao, T., Zhu, G., Lin, S., Wang, H., 2016. Indentation-induced tearing of a subducting continent: Evidence from the Tan–Lu Fault Zone, East China. Earth–Science Reviews 152, 14–36.

Zhao, W., Hu, S., Wang, Z., Zhang, S., Wang, T., 2018. Petroleum geological conditions and exploration importance of Proterozoic to Cambrian in China. Petroleum Exploration and Development 45, 1–14.

Zhong, S., Zhang, N., Li, Z.X., Roberts, J.H., 2007. Supercontinent cycles, true polar wander, and very long-wavelength mantle convection. Earth and Planetary Science Letters 261, 551–564.

Zhou, Z., Hu, M., Wu, C., Wang, G., Liu, C., Cai, A., Jiang, T., 2018. Coupled U–Pb dating and Hf isotopic analysis of detrital zircons from Bayan Obo Group in Inner Mongolia: Constraints on the evolution of the Bayan Obo rift belt. Geological Journal 53, 2649–2664.

Zhu, S., Zhu, M., Knoll, A.H., Yin, Z., Zhao, F., Sun, S., Qu, Y., Shi, M., Liu, H., 2016. Decimetre-scale multicellular eukaryotes from the 1.56-billion-year-old Gaoyuzhuang Formation in North China. Nature Communications 7: 11500.

附 录

附表. 编录的华北克拉通已报道 1.24–1.21 Ga 侵入体的全岩地球化学数据

Supplementary Table. Complied whole-rock geochemistry data of 1.24–1.21 Ga intrusions in the North China Craton

Sample	517MJG1	05LC06	07MY12	DHZK01-1	DHZK01-2	DHZK01-3	12JP01-1	12JP01-2	11JP14-1	12JP03-1	12JP04-1	12JP07-2
Reference	1	2	3	4	4	4	5	5	5	5	5	5
SiO_2	50.1	49.1	49.1	48.8	47.9	48.3	48.0	48.1	49.9	43.8	42.6	45.4
TiO_2	2.91	2.66	2.50	1.95	1.93	2.70	2.16	1.84	2.67	2.71	2.66	2.82
Al_2O_3	12.9	14.1	13.4	14.5	15.0	14.6	17.2	17.8	14.6	17.2	16.9	17.3
tFe_2O_3	13.3	15.9	16.2	13.4	13.3	14.4	10.7	9.7	13.0	13.9	13.8	11.5
MnO	0.23	0.24	0.19	0.19	0.18	0.19	0.14	0.13	0.19	0.18	0.26	0.14
MgO	5.18	3.12	6.05	6.84	7.10	4.74	5.39	4.84	4.92	6.74	7.75	7.01
CaO	8.29	6.44	9.33	9.73	9.80	7.35	7.69	7.52	8.42	7.27	5.70	8.3
Na_2O	2.92	3.03	2.18	2.09	2.02	3.36	5.15	6.63	2.80	4.22	5.12	4.17
K_2O	1.52	2.26	0.799	0.600	0.760	1.28	0.982	0.884	1.04	1.63	0.690	0.78
P_2O_5	0.55	0.87	0.26	0.20	0.17	0.34	0.47	0.32	0.51	1.47	1.28	0.49
LOI	1.74	2.60	1.46	2.28	2.60	3.44	1.91	1.78	1.98	0.56	2.86	1.71
Total	99.6	100.3	101.4	100.6	100.6	100.7	99.7	99.5	100.0	99.6	99.6	99.6
Mg#	43.8	28.2	42.8	50.6	51.7	39.7	50.3	49.9	43.2	49.3	53.0	55.0
Cr	205	6.49	178	168	208	61.6	73.0	55.0	107	15.0	34.0	68
Ni	73.3	20.0	82.0	75.7	87.5	33.6	36.0	31.0	50.0	40.0	52.0	50.0
Rb	61.6	68.8	16.3	16.4	24.8	35.3	26.0	25.0	27.0	77.0	36.0	25.0
Ba	661	1545	318	323	320	382	424	362	552	1023	702	334
Th	5.01	4.45	2.15	1.5	1.24	1.98	3.35	3.57	3.4	0.869	0.856	1.70
U	1.09	1.11	0.500	0.340	0.340	0.500	0.778	0.837	0.733	0.293	0.205	0.523

Sample	517MJG1	05LC06	07MY12	DHZK01-1	DHZK01-2	DHZK01-3	12JP01-1	12JP01-2	11JP14-1	12JP03-1	12JP04-1	12JP07-2
Reference	1	2	3	4	4	4	5	5	5	5	5	5
Nb	26.6	33.5	16.5	14.5	12.9	23.9	29.0	27.0	25.0	14.0	18.3	22.0
Ta	1.71	2.27	1.13	1.07	0.95	1.77	2.39	1.95	1.79	1.61	1.69	1.63
La	44.6	56.2	21.5	21.5	16.4	35.7	35.0	30.0	36.0	30.0	28.0	21.0
Ce	96.2	122	47.7	48.8	37.3	81.7	79.0	70.0	77.0	70.0	66.0	46.0
Pr	12.4	15.9	6.29	6.40	5.06	11.2	10.0	8.48	10.2	9.56	9.27	6.22
Sr	440	553	364	353	382	384	725	1052	651	550	627	705
Nd	53.6	65.6	26.0	29.3	22.7	48.0	39.0	32.0	46.0	41.0	39.0	25.0
Zr	349	436	143	135	117	213	230	212	310	172	178	142
Hf	9.13	10.7	4.00	4.75	3.70	6.27	5.34	4.88	8.58	4.01	4.14	3.34
Sm	10.7	13.7	5.86	6.47	5.07	10.3	7.79	6.43	8.39	8.69	8.52	5.50
Eu	4.15	4.34	2.02	2.26	1.88	3.42	2.82	2.54	3.18	3.51	3.11	2.16
Gd	9.22	11.1	5.16	5.43	4.23	8.32	7.40	6.15	8.00	8.69	8.46	5.29
Tb	1.25	1.57	0.760	0.920	0.760	1.39	1.04	0.866	1.29	1.31	1.29	0.783
Dy	6.57	8.25	4.37	5.51	4.51	8.00	4.95	4.08	6.09	6.73	6.64	3.79
Y	30.6	32.5	19.7	23.3	19.3	32.6	25.0	21.0	29.0	39.0	38.0	19.8
Ho	1.23	1.52	0.84	1.02	0.84	1.40	0.921	0.768	1.12	1.36	1.35	0.715
Er	2.94	3.95	2.15	2.75	2.31	3.78	2.28	1.91	2.74	3.56	3.55	1.77
Tm	0.410	0.520	0.310	0.420	0.360	0.550	0.304	0.256	0.429	0.494	0.487	0.24
Yb	2.50	3.11	1.90	2.38	2.08	3.20	1.83	1.55	2.66	3.07	3.02	1.41
Lu	0.380	0.460	0.270	0.430	0.410	0.640	0.265	0.228	0.338	0.472	0.463	0.206
La/Yb_N	12.8	13.0	8.12	6.47	5.64	8.00	13.7	13.9	9.71	7.01	6.65	10.7
REE	246	308	125	134	104	218	193	165	203	188	179	120
Eu*	1.28	1.08	1.12	1.17	1.24	1.13	1.14	1.23	1.19	1.23	1.12	1.22

tFe_2O_3 = 以 Fe_2O_3 表达的全铁；Mg# = 100 × MgO/ (FeO_{total} + MgO)，分子比； $Eu^* = Eu_N/[(Sm_N) \times (Gd_N)]^{1/2}$；$La/Yb_N$：经球粒陨石标准化比值，标准化值来自 Sun and McDonough (1989)。参考文献：1. Wang et al., 2016b; 2. Peng et al., 2011a; 3. Peng et al., 2012; 4. 相振群, 2014; 5. Wang et al., 2015a; 6. Peng et al., 2013

附表－续

Sample	12JP07-3	12JP07-4	12JP07-5	12JP08-1	12JP09-1	12JP11-1	OCY27-1	13JP03-1	13JP03-2	12LN54-1	13QL12-4	13QL12-5
Reference	5	5	5	5	5	5	5	5	5	5	5	5
SiO_2	47.6	44.5	46.5	48.7	43.7	44.9	46.2	52.9	47.7	47.9	48.8	49.9
TiO_2	2.31	3.22	2.63	1.09	3.56	3.08	3.56	1.37	3.51	3.02	2.41	2.90
Al_2O_3	17.5	17.7	16.3	19.0	15.3	16.7	13.1	11.0	14.6	12.2	15.4	13.9
tFe_2O_3	10.9	11.8	11.9	8.0	13.8	12.4	16.0	12.4	15.8	14.1	13.8	15.5
MnO	0.15	0.14	0.15	0.10	0.16	0.16	0.21	0.23	0.22	0.20	0.18	0.20
MgO	5.60	6.75	7.11	4.91	7.92	6.59	6.39	6.88	4.56	6.86	5.18	3.72
CaO	7.84	8.69	7.95	8.38	9.15	8.51	9.87	9.36	7.79	10.3	8.60	7.22
Na_2O	4.67	4.14	4.02	6.29	3.52	4.50	2.34	3.81	2.30	2.14	2.73	3.58
K_2O	0.959	0.758	1.13	0.547	0.450	0.805	0.660	0.704	1.26	1.13	1.09	1.40
P_2O_5	0.72	0.35	0.53	0.49	0.43	0.47	0.26	0.36	0.42	0.46	0.26	0.42
LOI	1.53	1.60	1.46	2.19	1.54	1.60	1.17	0.82	1.63	1.52	1.36	1.06
Total	99.7	99.7	99.7	99.7	99.5	99.7	99.7	99.8	99.8	99.8	99.8	99.8
Mg#	50.7	53.3	54.4	55.3	53.5	51.4	44.4	52.6	36.6	49.3	43.0	32.4
Cr	51.0	64.0	106	98.0	55.0	69.0				201		
Ni	35.0	55.0	53.0	17.0	86.0	43.0				64.0		
Rb	23.0	28.0	48.0	12.7	12.9	26.0	16.0	7.69	51.0	34.0	28.0	36.0
Ba	428	358	676	240	268	437	307	592	508	618	474	607
Th	2.70	1.41	2.22	2.34	1.37	1.67	1.59	3.51	2.36	2.16	2.12	3.69
U	0.660	0.314	0.521	0.492	0.283	0.360	0.372	0.705	0.470	0.506	0.499	0.851
Nb	23.0	19.0	22.0	12.2	23.0	21.0	24.0	17.3	21.0	16.6	15.9	26.0
Ta	1.45	1.50	1.76	0.994	1.79	1.64	1.07	1.16	1.37	1.06	1.03	1.59
La	29.0	15.8	25.0	20.0	17.6	19.4	16.6	35.0	27.0	23.0	23.0	40.0
Ce	65.0	37.0	59.0	52.0	43.0	46.0	42.0	84.0	61.0	55.0	53.0	88.0
Pr	8.67	4.89	7.61	6.11	5.77	5.98	5.29	11.0	7.97	7.21	6.91	11.2

Sample	12JP07-3	12JP07-4	12JP07-5	12JP08-1	12JP09-1	12JP11-1	OCY27-1	13JP03-1	13JP03-2	12LN54-1	13QL12-4	13QL12-5
Reference	5	5	5	5	5	5	5	5	5	5	5	5
Sr	672	689	670	775	673	705	469	445	720	626	455	435
Nd	36.0	20.0	31.0	25.0	25.0	25.0	25.0	51.0	36.0	34.0	32.0	50.0
Zr	178	109	165	133	127	133	132	223	170	175	167	256
Hf	4.79	2.7	3.94	3.12	3.17	3.17	3.68	6.58	4.81	4.56	4.7	7.19
Sm	7.10	4.36	6.53	5.23	5.50	5.34	5.39	10.4	7.11	7.19	6.37	9.45
Eu	2.63	1.81	2.54	2.18	2.14	2.17	2.04	3.34	2.50	3.06	2.14	3.06
Gd	6.85	4.27	6.37	5.13	5.39	5.19	5.47	10.2	6.97	7.07	6.18	8.97
Tb	0.960	0.635	0.938	0.742	0.817	0.770	0.778	1.40	0.939	0.910	0.851	1.17
Dy	4.77	3.15	4.60	3.56	4.10	3.76	4.06	7.53	4.99	4.53	4.57	6.20
Y	23.0	16.3	24.0	18.5	21.0	19.6	16.2	35.0	24.0	18.3	22.0	30.0
Ho	0.900	0.601	0.882	0.673	0.785	0.712	0.729	1.40	0.928	0.804	0.871	1.16
Er	2.19	1.49	2.20	1.66	1.96	1.75	1.95	3.60	2.36	2.20	2.27	3.03
Tm	0.310	0.204	0.297	0.224	0.265	0.233	0.248	0.504	0.333	0.264	0.334	0.437
Yb	1.76	1.21	1.78	1.32	1.59	1.39	1.58	3.09	2.04	1.69	2.07	2.71
Lu	0.260	0.177	0.262	0.195	0.234	0.202	0.220	0.428	0.282	0.238	0.291	0.373
La/Yb_N	11.8	9.37	10.1	10.9	7.94	10.0	7.54	8.12	9.49	9.76	7.97	10.6
REE	166	96	149	124	114	118	111	223	160	147	141	226
Eu*	1.15	1.28	1.20	1.29	1.20	1.26	1.15	0.99	1.09	1.31	1.04	1.02

附表－续

Sample	13QL12-6	13QL12-7	12QL16-1	13QL16-2	13QL16-3	08YS-61	08YS-62	08YS-63	08YS-65	08YS-67	08YS-68	08YS-69	08YS-71
Reference	5	5	5	5	5	6	6	6	6	6	6	6	6
SiO_2	47.8	48.6	49.3	47.1	47.3	46.4	46.3	46.2	46.7	45.6	46.7	46.1	46.3
TiO_2	2.12	2.01	2.11	2.38	2.04	3.31	3.49	3.30	3.12	3.56	3.18	3.47	3.38
Al_2O_3	14.3	14.1	15.2	14.0	14.2	12.6	12.5	12.6	12.9	11.9	13.1	12.4	13.1
tFe_2O_3	13.5	13.0	13.0	14.4	13.0	16.7	16.8	16.6	16.4	18.1	16.2	17.0	16.3
MnO	0.19	0.18	0.18	0.19	0.19	0.21	0.22	0.21	0.21	0.23	0.21	0.23	0.22
MgO	6.51	6.81	6.05	5.90	5.73	6.19	6.25	6.13	6.16	6.45	5.97	6.22	5.56
CaO	9.14	8.80	9.47	9.77	9.64	10.0	10.0	10.0	10.0	9.87	9.94	10.0	9.83
Na_2O	3.39	3.82	1.88	3.68	5.34	2.34	2.28	2.68	2.32	2.17	2.37	2.36	2.39
K_2O	1.08	0.907	0.959	0.695	0.810	0.670	0.670	0.680	0.680	0.690	0.680	0.660	0.510
P_2O_5	0.21	0.21	0.21	0.20	0.18	0.41	0.41	0.39	0.40	0.39	0.40	0.39	0.45
LOI	1.60	1.45	1.48	1.56	1.34	0.62	0.62	0.71	0.71	0.63	0.80	0.63	1.51
Total	99.9	99.9	99.9	99.8	99.8	114.7	114.9	114.7	114.5	116.0	114.3	115.0	114.5
Mg#	49.1	51.3	48.2	45.1	46.8	42.5	42.6	42.4	42.9	41.7	42.4	42.2	40.6
Cr						142	137	234	133	140	144	150	110
Ni						71.0	69.0	107.0	65.0	83.0	69.0	78.0	60.0
Rb	25.0	18.6	27.0	16.7	19.3	18.0	18.0	19.0	18.0	19.0	19.0	19.0	14.0
Ba	272	287	381	259	398	380	379	388	387	384	393	393	337
Th	1.65	1.56	1.67	1.53	1.55	1.61	1.52	1.52	1.59	1.62	1.56	1.61	1.79
U	0.387	0.348	0.365	0.335	0.338	0.350	0.370	0.360	0.370	0.370	0.360	0.380	0.380
Nb	13.5	12.5	13.8	12.5	13.2	19.2	19.5	19.3	18.1	20.1	18.4	20.2	20.9
Ta	0.916	0.768	0.816	0.749	0.785	1.27	1.28	1.26	1.19	1.28	1.19	1.34	1.32
La	17.7	16.8	17.2	16.3	16.4	23.6	23.3	23.6	24.0	23.7	23.9	24.4	26.6
Ce	43.0	40.0	41.0	40.0	40.0	54.0	53.7	53.4	54.4	54.6	54.1	55.4	60.0
Pr	5.54	5.24	5.4	5.23	5.14	6.44	6.37	6.44	6.37	6.51	6.44	6.7	7.11

Sample	13QL12-6	13QL12-7	12QL16-1	13QL16-2	13QL16-3	08YS-61	08YS-62	08YS-63	08YS-65	08YS-67	08YS-68	08YS-69	08YS-71
Reference	5	5	5	5	5	6	6	6	6	6	6	6	6
Sr	412	400	450	444	429	524	511	530	526	493	553	535	539
Nd	26.0	25.0	26.0	25.0	24.0	30.6	30.6	30.1	30.0	30.8	30.1	31.6	33.3
Zr	142	129	140	129	135	215	219	222	211	219	214	224	230
Hf	4.05	3.79	4.08	3.81	3.94	4.75	4.86	4.85	4.74	4.96	4.78	5.00	5.23
Sm	5.45	5.12	5.25	5.22	5.06	6.04	5.97	5.78	5.97	6.15	5.87	6.21	6.5
Eu	1.86	1.75	1.83	1.79	1.79	2.34	2.31	2.33	2.27	2.34	2.39	2.44	2.50
Gd	5.42	5.13	5.22	5.20	5.07	4.95	4.89	4.97	4.76	4.77	4.96	4.94	5.11
Tb	0.763	0.718	0.722	0.712	0.714	0.810	0.800	0.800	0.790	0.820	0.800	0.830	0.840
Dy	4.22	4.02	4.04	3.99	4.04	4.69	4.56	4.52	4.52	4.78	4.52	4.73	4.75
Y	21.0	19.7	19.9	19.5	19.8	24.1	23.8	23.8	23.5	24.3	23.6	24.8	25.5
Ho	0.816	0.78	0.778	0.770	0.782	0.870	0.850	0.850	0.830	0.870	0.850	0.880	0.900
Er	2.22	2.07	2.06	2.07	2.10	2.19	2.24	2.26	2.21	2.32	2.24	2.36	2.39
Tm	0.319	0.300	0.307	0.301	0.313	0.29	0.300	0.290	0.280	0.310	0.290	0.300	0.310
Yb	2.02	1.89	1.94	1.90	1.98	1.92	1.89	1.82	1.79	1.94	1.79	1.96	1.99
Lu	0.281	0.261	0.260	0.254	0.265	0.280	0.270	0.280	0.270	0.280	0.270	0.290	0.280
La/Yb_N	6.29	6.38	6.36	6.15	5.94	8.82	8.84	9.30	9.62	8.76	9.58	8.93	9.59
REE	116	109	112	109	108	139	138	137	138	140	139	143	153
Eu*	1.05	1.04	1.07	1.05	1.08	1.31	1.31	1.33	1.30	1.32	1.35	1.35	1.33

致 谢

博士阶段临近尾声，感慨万千。回想自己 2013 年刚考上研究生，初入地质所时的青涩小伙，到现在白驹过隙已不想当年。在此，特别感谢我的三位导师，彭澎研究员、李正祥教授和 Sergei Pisarevsky 博士对我在学术上的引导、传授和教诲。

彭老师将我引入基性岩墙群与超大陆研究领域，他以高度的人格魅力，扎实专业的前寒武纪地质功底，给了我莫大的指导。前期学习阶段专注于野外调查、岩石学、年代学与地球化学的工作，特别感谢彭老师系统的培养，包括英文写作的指导和磨练，使我得到了快速提升。彭老师培养学生松弛有度、指导思路开放不局限，尊重学生个人想法，是难得的良师。

为了客观科学的重建前寒武纪古大陆，我决定学习古地磁重建方法。自学古地磁的过程是特别痛苦的，曾经把 Henry Halls 教授的文章翻译成中文，但也难以理解。挣扎之时特别感谢闫永刚耐心的解惑。2017 年，带着虔诚之心去上了黄宝春老师在北大开设的《构造磁学》课程，在上课的那些日子里我每次都提前打印好课件，每次都坐在前排认真听课。黄老师也比较照顾我，课上和课后多次跟我互动。黄老师讲课幽默、慢条斯理，虽然课时和内容有限，但恰好对我入门有莫大的作用。黄老师是我学习古地磁的引路人。

特别感谢李正祥老师提供留学机会，进入科廷大学的学习使我对超大陆的认知以及对古地磁的学习进入 2.0 时代。永远不会忘记第一次跟李老师开小会时李老师告诫我要有批判精神。李老师一流的国际水平、超前的研究思维、高标准严格的培养要求，严谨的态度、精益求精的精神让我受益终身。同时，特别感谢 Sergei 对我的指导。Sergei 严肃认真、谦逊、幽默而又自信。他总是那么严谨、耐心、认真的引导我思考，一遍又一遍不厌其烦的帮我修改论文，在细节上严格把关，潜移默化对我有很大的影响。

特别感谢郭敬辉老师、翟明国老师、李献华老师和赵太平老师对学生的指导以及润物细无声般的影响。郭老师总是那么的温文尔雅让我倍感亲切踏实；翟老师谦逊务实的指导无形中给我很多鼓励，老一辈科学家的担当让我备受鼓舞。最近几年，李献华老师反复提到的“专业思维”以及“先讲观测，后讲观

点”让我思考许久，逻辑方法的指导让我非常受益。赵太平老师豁达的心态、务实而不油腻作风一直深受我们学生欢迎，赵老师的生活态度值得我们学习。

感谢王欣平、杨书艳、孙风波、苏向东、张志越、周小童、欧阳东剑、秦照原、刘鹏、王浩铮、崔夏红、胡俊、周李岗、王丹、邹屹、黄广宇等同门在科研上和生活上的帮助，感谢前寒武纪地质学科组大家庭对我的照顾。特别感谢赵千、郝文星、徐慧茹和袁杰对打钻的技术指导及知识上的交流。留学期间，特别感谢科廷大学地球动力学组的老师、同学在学业上的帮助，特别感谢刘也博、姚卫华、Josh Beardmore、Uwe Kirscher、张南、Ross Mitchell、Hamed Gamal El Dien、吴磊、Adam Nordsvan、Erin Martin、Amaury Pourteau、Bill Collins、Chris Spencer、Brendan Murphy、Luc Doucet、Silvia Volante 等。感谢组里活跃开放的科研氛围，这种环境里让我了解更多、思考更多、提升更多。感谢 Steven Denyszyn 博士在定年中给予的帮助。特别感谢刘也博和刘玉荣夫妇、李劭杰、王开、姚卫华、李江瑜、王忠伟、杨雪梅、江强、曹明坚等对我生活上的照顾。感谢 Wilson 社区教堂几位澳洲友人帮助我提高语言，与她们相处的一年非常融洽。感谢国科大 13 级 603 班、16 级统考博士班同学对我的照顾和帮助，同时也感谢本所教育处老师对我的帮助。

特别感谢父母亲人对我学业的理解和支持。感谢曾经帮助过我的所有人，感谢曾经认识的人，感谢人生旅途中的缘分和点滴。

本研究受国家自然科学基金 41890833、41772192，澳大利亚研究委员会 Laureate Fellowship 项目 FL150100133 资助；参加会议同时受科廷大学研究生院、科廷大学地球科学研究所和澳大利亚 IGCP 委员会资助，特此鸣谢。

作者简历及攻读学位期间发表的学术论文与研究成果

王冲，1990.09 出生于山东滕州，中共党员

教育经历：2009.09－2013.06 山东科技大学 工学学士

2013.09－2016.07 中国科学院地质与地球物理研究所—中国科学院大学 理学硕士

2016.09－ 中国科学院地质与地球物理研究所—中国科学院大学 攻读理学博士

2017.08－ 澳大利亚科廷大学（2017.08–2019.01）联合培养攻读博士

研究兴趣：岩石学、古地磁学

基性岩墙群、大火成岩省、超大陆

博士期间成果：

Wang, C., Li, Z.X., Peng, P., Pisarevsky, S., Liu, Y., Kirscher, U., Nordsvan, A., 2019. Long-lived connection between the North China and North Australian cratons in supercontinent Nuna: paleomagnetic and geological constraints. Science Bulletin. https://doi.org/10.1016/j.scib.2019.04.028

Wang, C., Peng, P., Wang, X., Yang, S., 2016. Nature of three Proterozoic (1680Ma, 1230Ma and 775Ma) mafic dyke swarms in North China: Implications for tectonic evolution and paleogeographic reconstruction. Precambrian Research 285, 109–126.

彭澎, **王冲**, 杨正赫, 金正男, 2016. 朝鲜~19 亿年侵入岩的岩石类型与构造背景初探. 岩石学报 32, 2993–3018.

Wang, C., Peng, P., Li, Z.X., Pisarevsky, S., Denyszyn, S., Liu, Y., Gamal El Dien, H., Su. X., Geochronology, geochemistry and paleomagnetism of the 1.24–1.21 Ga Licheng large igneous province in the North China Craton: Implications for paleogeographic reconstruction during Nuna break-up. In preparation

Su, X., Peng, P., **Wang, C.**, Sun, F., Zhang, Z., Zhou, X., 2018. Petrogenesis of a ~900 Ma mafic sill from Xuzhou, North China: Implications for the genesis of Fe–Ti–rich rocks. Lithos 318–319, 357–375.

彭澎, 孙风波, **王冲**, 王欣平, 苏向东, 张志越, 周小童, 2018. 华北和圣弗朗西斯科克拉通前寒武纪地质对比. 地质科学 53, 363–399.

Wang, X., Peng, P., **Wang, C.**, Yang, S., Söderlund, U., Su, X., 2017. Nature of three episodes of Paleoproterozoic magmatism (2180 Ma, 2115 Ma and 1890 Ma) in

the Liaoji belt, North China with implications for tectonic evolution. Precambrian Research 298, 252–267.

彭澎, 王欣平, 周小童, **王冲**, 孙风波, 苏向东, 陈亮, 郭敬辉, 翟明国, 2017. 8.1 亿年千里山基性岩墙群的厘定及其对华北克拉通西部地质演化的启示. 岩石学报 34, 1191–1203.

Yang, S., Peng, P., Qin, Z., Wang, X., **Wang, C.**, Zhang, J., Zhao, T., 2017. Genetic relationship between 1780Ma dykes and coeval volcanics in the Lvliang area, North China. Precambrian Research.

Peng, P., Yang, S., Su, X., Wang, X., Zhang, J., **Wang, C.**, 2017b. Petrogenesis of the 2090 Ma Zanhuang ring and sill complexes in North China: A bimodal magmatism related to intra-continental process. Precambrian Research 303, 153–170.

Peng, P., Feng, L., Sun, F., Yang, S., Su, X., Zhang, Z., **Wang, C.**, 2017a. Dating the Gaofan and Hutuo Groups–Targets to investigate the Paleoproterozoic Great Oxidation Event in North China. Journal of Asian Earth Sciences 138, 535–547.

参加学术会议：

美国地球物理学会（American Geophysical Union）秋季会议，2018.12.10–12.14 华盛顿. 海报

澳大利亚地质协会地球科学学生研讨会（Geological Society of Australia Earth Science Student Symposium）西澳洲分会，2018.11.29 珀斯. 口头报告

澳大利亚地球科学会议（Australian Geoscience Council Convention），2018.10.14–10.18 阿德莱德. 口头报告

变质岩与前寒武纪地质学 2017 年全国学术研讨会，2017.05.06–05.07 北京. 口头报告

第七届国际岩墙会议（7th International Dyke Conference），2016.08.18–08.20 北京. 口头报告

获奖情况：

中国科学院大学 三好学生（2017）

中国科学院大学 一等学业奖学金（2017）

博士研究生国家奖学金（2017）

School of Earth and Planetary Sciences
Faculty of Science and Engineering

Paleogeographic Reconstruction of the North China Craton in the Supercontinent Nuna/Columbia: Paleomagnetic and Geological Constraints

Chong Wang
0000-0002-7948-6554

This thesis is presented for the Degree of
Doctor of Philosophy
of
Curtin University

January 2020

Declaration

To the best of my knowledge and belief this thesis contains no material previously published by any other person except where due acknowledgment has been made.

This thesis contains no material which has been accepted for the award of any other degree or diploma in any university besides the joint HDR program between the Institute of Geology and Geophysics, Chinese Academy of Sciences, and Curtin University, Australia.

Signature: 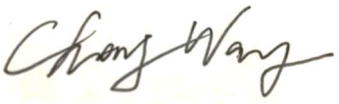

Date: 14.01.2020

Content

ABSTRACT

It has been proposed that the assembly of the supercontinent Nuna (also known as Columbia) occurred during ~1.8–1.6 Ga, and that of the supercontinent Rodinia occurred at ~1.0–0.9 Ga, but the exact configurations of the two early supercontinents are still in debated. The North China Craton (NCC) has abundant Precambrian geological records, but its positions in the two supercontinents are still controversial. This study aims to explore the position of the NCC in Nuna through geochronological, geochemical and paleomagnetic analyses of mafic dykes in the Jidong, Luxi and southern Taihang regions. Through baddeleyite U–Pb analyses, dykes with ages of 1233 ± 27 Ma (SIMS), 1206.7 ± 1.7 Ma (TIMS), 1214.0 ± 4.9 Ma (TIMS) and 1236.3 ± 5.4 Ma (TIMS) have been identified. The ~1.24–1.21 Ga magmatism in the NCC is subalkaline to alkaline basaltic composition. Geochemical data indicate an intraplate tectonic setting with ocean island basalt (OIB)–like trace element signatures. In addition, the radiating dykes cover an area of > 0.1 Mkm^2, indicating a ~1.24–1.21 Ga LIP event caused by a mantle plume in the NCC, namely the Licheng LIP. Detailed rock magnetic and paleomagnetic analyses have been carried out on these and other previously dated mafic dykes, with ages of ~1.68, 1.24 and 1.21 Ga in the three previously mentioned regions of the NCC. Rock magnetic experiments, including κ–T curves, Lowrie and hysteresis loop experiments show that the main magnetic carrier is the paleomagnetically stable single (or pseudo–single) domain low–Ti titanomagnetite. Three ~1.68 Ga dykes give a mean paleopole at 55.6°N, 258.1°E (A_{95} = 7.2°). Combining this pole with previously published data from the <1.71–1.61 Ga (best estimate ~1.70–1.67 Ga) Yunmengshan Formation in southern NCC, these units give a mean ~1.68 Ga paleomagnetic pole at 59.8°N, 265.3°E (A_{95} = 3.3°, N = 18). Nine ~1.24 Ga dykes give a mean paleomagnetic pole at 2.6°N, 165.1°E (A_{95} = 10.8°), supported by a positive baked contact test. One ~1.21 Ga dyke give a VGP at -23.0°N, 92.5°E (A_{95} = 6.1°). Comparable coeval paleopoles and apparent polar wander paths for the North China and proto-Australian cratons suggest their possible connection during ~1.78–1.32 Ga, but separation after that time.

Such an interpreted long-lived connection is supported by ~1.73–1.32 Ga geological similarities between the Yanliao rift of the NCC and the McArthur Basin of the North Australian Craton. Their similarities include (1) comparable sedimentary lithology, and eukaryotic microfossils *Valeria lophostriata*, (2) styles of ore deposits (manganese and iron), (3) hydrocarbon-bearing potential (hydrocarbon source rocks), and (4) coeval

magmatism (mafic and fesic intrusive magmatism, and volcanic events). In summary, based on the comparable paleomagnetic data and geological histories, this work proposes a long-lived connection between the northeastern NCC and northwestern proto-Australia for the duration of the supercontinent Nuna/Columbia.

Key Words: North China Craton, Mafic dyke swarm, Large igneous province, Paleomagnetism, Supercontinent Nuna/Columbia

ACKNOWLEDGEMENTS

I sincerely appreciate my supervisors Prof. Peng Peng, Prof. Zheng-Xiang Li and Dr. Sergei Pisarevsky, for their academic guidance during my PhD career.

Prof. Peng introduced me to the field of mafic dykes and supercontinents. He gave me great guidance with a high degree of personality, charm and solid professional Precambrian geological skills. In the early learning stage, I focused on field investigation, petrology, geochronology, and geochemistry. I especially thank Prof. Peng for his systematic training, including the guidance of English writing, which has enabled me to quickly improve. Prof. Peng is an excellent supervisor who trains students in a skilful way, and respects students' personal ideas.

To reconstruct the Precambrian paleogeography objectively and scientifically, I decided to study paleomagnetism. Special thanks to Prof. Zheng-Xiang Li for providing the opportunity to study abroad. Learning at Curtin University has improved my knowledge of supercontinents and the study of paleomagnetism significantly. I will never forget the first time I had a meeting with Prof. Li, when he encouraged me to be critical. Prof. Li's first-class international level, advanced research thinking, high standards and strict training requirements, rigorous attitude, and the spirit of excellence will benefit me for life. Special thanks also to Sergei for his guidance. Sergei is serious, humble, humorous, and confident. He always guided me with such rigor, patience, and seriousness. He helped me revise my manuscript many times. He is so strict on the details, which influenced me greatly.

Special thanks to Profs. Jinghui Guo, Mingguo Zhai, Xianhua Li, Taiping Zhao and Baochun Huang for their guidance and indeed impact on me. Thanks to Xinping Wang, Shuyan Yang, Fengbo Sun, Xiangdong Su, Zhiyue Zhang, Xiaotong Zhou, Dongjian Ouyang, Zhaoyuan Qin, Peng Liou, Haozheng Wang, Xiahong Cui, Jun Hu, Ligang Zhou, Dan Wang, Yi Zou, Guangyu Huang and others. Thank you for your help from the extended family of the Precambrian Geology Group. Special thanks to Yonggang Yan, Qian Zhao, Wenxing Hao, Huiru Xu and Jie Yuan for their technical guidance on drilling and knowledge exchange. During my study abroad, I would like to thank the teachers and students of the Earth Geodynamics Research Group for their academic help and especially thank Yebo Liu, Weihua Yao, Josh Beardmore, Uwe Kirscher, Nan Zhang, Ross Mitchell, Hamed Gamal El Dien, Lei Wu, Adam Nordsvan, Erin Martin, Amaury Pourteau, Bill Collins, Chris Spencer, Brendan Murphy, Luc Doucet, Silvia

Volante and others. Thanks for the high-level of active and open international research group led by Prof. Li. In this group, I know more, think more, and improve more. Thanks to Dr. Steven Denyszyn for his help during the dating. Special thanks to Yebo Liu and Yurong Liu, Shaojie Li, Kai Wang, Weihua Yao, Jiangyu Li, Zhongwei Wang, Xuemei Yang, Qiang Jiang and Mingjian Cao for taking care of my life abroad. Thanks to my Australian friends at the Wilson Community Church for helping me improve my English.

Special thanks to my parents for their understanding and support of my studies. Thanks to everyone who has helped me, to those who have known me, to fate and all the other bits of life.

This research was funded by the National Science Foundation of China projects 41890833, 41772192, and the Australian Research Council Laureate Fellowship project FL150100133 to Prof. Li. Participation in the conference was also supported by the Curtin University Graduate School, TIGeR, and the Australian IGCP Committee.

1. Introduction

Three supercontinents have been hypothesized in Earth's history, i.e., Pangea, Rodinia and Nuna/ Columbia (e.g., Li et al., 2008; Rogers and Santosh, 2002; Seton et al., 2012; Zhao et al., 2002). Among these, the configuration and evolution history of both Rodinia and Nuna/Columbia are still controversial (Evans et al., 2016). Recent paleomagnetic and geological studies suggest that Nuna/Columbia may have formed at ~1.6 Ga (Kirscher et al., 2019; Nordsvan et al., 2018; Pisarevsky et al., 2014a; Pourteau et al., 2018), much later than the previously proposed 2.0–1.8 Ga (Zhang et al., 2012; Zhao et al., 2002). However, its break-up process and timing are far less well constrained, with a possible starting age of ~1.45–1.38 Ga (Pisarevsky et al., 2014a). Evans and Mitchell (2011) proposed that Nuna's core (Laurentia-Baltica-Siberia) broke up between 1.50 Ga and 1.25 Ga, marked by 1.38–1.35 Ga and 1.27 Ga magmatic events. Details of Nuna's break-up in the Proterozoic are unclear (e.g., Meert, 2014; Pisarevsky et al., 2014b).

Paleogeographic reconstruction of the North China Craton (NCC) in Nuna is always controversial (e.g., Hou et al., 2008; Peng, 2015b; Wan et al., 2015; Zhang et al., 2012; Zhao et al., 2002). For example: (1) the northern part of North China is connected to the eastern part of India at ~1.8 Ga based on comparison of Central India Tectonic zone (CIZ) and Trans–North China Orogen (TNCO) and basements, including Archean crust–forming event, dome and basin structures and metamorphic evolution of the late Archean granulites (Zhao et al., 2002) and suggested Andean–type continental margin arc in the south of NCC (Zhao et al., 2011; Zhao et al., 2003) (Figure 1a); (2) the southern part of NCC is connected to the southwest of India (1.78 Ga) (Peng et al., 2005), and/or the southeast NCC is connected to the western part of Laurentia (1.78Ga) (Hou et al., 2008); (3) the southern part of NCC is connected to southern Baltica and Congo–São Francisco craton (1.78 –0.92 Ga) based on magmatic barcode (Peng, 2015a) (Figure 1d); (4) the northeastern part of NCC is connected to North Australian Craton (NAC) based on the 1.32 Ga mafic sills and proposed LIP (Zhang et al., 2017) (Figure 1f); (5) northern part of NCC is connected to NAC based on paleomagnetic data (Figure 1e) (Zhang et al., 2012). There are other versions though (e.g., Cederberg et al., 2016; Teixeira et al., 2017). In summary, there are wide debates about the paleogeographic positions of the NCC in Paleo–, Meso– and Neoproterozoic.

Based on previous studies, the applicant carried out geochronological, petrological and paleomagnetic analyses on the late Paleoproterozoic to Mesoproterozoic mafic dykes

in the NCC, especially on ~1.68 Ga and ~1.24–1.21 Ga dykes, to reconstruct the paleogeographic history of NCC by paleomagnetism and comprehensive geological comparisons.

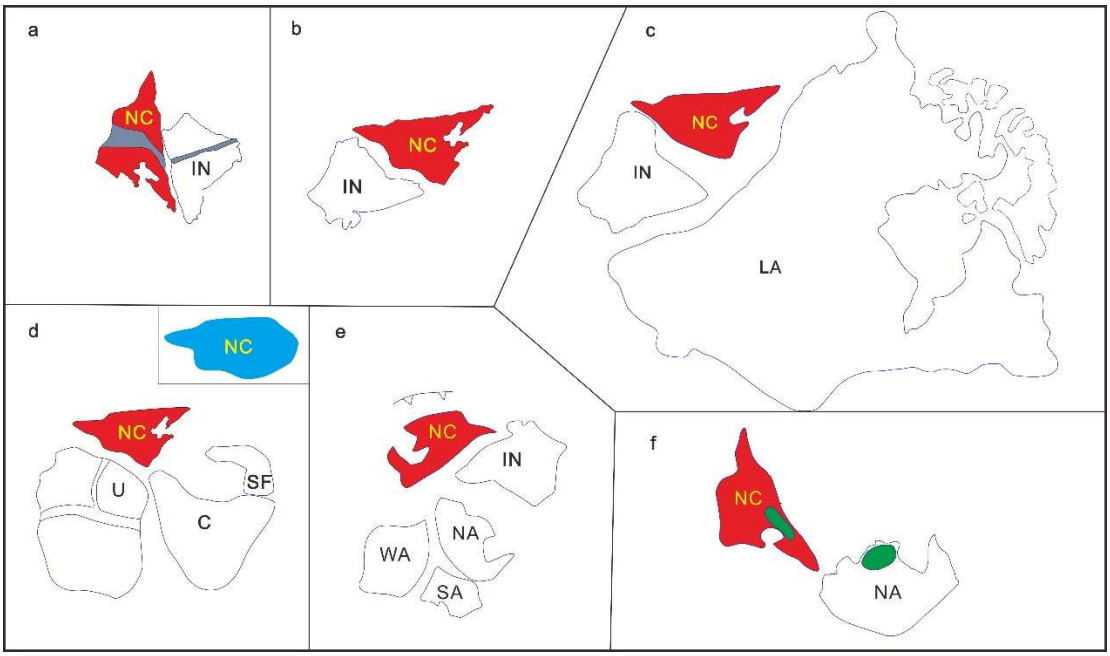

Figure 1 Reported models showing the NCC and its neighbours in Precambrian. a: northern part with India by late Paleoproterozoic orogenic belt (Zhao et al., 2002); b: southwest part with India by 1.78 Ga dykes and rifts (Peng et al., 2005); c: NC, India and Laurentian connection by late Paleoproterozoic dyke swarms (Hou et al., 2008); d: Southern part of NC connected with the Baltica Craton and Congo– São Francisco Craton at ~1.78–0.92 Ga based on dyke swarms (Peng, 2015b); e: Northern part of NCC with India and Northern Australia by paleomagnetism (Zhang et al., 2012); f: Northern part of NC with Northern Australia by ~1.32 Ga mafic sills (Large Igneous Province) (Zhang et al., 2017). Note that the original outline of the NCC in Peng (2015b) showing in the inset part of d, which reconstruct the sinistral slip of the Tan–Lu fault. NC–North China; IN–India; NA–Northern Australia; WA–Western Australia; SA–Southern Australia; U–Ukrainian; C–Congo; SF– São Francisco; LA–Laurentian

2. Geological Background

The NCC (or the Sino-Korea Craton) is the oldest craton in China. It has been widely accepted that the NCC experienced orogenic movement at ~1.95–1.85 Ga according to high-pressure and ultrahigh-temperature granulite studies, however, the precise orogenic time and belt divisions are much controversial (Kusky et al., 2007; Peng et al.,

2014; Zhai and Santosh, 2011; Zhao et al., 2012). The final cratonization of the NCC occurred at ~1.8 Ga (Zhai, 2011). Four rift systems have developed on the craton, with their ages ranging from the late Paleoproterozoic to the Neoproterozoic: the Yan–Liao, Zhaertai–Bayan Obo–Huade, Xiong'er and Xu–Huai rift systems (Figure 2a).

The Yan–Liao rift lies in the northern part of the NCC. It has two branches: one to the northeast, and another to central NCC. This rift is mainly filled with the ~1.7–1.6 Ga sandstones and shales (Changcheng System), the 1.6–1.4 Ga carbonates (Jixian System), the 1.4–1.35 Ga clastic rocks (Xiamaling Formation), and the possible Neoproterozoic clastic rocks (Qingbaikou System) (Su et al., 2010). Besides, several generations of magmatism have been reported in this area, including the ~1.75–1.68 Ga anorthosite–rapakivi granite suites intruding the Archean units (Yang et al., 2005; Zhang et al., 2007; Zhao et al., 2004a), the 1.64–1.62 Ga volcanics accompanying the strata (Lu and Li, 1991; Zhang et al., 2013), the ~1.32 Ga mafic sills intruding several formations (e.g., Zhang et al., 2017), as well as the ~1.68 and ~1.23 Ga mafic dykes intruding the Archean basement (Wang et al., 2016; Wang et al., 2015).

The E–W trending Zhaertai–Bayan Obo–Huade rift lies in the northern part of the NCC. It contains four possibly paratactic groups (the Zhaertai, Bayan Obo, Huade and Langshan groups) outcropped in various places. The sedimentary sequences are metamorphosed to low grades. Some of the strata have recently been dated with ages spreading from late Paleoproterozoic to the Neoproterozoic (e.g., Liu et al., 2017).

The Xiong'er rift lies in the southern part of the NCC. It has three branches: two along the southern margins, and one towards the interior of the NCC. This rift contains mainly of clastic deposits (the ~1.8–1.6 Ga Xiong'er, Ruyang and Luoyu groups) and carbonates (the <1.6 Ga Guandaokou Group). Importantly, 1.78 Ga volcanics are developed within the Xiong'er rift (Zhao et al., 2004b). These volcanics may be part of a LIP including a coeval giant mafic dyke swarm (Peng et al., 2008).

The Xu–Huai rift lies in the southeastern part of the NCC. This rift mainly formed in the early Neoproterozoic (He et al., 2017). Notably, 0.92–0.89 Ga mafic sills are found intruding several formations of this rift (e.g., Peng et al., 2011a; Zhang et al., 2016).

Episodes of Precambrian mafic intrusions have been reported from the NCC, including events at 1.78 Ga, 1.73 Ga, 1.68 Ga, 1.62 Ga, 1.32 Ga, 1.23 Ga, 0.92–0.89 Ga and 0.81 Ga (Peng, 2015b). Among them, the 1.78, 1.32 and 0.92–0.89 Ga events have been widely studied (e.g., Peng et al., 2011a; Peng et al., 2011b; Peng et al., 2008; Zhang et al., 2017; Zhang et al., 2016).

For the 1.68 Ga generation, two mafic dykes with baddeleyite ages have been reported. One is from Luxi area, namely Laiwu dyke (LX307; Figure 2b) (Li et al., 2015). This dyke is NNW (340–350°) trending, yielding age of 1680 ± 5 Ma, with ~30 vol.% clinopyroxene and ~65 vol.% plagioclase (Li et al., 2015). Another one is from Jidong area, namely Tujiagou dyke (JD689; Figure 2c) (Wang et al., 2016). This dyke is NE trending (?), yielding age of 1677 ± 12 Ma, with typical ophitic texture (Wang et al., 2016).

For the 1.23 Ga generation, Wang et al. (2015) reported several NE-trending mafic dykes in the north and northeast of the Jidong area (Figure 2c), and suggested that the 1.27–1.21 Ga magmatism represents a mantle plume event correlated with similar-aged events in other continents. The age of this magmatic event was determined by U-Pb SIMS baddeleyite dating on the Licheng dyke swarm in central NCC at 1229 ± 4 Ma (Peng, 2015b), and on dykes in nearby regions at 1228 ± 4 Ma and 1236 ± 7 Ma (Wang et al., 2016; Xiang, 2014) (Figure 2c, d). In addition, one gabbro intrusion with a U-Pb SHRIMP zircon age of 1209 ± 6 Ma was reported from Yishui, Luxi region (Peng et al., 2013) (Figure 2b) and two dykes with U-Pb LA-ICPMS zircon ages of 1244 ± 28 Ma and 1226 ± 11 Ma were reported from the east Tan-Lu fault (northeast NCC) (Pei et al., 2013; Wang et al., 2015) (Figure 2a). Thin mafic dykes in the Bayan Obo region yielded a Sm-Nd isochron age of 1227 ± 60 Ma (Yang et al., 2011).

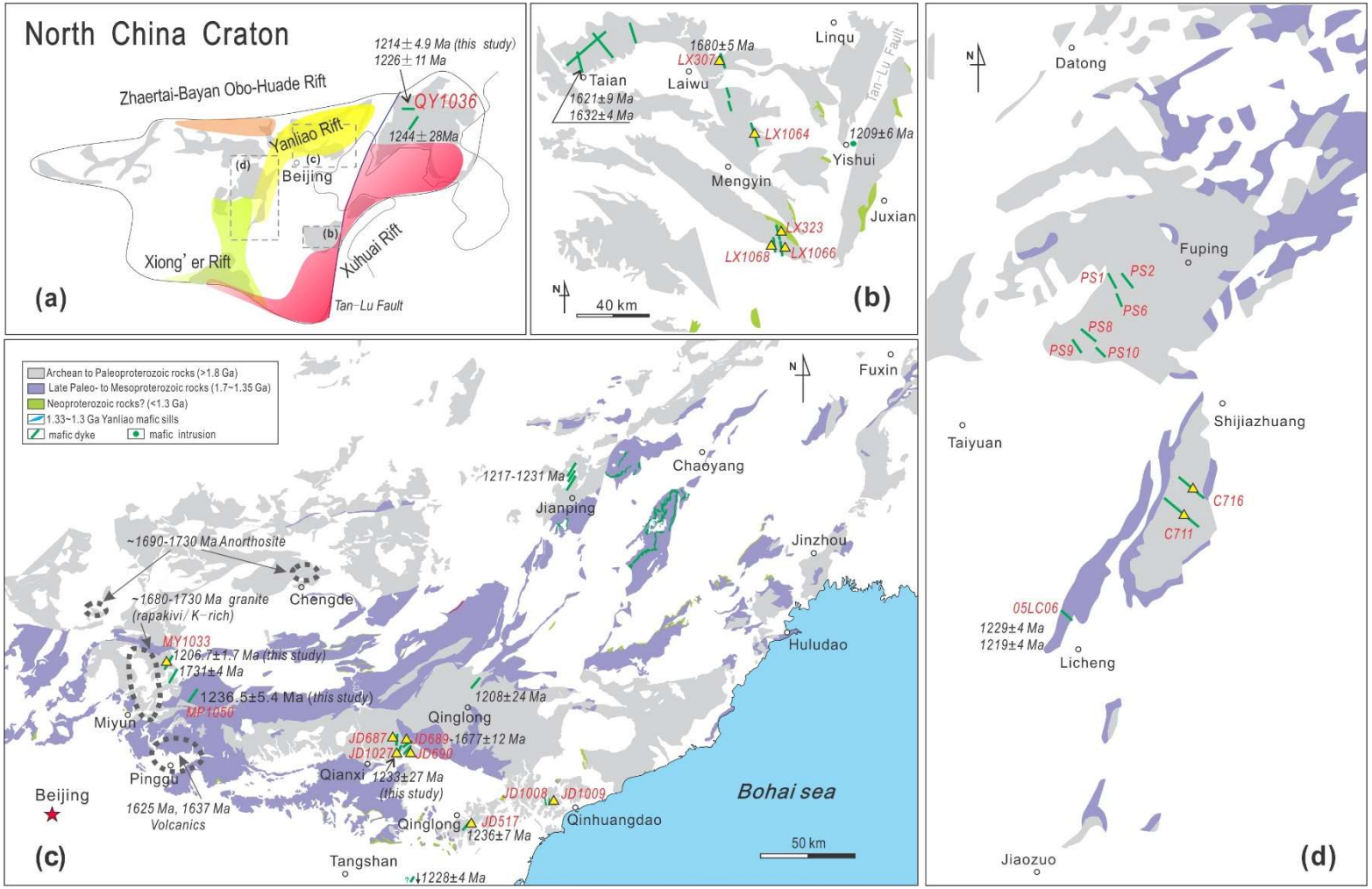

Figure 2 Sketched geological map of the study areas. (a) NCC, with distributions of late Paleoproterozoic to Neoproterozoic rifts; (b–d) Luxi, Beijing to Jidong, and southern Taihang Mt. respectively. Triangles represent paleomagnetic sample locations.

3. Field observations, Petrology and Sampling

Most studied dykes intrude the Archean basement (Figure 2b-d). The geological map shows that the Mipu dyke (MP1050) (Figure 2c) intrudes the ~1.56 Ga Gaoyuzhuang Formation and the older Changcheng Group in the Yan–Liao rift. However, their relationship is hard to identify in the field as the severe vegetation cover and weathering. These dykes show varying trends. In the Jidong area, the Laowangjia dyke at Taipingzhai Town, Qianxi County (JD1027; Figure 2c) is located adjacent to near the previous studied Laolijia dyke (JD687; Wang et al., 2016). The Laowangjia dyke (about 24° strike and > 30 m wide) intrudes the Archean gneisses with clear but weathered and fragmented chilled margins. The interior part of this dyke has coarse granular texture (Figure 3a, b). The Xitongye (JD1008) and Dongtongye (JD1009) dykes show near N-S trends (striking ~350–002°, azimuth directions). The exposed part of the JD1009 dyke is ~10 m wide but no margin is exposed. The studied rocks mainly consist of plagioclase (50–55%) and pyroxene (35–40%) with minor amount of biotite, Fe-Ti oxides and zircon (Figure 3g, h). The Baihejian dyke (MY1033) is located northeast of the Miyun town (Figure 2c). This dyke has a 35° strike and is approximately 80 m wide with clear chilled margins (Figure 3c). The rocks are diabase with ophitic texture (Figure 3i). The Mipu dyke (MP1050) is located southeast of dyke MY1033, in Xinglong Town, Chengde City. This dyke trends NE. The rocks have coarse minerals but suffered from weathering.

In central NCC, two dykes (C711 and C716; Figure 2d) intruded the Archean units (Figure 3d, e). These dykes are over 15 m wide, trending to the NW (~310°). Spheroidal weathering is ubiquitous (Figure 3e). These rocks are composed of plagioclase (~50%) and pyroxene (~40%), with hornblende (clear cleavage; 2–5%), biotite (2–5%) and Fe-Ti oxides (~5%) (Figure 3j, k). In the Luxi area (Figure 2b), four studied dykes (LX323, LX1064, LX1066 and LX1068) show NNW trend (~352°) and are 10–20 m wide. Chilled margins are easily identifiable along contact with the host granites (Figure 3f). The Jiaopo dyke (LX1064) has been petrographically described by Wang et al. (2007). It consists of ~40% clinopyroxene and ~50% plagioclase with minor hornblende, biotite, quartz and chlorite (sample 05SD-21). In general, the plagioclase grains in these dykes are over 1 mm in length, with various degrees of saussuritization (Figure 3g-l). Clinopyroxene is fresh and small compared to plagioclase (Figure 3g-l). Fe-Ti oxides are usually 0.1– 0.5 mm in size and exist as euhedral crystals within a plagioclase and clinopyroxene groundmass (Figure 3g-l).

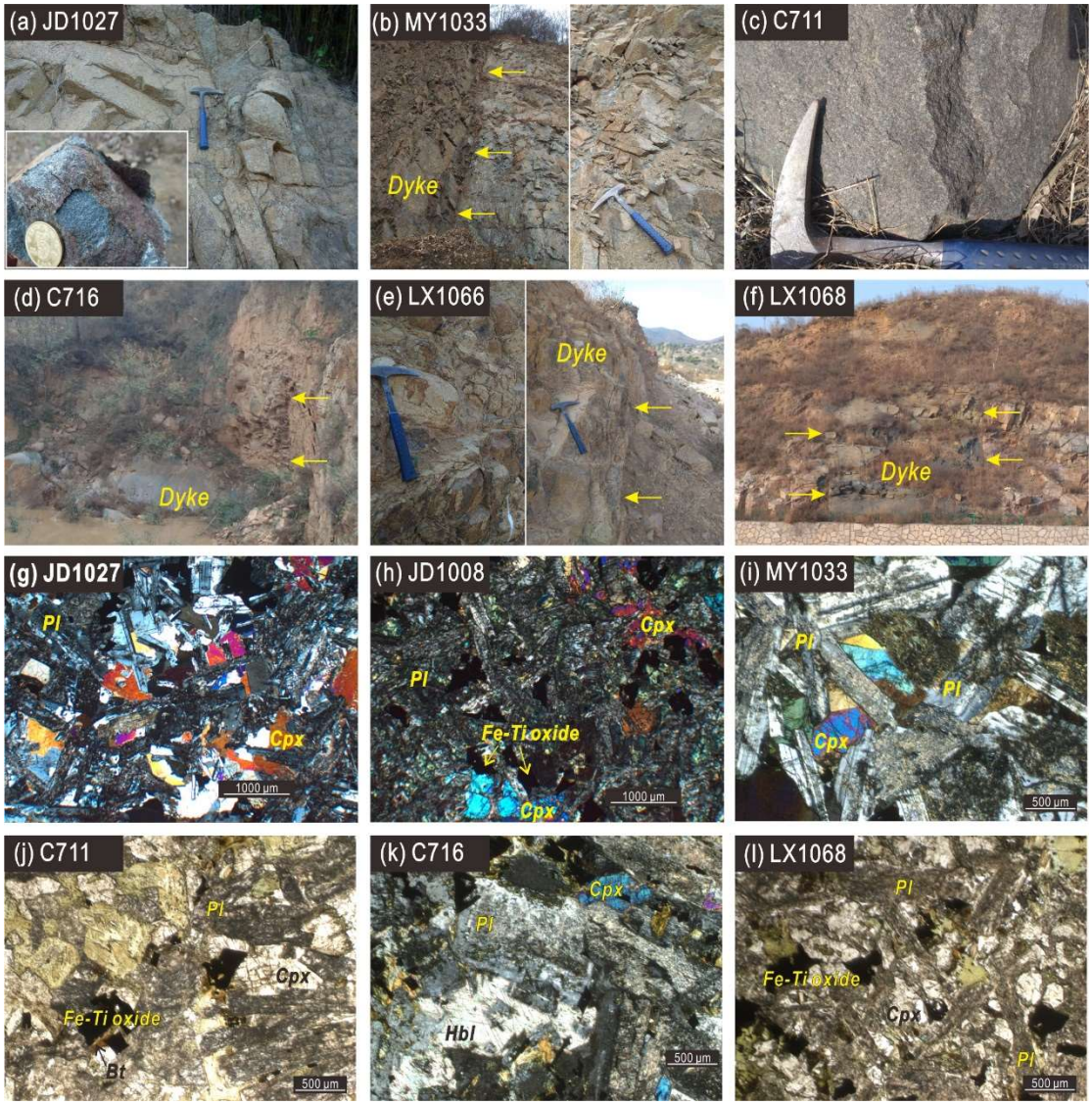

Figure 3 Representative photos of outcrops and block samples (a-f) and thin sections microphotographs (g-l). Arrows in (b, d-f) indicate (near) vertical and regular boundaries between mafic dykes and country rocks. Pl-plagioclase, Cpx-clinopyroxene, Hbl-hornblende, Bt-biotite. Microphotographs (j) and (l) are under single polarized and (g-i, k) are under cross polarized lights.

For geochronological analyses, baddeleyites were extracted from the Baihejian (MY1033), Mipu (MP1050) and Laowangjia (JD1027) dykes of the Jidong region (Figure 2c). Additionally, one dyke in Qingyuan, northern Liaoning province (sample 12LN54-1; Wang et al., 2015) is re-dated by using baddeleyite U-Pb TIMS method (dyke QY1036; Figure 2a). Samples for geochemical analyses were collected from the Laowangjia (JD1027), Xitongye (JD1008), and Dongtongye (JD1009) dykes of the Jidong area (Figure 2c), from the Wucaizhuang (LX323), Jiaopo (LX1064), Xiayandian

(LX1066) and Gaojiaweizi (LX1068) dykes of the Luxi area (Figure 2b) and from the Renjiadong (C716) and Nangou (C711) dykes of the central NCC (Figure 2d).

For paleomagnetic study, 13 dykes have been drilled (Figure 2), excluding the Xitongye, Mipu and Qingyuan dykes (JD1008, MP1050 and QY1036), but including the Laolijia dyke (JD687) and 1236 ± 7 Ma Maojiagou dyke (JD517), 1677 ± 12 Ma Tujiagou dyke (JD689) and nearby dyke (JD690) in Jidong (Wang et al., 2016) (Figure 2c), as well as 1680 ± 5 Ma Laiwu dyke in Luxi (Li et al., 2015) (Figure 2b). For each dyke (treated as one site), 7–15 oriented samples were collected from scattered outcrops. All samples were oriented using a magnetic compass, but some also by sun compass depending on the weather conditions.

4. Research Methods

4.1 Geochronology

Standard density and magnetic techniques were used for baddeleyite separation from rock powders at the Yu'neng Geological and Mineral Separation Survey Centre, Langfang City, and the Institute of Geology and Geophysics, Chinese Academy of Sciences (IGGCAS). The U–Pb dating of sample 1027LWJ1 was carried out on a CAMECA SIMS 1280 facility at the IGGCAS, after the procedures illustrated by Li et al. (2009). Before measurement crystal grains were fixed and polished on a resin disk, then observed by backscattered electron (BSE) images and by transmitted and reflected photomicrographs. Standard baddeleyite *Phalaborwa* was measured to check the Pb isotope fractionation. Non-radiogenic ^{204}Pb from present crust is used for correcting the raw data (Stacey and Kramers, 1975).

The U–Pb dating of samples 1033BHJ1, 1036QY1 and 1050MP1 were carried out on a Thermo Triton Plus mass spectrometer TIMS facility at Curtin University, Australia. No pre-treatment methods were used beyond cleaning the grains with concentrated distilled HNO_3 and HCl and, due to their small size, no chemical separation methods were required. Before measurement, the samples were spiked with an in-house ^{205}Pb-^{235}U tracer solution and dissolved in the clean-lab facilities of the University of Western Australia. Dissolution and equilibration of spiked single crystals was by vapour transfer of HF, using Teflon microcapsules in a Parr pressure vessel placed in a 230°C oven for six days. The resulting residue was re-dissolved in HCl and H_3PO_4 and placed on an outgassed, zone-refined rhenium single filament with 5 μL of silicic acid gel. Uranium

was measured as an oxide (UO_2). Fractionation was monitored using SRM981 and SRM 982. Mass fractionation was 0.04 ± 0.09 %/amu, and U decay constants used were from Jaffey et al. (1971). Data were reduced and plotted using the software packages Tripoli (from CIRDLES.org) and Isoplot 4.15. The weights of the baddeleyite crystals were calculated from measurements of photomicrographs and estimates of the third dimension.

4.2 Geochemistry

Representative samples were ground into powder at the IGGCAS. The whole-rock major and trace elements measurements were carried out at the IGGCAS (including dykes of JD1008, JD1009, JD1027 and C716) and the ALS Minerals – ALS Chemex (Guangzhou) Co Ltd (including dykes of C711, LX323, LX1064, LX1066 and LX1068). The loss on ignition (LOI) was determined as the weight loss after one hour's baking at constant 1000°C. Powdered samples were mixed with lithium tetraborate and cosolvent into fused disks and then analysed by X-ray fluorescence AXIOS Minerals (IGG) and PANalytical PW2424 (ALS). Precision was better than 5%.

At the IGG, samples for trace-element analyses were digested in acid (HNO_3+HF) for seven days at 200°C, then measured by Inductively Coupled Plasma Mass Spectrometry (ICP-MS) Element. At the ALS, samples for trace-element analyses were dissolved at high temperature (>1025°C) with Lithium metaborate/ lithium tetraborate, then constant volume by HNO_3+HCl+HF, and measured by an ICPMS Agilent 7700x. While, for Cr and Ni elements analyses at the ALS, the samples were dissolved by $HClO_4$+HNO_3+HF, then measured by an ICPMS Agilent 7900 after HCl constant volume. The relative standard deviation was better than 10%.

4.3 Rock magnetism, magnetic fabric and paleomagnetism

Rock magnetic analyses include thermal-magnetic experiments (κ-T curves) and progressive thermal demagnetization of triaxially orthogonal isothermal remanent magnetization (IRM) (Lowrie, 1990). κ-T curves were obtained from uniform fine-powders on a kappabridge susceptibility meter (MFK1-FA) linked with a CS4 furnace. Representative samples have been magnetically saturated along three mutually orthogonal axes by 0.12, 0.4, and 3.0 T, then thermally demagnetised in the Magnetic Measurements Thermal Demagnetizer (MMTD) and measured in a JR-6A spinner magnetometer. Anisotropy of magnetic susceptibility (AMS) was measured with the MFK1-FA before demagnetization.

Most specimens were put through progressive thermal demagnetization, some were applied to the alternating field (AF) demagnetization. Thermal demagnetization was conducted in about 17 steps from 100°C to 580°C using an ASC TD-48SC and a MMTD. The remanent magnetization has been measured in a magnetically shielded room with a 2G 755 superconducting rock magnetometer with a vertical Model 855 automated sample handler, though sometimes a spinner magnetometer JR-6A was used. Remanence vectors were computed by principal component analysis (Kirschvink, 1980) with a maximum angle of deviation (MAD) less than 10° for almost all the samples, and site-mean directions were calculated directly by stable endpoints with the PuffinPlot software (Lurcock and Wilson, 2012). Paleogeographic reconstructions were built with the GPlates software. All analyses have been carried out at Curtin University, Australia.

5. Geochronology

About 40 baddeleyite crystals were isolated from 20 kg of sample 1027LWJ1 (Laowangjia dyke-JD1027; Figure 2c). These crystals have a tabular shape (50–80 μm × 10–20 μm) and are brownish in colour (Figure 4a). Only six spots (from six grains) were analysed by SIMS due to the small size of the crystals. $^{206}Pb/^{204}Pb$ ratios range from 1069 to 47966. Four have $^{207}Pb/^{206}Pb$ apparent ages of 1202–1246 Ma (Figure 4a; Table 1). Six analyses yield a weighted-mean $^{207}Pb/^{206}Pb$ age of 1233 ± 27 Ma (MSWD = 0.55) (Figure 4a). It has been observed that no microcrystalline zircon coatings were observed around these baddeleyites, so the high uncertainties for the two spots could arise from common ^{204}Pb contamination during analyses, possibly resulting from beam diameters (30 × 20 μm) significantly overlapping the crystal's edge (spot 3) or internal fissures (spot 6) (Figure 4a). Nevertheless, given the overall coherence of the $^{207}Pb/^{206}Pb$ age, we argue that the 1233 ± 27 Ma age represents the crystallization age of this dyke.

For U-Pb ID-TIMS analysis, five small baddeleyite crystals were analysed from sample 1033BHJ1, Miyun town (dyke MY1033; Figure 2c and Table 1). Calculated U concentrations were between 85 and 218 ppm. The data are variably discordant (Figure 4b), indicating some degree of Pb loss, probably largely from the microcrystalline zircon overgrowths. The coherence of the $^{207}Pb/^{206}Pb$ dates indicates any Pb loss was recent, which supports our interpretation of the weighted-mean $^{207}Pb/^{206}Pb$ age

representing the magmatic emplacement age of the dyke. The weighted-mean $^{207}Pb/^{206}Pb$ age of all five analyses is 1206.7 ± 1.7 Ma (MSWD = 1.09).

Six single baddeleyite grains were analysed from sample 1036QY1, Qingyuan (dyke QY1036; Figure 2a and Table 1). The grains are rather small, with calculated weights of about 0.2 µg and calculated U concentrations between 178 and 276 ppm. As with the sample 1033QY1, frostings of microcrystalline zircon are considered the source of analysed material that has lost Pb, resulting in 4 of 6 fractions being variably discordant, though 2 fractions yielded concordant data (Figure 4c). A coherent set of $^{207}Pb/^{206}Pb$ dates again indicates that Pb loss was recent, and the weighted-mean $^{207}Pb/^{206}Pb$ age of all six analyses is 1214.0 ± 4.9 Ma (MSWD = 0.49). We consider this to represent the magmatic emplacement age for this dyke.

Four baddeleyite grains were analysed from sample 1050MP1, Mipu dyke (MP1050; Figure 2c and Table 1). U concentrations range from 139 to 198 ppm. Three sets of data are near concordant (Figure 4d). The weighted-mean $^{207}Pb/^{206}Pb$ age of all analyses is 1236.3 ± 5.4 Ma (MSWD = 0.2), representing the emplacement age.

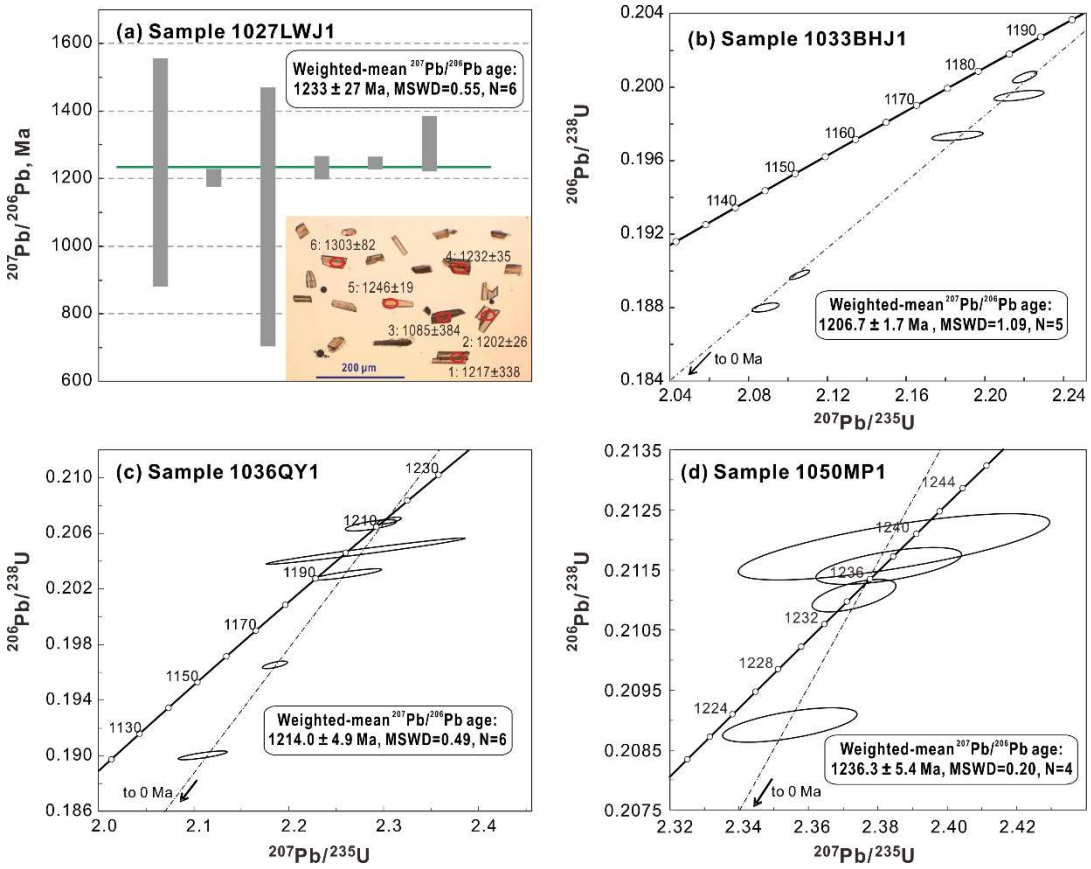

Figure 4 Baddeleyite dating results of mafic dykes. (a) sample 1027LWJ1 from Laowangjia dyke (JD1027) with mineral picture under transmitted light; (b) sample

1033BHJ1 from Baihejian dyke (MY1033); (c) sample 1036QY1 from Qingyuan dyke (QY1036); and (d) sample 1050MP1 from Mipu dyke (MP1050).

Table 1 U–Pb isotopic data for baddeleyites dating of mafic dykes

Spot	^{204}Pb (cps.)	^{206}Pb/^{204}Pb	^{207}Pb/^{206}Pbc	±1σ %	^{207}Pb/^{206}Pb (Ma)	±1σ %
Sample 1027LWJ1						
1	48.8	1069	0.081	8.59	1217.0	338
2	12.6	6699	0.080	0.66	1202.3	26
3	17.1	7766	0.076	9.58	1084.6	384
4	56.6	1358	0.081	0.89	1232.2	35
5	2.2	47966	0.082	0.48	1246.2	19
6	5.8	17229	0.084	2.12	1303.2	82

Grain	wt. (µg)	U (ppm)	Pb_c (pg)	mol% Pb*	Th/U	^{206}Pb/^{204}Pb	^{207}Pb/^{206}Pb	±2σ (%)	^{207}Pb/^{235}U	±2σ (%)	^{206}Pb/^{238}U	±2σ (%)	ρ	^{206}Pb/^{238}U Age (Ma)	±2σ (Ma)	^{207}Pb/^{206}Pb Age (Ma)	±2σ (Ma)
Sample 1033BHJ1																	
1	0.1	131	0.9	94	0	197	0.0803	0.5	2.186	0.5	0.197369	0.1	0.5	1161.17	1.22	1205	8.8
2	0.1	174	0.3	97	0.1	572	0.0803	0.2	2.221	0.2	0.200563	0.1	0.7	1178.34	1.5	1205	3.2
3	0.1	85	0.3	95	0.1	330	0.0806	0.4	2.218	0.5	0.199551	0.1	0.6	1172.91	1.38	1212	8.2
4	0.1	164	0.5	94	0.1	346	0.0805	0.2	2.087	0.3	0.188052	0.1	0.6	1110.81	1.19	1209	4.5
5	0.2	218	0.5	99	0.1	977	0.0804	0.1	2.105	0.2	0.18983	0.1	0.8	1120.45	1.22	1207	2.5
Sample 1036QL1																	
1	0.2	231	0.4	92	0.1	1377	0.0805	0.9	2.11	1	0.190042	0.1	0.8	1121.6	1.58	1209	17.6
2	0.1	193	0.6	94	0.1	428	0.0803	0.9	2.287	1	0.20659	0.2	0.7	1210.62	1.91	1204	17.2
3	0.2	276	3.1	81	0.1	245	0.0808	3.4	2.281	3.8	0.204732	0.4	1	1200.69	4.57	1217	66.6
4	0.2	178	0.4	97	0	938	0.0808	1.2	2.262	1.3	0.203065	0.2	0.9	1191.77	1.91	1216	23.3
5	0.2	224	0.3	91	0.1	1596	0.0808	0.4	2.306	0.5	0.206913	0.1	0.7	1212.35	1.27	1217	7.6
6	0.2	180	0.3	95	0	1345	0.0807	0.4	2.186	0.5	0.196529	0.1	0.7	1156.65	1.26	1213	8.6
Sample 1050MP1																	
1	0.2	187	1.8	84	0.03	146	0.08174	0.61	2.3547	0.67	0.208917	0.11	0.6	1223.04	1.38	1239	11.9
2	0.1	187	1.1	82	0.01	121	0.08170	0.65	2.3832	0.72	0.211568	0.12	0.6	1237.17	1.47	1238	12.8
3	0.2	198	0.6	95	0.06	401	0.08154	0.36	2.3731	0.42	0.211071	0.10	0.6	1234.52	1.28	1235	7.1
4	0.1	139	0.7	79	0.06	89	0.08163	1.39	2.3847	1.54	0.211886	0.21	0.8	1238.86	2.65	1237	27.2

For sample 1027LWJ1: cps., counts per second; ^{207}Pb/^{206}Pbc, corrected ^{207}Pb/^{206}Pb; Pb_c = Total common Pb including analytical blank (0.8±0.3 pg per analysis).
For samples 1033BHJ1 and 1036QL1: weights are calculated from crystal dimensions and are associated with as much as 50% uncertainty (estimated)
Blank composition is: ^{206}Pb/^{204}Pb = 18.55 ± 0.63, ^{207}Pb/^{204}Pb = 15.50 ± 0.55, ^{208}Pb/^{204}Pb = 38.07 ± 1.56 (all 2σ), and a ^{206}Pb/^{204}Pb – ^{207}Pb/^{204}Pb correlation of 0.9.
Th/U calculated from radiogenic ^{208}Pb/^{206}Pb and age.
Measured isotopic ratios corrected for tracer contribution and mass fractionation (0.04 ± 0.09 %/amu).
ρ = error correlation coefficient of radiogenic ^{207}Pb/^{235}U vs. ^{206}Pb/^{238}U.
Ratios involving ^{206}Pb are corrected for initial disequilibrium in ^{230}Th/^{238}U using Th/U = 4 in the crystallization environment.

6. Geochemistry

Whole rock major and trace elements from nine dykes were reported (Table 2). Most samples plot in subalkaline to alkaline basalt zones in element classification diagrams (Figure 5). These dykes show a narrow range of SiO_2 contents (48.4–53.2 wt.%) and MgO contents (4.40–6.22 wt.%). The rocks are characterized by high TiO_2 content (>1.61 wt.%), moderate total iron (tFe_2O_3 content of 11.1–14.7 wt.%), with Na_2O + K_2O content of 3.34–6.22 wt.% (Table 2). The Mg# values are 42.0–52.7 (Mg# = 100 × Mg/ (Fe^{2+}_{total} + Mg), in molecular; Table 2). The compatible elements such as Cr and Ni are 28–336 ppm and 48–93 ppm, respectively (Figure 6f, g). In summary, the MgO present lineal trends with SiO_2, CaO, La, Th and Nb (Figure 6).

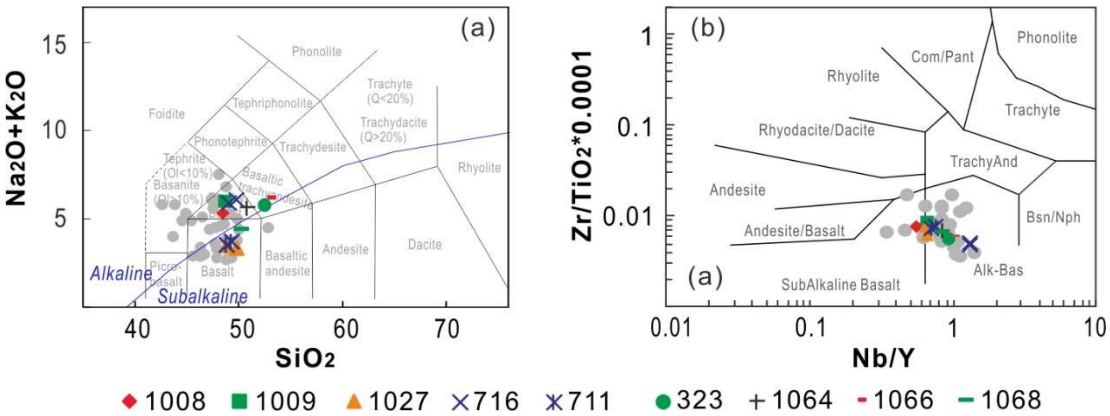

Figure 5 Element classification of the dykes. (a) TAS diagram; (b) Zr/TiO_2 * 0.0001 vs. Nb/Y diagram (after Winchester and Floyd, 1977)

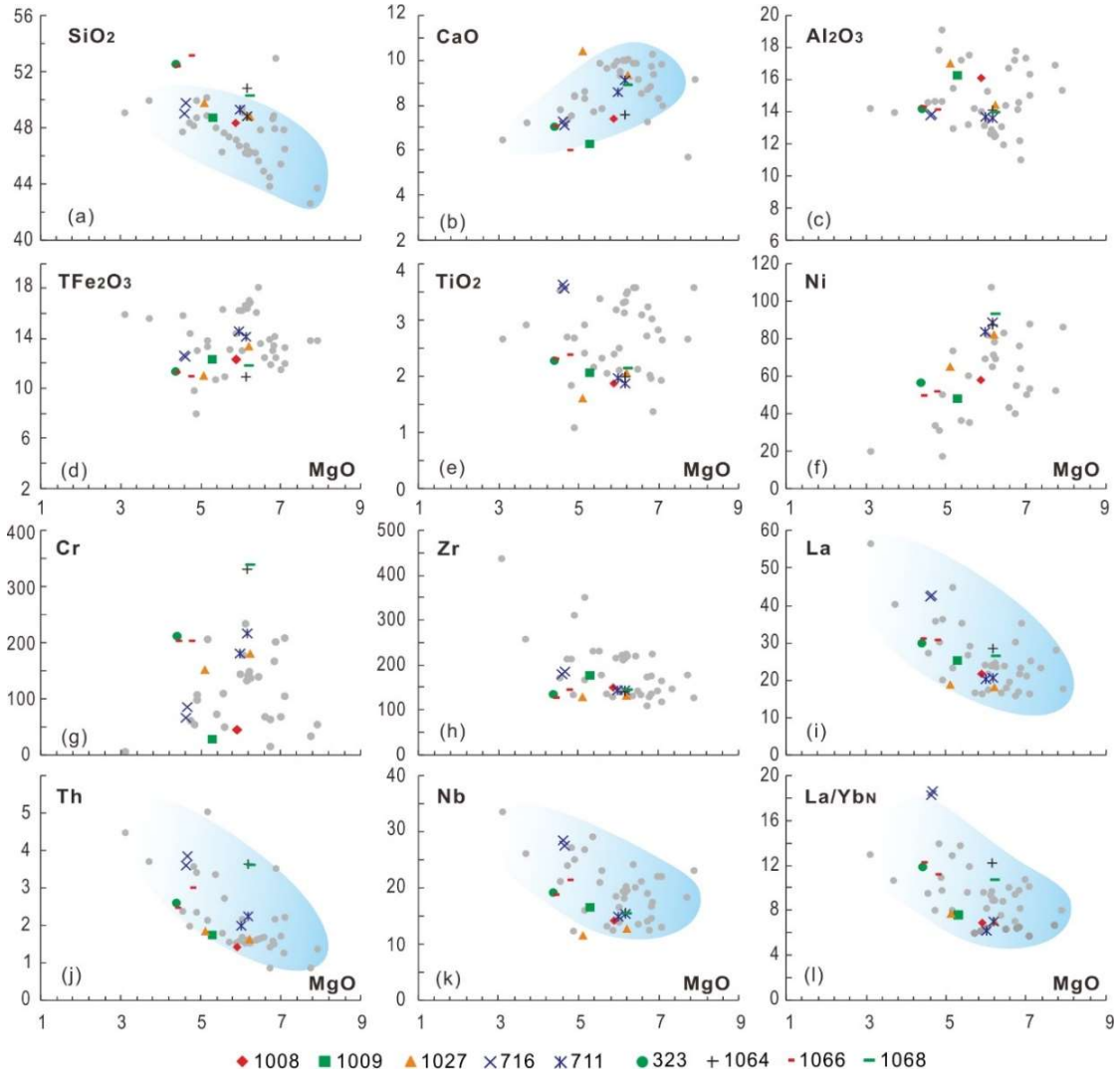

Figure 6 Major and trace elements (ratios) covariant plots. Grey dots represent complied data for the dated 1.24–1.21 Ga mafic intrusions (N = 37) (Peng et al., 2011a; Peng et al., 2012; Peng et al., 2013; Wang et al., 2016; Wang et al., 2015; Xiang et al., 2012).

The studied rocks show moderate to high total rare earth elements compositions (ΣREE = 107–235 ppm) with enriched light REEs (La/Yb_N = 6.15–18.6, Chondrite-normalized value), and minor to strikingly positive Eu anomalies ($Eu/Eu^* = Eu_N/ [(Sm_N) \times (Gd_N)]^{1/2}$, values of 0.97–1.73) (Figure 7a). On the primitive mantle normalized trace element spider diagrams, the Nb is slightly depleted relative to Th and La, whilst Zr in some samples show depleted to enrich spikes relatively to Nd and Ti, and Ti in most samples shows a bit depleted relatively to Zr and Gd (Figure 7b).

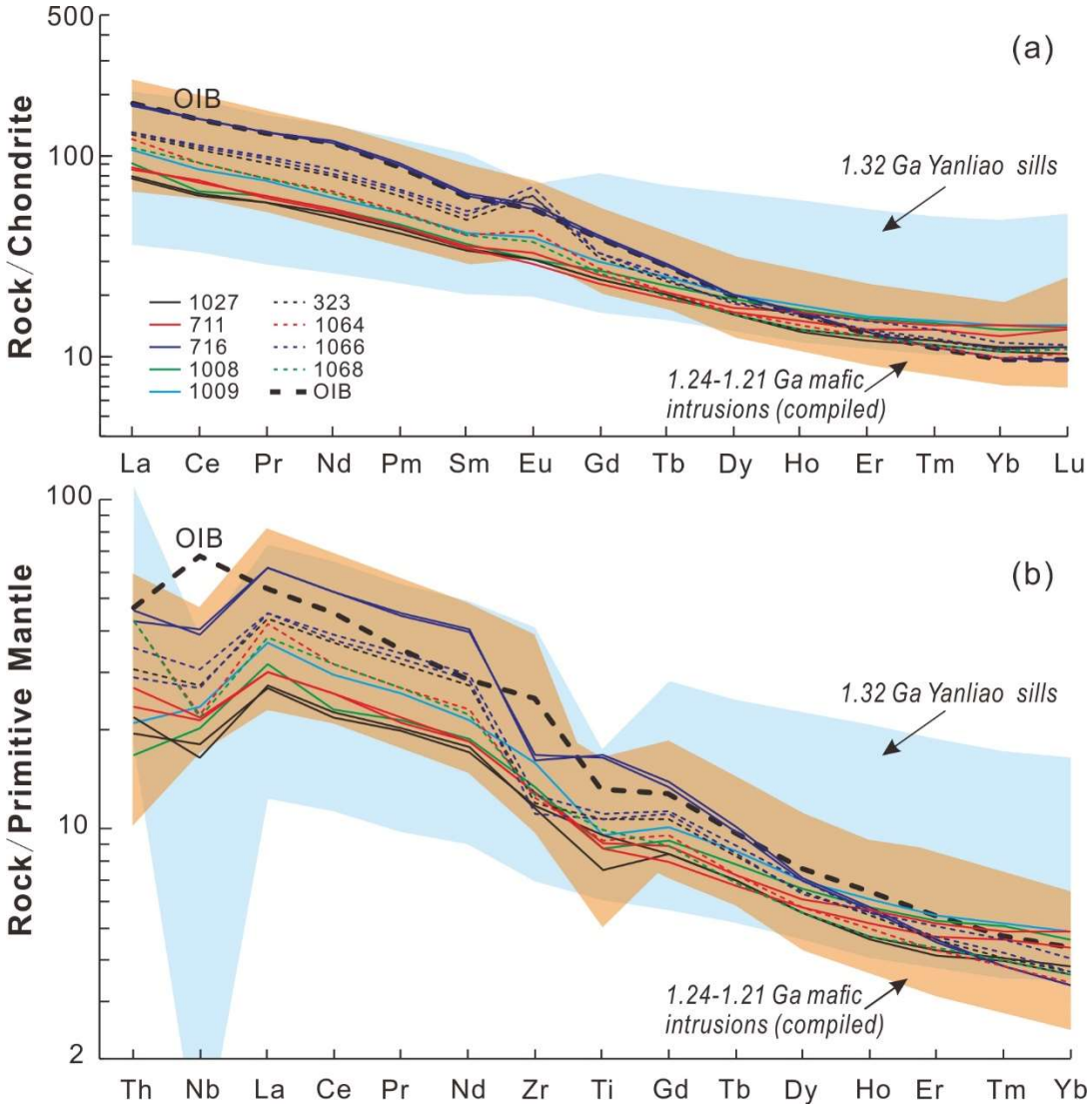

Figure 7 Chondrite-normalized REE patterns (a) and primitive mantle-normalized multi-element spider-grams (b). Chondrite normalized values and primitive mantle values are from Sun and McDonough (1989). The complied data for the 1.24–1.21 Ga mafic intrusions as in Figure 6. The data for the 1.32 Ga Yan–Liao LIP (N = 45) in the NCC are from Zhang et al. (2017).

Table 2 Major (wt.%) and trace (ppm) elements of 1.24–1.21 Ga mafic dykes

Sample	1008XT1	1009DT1	1027LW1	1027LW2	716RJD1	716RJD2	711NG22	711NG4	323WCZ2	1064JP1	1066XZ1	1066XZ2	1068-2
SiO_2	48.4	48.7	49.8	48.8	49.1	49.7	49.3	48.8	52.5	50.8	52.4	53.2	50.3
TiO_2	1.87	2.07	1.61	2.07	3.63	3.56	1.97	1.87	2.29	2.00	2.30	2.39	2.15
Al_2O_3	16.1	16.3	17.0	14.4	13.8	13.9	13.7	13.6	14.2	14.1	14.3	14.1	13.9
tFe_2O_3	12.4	12.4	11.1	13.4	12.7	12.6	14.7	14.2	11.4	11.0	11.3	11.0	11.8
MnO	0.16	0.18	0.15	0.20	0.19	0.19	0.23	0.21	0.20	0.19	0.20	0.21	0.18
MgO	5.88	5.28	5.09	6.21	4.6	4.64	5.98	6.16	4.38	6.15	4.39	4.74	6.22
CaO	7.40	6.25	10.43	9.31	7.27	7.10	8.57	9.12	7.04	7.55	7.02	5.93	8.89
Na_2O	3.37	3.67	2.47	2.13	3.78	3.77	2.20	2.15	3.61	3.70	3.79	3.94	2.76
K_2O	1.97	2.28	0.87	1.34	2.12	2.31	1.52	1.36	2.22	1.88	2.01	2.28	1.66
P_2O_5	0.31	0.42	0.22	0.21	0.60	0.57	0.21	0.19	0.29	0.23	0.28	0.29	0.23
LOI	2.96	2.70	2.00	2.30	2.08	2.14	1.91	2.42	1.92	2.45	2.15	2.02	2.05
Total	100.8	100.2	100.7	100.4	99.8	100.5	100.2	100.1	100.1	100.1	100.1	100.1	100.1
Mg#	48.7	46.0	47.8	48.1	42.0	42.4	44.9	46.5	43.4	52.7	43.7	46.2	51.3
Cr	44.2	27.9	151	181	65.7	85.3	181	215	212	329	202	202	336
Ni	57.7	47.7	65.4	82.4			84.0	88.7	56.9	87.6	49.6	51.6	93.0
Rb	62.0	83.7	21.1	45.0	50.6	53.9	72.3	53.4	49.1	96.6	52.1	60.1	96.0
Ba	1091	950	335	618	1157	1266	389	313	853	881	710	830	478
Th	1.42	1.76	1.84	1.64	3.59	3.86	2.00	2.26	2.59	3.63	2.46	2.99	3.61
U	0.41	0.51	0.44	0.42	0.86	0.89	0.44	0.59	0.66	1.02	0.61	0.70	0.93
Nb	14.3	16.8	11.7	12.9	28.7	27.5	15.1	15.4	19.2	15.8	18.9	21.5	15.5
Ta	0.88	1.02	0.78	0.85	1.72	1.68	1.3	1.3	1.3	1.4	1.2	1.5	1.1
La	21.7	25.1	18.7	18.1	42.2	42.7	20.4	20.6	29.9	28.5	30.8	30.7	26.2
Ce	40.5	51.7	39.7	38.8	92.7	91.9	45.5	45.3	65.4	56.2	66.2	68.6	56.4
Pr	5.91	7.07	5.57	5.48	12.5	12.3	5.81	6.03	8.71	7.39	9.09	9.42	7.37
Sr	835	716	447	347	901	894	293	324	534	479	531	520	492

Sample	1008XT1	1009DT1	1027LW1	1027LW2	716RJD1	716RJD2	711NG22	711NG4	323WCZ2	1064JP1	1066XZ1	1066XZ2	1068-2
Nd	25.1	29.0	23.8	22.9	54.8	53.4	24.7	25.0	36.9	31.1	37.9	39.4	30.0
Zr	149	176	128	130	179	185	143	143	133	139	124	142	141
Hf	3.81	4.41	3.57	3.67	4.93	4.98	4.0	3.9	3.5	3.6	3.3	3.9	3.7
Sm	5.54	6.2	5.21	5.13	9.85	9.58	5.43	5.18	7.34	6.05	7.58	8.04	6.05
Eu	1.75	2.26	1.77	1.74	3.29	3.16	1.88	1.65	3.68	2.45	4.02	3.66	2.16
Gd	5.46	6.04	4.99	4.97	8.18	7.91	5.23	4.68	6.29	5.64	6.64	6.72	5.29
Tb	0.84	0.92	0.75	0.75	1.09	1.05	0.78	0.72	0.88	0.78	0.90	0.95	0.74
Dy	4.84	5.15	4.08	4.04	5.17	5.13	4.44	4.20	4.70	4.24	4.69	5.10	4.07
Y	26.1	25.9	18.9	19.7	22.1	21.6	22.0	20.8	21.3	19.1	21.2	22.2	19.1
Ho	0.95	1.0	0.75	0.76	0.94	0.92	0.93	0.84	0.89	0.81	0.91	0.91	0.77
Er	2.50	2.61	1.98	2.06	2.20	2.16	2.46	2.25	2.19	2.06	2.24	2.44	2.08
Tm	0.37	0.38	0.29	0.30	0.28	0.28	0.36	0.34	0.30	0.28	0.31	0.34	0.29
Yb	2.28	2.38	1.76	1.86	1.65	1.65	2.38	2.14	1.81	1.67	1.81	1.99	1.77
Lu	0.34	0.36	0.26	0.28	0.24	0.24	0.35	0.34	0.28	0.26	0.28	0.29	0.27
Eu*	0.97	1.13	1.06	1.05	1.12	1.11	1.08	1.02	1.66	1.28	1.73	1.52	1.17
REE	118	140	110	107	235	232	121	119	169	147	173	179	143
Nb/Y	0.546	0.647	0.618	0.657	1.30	1.27	0.686	0.740	0.901	0.827	0.892	0.968	0.812
La/Sm	3.91	4.05	3.59	3.54	4.28	4.46	3.76	3.98	4.07	4.71	4.06	3.82	4.33
Th/Nb	0.10	0.10	0.16	0.13	0.13	0.14	0.13	0.15	0.13	0.23	0.13	0.14	0.23
Nb/La	0.66	0.67	0.63	0.71	0.68	0.64	0.74	0.75	0.64	0.55	0.61	0.70	0.59
La/Yb_N	6.82	7.56	7.62	7.00	18.3	18.6	6.15	6.90	11.85	12.24	12.21	11.07	10.62
Th/Yb	0.62	0.74	1.05	0.88	2.17	2.35	0.84	1.06	1.43	2.17	1.36	1.50	2.04
Nb/Yb	6.25	7.05	6.65	6.96	17.3	16.7	6.34	7.20	10.6	9.46	10.4	10.8	8.76
Zr/Y	5.69	6.79	6.76	6.60	8.07	8.57	6.50	6.88	6.24	7.28	5.85	6.40	7.38

tFe_2O_3, total Fe_2O_3; MgO# = 100*Mg/ (FeO_{total} + MgO), in molecular; $Eu/Eu^* = Eu_N/[(Sm_N) \times (Gd_N)]^{1/2}$; La/Yb_N, normalized to chondrite compositions, and hondrite normalized values are from Sun and McDonough (1989).

7. Paleomagnetism

7.1 ~1.68 Ga paleomagnetic results

I mostly used thermal demagnetization because AF demagnetization appeared to be less effective. The 1680 ± 5 Ma dyke LX307 (Figure 2b) is ~35 m wide. **S**amples from this dyke yielded two groups of high temperature components (HTC). Four samples (group A) show characteristic remanent magnetizations (ChRM) with a low inclination and NNE downward direction (D=26.0°, I=17.0°, a_{95}=8.2°, n=4) (Figure 8 and Figure 9; Table 3). Another five samples (group B) display scattered medium to high inclinations (four downward and one upward; Figure 9a). The low temperature component (LTC) direction of D=13.3°, I=54.8° (a_{95}=11.5°) falls close to the geocentric axial dipole (GAD) direction (D/I=0°/53.7°) and the present geomagnetic field (PGF) direction (D/I=354°/55°; International Geomagnetic Reference Field model – IGRF) (Figure 9d). The 1677 ± 12 Ma dyke JD689 (Figure 2c) is ~12 m wide. Most samples from this dyke are strongly magnetic, with their natural remanent magnetization (NRM) intensity varying from 1.9 to 1080 A/m (Figure 9b). The commonly single magnetic remanence vectors have scattered directions (Figure 8b and Figure 9b). The granite country-rock samples also yielded erratic remanence directions. Therefore, I consider that most samples from this dyke were remagnetized by lightning strikes, as indicated by the high (>10) Qn ratios (the Königsberger ratio) (Radhakrishnamurthy, 1993) for most samples (Figure 9). Only one sample (689-3-9) with low NRM intensity presents a high-temperature remanence direction (Figure 9b,) similar to that of group A direction from coeval dyke LX307 (Figure 8b and Figure 9a-b).

Dyke JD690 (Figure 2c) is ~1.5 m wide, located 150 meters southeast of the 1677±12 Ma JD689 dyke. The six most strongly magnetized samples (NRM values mostly between 51 and 77 A/m and Qn ratios mostly >10; Figure 9c) likely experienced lightning strikes. The remaining six samples, all with lower NRM (≤6.7 A/m) yielded a consistent HTC with a mean direction of D=17.3°, I=23.9°, a_{95}=20.8° (Figure 8c and Figure 9c; Table 3). The LTC (usually unblocked at 100–280°C) were isolated from four samples of this dyke, giving a mean direction of D=0.3°, I=45.1° (a_{95}=12.9°) (Figure 9e). This direction is similar to that of the PGF (D/I=352°/59°) and GAD direction (D/I=0°/49.8°) (Figure 9e).

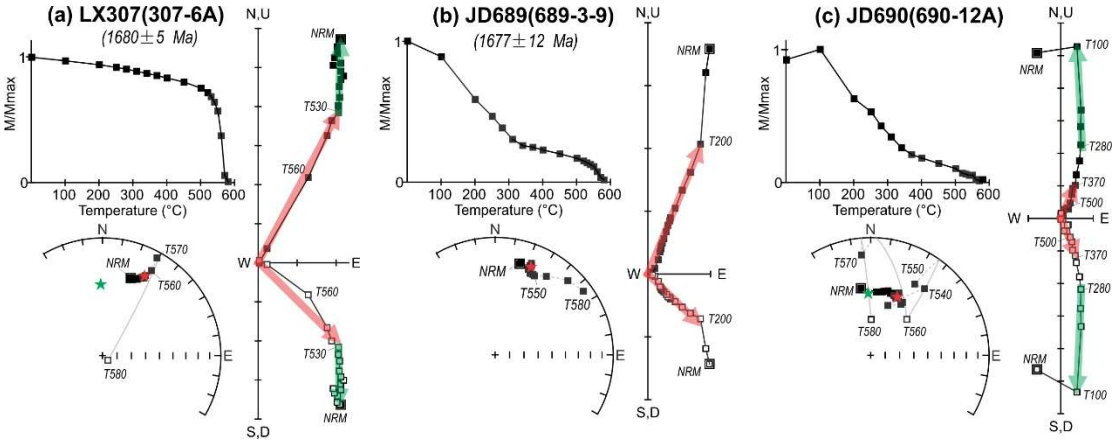

Figure 8 Representative demagnetization data of the ~1.68 Ga dykes, plotted as remanence intensity *vs.* demagnetization curves, equal-area stereo-plots (solid/ open are directions in the lower/upper hemisphere) and orthogonal projection diagrams (solid/open square points indicate vector end points projected onto the horizontal/vertical plane). The directions of HTC and LTC are shown by red and green arrows respectively.

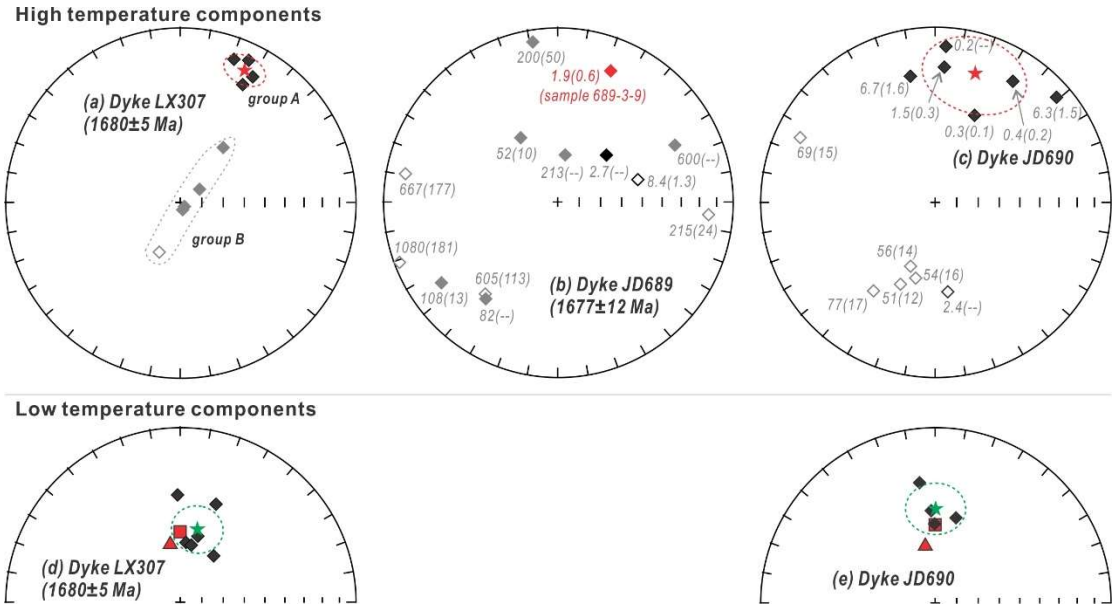

Figure 9 Equal-area projections of the high temperature (a-c) and low temperature (d-e) remanence directions of the ~1.68 Ga dykes. Each diamond point represents one sample. Solid/open symbols are projections on the lower/upper hemisphere. Site mean directions are represented by stars with dashed circles showing the 95% confidence cone. Some samples in (b) and (c) are marked with NRM values (A/m) and Qn ratios in brackets. Data shown in grey of (b) and (c) are those interpreted to reflect lightning could be struck. Triangles and squares in (d) and (e) represent the PGF direction and GAD direction respectively.

Table 3 Paleomagnetic high temperature components of the dykes

Dyke No.	Age (Ma)	Age References	Width (m)	Trend (°)	Latitude (°N)	Longitude (°E)	n/N	D (°)	I (°)	α_{95} (°)	Plat (°N)	Plong (°E)	A_{95} (°)
HTC of ~1.68 Ga dykes													
LX307	1680 ± 4	Li et al., 2015	~35	~340	36.278	117.890	4/9	26.0	17.0	8.2	53.6	250.9	6.1
JD690			~1.5	~30	40.250	118.533	6/12	17.3	23.9	20.8	58.4	264.9	16.3
JD689	1677 ± 12	Wang et al., 2016	>10	~65	40.250	118.532	1/13	22.0	20.2		54.3	259.3	
									3 site-level mean		55.6	258.1	7.2
HTC of ~1.24 Ga dykes													
JD517	1236 ± 7	Wang et al., 2016	>15	~34	39.857	118.920	10/13	107.0	48.3	5.6	6.8	176.0	5.9
JD687			~25	~4	40.261	118.482	12/12	118.9	44.5	10.8	–2.7	170.4	10.8
JD1027	1233 ± 27	This study	30–40	~24	40.245	118.486	8/12	130.3	36.6	5.4	–13.8	165.9	4.8
C711			>15	~310	37.400	114.187	11/11	98.0	21.0	2.7	0.4	190.7	2.0
C716			>15	~310	37.574	114.304	15/15	114.0	49.4	2.9	1.7	166.4	3.1
LX323			~15	~345	35.396	118.181	13/15	132.1	60.3	2.8	–1.6	152.1	3.7
LX1064			10	~350	35.872	118.120	7/15	101.9	69.3	1.9	21.5	157.5	3.0
LX1066			~20	~352	35.350	118.193	10/11	124.8	54.4	3.4	–2.9	160.6	3.9
LX1068			~15	~352	35.341	118.181	11/11	123.7	71.8	3.7	13.6	146.2	6.1
									9 site-level mean		2.6	165.1	10.8
Baked contact test of ~1.24 Ga dykes (HTC)													
JD1027					Baked rocks ~3 m		8/8	127.3	27.7	7.6			
					Unbaked rocks >100 m		5/8	215.5	–54.1	10.8			
JD687					Baked rocks ~0.35 m		5/6	118.7	52.6	15.0			
HTC of ~1.21 Ga dyke													
MY1033	1206.7 ± 1.7	This study	~80	~35	40.617	117.083	13/13	204.5	39.5	6.5	–23.0	92.5	6.1

n/N, number of samples used/ measured; D, declination; I, inclination; α_{95} and A_{95} are 95% radii confidence circles for direction and poles; Plat and Plong are latitudes and longitudes of paleopoles.

The calculated mean paleopole of the studied dykes (LX307, JD689 and JD690) falls at 55.6˚N, 258.1˚E, A_{95}=7.2° (Table 3). This pole is considered a ca. 1.68 Ga VGP because the small number of dykes is not large enough to average out the geomagnetic secular variation.

7.2 ~1.24 Ga and 1.21 Ga paleomagnetic results

(1) The 1.24 Ga dykes

The dyke JD687 is regarded as a coeval dyke as the dated dykes JD517 and JD1027 (both at ~1235 Ma; Figure 2c) according to their similar geochemical features (Wang et al., 2016), which is further verified by their similar paleomagnetic directions. Similar paleomagnetic directions also have been found in dykes C711, C716, LX323, LX1064, LX1066 and LX1068 (Figure 10, Figure 11 and Table 3). This E-SE moderate to shallow downward stable characteristic remanence magnetization (ChRM) has been isolated after both thermal and AF demagnetization. Its unblocking temperature is close to ~580°C, indicating magnetite as the remanence carrier (Figure 10a-f). No antipodal directions have been found (Figure 10 and Figure 11). Based on the similarity of remanence directions, I regard all these dykes belonging to the ~1.24 Ga group. In support to this suggestion we note that closely located dykes C711 and C716 have similar trends and mineralogical characteristics (Figure 2d and Figure 3j, k).

ChRM directions of nine 1.24 Ga dykes are shown in Table 3. The mean paleomagnetic pole for this group of dykes is at 2.6°N, 165.1°E (A_{95} = 10.8°). Seven out of nine dykes of this group (except LX323 and C716) also yield low temperature components (LTC) (Figure 12). Most LTCs, being acquired below 280–310°C (Figure 10), are close to the directions of the present geomagnetic field (PGF) and geocentric axial dipole (GAD) (Figure 12).

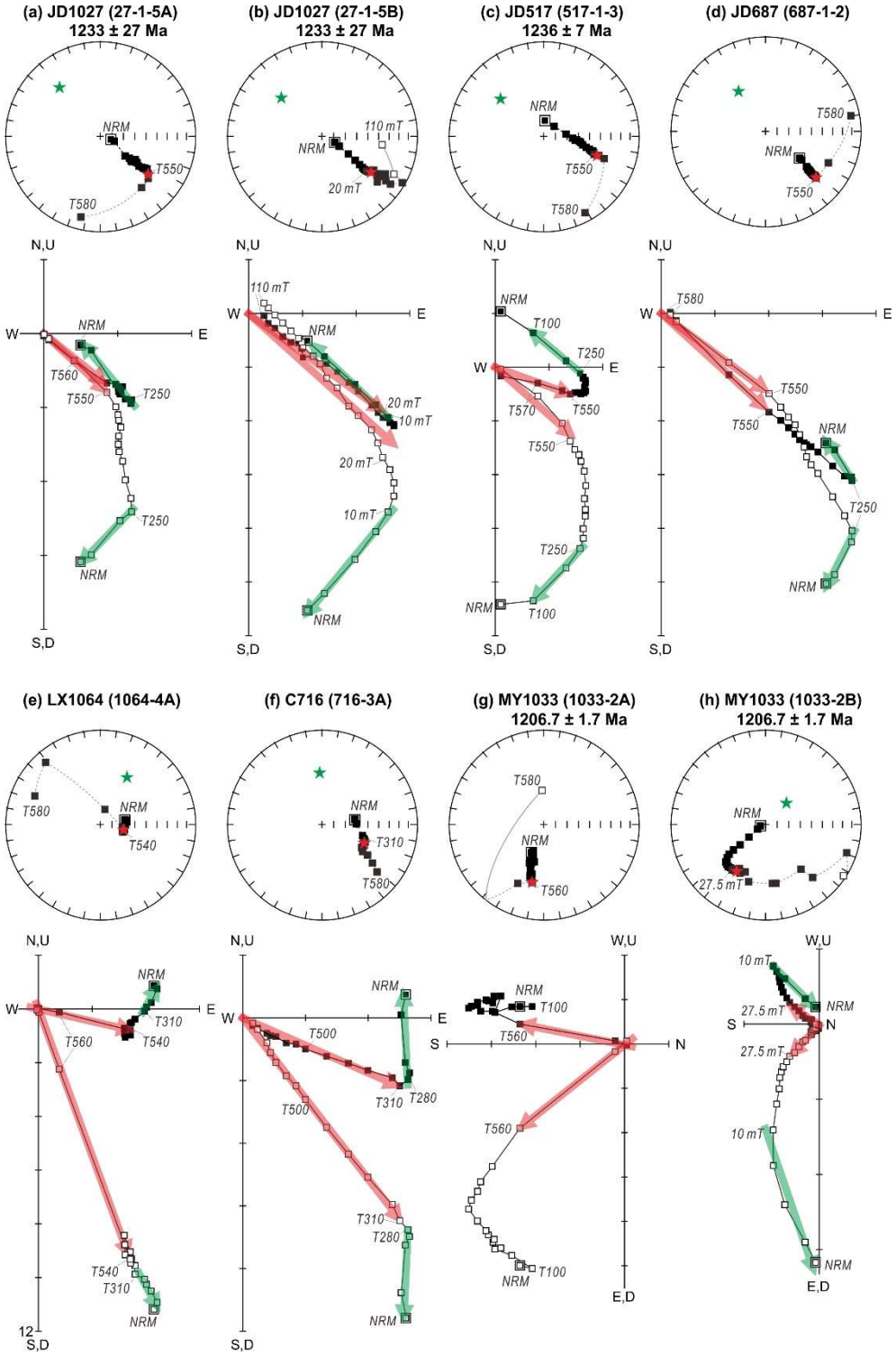

Figure 10 Representative thermal and AF demagnetizations of the 1.24 Ga (a–f) and the 1.21 Ga (g–h) dykes: equal area stereoplots (solid/open square points correspond for downward/ upward-pointing magne-tizations; Red and green stars are mean directions of the HTC and LTC, respectively), and orthogonal projection diagrams (solid/open square points show vector end points projections onto the horizontal/vertical plane; Red and green arrows are HTC and LTC, respectively).

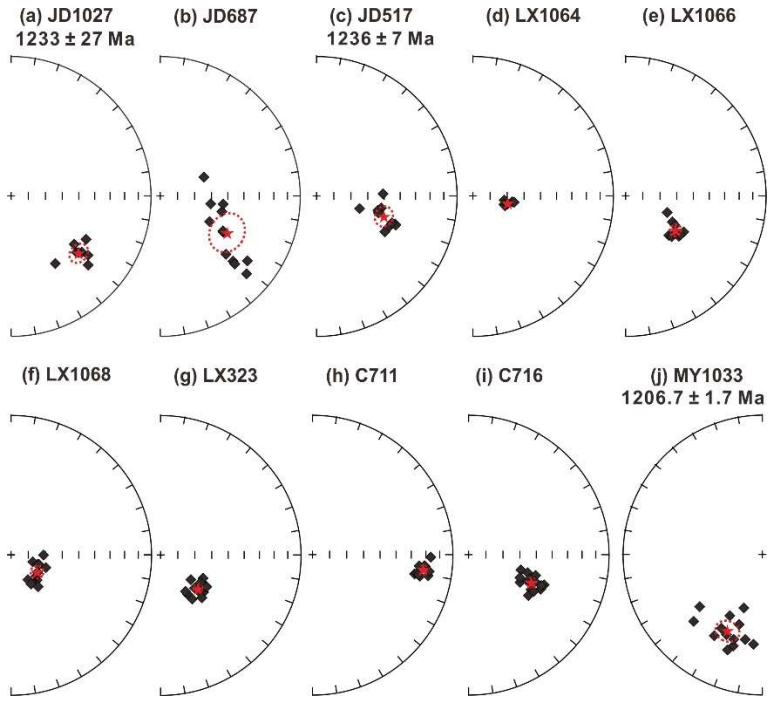

Figure 11 Equal-area projections showing the ChRM of each dyke. Each diamond represents one sample. Red dots and surround dashed line represent the site/dyke mean directions and α_{95} ovals. Solid symbols represent lower hemisphere vectors.

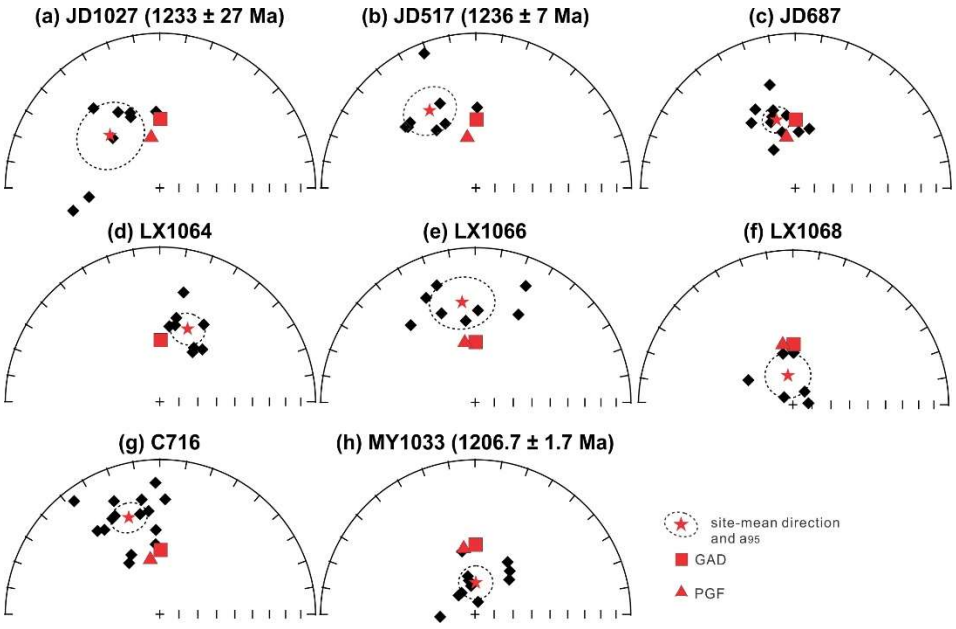

Figure 12 Equal-area projections showing the LTCs of the 1.24–1.21 Ga dyke. Each diamond represents one sample. Red stars and surround dashed line represent the site-mean directions and α95 ovals. Solid symbols represent lower hemisphere vectors.

Baked contact tests have been performed on dykes JD1027 and JD687 (Figure 2c), where country rocks are Archean gneisses. JD1027 is a ~30 m wide dyke and we collected host rock samples adjacent to it within ~3m and at >100 m from the dyke's margin. These gneisses are paleomagnetically stable, yielding moderate southeast downward ChRM direction near the dyke and moderate southwest upward direction at >100 m from the dyke (Figure 13a). This result illustrates that the host rocks adjacent to the dyke were reheated and remagnetized during the emplacement of the dyke, however, the host rocks far from the dyke were not affected by the dykes. We interpret this as a positive contact test and consider the ChRM as primary.

For the ~25 m- wide JD687 dyke, we collected country rocks within ~35 cm and at >35 m from the dyke. The adjacent host rocks also show stable remanence direction similarly to the dyke's direction. However, the unbaked host rocks yield scattered ChRM directions (Figure 13b), implying an incomplete contact test.

(2) The 1.21 Ga dyke

The 1206.7 ± 1.7 Ma dyke MY1033 locates in the Miyun county (Figure 2c). This dyke is about 30 Ma younger than the other studied dykes and gives a different remanent direction: SW moderate downward (Figure 10g-h and Figure 11j; Table 3). Both thermal (Figure 10g) and AF (Figure 10h) demagnetization isolated a stable ChRM with 540–580°C unblocking temperatures and > 40 mT coercivity. The mean paleomagnetic direction is D = 204.5°, I = 39.5°, α_{95} = 6.5°, and the corresponding paleopole is -23.0°N, 92.5°E, A_{95} = 6.1°. This pole should be considered a virtual geomagnetic pole (VGP) because it is based on the paleomagnetic direction from just one dyke that does not average out secular variations. The LTC direction, mostly being acquired below 520°C, is D = 1.3°, I = 73.3°, α_{95} = 8.9°, which is close to the PGF and GAD directions (Figure 12h).

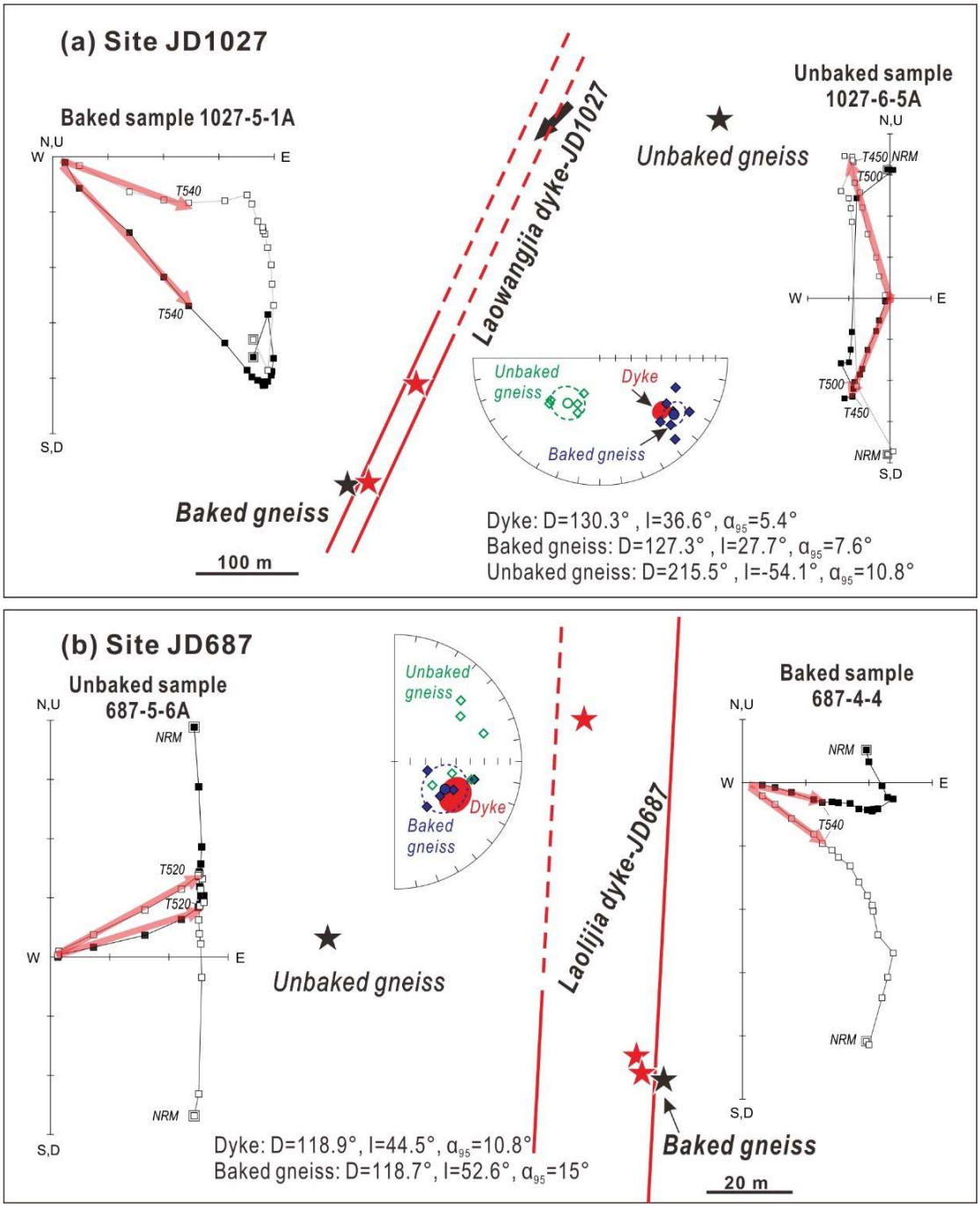

Figure 13 Baked contact tests for dykes JD1027 (a) and JD687 (b). Schematic diagrams include the margins of dykes (red solid lines; dashed lines are putative margins), sampling locations (stars), representative demagnetization of host gneisses (solid/open square points show vector end points projections onto the horizontal/vertical plane) and site-mean plots (solid/open square points correspond for downward / upward-pointing magnetizations).

8. Rock magnetic and magnetic fabric results

All the representative samples have an unblocking temperature of ~580°C (the Curie temperature of magnetite) and show Hopkinson peaks (Dunlop and Özdemir, 1997) in thermo-magnetic curves, indicating the presence of highly paleomagnetically stable single-domain (SD) or pseudo-single-domain (PSD) low-Ti titanomagnetite or pure magnetite. Many representative samples also show nearly reversible heating and cooling curves, confirming that little mineralogical changes occurred at high temperatures. A minor presence of pyrrhotite can explain the increases in magnetic susceptibility of heating curves around 200–300°C and the decreases around 300–400°C in some samples. The triaxial thermal demagnetization of IRM analyses demonstrated a domination of soft magnetic components, with unblocking temperature of 550–600°C (~520°C for sample 517-4-1), implying the occurrence of Ti-poor multi-domain (MD) titanomagnetite in many samples. However, in some cases the paleomagnetically stable SD or PSD magnetite (intermedium fractions) is also present. Both magnetic anisotropy parameters P and Pj are less than 1.10. Dykes C711 shows more positive T values (AMS ellipsoid parameter) indicating a dominant oblate fabric; JD1027 shows more negative T values indicating a dominant prolate fabric. Moreover, these two dykes show normal magnetic fabrics (K_1–K_2 planes parallel to the dyke trends).

9. Discussion

9.1 Petrogenesis of the 1.24–1.21 Ga dykes

To estimate the geochemical effect of the alteration of the bulk rock chemical composition, I compared the LOI with the major and trace elements. Most elements show no correlation with LOI. However, there are some elements such as Al, Ca and Rb displayed weak linear correlation with LOI, reflecting mobilization of these elements during (plagioclase) alternation process (Figure 3g-l) (see thin sections in Peng et al., 2013; Wang et al., 2016; Wang et al., 2015). In addition, Zr is generally considered as the most immobile element during alteration (e.g., Polat et al., 2002). Zr shows a positive linear correlation with high field strength elements (HFSE) Nb, Ta, Hf and Th, REE (La, Sm and Yb) and U, and no correlation with large-ion lithophile elements (LILE) Rb, Sr and Ba. Thus, the HFSE and REE are considered more reliable in deciphering the petrogenesis of the studied rocks than LILE.

Mafic intrusions can be contaminated by the host crustal rocks during emplacement. Some trace elements (e.g. Nb, La and Th) and their ratios are sensitive to this process because of their distinct differentiation between crust and mantle (e.g., Pearce, 2008). The Nb/La ratios of N-MORB, E-MORB, OIB and averaged crust are 0.93, 1.32, 1.30 and 0.67, while the Th/Nb ratios are 0.05, 0.07, 0.08 and 0.48, respectively (Sun and McDonough, 1989; Taylor, 1964). Part samples of this magmatism present narrow increasing Th/Nb range (~0.05 to 0.09) although obviously decreasing Nb/La (~1.3 to 0.8), indicating the unremarkable crustal contamination (Figure 14a). These samples are mainly from Jianping dyke (Figure 2c), which contain few inherited zircons (Wang et al., 2015), supporting little crustal contamination during emplacement. However, part samples show relatively high Th/Nb, e.g., ratios of ~0.13–0.16 from JD1027 dyke, and of ~0.23 from LX1064 and LX1068 dykes (Figure 14a), indicating some degree of crustal contamination. Also, zircon xenocrysts were found in the Laowangjia dyke (JD1027; not shown), supporting contamination process. All these suggest non-homogeneous crustal contamination among these dykes.

Multiple geochemical proxies, especially the continuous variations in elements (Figure 5 and Figure 6), parallel REE and spider patterns (Figure 7), indicate that these dykes are from the same stable source even if the event lasted for about 30 Ma. None of the studied samples were derived from primary magma since their Mg# values are all < 60. There is no obvious correlation between MgO and Al_2O_3, tFe_2O_3, TiO_2, Cr, Ni (Figure 6c-g), so the fractional crystallization seems to be minor, which is also indicated by the La/Sm versus La diagram (Figure 14c). In the early stage of magmatic evolution, the magma mainly experienced partial melting showing oblique linear tendency between La/Sm and La (Figure 14c). In the later stage, it gave way to weak crystallization-influenced differentiation when La reached level over ~30 ppm (Figure 14c). Part samples show a weakly to significantly positive Eu- anomaly (Figure 7a), reflecting that feldspars were unseparated from the magma.

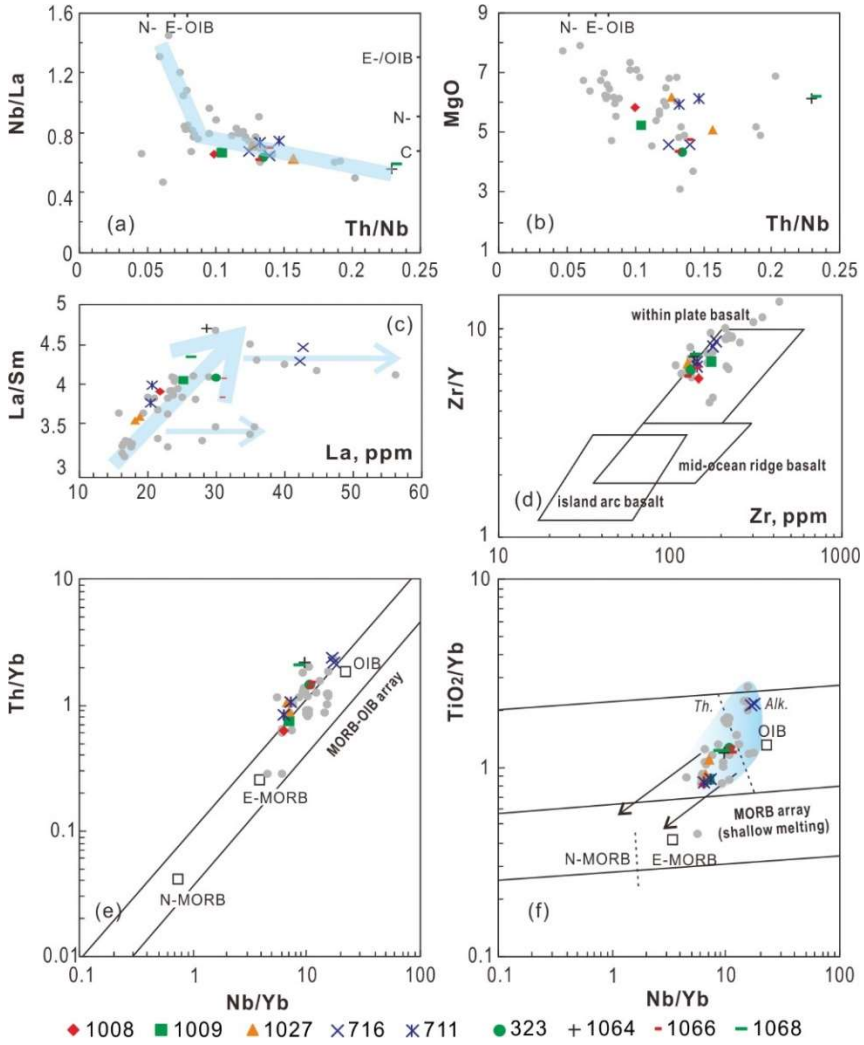

Figure 14 Trace elements ratio diagrams of the 1.24-1.21 Ga dykes.

The ratios of La/Yb_N range from 6.8 to 13.9, even up to 18.6 (Figure 6l), reflecting the variations of degree of partial melting. The highest La/Yb_N samples are from the C716 dyke in the central NCC, which display alkaline features (Figure 5), but the C716 dyke shows no other extraordinary geochemical features compared with other dykes, besides showing more depleted HREE (Figures 5 and 6). All the samples have high REE contents (96–308 ppm), high La/Yb_N (6.8–18.6), which distinguish them from MORB. The Th-Nb proxy indicates an OIB affinity, but with slight interaction with E-MORB (Figure 14e). Their high TiO_2/Yb ratios (Figure 14f) are indicative of garnet residues, and the rocks likely originated from melting beneath a thick lithosphere (Pearce, 2008). The diagonal trends from the OIB to the MORB fields reflect hot mantle flows within the lithosphere (Figure 14e, f) (Pearce, 2008). Some samples show εHf (t = 1230 Ma) of 1.8–10 (Wang et al., 2015) and εNd (t = 1230 Ma) of 0–1.6 (Peng et al., 2013; Wang et al., 2016), which is suggestive of their originating from a depleted asthenosphere.

Additionally, these dykes have high Ti contents (usually >1.5 wt.%), indicating possibly plume-related source as the Emeishan flood basalts (Xu et al., 2001). Moreover, this dyke swarm present fan-like radiating geometry in the field (Figure 2). Considering all, we interpret that the studied rocks should be originated from a mantle plume.

9.2 Identification of a 1.24–1.21 Ga LIP event in the NCC

LIP refers to huge magmatic activities during a short time period, which are sometimes associated with continental breakup or the formation of ore deposits, and can also have severe environmental consequences (Ernst, 2014). A LIP event can be characterised by its volume, area, and duration, and commonly represents a pulsed sequence of magmatism in an intraplate tectonic setting (Ernst, 2014 and references therein). Several of these characteristics can be identified for the 1.24–1.21 Ga magmatism in the NCC.

Firstly, the studied dykes are discontinuous in the field, and each can only be traced over several hundred metres, or a few kilometres, making it difficult to evaluate the total areal extent and volume. These dykes are in general over 10 m in width, even up to 80 m, a scale commonly associated with LIPs (Ernst, 2014). After restoring the effect of the Tan-Lu fault (a sinistral strike-slip fault in the Phanerozoic; Zhao et al., 2016), this event is estimated to cover an area of $> 0.1 \times 10^6$ km^2 in the central and eastern NCC (Figure 2). If the small dykes in the Bayan Obo rift (1227 ± 60 Ma, Sm-Nd isochron; Yang et al., 2011) are included, and if the Pingshan (PS) dykes (Figure 2d) are belong to the same generation based on similar paleomagnetic directions (Ding, 2017), the areal extent is even greater. Moreover, mafic dykes from the central-western Korean Peninsula yield an age of 1259 ± 12 Ma, and with an alkaline-basalt geochemical affiliation, and OIB-like within-plate characteristics (Kim et al., 2018), which may originate from the same source as the 1.24–1.21 Ga magmatism in this study.

Secondly, constrained by the quality of some age data, this magmatic event lasted from roughly 1244 Ma to 1207 Ma (U–Pb ages), with a total duration of ~30 Ma. Considering the age uncertainties, and their consistent geochemical and paleomagnetic characteristics (Figure 5 to Figure 11), we regard these dykes to belonging to the same LIP event. Ernst (2014) concluded that LIPs with > 20 Ma age span were emplaced in several shorter duration pulses rather than as a continuous activity. The resolution of our ages and limited sampling precludes a confident identification of discrete pulses of

dyke emplacement. The three age populations, however — ~1230 Ma, ~1220 Ma and ~1207–1210 Ma — might indicate three pules of magmatism.

Thirdly, these intrusions were emplaced within the NCC, and have intraplate geochemical characteristics (Figure 14d). We suggest that the dyke swarms collectively form a 1.24–1.21 Ga LIP related to a plume event in the NCC, which we name the Licheng LIP (after the 1.23 Ga Licheng dyke swarm first identified by Peng (2015b)).

Magnetic anisotropy has been widely used to estimate the directions of magma flows (e.g., Ernst and Baragar, 1992). The normal magnetic fabric of dyke JD1027 presents K_1 axis with shallow inclination, indicating the magma flowed laterally in this region far from the plume centre. Conversely, the C711 dyke might have been emplaced closer to the magmatic centre since K_1 axis yields medium to steep inclinations. The geometry of the dykes and their magnetic fabrics suggest that the magmatic centre was possibly in southeastern NCC, probably around the Luxi area.

9.3 Paleomagnetic reconstruction

9.3.1 ~1.68 Ga and 1.24 Ga paleomagnetic poles

Although there is no baked contact test for 1.68 Ga dykes, various observations indicate that the ~1.68 Ga remanent magnetization is primary. First, the studied dykes are non-deformed and non-metamorphosed, with clear ophitic textures (Li et al., 2015; Wang et al., 2016). Some alterations are associated with low temperature (<300°C), but the magnetic minerals with high unblocking temperatures (550–580°C) would not have been affected by such processes. Second, rock magnetic results show the presence of the paleomagnetically highly stable SD/PSD magnetite. Finally, positive field tests on 1.32 Ga and 1.22 Ga mafic rocks near the JD689 dyke in the Jidong area (Chen et al., 2013; Ding, 2017) indicate the absence of any significant regional remagnetization event since 1.32 Ga. In addition, the absence of the 1.60–1.35 Ga magmatism in the study areas (Peng, 2015b) precludes older remagnetization of the studied 1.68 Ga dykes. Moreover, our 1.68 Ga VGP is similar to the paleopole from the lower Yunmengshan Formation (60.6°N, 267.0°E, A_{95} = 3.7°) (Zhang et al., 2006). This formation found in southern NCC was initially thought to be deposited in the late Mesoproterozoic based on Rb–Sr dating, but new zircon U–Pb geochronology on tuffs and detrital zircons constrained the deposition age to the late Paleoproterozoic (between <1.71 Ga and >1.61 Ga) (Hu et al., 2014; Su et al., 2012). If we assume the Yunmengshan Formation to have started its deposition at ~1.70 Ga, and a uniform deposition rate for

the Paleoproterozoic strata, the estimated younger limit for the Yunmengshan Formation would be ~1.67 Ga. The lower Yunmengshan paleomagnetic pole from Zhang et al. (2006) has been regarded as a primary pole because it passed positive fold and reversal tests. Because the lower Yunmengshan pole data (both at mean pole position and the pole position calculated for each site) overlap with that of our new 1.68 Ga dykes, and their estimated ages overlap, we combine the total of 18 sites from the two studies (3 dykes from this study and 15 sites from the lower Yunmengshan Formation) to obtain a grand-mean ~1.68 Ga paleopole for the NCC at 59.8°N, 265.3°E, A_{95}=3.3°.

Dyke LX1064 was dated at 1841 ± 17 Ma through the zircon U-Pb LA-ICPMS method (Wang et al., 2007). It's hard to judge the genesis of dated zircons by few unclear zircon CL images in Wang et al. (2007). This generation of magmatism in the NCC has not been confirmed in recent studies (Peng, 2015b and references therein). Considering that this dyke has a similar magnetic direction as those from ~1.24 Ga dykes, we suggest that it could be part of the ~1.24 Ga magmatism. Therefore, our results from a total of nine dykes yield a mean paleomagnetic pole at 2.6°N, 165.1°E, A_{95} = 10.8° (Table 3) with positive field baked contact test (Figure 13), representing a primary key paleopole for the NCC. The slightly younger 1206.7 ± 1.7 Ma Baihejian dyke (MY1033) yields a different ChRM direction (Figure 11j; Table 3) and provides a ~1.21 Ga VGP.

9.3.2 Reconstruction

To test the connection between the NCC and the Australia paleomagnetically, reliable paleopoles have been selected (Table 4). Some poles have precise ages and positive field tests, whereas others obtained from sedimentary rocks have large age uncertainties (Table 4). From Figure 15a, we see that the ~1.78 Ga paleopole for the NCC falls close to the newly published ~1.79 Ga paleopole for the NAC in a revised NCC-NAC configuration, similar to the model proposed by Zhang et al. (2017). Although no other coeval poles exist for the two cratons (Figure 15b), preliminary paleomagnetic evidence suggests for a similar configuration at ~1.32 Ga (Kirscher et al., 2018). Therefore, the NCC and the NAC were likely connected to each other between ~1.78 Ga and 1.32 Ga. In such a paleomagnetism-based reconstruction, coeval ~1.32 Ga mafic magmatic events in both cratons, including the orientation of mafic dykes, are interpreted to be the products of the same mantle plume (Figure 15a).

Paleomagnetic reconstruction based on updated 1.24 Ga paleomagnetic poles indicates that the two continents likely have started to pull away from each other, or at least the connection of NE-NCC and N-NAC has been broken by that time (Figure 15b). This is consistent with the previously suggestion: the breakup of the NCC from the NAC at ca. 1.32 Ga based on the presence of unconformities within the NCC (between the Xiamaling Formation and the overlying Changlongshan Formation) and the NAC (between the Roper Group and the overlying Cambrian volcanics) (Ahmad et al., 2013; Zhang et al., 2017). Considering the likely plume-triggered 1.32 Ga mafic magmatism occurred after the Xiamaling Formation and the Roper Group, the two unconformities might represent the breakup event or may also represent above-plume erosion (Zhang et al., 2017).

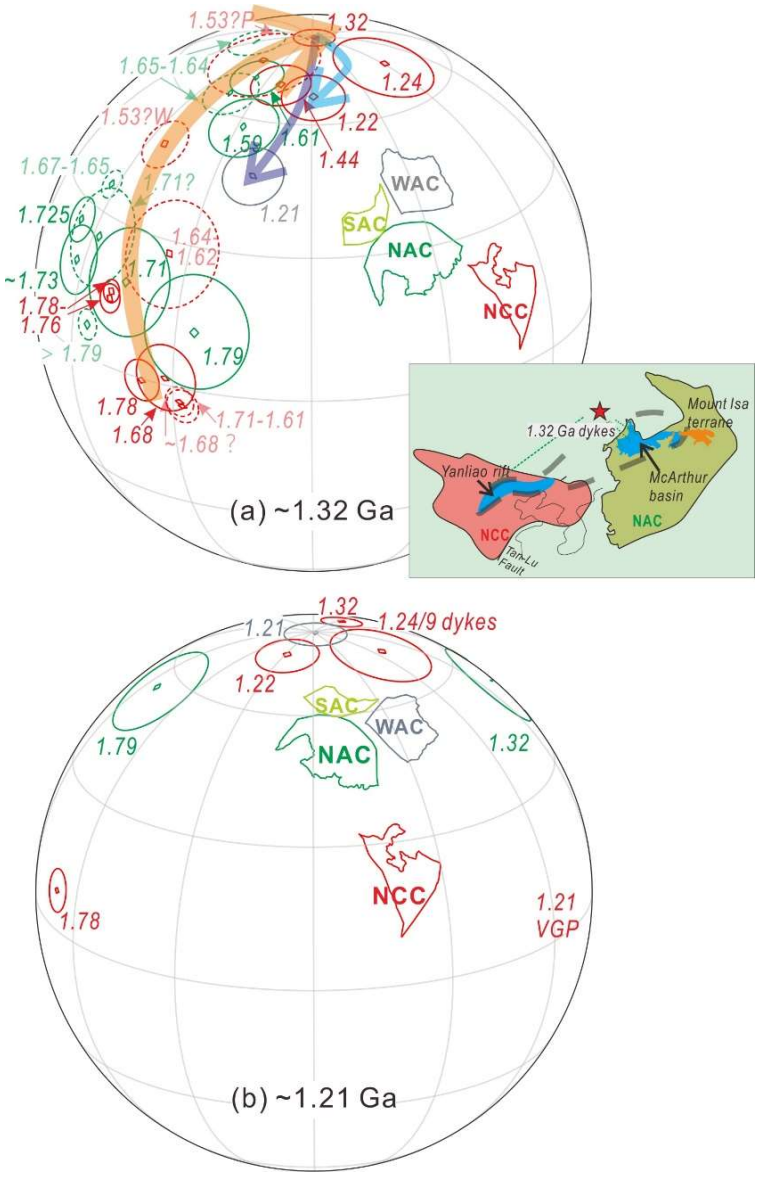

Figure 15 Paleomagnetic reconstruction between the NCC and proto-Australia at ~1.32 Ga (a) and ~1.21 Ga (b). (a) Selected ~1.8–1.3 Ga paleomagnetic poles showing the comparable APWP (bold yellow line) between the NCC (red) and the NAC (green); while the different APWPs after ~1.32 Ga indicating their separation. Insert figure showing schematic paleogeography corresponding to the similar paleomagnetic reconstruction. The comparable model of the ~1.32 Ga radial dykes and plume centre was proposed by Zhang et al. (2017). (b) showing the relative configuration between the NCC and proto–Australia at ~1.21 Ga. The paleopoles are marked with ages in Ga. Dashed poles have putative ages only. The proto–Australia configuration is after Li and Evans (2010). Euler rotation parameters are in Table 5. NCC–North China Craton, NAC–North Australian Craton, WAC–West Australian Craton, SAC–South Australian Craton.

Table 4 Selected ~1.8–1.2 Ga paleomagnetic poles for the North China and Australia blocks

No.	Rock unit	Age (Ga)	Plat (°N)	Plong (°E)	A_{95} (°)	Q	References
NCC							
1	Xiong'er volcanics	1.78	50.2	263.0	4.5	+ + + – + + +	Zhang et al., 2012
2	Taihang dykes	1.78–1.76	36.0	247.0	3.0	+ + + + + + – +	Halls et al., 2000
3	Yinshan dykes	1.78–1.76	35.5	245.2	2.4	+ + + + + + – +	Xu et al., 2014
4	Laiwu and Tujiagou dykes- 3 sites	1.68	55.6	258.1	7.2	+ – + – + – +	This study
5	Lower Yunmengshan Fm- 15 sites	*1.71– 1.61*	60.6	267.0	3.7	– + + + + + +	Zhang et al., 2006
4+5		~1.68?	59.8	265.3	3.3	– + + + + + +	This study
6	Cuizhuang and Sanjiaotang Fms	*1.64–1.62?*	41.0	224.8	11.3	– + + – + + +	Zhang et al., 2006
7	Yangzhuang Fm	*1.53?*	17.3	214.5	5.7	– + + + + + +	Wu et al., 2005
8	Yangzhuang Fm	*1.53?*	2.4	190.4	11.9	– + + + + + +	Pei et al., 2006
9	Tieling Fm	1.44	11.6	187.1	6.3	+ + + + + – +	Wu, 2005
10	Yanliao sills	1.32	5.9	359.6	4.3	+ + + + + – +	Chen et al., 2013
11	Licheng LIP/dykes	1.24	2.6	165.1	10.8	+ + + + + – +	This study
12	Jianping and Pingshan dykes	1.22	16.0	180.3	6.6	+ + + + + – +	Ding, 2017
13	Baihejian dyke, Miyun/VGP	1.21	–23.0	92.5	6.1	+ – + – + – +	This study
Australia							
14	Elgee and Pentecost Fms	*> 1.79*	5.4	31.8	3.2	– + + + + – –	Li, 2000; Schmidt and Williams, 2008
15	Hart sills	1.79	6.9	2.6	12.0	+ + + – + + +	Kirscher et al., 2019
16	Peters Creek volcanics	1.725	26.0	41.0	4.8	+ + + + + + +	Idnurm, 2000
17	Wollogorang Fm	~1.73	17.9	38.2	7.2	+ – + + + + –	Idnurm et al., 1995
18	Fiery Creek Fm	*1.71?*	23.9	31.8	10.4	– + + – + – –	Idnurm, 2000
19	West Branch Volcanics	1.71	15.9	20.5	11.3	+ + + + + – –	Idnurm, 2000

No.	Rock unit	Age (Ga)	Plat (°N)	Plong (°E)	A_{95} (°)	Q	References
20	Mallapunyah Fm	*1.67–1.65*	35.0	34.3	3.1	+ + + + + + +	Idnurm et al., 1995
21	Tooganinie Fm	*1.65–1.64*	61.0	6.7	6.1	+ + + + + + +	Idnurm et al., 1995
22	Emmerugga dolomite	*1.65–1.64*	79.1	22.6	6.1	+ + + + + – –	Idnurm et al., 1995
23	Balbirini dolomite – lower	1.61	66.1	357.5	5.7	+ + + – + + +	Idnurm, 2000
24	Balbirini dolomite – upper	1.59	52.0	356.1	7.5	+ + + – + + +	Idnurm, 2000
25	WAC– Gnowangerup–Fraser dykes	1.21	–55.8	143.9	6.5	+ + + + + + –	Pisarevsky et al., 2014b

Putative ages are in italics. Quality criteria from left to right are: well–determined rock age, sufficient number of samples (N > 24, k ≥10, A95 ≤ 16.0°), step-wise demagnetization, positive field tests, structural control and tectonic coherence with the craton discussed, and presence of reversals, and no resemblance to paleopoles of younger age. Marking as "+" when meeting, or marked as "–".

Table 5 Euler rotation parameters (to the absolute framework)

Block	Pole (°N)	(°E)	Angle (°)	Block	Pole (°N)	(°E)	Angle (°)
1.32 Ga				~1.21 Ga			
NCC	–32.72	–44.19	–124.58	NCC	–28.56	–59.28	–101.23
NAC	–4.44	–55.92	–178.78	NAC	–8.42	–80.02	–132.82
WAC	–7.96	–47.31	–214.38	WAC	–14.45	–67.02	–162.38
SAC	–7.96	–47.31	–214.38	SAC	–14.45	–67.02	–162.38

9.4 Geological constraints of reconstruction

The McArthur Basin in the NAC was suggested to be correlative to the Yanliao Rift because of the presence of coeval ~1.32 Ga mafic sills and comparable strata, e.g., the Xiamaling Formation with the Roper Group (Figure 16) (Zhang et al., 2017). The Yanliao Rift consists of the Changcheng (~1.70–1.60 Ga) and Jixian (~1.60–1.40 Ga) groups, the Xiamaling Formation (~1.40–1.35? Ga), and the geochronologically poorly constrained Qingbaikou Group (Su et al., 2010) (Figure 16). The McArthur Basin is better documented and is broadly divided geographically into the southern and northern McArthur Basin (Ahmad et al., 2013). Stratigraphically, the basin is sub-divided into five disconformity-bound packages according to lithofacies, age dating results and stratigraphic relationships (Ahmad et al., 2013). It is generally considered that during deposition sedimentary units were continuous across most of the basin and are well correlated throughout (Ahmad et al., 2013). In this thesis, I discuss the Katherine River (~1.82? –1.71 Ga) and Parsons Range (~1.71–1.67 Ga) groups from the northern McArthur Basin, and the McArthur (~1.67–1.60 Ga), Nathan (~1.60–1.58 Ga) and Roper (~1.5–1.35? Ga) groups from its southern and central regions (Ahmad et al., 2013). Apart from those recognised by Zhang et al. (2017), there are more comparable geological features between the two basins (Figure 16) that are consistent with the proposed NCC-NAC connection during the Proterozoic.

(1) Strata and environmentally sensitive fossil record. Basins on both cratons dominantly received clastic sediments during ~1.70–1.60 Ga, with minor carbonates – – the ~1.64 Ga dolostone in the Changcheng Group (Yanliao Rift) and the McArthur Group (McArthur Basin). Both basins also recorded mainly clastic sedimentation after ~1.4 Ga (Ahmad et al., 2013; Su et al., 2010) (Figure 16). Furthermore, the oldest eukaryotic microfossils *Valeria lophostriata*, showing complex wall structure and concentric striations, have been found in both the lower Changcheng Group of the Yanliao Rift and the Mallapunyah Formation of the McArthur Group (lower McArthur Basin) (Javaux and Lepot, 2018) (Figure 16).

Nonetheless, there are also differences between the two basins. In contrast to the Yanliao Rift, the McArthur Basin contains pre–1.70 Ga strata and ~1.58–1.50 Ga sediments are absent (Figure 16). This depositional hiatus in the McArthur Basin was characterised by east-northeast to south-southwest shortening throughout the entire basin and is correlative with the ~1.60 to 1.50 Ga Isan Orogeny in the Mount Isa Inlier

(to the east of the McArthur Basin) (Rawlings, 1999). Other stratigraphic differences between the two cratons (Figure 16) could be caused by lateral variations within large sedimentary system (e.g., Ahmad et al., 2013).

(2) Magmatic events. The ~1.73 Ga Miyun dolerite dykes intruded the Archean basement in the Yanliao Rift (Peng, 2015b). Similarly, in the McArthur Basin ~1.73 Ga Oenpelli dolerite sills were emplaced into sandstones of the Katherine River Group as well as the neighbouring Pine Creek Orogen to the northwest (Whelan et al., 2016). Furthermore, the ~1.72 Ga Jimbu Microgranite featuring abundant K–feldspar phenocrysts rimmed by albite intruded the Katherine River Group in northwestern McArthur Basin (Rawlings and Page, 1999), which can be correlated with ~1.73–1.68 Ga rapakivis or K–rich granites, anorthosites, mangerites, and alkali granitoids emplaced in the basement of the Yanliao Rift (e.g., Zhang et al., 2007). The Yanliao Rift recorded ~1.64 and 1.62 Ga volcanic eruptions (Zhang et al., 2013) that might be coeval with tuffs layers in the McArthur Basin (Ahmad et al., 2013) (Figure 16), and ~1.49–1.48 Ga tuffaceous layers are also found in both basins (Ahmad et al., 2013; Li et al., 2014) (Figure 16).

Coeval ~1.32 Ga magmatic events are recorded in both basins (Figure 16): the Datong dyke (1326 ± 4 Ma) and Yanliao sills (peak age at ~1323 Ma) in the NCC (Peng, 2015b; Zhang et al., 2017), and the Galiwinku dyke swarm (1324–1329 Ma) and Derim–Derim sills (1324±4 Ma) in the NAC (Whelan et al., 2016). The ~1.32 Ga magmatism in the NCC was interpreted to represent a large igneous province (LIP) because (i) it covers $>1.2 \times 10^5$ km^2; (ii) pre–magmatic uplift occurred 20 myr prior to the LIP, and (iii) the sills are typical of within-plate tectonic settings (Zhang et al., 2017). The Galiwinku dykes and the Derim–Derim sills also cover a large area (Whelan et al., 2016) and could be plume products.

Zhang et al. (2017) suggested that both the unconformity (or disconformity) between the Xiamaling Formation and the Qingbaikou Group (Yuxian uplift), and the unconformity between the Roper Group and the overlying Cambrian strata in the McArthur Basin, represent the same pre-magmatic uplift of the ~1.32 Ga LIP event, possibly related to the breakup of the supercontinent Nuna.

(4) Ore deposits. Dolostone-hosted manganese deposits are found in both the Jixian Group of the Yanliao Rift (Fan et al., 1999) and the Nathan Group of the McArthur Basin (Ahmad et al., 2013) (Figure 16). The deposits in both basins occur as irregular

lenses or veinlets in strata, mainly hosted in shallow marine sediments, implying a similar genesis (Ahmad et al., 2013; Fan et al., 1999).

Correlative iron deposits are also found in both basins (Figure 16). The Sherwin Formation (upper Roper Group, McArthur Basin) comprises shale, sandy mudstone and sandstone, within lenses of massive oolitic to pisolitic beds, interbedded with medium to rather coarse chamosite–siderite (Ferenczi, 2001). The iron ore of the Sherwin Formation consists of hematite and/or goethite, and greenalite ooids. Chamosite and hematite are partly replaced by siderite by post-diagenetic processes, producing the silica (chert) cement. The stratiform siderites with minor hematite have been reported from the middle part of the Xiamaling Formation (~1.40–1.35? Ga) in the Yanliao Rift (Tang et al., 2018). The siderites of the Xiamaling Formation contain hematite inclusions, indicating iron reduction process during early diagenesis (Tang et al., 2018).

(5) Hydrocarbon-bearing potential. Several potential hydrocarbon source rocks have been reported from the McArthur and Roper groups of the McArthur Basin (Figure 16). Among those, ~1.64 Ga mudstones have high Total Organic Carbon (TOC) contents (up to 8%) (Ahmad et al., 2013), whereas those from the middle Roper Group have TOC of 1–3% (some up to 8–12%) (Ahmad et al., 2013). Similarly, rocks with hydrocarbon-bearing potential have also been discovered in the Yanliao Rift (Figure 16). The middle Changcheng Group (~1.65 Ga?) and the Xiamaling Formation have TOC values of 0.6–15% (average 2%) and 3–21% (average 5.2%), respectively (Zhao et al., 2018).

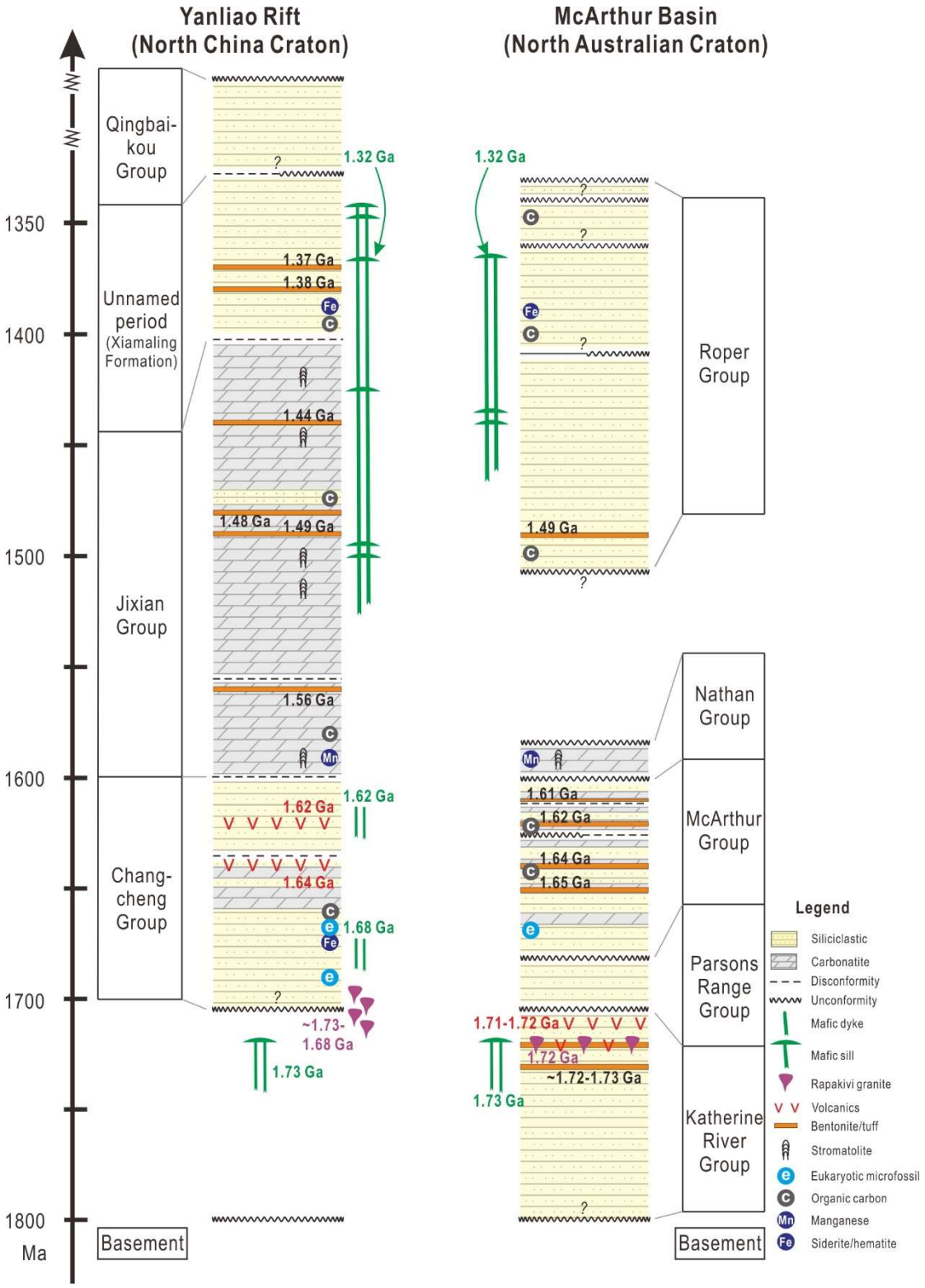

Figure 16 Time-space diagram outlining tectonostratigraphic correlations between the Yanliao Rift of the North China Craton and the McArthur Basin of the North Australian Craton. Columns of the Yanliao Rift and McArthur Basin are compiled after Su et al. (2010) and Ahmad et al. (2013), respectively.

10. Conclusion

(1) By detailed field observation, petrology, geochronology and geochemistry analyses, a ~1.24-1.21 Ga large igneous province has been proposed.

(2) By paleomagnetic studies, I preliminarily obtain the 1.68 Ga and 1.24 Ga paleopoles of the North China Craton, with the latter passing the baked contact test.

(3) The paleomagnetic reconstruction supports the long-lived connection between northeastern North China and northwestern Australia between ~1.78 Ga and ~1.32 Ga. The two blocks may have separation at ~1.24-1.21 Ga.

(4) The geological records between the Yan-Liao rift of the North China and the McArthur basin of the Australia support the paleomagnetic reconstruction.

References

Ahmad, M., Dunster, J., Munson, T., 2013. Chapter 15: McArthur Basin: in Ahmad M and Munson TJ (compilers). Geology and mineral resources of the Northern Territory. Northern Territory Geological Survey, Special Publication 5.

Cederberg, J., Söderlund, U., Oliveira, E.P., Ernst, R.E., Pisarevsky, S.A., 2016. U-Pb baddeleyite dating of the Proterozoic Pará de Minas dyke swarm in the São Francisco craton (Brazil) – implications for tectonic correlation with the Siberian, Congo and North China cratons. Gff 138, 219-240.

Chen, L., Huang, B., Yi, Z., Zhao, J., Yan, Y., 2013. Paleomagnetism of ca. 1.35Ga sills in northern North China Craton and implications for paleogeographic reconstruction of the Mesoproterozoic supercontinent. Precambrian Research 228, 36-47.

Ding, J., 2017. A combined Geochronological and Paleomagnetic study on ~1220 Ma mafic dykes in the North China Craton and its implications for the transition from Nuna to Rodinia. China University of Geosciences (Beijing) PhD thesis, 1-112.

Dunlop, J.D., Özdemir, Ö., 1997. Rock Magnetism: Fundamentals and frontiers. Cambridge University Press, pp. 1-573.

Ernst, R.E., 2014. Large igneous provinces. Cambridge University Press.

Ernst, R.E., Baragar, W.R.A., 1992. Evidence from magnetic fabric for the flow pattern of magma in the Mackenzie giant radiating dyke swarm. Nature 356, 511-513.

Evans, D., Li, Z.-X., Murphy, J., 2016. Four-dimensional context of Earth's supercontinents. Geological Society, London, Special Publications 424, SP424. 412.

Evans, D.A.D., Mitchell, R.N., 2011. Assembly and breakup of the core of Paleoproterozoic-Mesoproterozoic supercontinent Nuna. Geology 39, 443-446.

Fan, D., Yang, P., Wang, R., 1999. Characteristics and origin of the middle Proterozoic Dongshuichang chambersite deposit, Jixian, Tianjin, China. Ore Geology Reviews 15, 15-29.

Ferenczi, P., 2001. Iron ore, manganese and bauxite deposits of the Northern Territory. Northern Territory Geological Survey.

Halls, H.C., Li, J., Davis, D., Hou, G., Zhang, B., Qian, X., 2000. A precisely dated Proterozoic palaeomagnetic pole from the North China craton, and its relevance

to palaeocontinental reconstruction. Geophysical Journal International 143, 185-203.
He, T., Zhou, Y., Vermeesch, P., Rittner, M., Miao, L., Zhu, M., Carter, A., Pogge von Strandmann, P.A.E., Shields, G.A., 2017. Measuring the 'Great Unconformity' on the North China Craton using new detrital zircon age data. Geological Society, London, Special Publications 448, 145-159.
Hou, G., Santosh, M., Qian, X., Lister, G.S., Li, J., 2008. Configuration of the Late Paleoproterozoic supercontinent Columbia: Insights from radiating mafic dyke swarms. Gondwana Research 14, 395-409.
Hu, G., Zhao, T., Zhou, Y., 2014. Depositional age, provenance and tectonic setting of the Proterozoic Ruyang Group, southern margin of the North China Craton. Precambrian Research 246, 296-318.
Idnurm, M., 2000. Towards a high resolution Late Palaeoproterozoic–earliest Mesoproterozoic apparent polar wander path for northern Australia. Australian Journal of Earth Sciences 47, 405-429.
Idnurm, M., Giddings, J., Plumb, K., 1995. Apparent polar wander and reversal stratigraphy of the Palaeo-Mesoproterozoic southeastern McArthur Basin, Australia. Precambrian Research 72, 1-41.
Jaffey, A., Flynn, K., Glendenin, L., Bentley, W.t., Essling, A., 1971. Precision measurement of half-lives and specific activities of U 235 and U 238. Physical Review C 4, 1889.
Javaux, E.J., Lepot, K., 2018. The Paleoproterozoic fossil record: Implications for the evolution of the biosphere during Earth's middle-age. Earth-Science Reviews 176, 68-86.
Kim, S.W., Cho, D.-L., Lee, S.-B., Kwon, S., Park, S.-I., Santosh, M., Kee, W.-S., 2018. Mesoproterozoic magmatic suites from the central-western Korean Peninsula: Imprints of Columbia disruption in East Asia. Precambrian Research 306, 155-173.
Kirscher, U., Liu, Y., Li, Z.X., Mitchell, R.N., Pisarevsky, S.A., Denyszyn, S., Nordsvan, A., 2019. Paleomagnetism of the Hart Dolerite (Kimberley, Western Australia) - a two-stage assembly of the supercontinent Nuna? Precambrian Research 329, 170-181.
Kirscher, U., Mitchell, R., Liu, Y., Li, Z., Cox, G., Nordsvan, A., Wang, C., Pisarevsky, S., 2018. Long lived supercontinent Nuna-updated paleomagnetic constraints from Australia, AGU Fall Meeting Abstracts.
Kirschvink, J., 1980. The least-squares line and plane and the analysis of palaeomagnetic data. Geophysical Journal of the Royal Astronomical Society 62, 699-718.
Kusky, T., Li, J., Santosh, M., 2007. The Paleoproterozoic North Hebei Orogen: North China craton's collisional suture with the Columbia supercontinent. Gondwana Research 12, 4-28.
Li, H., Su, W., Zhou, H., Xiang, Z., Tian, H., Yang, L., Huff, W.D., Ettensohn, F.R., 2014. The first precise age constraints on the Jixian System of the Meso-to Neoproterozoic Standard Section of China: SHRIMP zircon U-Pb dating of bentonites from the Wumishan and Tieling formations in the Jixian Section, North China Craton. Acta Petrologica Sinica 30, 2999-3012.
Li, X.H., Liu, Y., Li, Q.L., Guo, C.H., Chamberlain, K.R., 2009. Precise determination of Phanerozoic zircon Pb/Pb age by multicollector SIMS without external standardization. Geochemistry, Geophysics, Geosystems 10.
Li, Y., Peng, P., Wang, X., Wang, H., 2015. Nature of 1800–1600Ma mafic dyke swarms

in the North China Craton: Implications for the rejuvenation of the sub-continental lithospheric mantle. Precambrian Research 257, 114-123.
Li, Z.-X., 2000. Palaeomagnetic evidence for unification of the North and West Australian cratons by ca. 1.7 Ga: new results from the Kimberley Basin of northwestern Australia. Geophysical Journal International 142, 173-180.
Li, Z.X., Bogdanova, S.V., Collins, A.S., Davidson, A., De Waele, B., Ernst, R.E., Fitzsimons, I.C.W., Fuck, R.A., Gladkochub, D.P., Jacobs, J., Karlstrom, K.E., Lu, S., Natapov, L.M., Pease, V., Pisarevsky, S.A., Thrane, K., Vernikovsky, V., 2008. Assembly, configuration, and break-up history of Rodinia: A synthesis. Precambrian Research 160, 179-210.
Li, Z.X., Evans, D.A.D., 2010. Late Neoproterozoic 40 intraplate rotation within Australia allows for a tighter-fitting and longer-lasting Rodinia. Geology 39, 39-42.
Liu, C., Zhao, G., Liu, F., Shi, J., 2017. Detrital zircon U-Pb and Hf isotopic and whole-rock geochemical study of the Bayan Obo Group, northern margin of the North China Craton: Implications for Rodinia reconstruction. Precambrian Research 303, 372-391.
Lowrie, W., 1990. Identification of ferromagnetic minerals in a rock by coercivity and unblocking temperature properties. Geophysical research letters 17, 159-162.
Lu, S., Li, H., 1991. A precise U-Pb single zircon age determination for the volcanics of Dahongyu Foramation, Changcheng System in Jixian. Acta Geosicientia Sinica 22, 137-145.
Lurcock, P.C., Wilson, G.S., 2012. PuffinPlot: A versatile, user-friendly program for paleomagnetic analysis. Geochemistry, Geophysics, Geosystems 13.
Meert, J.G., 2014. Strange attractors, spiritual interlopers and lonely wanderers: The search for pre-Pangean supercontinents. Geoscience Frontiers 5, 155-166.
Nordsvan, A.R., Collins, W.J., Li, Z.-X., Spencer, C.J., Pourteau, A., Withnall, I.W., Betts, P.G., Volante, S., 2018. Laurentian crust in northeast Australia: Implications for the assembly of the supercontinent Nuna. Geology 46, 251-254.
Pearce, J.A., 2008. Geochemical fingerprinting of oceanic basalts with applications to ophiolite classification and the search for Archean oceanic crust. Lithos 100, 14-48.
Pei, F., Ye, Y., Wang, F., Cao, H., Lu, S., Yang, D., 2013. Discovery of Mesoproterozoic diabase dyke in Tonghua region, Jilin Province and its tectonic implications. Journal of Jilin University (Earth Science Edition) 43, 110-118.
Pei, J., Yang, Z., Zhao, Y., 2006. A Mesoproterozoic paleomagnetic pole from the Yangzhuang Formation, North China and its tectonics implications. Precambrian Research 151, 1-13.
Peng, P., 2015a. Late Paleoproterozoic–Neoproterozoic (1800–541 Ma) Mafic Dyke Swarms and Rifts in North China. 171-204.
Peng, P., 2015b. Precambrian mafic dyke swarms in the North China Craton and their geological implications. Science China Earth Sciences 58, 649-675.
Peng, P., Bleeker, W., Ernst, R.E., Söderlund, U., McNicoll, V., 2011a. U–Pb baddeleyite ages, distribution and geochemistry of 925Ma mafic dykes and 900Ma sills in the North China craton: Evidence for a Neoproterozoic mantle plume. Lithos 127, 210-221.
Peng, P., Liu, F., Zhai, M., Guo, J., 2012. Age of the Miyun dyke swarm: Constraints on the maximum depositional age of the Changcheng System. Chinese Science Bulletin 57, 105-110.
Peng, P., Wang, X., Windley, B.F., Guo, J., Zhai, M., Li, Y., 2014. Spatial distribution

of ~1950–1800Ma metamorphic events in the North China Craton: Implications for tectonic subdivision of the craton. Lithos 202-203, 250-266.
Peng, P., Zhai, M.-G., Li, Q., Wu, F., Hou, Q., Li, Z., Li, T., Zhang, Y., 2011b. Neoproterozoic (~900Ma) Sariwon sills in North Korea: Geochronology, geochemistry and implications for the evolution of the south-eastern margin of the North China Craton. Gondwana Research 20, 243-254.
Peng, P., Zhai, M., Ernst, R.E., Guo, J., Liu, F., Hu, B., 2008. A 1.78 Ga large igneous province in the North China craton: The Xiong'er Volcanic Province and the North China dyke swarm. Lithos 101, 260-280.
Peng, P., Zhai, M., Zhang, H., Guo, J., 2005. Geochronological Constraints on the Paleoproterozoic Evolution of the North China Craton: SHRIMP Zircon Ages of Different Types of Mafic Dikes. International Geology Review 47, 492-508.
Peng, T., Wilde, S.A., Fan, W., Peng, B., Mao, Y., 2013. Mesoproterozoic high Fe–Ti mafic magmatism in western Shandong, North China Craton: Petrogenesis and implications for the final breakup of the Columbia supercontinent. Precambrian Research 235, 190-207.
Pisarevsky, S.A., Elming, S.-Å., Pesonen, L.J., Li, Z.-X., 2014a. Mesoproterozoic paleogeography: Supercontinent and beyond. Precambrian Research 244, 207-225.
Pisarevsky, S.A., Wingate, M.T.D., Li, Z.-X., Wang, X.-C., Tohver, E., Kirkland, C.L., 2014b. Age and paleomagnetism of the 1210Ma Gnowangerup–Fraser dyke swarm, Western Australia, and implications for late Mesoproterozoic paleogeography. Precambrian Research 246, 1-15.
Polat, A., Hofmann, A.W., Rosing, M.T., 2002. Boninite-like volcanic rocks in the 3.7–3.8 Ga Isua greenstone belt, West Greenland: geochemical evidence for intra-oceanic subduction zone processes in the early Earth. Chemical Geology 184, 231-254.
Pourteau, A., Smit, M.A., Li, Z.-X., Collins, W.J., Nordsvan, A.R., Volante, S., Li, J., 2018. 1.6 Ga crustal thickening along the final Nuna suture. Geology 46, 959-962.
Radhakrishnamurthy, C., 1993. M-26. Magnetism and Basalts. GSI Publications 1.
Rawlings, D., 1999. Stratigraphic resolution of a multiphase intracratonic basin system: the McArthur Basin, northern Australia. Australian Journal of Earth Sciences 46, 703-723.
Rawlings, D., Page, R., 1999. Geology, geochronology and emplacement structures associated with the Jimbu Microgranite, McArthur Basin, Northern Territory. Precambrian Research 94, 225-250.
Rogers, J.J.W., Santosh, M., 2002. Configuration of Columbia, a Mesoproterozoic Supercontinent. Gondwana Research 5, 5-22.
Schmidt, P.W., Williams, G.E., 2008. Palaeomagnetism of red beds from the Kimberley Group, Western Australia: implications for the palaeogeography of the 1.8 Ga King Leopold glaciation. Precambrian Research 167, 267-280.
Seton, M., Müller, R.D., Zahirovic, S., Gaina, C., Torsvik, T., Shephard, G., Talsma, A., Gurnis, M., Turner, M., Maus, S., Chandler, M., 2012. Global continental and ocean basin reconstructions since 200Ma. Earth-Science Reviews 113, 212-270.
Stacey, J.S., Kramers, J.D., 1975. Approximation of terrestrial lead isotope evolution by a two-stage model. Earth and Planetary Science Letters 26, 207-221.
Su, W., Li, H., Huff, W., Ettensohn, F., Zhang, S., Zhou, H., Wan, Y., 2010. SHRIMP U-Pb dating for a K-bentonite bed in the Tieling Formation, North China. Chinese Science Bulletin 55, 3312-3323.

Su, W., Li, H., Xu, L., Jia, S., Geng, J., Zhou, H., Wang, Z., Pu, H., 2012. Luoyu and Ruyang Group at the south margin of the North China Craton (NCC) should belong in the Mesoproterozoic Changchengian System: Direct constraints from the LA-MC-ICPMS U-Pb age of the tuffite in the Luoyukou Formation, Ruzhou, Henan, China. Geological Survey and Research 35, 96-108.

Sun, S.-S., McDonough, W.-S., 1989. Chemical and isotopic systematics of oceanic basalts: implications for mantle composition and processes. Geological Society, London, Special Publications 42, 313-345.

Tang, D., Shi, X., Jiang, G., Wu, T., Ma, J., Zhou, X., 2018. Stratiform siderites from the Mesoproterozoic Xiamaling Formation in North China: Genesis and environmental implications. Gondwana Research 58, 1-15.

Taylor, S.R., 1964. Abundance of chemical elements in the continental crust: a new table. Geochimica et Cosmochimica Acta 28, 1273-1285.

Teixeira, W., Oliveira, E.P., Peng, P., Dantas, E.L., Hollanda, M.H.B.M., 2017. U-Pb geochronology of the 2.0 Ga Itapecerica graphite-rich supracrustal succession in the São Francisco Craton: Tectonic matches with the North China Craton and paleogeographic inferences. Precambrian Research 293, 91-111.

Wan, B., Windley, B.F., Xiao, W., Feng, J., Zhang, J., 2015. Paleoproterozoic high-pressure metamorphism in the northern North China Craton and implications for the Nuna supercontinent. Nat Commun 6, 8344.

Wang, C., Peng, P., Wang, X., Yang, S., 2016. Nature of three Proterozoic (1680Ma, 1230Ma and 775Ma) mafic dyke swarms in North China: Implications for tectonic evolution and paleogeographic reconstruction. Precambrian Research 285, 109-126.

Wang, W., Liu, S., Santosh, M., Zhang, L., Bai, X., Zhao, Y., Zhang, S., Guo, R., 2015. 1.23 Ga mafic dykes in the North China Craton and their implications for the reconstruction of the Columbia supercontinent. Gondwana Research 27, 1407-1418.

Wang, Y., Zhao, G., Fan, W., Peng, T., Sun, L., Xia, X., 2007. LA-ICP-MS U–Pb zircon geochronology and geochemistry of Paleoproterozoic mafic dykes from western Shandong Province: Implications for back-arc basin magmatism in the Eastern Block, North China Craton. Precambrian Research 154, 107-124.

Whelan, J.A., Beyer, E.E., Donnellan, N., Bleeker, W., Chamberlin, K.R., Söderlund, U., Ernst, R.E., 2016. 1.4 billion years of Northern Territory geology: Insights from collaborative U-Pb zircon and baddeleyite dating, Annual Geoscience Exploration Seminar (AGES) Proceedings, Alice Springs, Northern Territory 15–16 March 2016.

Winchester, J.A., Floyd, P.A., 1977. Geochemical discrimination of different magma series and their differentiation products using immobile elements. Chemical Geology 20, 325-343.

Wu, H., 2005. New paleomagnetic results from Mesoproterozoic successions in Jixian Area, North China Block, and their implications for paleocontinental reconstructions. China University of Geosciences (Beijing) PhD thesis, 1-133.

Wu, H., Zhang, S., Li, Z.-X., Li, H., Dong, J., 2005. New paleomagnetic results from the Yangzhuang Formation of the Jixian System, North China, and tectonic implications. Chinese Science Bulletin 50, 1483-1489.

Xiang, Z., 2014. Mesoproterozoic magmatic events and mineralization in the North China Craton. China University of Geosciences, Beijing, pp. 1-227.

Xiang, Z., Li, H., Lu, S., Zhou, H., Li, H., Wang, H., Chen, Z., Niu, J., 2012. Emplacement age of the gabbro-diabase dike in the Hongmen scenic region of

Mount Tai, Shandong Province, North China: Baddeleyite U-Pb precise dating. Acta Petrologica Sinica 28, 2831-2842.
Xu, H., Yang, Z., Peng, P., Meert, J.G., Zhu, R., 2014. Paleo-position of the North China craton within the supercontinent Columbia: Constraints from new paleomagnetic results. Precambrian Research 255, 276-293.
Xu, Y., Chung, S.-L., Jahn, B.-m., Wu, G., 2001. Petrologic and geochemical constraints on the petrogenesis of Permian–Triassic Emeishan flood basalts in southwestern China. Lithos 58, 145-168.
Yang, J., Wu, F., Liu, X., Xie, L., 2005. Zircon U–Pb ages and Hf isotopes and their geological significance of the Miyun rapakivi granites from Beijing, China. Acta Petrologica Sinica 21, 1633-1644.
Yang, K.-F., Fan, H.-R., Santosh, M., Hu, F.-F., Wang, K.-Y., 2011. Mesoproterozoic mafic and carbonatitic dykes from the northern margin of the North China Craton: Implications for the final breakup of Columbia supercontinent. Tectonophysics 498, 1-10.
Zhai, M.-G., Santosh, M., 2011. The early Precambrian odyssey of the North China Craton: A synoptic overview. Gondwana Research 20, 6-25.
Zhai, M., 2011. Cratonization and the Ancient North China Continent: A summary and review. Science China Earth Sciences 54, 1110-1120.
Zhang, S.-H., Liu, S.-W., Zhao, Y., Yang, J.-H., Song, B., Liu, X.-M., 2007. The 1.75–1.68 Ga anorthosite-mangerite-alkali granitoid-rapakivi granite suite from the northern North China Craton: Magmatism related to a Paleoproterozoic orogen. Precambrian Research 155, 287-312.
Zhang, S.-H., Zhao, Y., Li, X.-H., Ernst, R.E., Yang, Z.-Y., 2017. The 1.33–1.30 Ga Yanliao large igneous province in the North China Craton: Implications for reconstruction of the Nuna (Columbia) supercontinent, and specifically with the North Australian Craton. Earth and Planetary Science Letters 465, 112-125.
Zhang, S.-H., Zhao, Y., Ye, H., Hu, G.-H., 2016. Early Neoproterozoic emplacement of the diabase sill swarms in the Liaodong Peninsula and pre-magmatic uplift of the southeastern North China Craton. Precambrian Research 272, 203-225.
Zhang, S., Li, Z.-X., Evans, D.A.D., Wu, H., Li, H., Dong, J., 2012. Pre-Rodinia supercontinent Nuna shaping up: A global synthesis with new paleomagnetic results from North China. Earth and Planetary Science Letters 353-354, 145-155.
Zhang, S., Li, Z., Wu, H., 2006. New Precambrian palaeomagnetic constraints on the position of the North China Block in Rodinia. Precambrian Research 144, 213-238.
Zhang, S., Zhao, Y., Ye, H., Hu, J., Wu, F., 2013. New constraints on ages of the Chuanlinggou and Tuanshanzi formations of the Changcheng System in the Yan-Liao area in the northern North China Craton. Acta Petrologica Sinica 29, 2481-2490.
Zhao, G., Cawood, P.A., Li, S., Wilde, S.A., Sun, M., Zhang, J., He, Y., Yin, C., 2012. Amalgamation of the North China Craton: Key issues and discussion. Precambrian Research 222-223, 55-76.
Zhao, G., Cawood, P.A., Wilde, S.A., Sun, M., 2002. Review of global 2.1–1.8 Ga orogens: implications for a pre-Rodinia supercontinent. Earth-Science Reviews 59, 125-162.
Zhao, G., Li, S., Sun, M., Wilde, S.A., 2011. Assembly, accretion, and break-up of the Palaeo-Mesoproterozoic Columbia supercontinent: record in the North China Craton revisited. International Geology Review 53, 1331-1356.

Zhao, G., Sun, M., Wilde, S.A., Li, S., 2003. Assembly, Accretion and Breakup of the Paleo-Mesoproterozoic Columbia Supercontinent: Records in the North China Craton. Gondwana Research 6, 417-434.

Zhao, T., Chen, F., Zhai, M., Xia, B., 2004a. Single zircon U-Pb ages and their geological significance of the Damiao anorthosite complex, Hebei Province, China. Acta Petrologica Sinica 20, 685-690.

Zhao, T., Zhai, M., Xia, B., Li, H., Zhang, Y., Wan, Y., 2004b. Zircon U-Pb SHRIMP dating for the volcanic rocks of the Xiong'er Group: Constraints on the initial formation age of the cover of the North China Craton. Chinese Science Bulletin 49, 2495-2502.

Zhao, T., Zhu, G., Lin, S., Wang, H., 2016. Indentation-induced tearing of a subducting continent: Evidence from the Tan–Lu Fault Zone, East China. Earth-Science Reviews 152, 14-36.

Zhao, W., Hu, S., Wang, Z., Zhang, S., Wang, T., 2018. Petroleum geological conditions and exploration importance of Proterozoic to Cambrian in China. Petroleum Exploration and Development 45, 1-14.